LA--11808-C

DE90 010253

US-Japan Workshop on Field-Reversed Configurations with Steady-State High-Temperature Fusion Plasmas and the 11th US-Japan Workshop on Compact Toroids

Compiled by
D. C. Barnes
J. C. Fernández
D. J. Rej

Los Alamos Los Alamos National Laboratory
Los Alamos,New Mexico 87545

US-JAPAN WORKSHOP ON FRCs WITH STEADY STATE HIGH-TEMPERATURE FUSION PLASMAS

11th US-JAPAN WORKSHOP ON COMPACT TOROIDS

Los Alamos National Laboratory
November 7-9, 1989

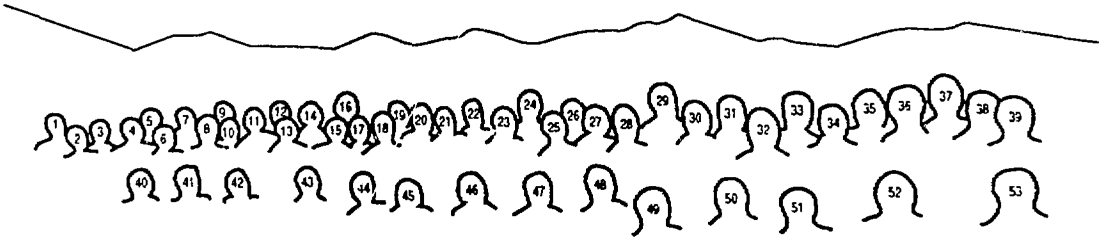

1. C. Sovinec
2. D. Rej
3. T. Jarboe
4. H. Berk
5. E. Ruden
6. S. Sugimoto
7. D. Taggart
8. M.-Y. Hsiao
9. J. Hammer
10. R. Stachowski
11. W. Kernbichler
12. J.-L. Gauvreau
13. R. Mayo
14. I. Henins
15. Y. Tomita
16. C. Barnes
17. A. Hoffman
18. J. Staudenmeier
19. G. Cunningham
20. W. Dove
21. R. Milroy
22. A. Molvik
23. A. Sgro
24. R. Linford
25. S. Hamaguchi
26. J. Fernandez
27. R. Hess
28. J. Slough
29. B. Wright
30. J. B. Taylor
31. Y. Nogi
32. M. Nishikawa
33. N. Amemiya
34. A. Ishida
35. E. Crawford
36. M. Ohnishi
37. A. Filuk
38. G. Marklin
39. H. Momota
40. N. Krall
41. R. Nebel
42. E. Morse
43. R. Gerwin
44. M. Brown
45. R. Siemon
46. R. Brooks
47. M. Baron
48. C. Hartman
49. S. Goto
50. M. Katsurai
51. M. Tuszewski
52. D. Barnes
53. L. Steinhauer

CONTENTS

FRC Reactors:

FRC Large orbit stability:

FRC Transport:

FRC experiments:

High-energy ion rings:

Spheromak theory and experiment:

PROCEEDINGS OF THE US-JAPAN WORKSHOP ON FIELD-REVERSED CONFIGURATIONS WITH STEADY-STATE HIGH-TEMPERATURE FUSION PLASMAS AND THE 11TH US-JAPAN WORKSHOP ON COMPACT TOROIDS

ABSTRACT

The US-Japan Workshop on Field-Reversed Configurations with Steady-State High-Temperature Fusion Plasma and the 11th US-Japan Workshop on Compact Toroids were held at Los Alamos National Laboratory, Los Alamos, New Mexico on November 7-9, 1989. These proceedings contain the papers presented at the workshops as submitted by the authors.

Technical Summary

US-JAPAN WORKSHOP ON FIELD-REVERSED CONFIGURATIONS WITH STEADY-STATE HIGH-TEMPERATURE FUSION PLASMAS

and

11th US-JAPAN WORKSHOP ON COMPACT TOROIDS

D. C. Barnes, J. C. Fernández, and D. J. Rej
Los Alamos National Laboratory, Los Alamos NM 87545, USA

Two US-Japan Workshops on the physics and technology of compact toroid plasmas were hosted by Los Alamos National Laboratory on November 7 through November 9, 1989. Compact toroids (CTs) are configurations confined principally by magnetic fields generated by internal plasma currents. The toroidal currents are unencumbered by material objects such as magnet coils or vacuum vessel. CTs are usually classified into two categories, the field-reversed configuration (FRC), a very high-β prolate plasma, and the spheromak, often a more oblate configuration.

The first workshop, *The US-Japan Workshop on Field-Reversed Configurations with Steady-State High-Temperature Fusion Plasmas,* dealt exclusively with the theoretical aspects of the FRC. Both experimental and theoretical papers on FRCs and Spheromaks were presented at the second workshop, *The 11th US-Japan CT Workshop* which immediately followed the first.

The technical program is reprinted in Appendix A. All together, there were 48 presentations, evenly divided in oral and poster sessions. There were 61 registered participants from 23 different institutions (see Appendix A). Ten participants were from Japan, two from Europe, with the remainder from the US.

US-JAPAN WORKSHOP ON FIELD-REVERSED CONFIGURATIONS WITH STEADY-STATE HIGH-TEMPERATURE FUSION PLASMAS

There were 15 papers presented during the workshop from 9 different institutions. These contributions were in three subject areas related to the possible achievement of a steady-state high-temperature FRC plasma in a reactor-relevant regime. Areas emphasized were reactor studies, stability, and transport.

In the area of reactor studies, the main issues facing the FRC are to increase confinement by several orders of magnitude to a few seconds in a reactor relevant regime, and to address other issues specific to the FRC geometry, including the optimum ion temperature for a D-T reactor, the possibility of non-ignited systems, operation in an intermediate s regime (similar to the Field-Reversed Mirror regime), and the attractive possibility to utilize advanced fuel cycles, such as D-^{3}He.

Progress on FRC reactor studies reported during the workshop includes optimized startup scenarios using neutral-beam injection to increase flux and current by the Ohkawa current, and a novel design for direct conversion of 15-MeV protons using an "inverse linac" approach. In addition, several presentations consistently identified the design points for D-T and D-^{3}He systems. For D-T, $r_s \sim$ 1.2-1.5 m, $s \sim 20$, and $\tau_E \sim 2$ s are required, while for D-^{3}He, r_s is comparable, s is raised to ~ 40, and τ_E to ~ 5 s.

The current directions for near-term FRC reactor research were identified. First, considerable work is planned by the Nagoya University group in identifying a startup scenario to avoid the need for a D-T burn phase. Secondly, reactor designs will continue to evolve as more complete models of equilibrium and stability become available. In addition, the unique features of the FRC may lead to reactor embodiments differing considerably from the *in situ* designs presently of interest, such as formation at low density using fast reconnection, translation, compression heating, *etc.*

Considerable progress on stability issues, primarily concerned with the internal tilt mode, was reported. The main issues continue to be possible avenues to tilt stability at increasing s, and improved fluid models to corroborate and extend Vlasov calculations. Recent progress was reported in extending the linearized fluid work begun at Niigata University and Spectra Technology by the inclusion of gyroviscosity. A new Migma-like system called *Exyder* was described and shown to derive stability from the properties of the applied magnetic field. Finally, two Los Alamos papers described tilt stability results for non-Maxwellian ion distributions, in the two extreme cases of a two-temperature ion distribution and in the case of a relatively cold rotating ion beam component. In the latter case, stability with energetic beam components of a few 10^{-3} inventory fraction was demonstrated by simulation of a MHD/beam system.

The main directions for FRC stability studies are to incorporate additional large-orbit and two-fluid effects into fluid stability studies to sharpen the predictions of stability boundaries, to continue to examine MHD/beam systems to optimize the required beam fraction, and to refine detailed comparisons of theoretical stability predictions with experimental observations.

Progress on FRC transport issues was also reported. Transport issues are anomalous transport associated with low-level turbulence, geometric and profile effects on global confinement, and narrowing of various candidate models which make vastly different predictions for confinement when extrapolated to the reactor regime. Progress reported at this workshop included (angular) momentum constraints associated with anomalous transport, a new "1.4-D" transport model incorporating dominant geometric effects in a fast algorithm, and further understanding of the nonlinear stage of high-frequency flute-like electrostatic modes. In addition, possible enhancement of the FRC flux loss rate by turbulent and stochastic ion orbit effects was considered. Velocity space particle loss was also discussed and shown to be an important effect in the current FRC regime.

Current directions include a more detailed comparison of competing models with the expanding experimental data base, and the extension of plasma simulation methods to longer time scales.

Finally, an examination of the several conclusions supported by the papers and discussion sessions of the workshop indicates that two main points emerged. Recent improvements in the calculation of the equilibrium and stability of MHD/beam FRC systems suggests that an early experimental investigation of the formation and stability properties of a beam-stabilized FRC is an appropriate element of the present large-s experimental thrust of the international program. Secondly, understanding the physics of anomalous transport will likely require a more detailed measurement of the fluctuation spectra, and simultaneously an improvement in the theoretical predictions.

11th US-JAPAN WORKSHOP ON COMPACT TOROIDS

Field-reversed configurations

There were 14 papers related to the field-reversed configuration (FRC) presented at the CT Workshop by researchers from 6 different institutions. Results from experiments dominated the presentations. Principal topics included FRC formation, equilibrium, stability, heating and confinement, and high-energy ion production and injection.

The Spectra Technology group optimized FRC formation at large reversed-bias magnetic fields on the *TRX* device. Rapid losses caused by violent axial contractions were eliminated with the application of duodecopole barrier fields during the preionization (PI) phase. Survival of the contractions was attributed to an increased symmetry in the PI plasma caused by the barrier field. Advanced formation techniques developed on the *TRX* devices have been incorporated into the design of the new *LSX* facility, under construction at STI. The scientific goals, engineering details, schedule, and status of *LSX* were the subject of another paper presented at the Workshop.

Tomographic inversions of visible continuum light was successfully implemented for the first time on an FRC. The 50-chord system, developed at Osaka University, was used to reconstruct the radial and azimuthal equilibrium profile of the emission intensity of FRCs in the *FIX* device. Axially-integrated 2-D intensity profiles were also inferred with a new soft x-ray imaging diagnostic under development by a Los Alamos group.

The magnitude of the $n=2$ rotational instability was suppressed by oscillating toroidal fields on the *NUCTE* device at Nihon University. The B_θ fields, generated by oscillating axial currents applied to an equilibrium FRC, did however drive a disruptive kink mode. Control of the $n=2$ mode without kinking should be achievable provided the B_θ stability threshold is sufficiently small with a shear factor q < 1. A theory developed at Osaka University predicts such a threshold at higher B_θ frequencies.

Odd *n=1* magnetic asymmetries, consistent with MHD predictions of the internal tilt mode, were detected with external magnetic probes on FRCs in the θ-pinch source of the *FRX-C/LSM* device at Los Alamos. Large magnitudes of the asymmetry were found correlated with short confinement times.

High-power auxiliary heating was also demonstrated on *FRX-C/LSM*. Translated FRCs were compressed by a magnetic field and substantial heating was observed. Ion temperatures in excess of 1 keV were confirmed by pressure balance, neutron emission, and impurity Doppler broadening. Significant electron heating was also measured.

While FRCs were translated and compressed at Los Alamos, they where translated and expanded on the *FIX* device at Osaka University. Large separatrix volumes (up to 0.4 m^3) resulted, and remarkably long configuration lifetimes of up to 0.5 ms were observed, without any evidence of the *n=2* mode. Another important first, realized on *FIX*, was the injection of high-energy neutral particle beams into FRCs. Preliminary observations with hydrogen and helium beams, used as ion and electron temperature diagnostics, were reported.

A new parallel-powered coil configuration was brought into operation on the *CSS* device at the University of Washington. Annular FRCs were formed at relatively low loop voltages (≤100 V), and the poloidal flux confinement times were longer than in previous experiments. A power balance model for *CSS* was also presented. A concentrated current density profile results in more localized ohmic heating; consequently, impurity radiation losses, believed to dominate earlier shorter-lived experiments, may be better tolerated during formation.

The important new theoretical results on energetic particle ring stabilization of the FRC internal tilt mode were complemented by the experimental work performed by two groups at Cornell University. First results from ion injection and ring formation in the *MICE* device were presented, along with a review of the physics, parameters, and projections for a ring-FRC merging experiment. Two principal issues include the number of particles that can be extracted from an intense particle beam accelerator and the trapping mechanism in an FRC. Experiments with a plasma anode, similar to the one that enhanced ion production on the *LONGSHOT* experiment, were about to start on the higher-energy *NEPTUNE* accelerator.

Spheromaks

There were 19 papers related to the spheromak, a number which reflects the fact that, in addition to the traditional spheromak research motivated by fusion energy applications, there are now at least comparable resources devoted to spheromak research motivated by defense-related applications (radiation production, hypervelocity projectiles, *etc.*). Happily, regardless of the motivation behind the research, the results from all groups are generally useful, either because of their complementary or comparative natures. Although the majority of the contributions are experimental in nature, there are significant contributions of a more theoretical, modeling, or systems-analysis nature.

The *TS-3* group from the University of Tokyo presented results from their recently-modified device, which allowed flexible magnetic helicity injection (and spheromak production) with an axial discharge between the outer electrodes of two opposed coaxial guns and/or with a z-θ discharge. An external bias field could also be used. They presented data about the production of stable flux-core spheromaks FCS (also known as "bumpy z-pinches"). In the FCS, a current hole (flux trapped in the spheromak geometric axis along which no current flows) could modify the spheromak q-profile to increase magnetic shear and increase the β limit. The q-profile could be modified to the extent that it can resemble that of the ultra-low-q and tokamak configurations.

CTCC-II device at Osaka University features helicity injection by a magnetized plasma gun into an ellipsoidal aluminum flux conserver. The combination of a "choking coil" and a stainless-steel entrance region allowed current-limiting on the outer flux surfaces to produce a FCS. *CTCC-II* discharges are known to have 7-12% β at the magnetic axis, as determined from Thomson scattering. The Osaka paper illustrated how an MHD equilibrium model, incorporating separate parallel and perpendicular pressures, produces a significantly better fit to the experimentally measured magnetic profiles.

Although primarily a US-Japan Workshop, this conference broadened its scope with the British contribution from *SPHEX* device located at the University of Manchester. *SPHEX* features magnetic helicity injection into a flux conserver designed to minimize the magnetic flux penetrating the solid wall (field errors) and the associated helicity losses. The *SPHEX* group presented results which reproduce well some expected key features. These include magnetic profiles close to the minimum-energy state, the presence of rotating kink modes, and a gun current/flux ratio which must be exceeded to obtain plasma and helicity injection. The surprising feature is the large current which enters the flux conserver wall opposite to the gun, probably caused by processes other than simple flux diffusion.

The *MARAUDER* experiment, under construction at the Kirtland Air Force Base Weapons Laboratory, intends to form a spheromak with a 500-kJ capacitor bank driving a coaxial gun, and accelerate the spheromak with the 9-MJ *Shiva Star* bank. The aim is to achieve ultra-high directed energy and radiation. Simulations of spheromak formation were performed with the 2-D MHD code *MACH2*. The results explored the range of gun parameters which result (or do not result) in spheromak formation. A key feature identified is the need for sufficient mass density to allow a sufficiently high ratio of magnetic/kinetic energy, which in turn allows proper reconnection of the magnetic field.

In the Livermore *RACE* experiment, a coaxial gun forms spheromaks (plasma rings) which are then accelerated along coaxial electrodes. Rings have been generated with velocities of up to 3×10^8 cm/s, with kinetic energies of 20 kJ. Stagnation of the rings against a copper plate has produced 2.7 kJ of soft X-rays, with a spectrum above 10 eV. Focusing of the rings to about a third of the initial diameter has been demonstrated. Design of the Compact Torus Accelerator (*CTA*) within the *RACE* program is proceeding. *CTA* has potential, when scaled to high energies (~ 100 MJ), for fusion applications. These include radiation production for indirect ICF drive and magnetically-insulated, inertially-confined fusion.

A Caltech group experimented with helicity and plasma injection from a coaxial gun into the *ENCORE* tokamak. They injected into the magnetized vacuum vessel (no plasma) and observed a resulting magnetic structure with $m=1$ symmetry. In their experiments of injection into a tokamak discharge, they demonstrated toroidal current drive, with fast toroidal current increases of ~30%.

In *BCTX* at UC Berkeley, a coaxial magnetized gun injects magnetic helicity and plasma into a mesh-walled spheromak flux conserver. The purpose of this experiment is to eventually test a 20-40 MW pulsed lower-hybrid heating scheme. Spheromak lifetimes of 100 μs have been achieved in the 0.7-m-radius mesh flux conserver. These spheromaks exhibit the expected $m=1$ kink instability, rotating at a high rate. Optimization of plasma parameters is proceeding. Plasma heating experiments await the completion of the 40-MW, 450-MHz RF source. The RF drive components are now in place.

In the University of Maryland Spheromak *MS*, formation is achieved using the z-θ discharge method. The spheromak magnetic field structures were mapped out in detail. The plasma was asymmetric during formation, evolving into a tilt followed by rapid plasma loss. Asymmetries were attributed to the reversal field coils or feed connections to the I_z electrodes. As remedies for the tilt, a stainless steel liner and copper cones were ineffective, while Figure-8 coils slowed it down. Titanium gettering and Elkonite electrodes were used to reduce impurity problems. Doppler broadening of OII, OIII, OIV indicated anomalously-high ion temperatures of about 30, 75, 90 eV, respectively. HeII temperatures as high as 100 eV at the geometric axis were measured. Strong visible and UV radiation was observed surrounding the electrodes. Line-averaged electron density from a multi-chord interferometer was shown. Greater density than that provided by the fully ionized fill in some cases indicated a large impurity influx. The particle confinement time was about 95 μs. Results from a 0-D energy-balance code revealed that a reduction in impurity content is needed to get higher electron temperatures.

There are two spheromak devices at Los Alamos, *CTX* and *HESS*. Presently, the *CTX* facility is aimed at producing clean, high-magnetic-field spheromaks by helicity and plasma injection into a flux conserver with solid walls. Suitable spheromaks will be compressed by the wall, driven by high explosives (HE). Ultimately, the spheromak will be used as an energy transfer and switching medium for accelerating metal foils to hypervelocity. The poor energy confinement times found in the former mesh-flux-conserver was attributed to high edge helicity dissipation caused by magnetic field errors at the spheromak edge. Much-improved energy confinement times were subsequently observed in the solid flux conserver (designed to minimize field errors), as high as 180 μs, and a clear pressure-driven instability under these conditions was observed. The "bow-tie" flux conserver was proposed as a simple way to achieve higher stable plasma pressures. A detailed theoretical discussion of the "bow-tie" high-β flux conserver was presented. A detailed comparison of the measured plasma-gun impedance with an MHD model of plasma flow (assuming a nozzle is formed at the gun muzzle) yielded reasonable agreement. Thomson scattering, density interferometry, and B-field data from small, high B-field spheromaks were presented. The data showed T_e as high as 400 eV, n_e in the range of 3-8 × 10^{14} cm^{-3}, and maximum internal B-field in the range of 2.2-2.6 T. The stability properties of the $n=1$ and $n=2$ modes during decay were discussed. Bolometry, spectroscopy, and Doppler T_i data was also presented. Radiation losses were shown not to dominate, while impurity-line radiation behavior was consistent with the multi-hundred eV electron temperatures measured with Thomson scattering. Doppler T_i values increased during strong $n=2$ kink activity, to values as high as 1 keV. The detailed design of a new plasma gun and flux conserver suitable for the *CTX* programmatic goal was presented, as well as positive results from an HE-driven dome inversion experiment.

The mechanical-helicity-injection experiment *HESS* was explained. In this scheme, an HE-driven cylindrical wall generates helicity by driving an initial solenoidal magnetic field into twisted grooves in a concentric opposing wall. A detailed design and a summary of the construction progress was described.

DIRECT ENERGY CONVERSION OF 15MeV FUSION PROTONS

Hiromu Momota

National Institute for Fusion Science, Nagoya 464-01, Japan

In D-^{3}He fuels burning in a field reversed configuration, a certain amount of fusion energy is carried by fusion protons that escape directly out of the plasma$^{1)}$. In a 1GW$_e$ reactor, for instance, power carried by fusion protons amounts to approximately 300MW. Those protons have to be introduced to a pair of direct energy convertors installed at both wings of the field-reversed configuration. Unfortunately, the energy of the fusion protons is 15MeV which is much higher than the engineering limit of a traditional electrostatic direct energy convertor$^{2)}$. Here the author presents a use of the principle of a "Linac$^{3)}$" for a direct energy convertor applicable to 15MeV protons.

Physical Background

In an FRC/D-^{3}He burning plasma, both 300MW of 15MeV fusion protons escape directly out of plasma and 700MW of thermal ions are lost out of the plasma. The energy carried by a thermal component of plasma ions is possibly converted to electricity with traditional direct energy convertors behind an expander and an electron collector, while the energetic fusion protons are free to pass through the direct energy convertor, they will be once modulated and then decelerated at the down streams.

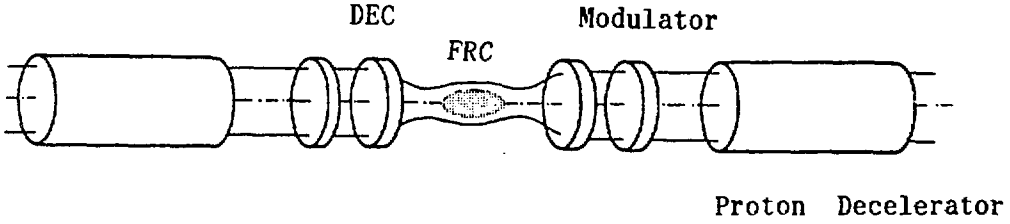

Fig.1

A schematic drawing of these convertors is exhibited in Fig.1. The radius of direct energy convertors for the thermal component is chosen as 10m so that it avoids the problems of heat into the collector plate. It may be natural to assume that the radius of the direct energy convertor for 15MeV proton is comparable to that of thermal component. Thus the relation:

$$300\text{MW}/2 = 15\text{MeV} \times 5\times10^{7}\text{m/s} \times N_p \times 314\text{m}^2 \qquad (1)$$

gives the density N_p of energetic protons to be $4\times10^{9}/\text{m}^3$. Since the characteristic length L of our interests is less than 100m, the potential V that is produced by the proton beams is

$$V = L^2 N_p e/\varepsilon_0 < 8\times10^5 \text{ Volts} \qquad (2)$$

that is much lower than the beam energy: 15MV. Thus collective effects in the beam dynamics can be ignored and the trajectory of a beam proton can be approximated by that of a single particle in an external field.

Beam Modulation

As fusion protons are streaming along the magnetic channels, they are once modulated with an electric field excited by grid meshes installed in the proton streams, so as to give a traveling electric field in the x-direction:

$$\begin{aligned} E(x,t) &= -E_0\{(x-Ut)/d - [(x-Ut)/d]\} \quad &&\text{for } -d<x<d \\ &= 0 &&\text{otherwise} \end{aligned} \qquad (3)$$

here, [ ] denotes the integral part of the respective quantity. Then a proton whose initial velocity is v and the position is x_0 between -d and d at the time $t = 0$ suffer a change δv in its velocity, provided that the change is much smaller than the initial velocity:

$$\delta v = -(eE_0/M)2Ux_0/v^2 \qquad (4)$$

The position of this particle at the time t is, therefore,

$$x(t) = vt + \{1-(eE_0/M)2Ut/v^2\}x_0 \qquad (5)$$

If all protons have a common velocity U, then the position of particles at the time $t = MU/2eE_0$ is independent of their initial position x_0, and consequently the particles whose positions at the time $t = 0$ are between $-d$ and d focus strongly to the point:

$$x = MU^2/2eE_0 = x_f \qquad (6)$$

The velocity of fusion protons, nevertheless, is distributive. Accordingly the focus point is also distributive as is described by the equation:

$$x = x_f + (x_f+2x_0)(v-U)/U \qquad (7)$$

The values U will be $5.3\text{x}10^7$m/s which corresponds to the energy of fusion protons of 14.7MeV and velocity spread of fusion protons is $0.3\text{x}10^7$m/s. As is discussed later, a spread of focus point has to be much less than a quarter of the wave length of the carrier wave, that is 3.2m in our case. Further, a small value of the velocity change δv associated with the beam modulation is also needed to avoid spoiling a trapping of the beam particles within a certain phase of the carrier wave. Assuming an electric field E_0 = 1MV/m is applicable to a set of grid meshes at the modulation region $-d<x<d$ with d = 2m, we have bunching of the 15MeV protons within a reasonable size of 0.8m, which determines the total length of the modulation region x_f = 15m. The change of beam velocity associated with this beam modulation is less than $7\text{x}10^6$m/sec.

Energy Recovery with a Carrier Wave

Assume that a modulated proton beam particle of a velocity U is picked up at $t = t_0$ and $x = x_f$ on the phase ϕ of a traveling wave[4) that is described by:

$$E(x,t) = E^0\cos\{ \int_{x_f}^{x} k(\xi)d\xi \quad -\omega(t-t_0)+\phi\} \tag{8}$$

with $$\omega/k(x) = \sqrt{U^2 +2(e/M)E^0(x-x_f)\cos(\phi)} \tag{9}$$

then, the particle suffers a constant force: $eE^0\cos(\phi)$ and its resultant velocity is the same as $\omega/k(x)$. This can be seen as follows: Let $\Psi(x,t)$ be the phase in the cosine on the rhs of eq.(6). The equation of motion for the particle and eq.(7) yield the differential equation along the particle's trajectory:

$$(1/k)d\{(1/k)d\Psi/dt\}/dt +(eE^0/\omega M)\cos\phi(1/k)d\Psi/dt$$
$$= (eE^0/kM)\{\cos\Psi-\cos\phi\} \tag{10}$$

with initial conditions: $\Psi = \phi$ and $d\Psi/dt = 0$. The solution to this equation satisfying initial conditions is obviously $\Psi(x,t) = \phi$ at any time. Thus the equation of motion for this particle is

$$M\, d^2x/dt^2 = eE^0\cos\,\phi \tag{11}$$

If the value ϕ has a value between $\pi/2$ and $3\pi/2$, the particle is decelerated by the carrier wave. This may be an opposite choice of the phase to the case of "Linac" where a charged particle is accelerated.

One of the other important problems is the self-phasing of the particles at a certain phase of the carrier wave. In order to study the self-phasing effect, we consider a small deviation $\xi(t)$ of the position of a particle from the position $x(t)$ placed at the phase $\Psi = \phi$. The equation of motion for this particle takes the form:

$$M\, d^2\{x+\xi\}/dt^2 = eE^0\cos\{\Psi+k\xi\} \tag{12}$$

or $$d^2\xi/dt^2 = -(e/M)E^0\sin\phi\ \ k\xi \tag{13}$$

If the initial phase ϕ takes the value between 0 and π, then the deviation is never growing: the self-phasing effect takes place. As a result, if we choose an initial phase ϕ between $\pi/2$ and π, the modulated particle beam is decelerating in a stable manner.

Since the initial velocity of particles U is 5.3×10^7m/s, a choice of E^0 = 1MV/m and $\phi = (3/4)\pi$ gives a reasonable length of deceleration channel of 15MeV fusion protons as approximately 21m.

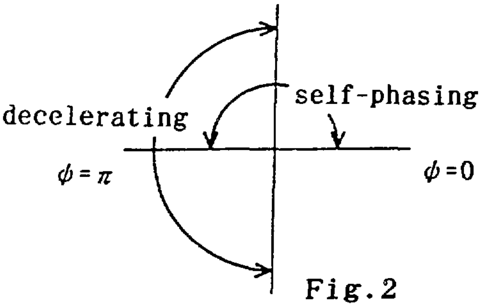

Fig.2

Trapping of Particles

Finally, we will justify the trapping of the fusion protons whose velocity distribution is somewhat spreading. Since the temperature of the fusion plasma is 100keV, the energy spread of fusion protons is approximately 1.8MeV, or its velocity spreads is around 3.2×10^6m/s. Further, the change of the beam velocity due to the beam modulation is less than 1.6×10^6m/s. The trapping of the particles can be analyzed on the bases of the equation of motion:

$$Md^2\xi/dt^2 = eE^0\{\cos(\Psi-k\xi)-\cos\phi\}$$

$$= -eE^0\{\cos(k\xi-\pi/4)-1/\sqrt{2}\} \qquad (14)$$

By defining the variable $\eta = d\xi/dt$, this equation can be rewritten as:

$$d\eta/d\xi = -(eE^0/M)\{\cos(k\xi-\pi/4)-1/\sqrt{2}\}/\eta \qquad (15)$$

Solutions to this equation are illustrated in Fig.3.

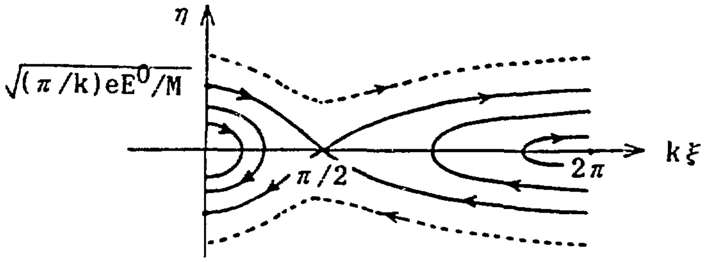

Fig.3

Particles once inside the separatrix are trapped and subsequently trapped, by virtue of the self-phasing property. The maximum of velocity deviation η that are trapped is $\sqrt{(\pi/k)eE^0/M}$, or for our choice of parameters, the maximum of the velocity deviation is 4.95×10^7m/s. Since this value is larger than the velocity spread attributed to the thermal spread of fuel plasma or beam modulation, the modulated proton beam is trapped during the deceleration process of the 15MeV protons.

So far we analyzed a method to convert the fusion energy carried by 15MeV fusion protons, and found that a use of the principle of "Linac" is reliable. Two dimensional detailed studies including the effects of shape of the grids are, however, left to future researches as well as drawing of a power system available to this direct energy convertor. A certain optimization study is needed to obtain a higher efficiency of the energy conversion with a decreased length of the convertor.

References

1) H.Momota, M.Okamoto, Y.Nomura, M.Ohnishi, H.L.Berk, and T.Tajima; Nuclear Instruments and Methods in Physics Research A271 (1988) 7

2) R.F.Post; Fusion Technology: Energy 70, Las Vegas, Nevada, September 1970.
also refer G.H.Miley; "Fusion Energy Conversion", American Nuclear Society, 1976 , Chap.3

3) D.W.Fry, R.B.R.S.Harvie, L.B.Mullett, and W.Walkinshaw; Nature 160 (1947), 351

4) M.I.Mirkin and R.J.Briggs; Phys.Fluids 16 (1973), 929

DYNAMICS OF FRC EQUILIBRIA TO D-^{3}He IGNITION STATE

Yukihiro Tomita

National Institute for Fusion Science, Nagoya 464-01, JAPAN

1. Introduction

D-^{3}He fuels reaction has high potential for commercial fusion reactor$^{1)}$. On the other hand a plasma confined in an FRC appears to be attractive for D-^{3}He fuels. A plasma temperature at D-^{3}He ignition state is as high as $100keV$. In FRC plasma produced by conventional method (e.g. FRTP), an attainable temperature is lower than $1keV$. This low temperature has to be heated up to a D-^{3}He ignition one. While a heating assisted by D-T reaction has been studied$^{2)}$, but certain engineering problems are still left, which are very hard to be resolved.

We investigate the possibility of evolution without D-T assistance, and clarify the condition required for this evolution.

2. Dynamics of FRC plasma

The FRC plasma is grown up to ignition state by means of magnetic compression, flux supply, plasma heating, and particle supply. Time evolution of the plasma can be described by the equation of internal poloidal magnetic flux φ_i ,

$$\frac{1}{\varphi_i}\frac{d\varphi_i}{dt}\Big]_{spl} = \frac{1}{B_e}\frac{dB_e}{dt} + \frac{2}{r_s}\frac{dr_s}{dt} + h(\langle\beta\rangle)\frac{1}{\langle\beta\rangle}\frac{d\langle\beta\rangle}{dt} + \frac{1}{\tau_{\varphi_i}}, \tag{1}$$

the equation of plasma energy W_p,

$$\frac{1}{W_p}\frac{dW_p}{dt} = \frac{1}{\langle p\rangle}\frac{d\langle p\rangle}{dt} + \frac{2}{r_s}\frac{dr_s}{dt} + \frac{1}{l_s}\frac{dl_s}{dt} \tag{2}$$

$$= \left(P_{in} + P_{fp} - P_{br} - P_{sy} - \frac{W_p}{\tau_\varepsilon} \right) / W_p,$$

and the continuity of the particle number N_j of respective species,

$$\frac{1}{N_j}\frac{dN_j}{dt}\Big]_{spl} = \frac{1}{\langle n_j\rangle}\frac{d\langle n_j\rangle}{dt} + \frac{2}{r_s}\frac{dr_s}{dt} + \frac{1}{l_s}\frac{dl_s}{dt} + \frac{1}{\tau_{Nj}}. \qquad (3)$$

The subscript j stands for D or ^{3}He and the subscript spl represents the externally supplied terms. The quantities B_e, $\langle p\rangle$, r_s, l_s, τ_ε, and τ_{Nj} denote the external magnetic field, spatially averaged plasma pressure, separatrix radius , separatrix length, energy confinement time, and particle confinement time, respectively. The quantities P_{in},P_{fp},P_{br}, and P_{sy} are the external injection power, heating power due to charged fusion products, Bremsstrahlung radiation power, and synchrotron radiation power, respectively. The coefficient $h(\langle\beta\rangle)$ indicates a change rate of φ_i due to that of spatially averaged beta value $\langle\beta\rangle$. This coefficient $h(\langle\beta\rangle)$ is shown in Fig.1 as a function of $\langle\beta\rangle$ for cases of rigid-rotor and Hill's vortex profile.

The internal poloidal magnetic flux is supplied by a injection of D neutral beams. Provided that an effective charge number of the plasma Z_{eff} is between 1 and 2, the drive current is proportional to $Z_{eff}-1$ for reason of Ohkawa effect.

3. Evolution of FRC plasma to ignition state

The objective plasma parameters are : at initial state ; $T=1keV$, $\langle n_e\rangle=1.3\times10^{20}m^{-3}$, $B_e=0.3T$, $\tau_\varepsilon=0.2\,\mathrm{sec}$, and at ignition state ; $T=100keV$, $\langle n_e\rangle=5.2\times10^{20}m^{-3}$, $B_e=6.4T$, $\tau_\varepsilon=2.5\,\mathrm{sec}$.

During an evolution of plasma to ignition state, the change rate of r_s is determined by the balance between flux supply and the sum of the increase of magnetic flux and the flux loss. Provided that average beta $\langle\beta\rangle$ depends on r_s only, a balance between the flux supply and the sum of the increase of flux and the flux loss is needed to keep a separatrix radius in a constant value :

$$\frac{d\varphi_i}{dt}\Big]_{spl} = \frac{\varphi_i}{\tau_{\varphi i}} + \frac{\varphi_i}{B_e}\frac{dB_e}{dt}. \qquad (4)$$

This required flux supply is presented in Fig.2 as a function of plasma temperature during the time of 50 sec for cases of rigid-rotor and Hill's vortex profile. A classical flux loss time $\tau_{\varphi i} = \varphi_i / 2\pi R \eta J_\theta]_{r=R}$, where R and η are a field-null radius and plasma resistivity, respectively. The required flux supply is $\sim 0.1V$ for rigid-rotor equilibrium and that of Hill's vortex profile is as large as nearly twice that of rigid-rotor's one.

Evolution time is determined by the condition that increment of internal flux is smaller than initial loss rate :

$$\frac{1}{B_e}\frac{dB_e}{dt} < \frac{1}{\tau_{\varphi i}} \tag{5}$$

, so as to avoid too large flux supplies. In this case, the evolution time becomes larger than 50 sec for both profiles : rigid-rotor and Hill's vortex.

On the other hand, heating input power determined a plasma pressure and separatrix length l_s. Under the condition of constant r_s, the balance between the sum of heat input and heating due to charged fusion products and the sum of the radiation loss , heat loss, and increment of plasma pressure :

$$P_{in} + P_{fp} = P_{br} + P_{sy} + \frac{W_p}{\tau_\varepsilon} + \frac{W_p}{\langle p \rangle}\frac{d\langle p \rangle}{dt}, \tag{6}$$

keep the separatrix length l_s to be constant. An anomaly factor of energy confinement time is introduced to an classical energy confinement time, which is proportional to $T^{\alpha_{ex}}$. The required heating power density is shown in Fig.3 as a function of evolution temperature for $\alpha_{ex} = 1.0$. The initial required power density is $0.3 MW/m^3$ and, on the way to evolution, the power density becomes $3.5 MW/m^3$. In Fig.4 the maximum required power density is presented as a function of α_{er}.

Required particle supply is shown in Fig.5 under the condition that both r_s and l_s are constant. This required value is approximately $10^{20}/m^3 \sec$.

4. Summary

The evolution of D-^{3}He/FRC plasma from the low $T(\sim 1keV)$ - low $n_e(\sim 10^{20}m^{-3})$ initial state to the ignition state ($T\sim 100keV$, $n_e \sim 5\times 10^{20}m^{-3}$) was shown to be reliable with reasonable supplies of particles, magnetic flux, and heat. The evolution time became larger than 50 sec to avoid too much power of supplies. Under the condition that both of r_s and l_s are constant, flux supply , maximum heating power density ,and particle supply are required to be $0.1V$, $3.5MW/m^3$, and $10^{20}/m^3 \sec$, respectively. As far as the anomaly factor depends on $T^1 \sim T^2$, D-^{3}He ignition state is attainable with reasonable power supplies and no D-T assistance.

References

1) H.Momota et al., Fusion Technol. 11 (1987) 436.

2) M.Ohnishi et al., Fusion Technol. 12 (1987) 249.

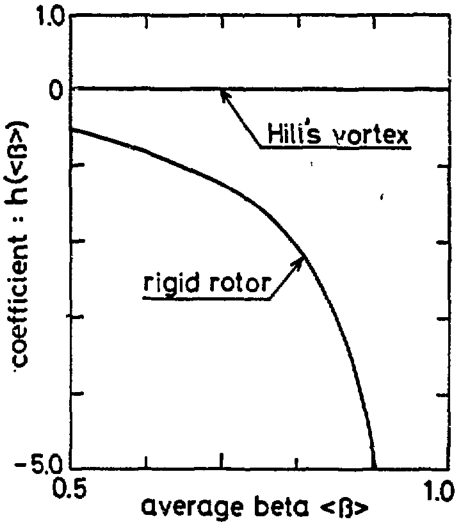

Fig.1 Change rate coefficient of φ_i due to change of $\langle\beta\rangle$, $h(\langle\beta\rangle)$, as a function of $\langle\beta\rangle$ for cases of rigid-rotor and Hill's vortex profile.

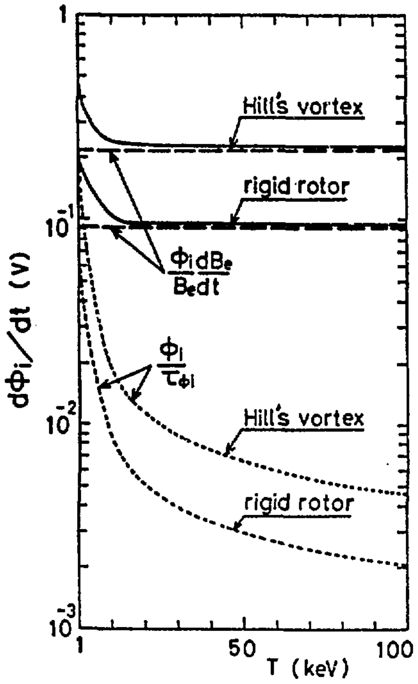

Fig.2 Required flux supply to keep r_s constant as a function of evolution temperature.

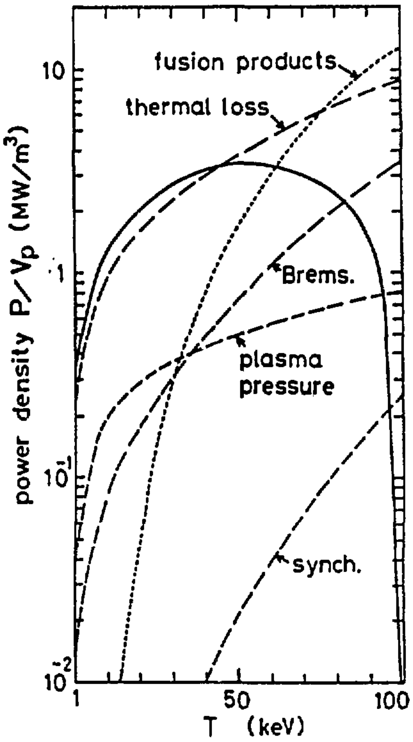

Fig.3 Required heat input power density to keep l_s constant for the case that anomaly factor is proportional to T, and respective power density are also shown.

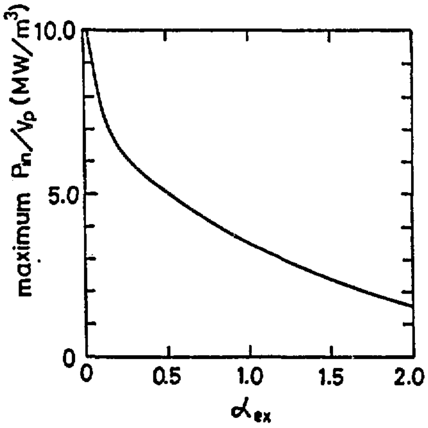

Fig.4 Maximum required power density as a function of exponent α_{ex} of anomaly factor.

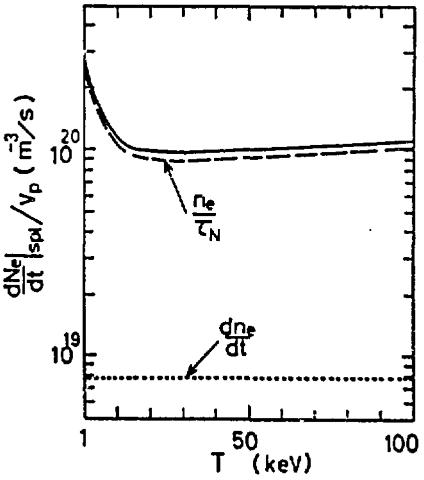

Fig.5 Required particle supply for evolution time 50sec and α_{ex}=1.0.

Reactor Potential of Steady-State Field-Reversed Configurations [1] [2]

WINFRIED KERNBICHLER
Alternate Energy Physics Program
Institute for Theoretical Physics
Graz University of Technology
A–8010 Graz, Austria

Abstract

The intrinsic potential of a Field-Reversed Configuration (FRC) for high-β operation – with β-values in the range of 50 to 100% – stimulates much interest in this device as an attractive candidate for a compact fusion device with high power density. Several additional benefits, e.g. the cylindrical geometry of the concept, the divertor action of the open field lines and the possibility for direct energy conversion of the charged particle flow, justify a closer look at the benefits and problems of FRCs. Present emphasis is on operation with D-^{3}He fuel under reactor relevant conditions, whereas D-T is taken as a reference case. A steady-state version of an FRC is considered to be more attractive than its pulsed counterpart. Frequent start-up to high temperatures would be particularly detrimental for D-^{3}He where start-up scenarios seem to rely on the transition from D-T to D-^{3}He, with unavoidable strong tritium contamination.

1. Introduction

Our investigation uses a profile-averaged computer model to simulate steady-state operation in an FRC. In this context much care is given to radiation losses, confinement expressions, fusion reactions among the fast and thermal plasma constituents, and to loss and slowing-down of fast fusion products. Rigid rotor type profiles are used for the radial dependency of density and magnetic field strength, whereas the temperature is taken to be spatially constant. These computations reveal the basic properties of fusion plasmas in an FRC. Here special emphasis is given to ignition windows in the temperature-density space and to power densities, energy content in the plasma, neutron production, wall loading, current requirement, output power split and fast ion behaviour. The sensitivity of these results to changes in the reactor size is discussed in detail.

---

[1] Supported by: Department of Science and Research, Friedrich Schiedel Foundation (all Austria) and International Atomic Energy Agency

[2] Presented at: U.S.–Japan Workshop on Field-Reversed Configurations with Steady-State High-Temperature Fusion Plasmas, Los Alamos National Laboratory, Los Alamos, NM, U.S.A, November 7–8, 1989

Table 1: FRC reference parameter set

		D-^{3}He	D-T	
Separatrix Radius	r_{sep}	1.5	1.5	m
Reversal Factor	k	1.0	1.0	
Elongation	κ	5.0	5.0	
External Field Strength	B_{ext}	7.5	2.5	T
Wall Radius	r_w	2.2	2.2	m
Major Radius	R	1.1	1.1	m
Field Strength at Separatrix	B_{sep}	5.7	1.9	T
Average Beta	$<\beta>$	0.76	0.76	
x_s-Factor	x_s	0.69	0.69	
Flux	Φ	1.8	0.6	Wb
Midplane Current	I	9.2	3.1	MA
Plasma Volume	V	53	53	m^3
First Wall Surface	S	137	137	m^2
Volume/Surface Ratio	V/S	0.39	0.39	m
Ion Temperature	T_i	80	20	keV
Electron Temperature	T_e	71	21	keV
Average Ion Density	$<n_i>$	4.6 10^{20}	2.5 10^{20}	m^{-3}
Average Electron Density	$<n_e>$	7.2 10^{20}	2.7 10^{20}	m^{-3}
Energy Confinement Time	τ	5	2	sec
Impurity Concentration	ϵ_{imp}	1	1	%
Charge of Impurities	Z_{imp}	6	6	
Mass of Impurities	A_{imp}	12	12	
Wall Reflectivity	Γ	0.9	0.9	

2. Reference Parameter Set

Table 1 gives a reference paramter set for both a D-^{3}He and a D-T version. The main differences in the choice of these parameter sets are (i) the much lower external magnetic field strength of 2.5 T for D-T as compared to 7.5 T for D-^{3}He, and (ii) the lower operating temperature of 20 keV for D-T as compared to 80 keV for D-^{3}He. These two choices recognize the different temperature behaviour of the reactivity parameter $<\sigma v>$ for both fuel cycles and its different absolut values. They ensure approximately the same range of fusion power density and overall wall loading values. The changes in flux, midplane current and particle densities are a result of field and temperature changes. In addition, the requirement for energy confinement is somewhat relaxed for D-T, therefore a reference time of 2 seconds was chosen for D-T in contrast to 5 seconds for the D-^{3}He case.

3. Results

Tables 1 and 2 give basic results for both D-^{3}He and D-T operation in FRCs. From these tables, one can see that for both fuel cycles a separatrix radius of 1.5 m results in about the same ignition margin which does not improve significantly with an increase in size but drops quickly below 1 with a decrease in size (which means that the

Table 2: Sensitivity of D-^3He plasma parameters to the plasma size

r_{sep}	[m]	0.75	1.0	1.5	2.0	2.5
Volume	[m^3]	6.6	15.7	53.0	125.6	245.3
Flux	[Wb]	0.45	0.81	1.83	3.25	5.08
Current	[MA]	4.6	6.2	9.2	12.3	15.4
T_{ig}^{low}	[keV]	-	77.5	47.9	45.7	45.2
T_{ig}^{up}	[keV]	-	89.6	160.	169.	172.
Ign. Margin	[-]	0.4	1.0	1.8	2.0	2.0
P_{fu}	[MWm^{-3}]	21.9	19.6	16.6	16.1	16.0
$P_{fu,tot}$	[MW]	145.	307.	879.	2020.	3922.
E-content	[MJ]	155.	354.	1130.	2654.	5175.
P_{tr}/P_{out}	[-]	0.19	0.23	0.25	0.26	0.26
P_{st}/P_{out}	[-]	0.00	0.00	0.21	0.26	0.27
P_{fast}/P_{out}	[-]	0.43	0.33	0.08	0.03	0.01
P_{br}/P_{out}	[-]	0.32	0.37	0.39	0.39	0.39
P_{sy}/P_{out}	[-]	0.02	0.02	0.02	0.02	0.02
P_n/P_{out}	[-]	0.03	0.03	0.03	0.03	0.03
S-Factor	[-]	18.8	25.2	37.8	50.4	63.0
Fast-to-i	[%]	22.9	28.7	37.1	39.2	39.7
Fast-to-e	[%]	26.6	37.3	54.2	58.0	58.8
Fast-loss	[%]	50.4	33.9	8.7	2.7	1.4
n_p/n_{fuel}	[%]	3.7	4.8	6.7	7.1	7.2
n_α/n_{fuel}	[%]	6.6	6.6	6.1	6.0	6.1
n_{p*}/n_p	[%]	13.5	16.0	18.1	18.0	18.0

energy confinement time taken from the reference set is not sufficient anymore). This behaviour is caused by the confinement quality of fast fusion products. According to Berk and Momota[1], the loss of fast particles is dominated by prompt loss and extremely sensitive to the ratio of the separatrix radius and the gyro radius of these particles at birth energy. Therefore the magnetic field strength in the device (and its radial dependency) and the plasma size are extremely important. In this work the external magnetic field and the reversal factor was fixed at 7.5 and 2.5 T for D-^{3}He and D-T resp. in order to avoid wall loading values beyond manageable limits. For D-^{3}He wall loading is dominated by about 2.5 MW/m^2 bremsstrahlung. Here it is assumed that the charged particle loss of about 3 MW/m^2 can be kept away from the first wall due to the divertor action of the open field lines. In the case of D-T as a fuel, 80% of the energy is carried away from the plasma by neutrons which therefore dominate the wall loading with about 5.5 MW/m^2. This is one of the most distinct disadvantages of D-T over D-^{3}He, because of induced radioactivity in the blanket and because of the uselessness of these neutrons for the purpose of direct energy conversion. A small increase in the magnetic field strength from 2.5 to 3 T, which in turn would allow a somewhat smaller device, would result in neutron wall loading values of about 10 MW/m^2 - well beyond acceptable limits.

Table 3: Sensitivity of D-T plasma parameters to the plasma size

r_{sep}	[m]	0.5	1.0	1.5	2.0	2.5
Volume	[m^3]	2.0	15.7	53.0	125.6	245.3
Flux	[Wb]	0.07	0.27	0.61	1.08	1.69
Current	[MA]	1.0	2.1	3.1	4.1	5.1
Ign. Margin	[-]	0.07	0.8	1.5	1.9	2.1
P_{heat}	[MWm^{-3}]	1.3	0.2	0.0	0.0	0.0
P_{fu}	[MWm^{-3}]	25.1	21.4	18.0	15.7	14.8
$P_{fu,tot}$	[MW]	49.2	335.	954.	1971.	3642.
E-content	[MJ]	5.5	42.	135.	309.	595.
P_{tr}/P_{out}	[-]	0.06	0.06	0.07	0.08	0.08
P_{st}/P_{out}	[-]	0.00	0.00	0.03	0.07	0.09
P_{fast}/P_{out}	[-]	0.17	0.13	0.08	0.03	0.01
P_{br}/P_{out}	[-]	0.01	0.01	0.02	0.02	0.02
P_n/P_{out}	[-]	0.76	0.80	0.80	0.80	0.80
S-Factor	[-]	6.0	12.0	18.1	24.3	30.4
Fast-to-i	[%]	2.6	10.6	19.7	28.3	32.2
Fast-to-e	[%]	5.6	22.2	39.5	55.0	62.0
Fast-loss	[%]	91.8	67.2	40.8	16.7	58.8
n_α/n_{fuel}	[%]	1.4	2.4	3.6	4.7	5.2
$n_{\alpha*}/n_\alpha$	[%]	3.9	10.5	13.9	14.8	15.0

A comparison of both fuel cycles on the basis of tables 1 and 2 reveals that the energy content in the D-^{3}He plasma is about 1 GJ which is a factor of 8 higher as compared to D-T. The necessary S-factor is in the range of 30 to 40 for D-^{3}He, whereas D-T could be operated around S=20. Due to the higher confinement time, the ash problem is more relevant for D-^{3}He with about 6 to 7% for both alphas and protons which has to be compared to about 3.5% alphas in a D-T plasma. The mean density of suprathermal fusion products denoted in tables 1 and 2 as p$*$ and $\alpha*$ is in the range of 10 to 20% of the overall proton or alpha density.

4. Conclusion

The results of this study lead to several optimistic conclusions about the reactor potential especially of D-^{3}He FRCs. However, many vital questions need to be answered either by further theoretical research in this field or by an experimental "next step" in the direction of a steady-state FRC. Dominating in this context are the questions of stability of large-S devices, transport mechanism and start-up scenarios. Compared to a D-T operation of Tokamaks it seems to be a much longer (and uncertain) way to go, but the final product of a high power density fusion plasma with low neutron production and direct energy conversion seems to be worth it.

5. References

[1] H.L.Berk, H.Momota, T.Tajima, Phys.Fluids 30(11) (1987) 3548-3565.

GYROVISCOSITY EFFECT ON TILT MODE IN AN FRC

Akio Ishida and Loren C. Steinhauer*
Department of Physics, Niigata University, Niigata 950-21
* Spectra Technology, Inc., Bellevue, Washington 98004

As is well known, there is an unresolved discrepancy between the FRC experiment and the theory of the internal tilt mode. Resolution of this discrepancy is important both for understanding the underlying physics and for the application of FRCs to the attractive D-^{3}He fusion reactor concept.

Although the present FRCs are highly kinetic, ideal MHD theory has been widely used. Ideal MHD, however, neglects three non-dissipative that can be included in a fluid description. These are 1) equilibrium plasma flow; 2) additional terms in the generalized Ohm's law (Hall current and electron pressure gradient) and 3) the ion gyroviscosity (FLR effect). The first two of these were investigated earlier[1] and it was found that while the Hall term provides some stabilization, it is not sufficient to account for the experimentally observed stability. Here we examine the effect of ion gyroviscosity on the internal tilt mode. Although preliminary results were given in the 10th U.S.-Japan workshop held at Hakone (1988), more extensive work and comparison with other theories are presented here.

I. Variational Formulation Including Ion Gyroviscosity

Schwarzmeier and Seyler[2] studied the FLR effect of ions on the internal tilt mode and found that while it has a strong effect, the stability boundary is sensitive to an ad hoc cutoff required to circumvent the singularity at the magnetic field null. There remains, then, a need for a simplified mathematical approach which incorporates finite ion-orbit effects without the limitations of FLR theory. An alternative is the present gyroviscous fluid model. This model uses Braginskii's gyroviscous terms[3], (the nondissipative part of the ion viscosity representing transverse ion kinetics). Unlike the standard FLR expansion, this formulation is regular at the O-point and X-points.

Consider the one fluid, nonflowing MHD equations. Using the displacement $\vec{\xi}$, which is assumed to vary as $\exp(i\ell\theta-i\omega t)$, the equation of motion is

$$\vec{H}(\vec{\xi};\omega) = 0 \tag{1}$$

where $\vec{H}$ includes both the ideal MHD and the ion gyroviscosity terms. The variational form, I, may be written as

$$I = \int d\vec{r}\ \vec{\xi}^{*}\cdot\vec{H}(\vec{\xi};\omega) = \omega^{2}K + \omega S - W\ , \tag{2}$$

where the asterisk designates the complex conjugate; K and W are the inertia and potential energy terms as in Bernstein et al.[4]; and

$$S = -\int d\vec{r}\ i\left\{\frac{1}{2}\ \eta_3\left[\vec{b}\times\underset{\sim}{D}\right]:\underset{\sim}{D}^{*} + (\eta_4 - \frac{1}{2}\ \eta_3)\vec{b}\cdot\left[(\vec{b}\cdot\underset{\sim}{D})\times(\vec{b}\cdot\underset{\sim}{D}^{*})\right]\right\}\quad . \tag{3}$$

Here η_3 and η_4 are the Branginskii's gyroviscosity coefficients, $\underset{\sim}{D} \equiv \nabla\vec{\xi} + (\nabla\vec{\xi})^{T}$ is the deformation tensor, and $\vec{b}$ is the unit vector along the magnetic field. Note that K, S, and W are all real.

It can be shown that the variational principle, $\delta I=0$, is equivalent to the equation of motion (1). Take the variation of I, $\delta I=\int d\vec{r}[\delta\vec{\xi}^{*}\cdot\vec{H}(\vec{\xi};\omega) + \vec{\xi}^{*}\cdot\vec{H}(\delta\vec{\xi};\omega)]$. It can be proved that the second term can be rewritten as $\int d\vec{r}\ \delta\vec{\xi}\cdot\vec{H}(\vec{\xi}^{*};-\omega)$. Then the variational principle leads to both Eq. (1) and

$$\vec{H}(\vec{\xi}^{*};-\omega) = 0\quad . \tag{4}$$

Since K, S, and W are each real, if ω_1 is a solution of Eq. (1), then ω_1^{*} is likewise. Suppose $(\omega_1,\ \vec{\xi}_1)$ and $(\omega_2 \equiv \omega_1^{*},\ \vec{\xi}_2)$ are solutions of Eq. (1). Their complex conjugates, $(\omega_2,\ \vec{\xi}_1^{*})$ and $(\omega_1,\ \vec{\xi}_2^{*})$, are solutions of Eq. (4). Thus, the variational principle, $\delta I=0$, is equivalent to the equation of motion (1).

To facilitate application of the Rayleigh-Ritz technique to the variational form I, expand the displacement function in terms of the basis functions, $\vec{\zeta}_i$ $\vec{\xi} = \sum_{i=1}^{N} C_i\ \vec{\zeta}_i$. The variational principle then leads to the eigenmode equation.

$$\det\ (\omega^{2}K_{ij} + \omega S_{ij} - W_{ij}) = 0 \tag{5}$$

where $K_{ij} = \int d\vec{r}\ Mn\vec{\zeta}_i^{*}\cdot\vec{\zeta}_j$, etc. This (5) is a 2N-order algebraic equation for ω.

II. Internal Tilt Mode Stability

The gyroviscous fluid theory is applied to the internal tilt mode of an FRC. An elongated Hill's vortex is assumed with radius a and half length b. The basis functions, $\vec{\zeta}_\alpha$, are expressed in terms of real components $X_{j\alpha}$ as

$$\vec{\zeta}_\alpha = \left[\hat{r}X_{1\alpha}(r,z) + i\hat{\theta}X_{2\alpha}(r,z) + \hat{z}X_{3\alpha}(r,z)\right]\ \exp(i\theta).$$

The mode is assumed to be incompressible; this determines X_2 in terms of X_1 and X_3 which vanish at the separatrix for an internal mode. The basis functions considered are shown in Table I.

It is important to emphasize the distinction between non self-adjoint systems (e.g. gyroviscous or Hall fluids) and self-adjoint systems (such as an ideal MHD fluid). In ideal MHD, if any trial function is unstable, then the actual solution is also unstable. This is not true for non self-adjoint case. The solution may, in fact, be stable even though an unstable trial function exists. This principle is illustrated in Fig. 1. The trial function (dashed line) is unstable for large b/a, whereas the Rayleigh-Ritz solution to a basis set containing that trial function (solid lines) is stable in this region.

The marginal stability boundaries for various Rayleigh-Ritz solutions are shown in Fig. 2. The normalized radius $S_* = a\omega_{pi}/c$ is identical to the familiar quantity, R/ρ_{io} for zero electron pressure. The dashed line shows (for reference) the stability boundary for the "generic" trial function, 1xA+1xB, used in Ref. 1. The Rayleigh-Ritz solution for the basis set (A,B) is shown by the solid lines. Comparing this with the generic trial function shows that (i) for large b/a the radial displacement, B, is unimportant and an axial shift assumption is appropriate, and (ii) for low b/a the radial displacement is necessary and moves the stability boundary close to unity, which is the expected stability boundary. Inclusion of modifications to the axial displacement are shown by the other curves. Here C_1 is a flux-dependent modification and E is a modification concentrated near the FRC ends. While the stability boundary for the intermediate b/a are sensitive to the selected basis functions, those for low and large b/a are insensitive. Evidently, the tilt mode is stabilized by the ion gyroviscosity if $S_* < (1.5 - 2.0)$ b/a.

III. Discussion

It is useful to compare the present results with related models, in particular the Hall theory[1] and the Vlasov-fluid (VF) theory[5]. The variational form for a Hall plasma is similar to that for a gyroviscous plasma [Eq. (2)]. For a Hall plasma, stability was found for large b/a if $S_* < 1.1$ b/a. Clearly gyroviscous and Hall effects are of the same order, indicating that theories isolating these two effects are not strictly correct. A combined theory is needed which incorporates both gyroviscous and Hall effects. Work on such a theory is in progress.

The gyroviscous theory which includes only perpendicular ion kinetics should also be compared with the VF theory that also includes parallel kinetics, the Hall effect, and resonant particle effects. The gyroviscous and VF theories are compared using the same trial function and a Hill's vortex equilibrium with b/a = 7 [which is similar to the "E2" equilibrium in Ref. (5)]. The VF plasma is a factor of four or so more stable in terms of S_* than the gyroviscous plasma. It is unclear which mechanism is primarily responsible to this difference. Understanding this difference is important to explain the experimental observation of grossly stable FRCs.

References

1. A. Ishida, H. Momota, and L.C. Steinhauer, Phys. Fluids **31**, 3024 (1988).
2. J.L. Schwarzmeier and C.E. Seyler, Phys. Fluids **27**, 2151 (1984).
3. S.I. Braginskii, in Reviews of Plasma Physics (Consultants Bureau, New York, 1965), Vol. 1, p. 205.
4. I.B. Bernstein et al., Proc. R. Soc. London Ser. A **244**, 17 (1958).
5. D.C. Bernes et al., Phys. Fluids **29**, 2616 (1986).

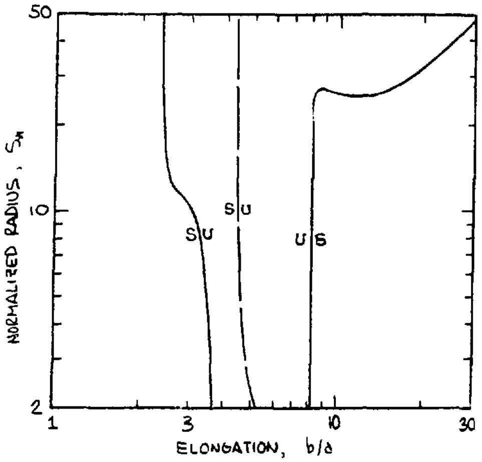

Fig. 1 Marginal Stability Boundaries for (a) Trial Function Approach (Dashed Line) with $x_1=0$, $x_3=D_1-3D_2/4$ and (b) the Variation Problem. The basis function designations, D_1, D_2, are taken from Table I.

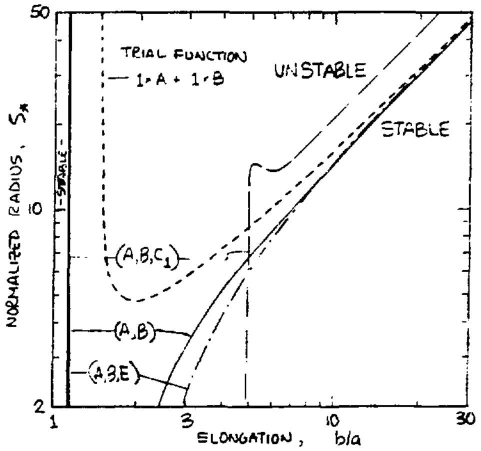

Fig. 2 Marginal Stability Boundaries for a Generic Trial Function, 1xA+1xB (for reference), and for Solutions to the Variation Problem for Three Different Combinations of Basis Functions. The basis function designations, A, B, ..., are taken from Table I.

TABLE I
BASIS FUNCTIONS EMPLOYED

$$g \equiv 1-(r/a)^2 - (z/b)^2; \quad \psi \equiv 4(r/a)^2 g; \quad \epsilon \equiv a/b$$

NAME	X_1	X_3	DESCRIPTION
A	0	$(r/a)g$	generic axial
B	$(\epsilon z/b)g$	0	generic radial
C_n	0	$(r/a)g\psi^n$	flux-dependent modification to A
D_n	0	ψ^n	rigid axial shift
E	0	$(r/a)g(\epsilon z/b)^2$	modification near ends

Linear Kinetic Stability of a Field-Reversed Configuration with Two Ion Components*

J. L. Staudenmeier†, D. C. Barnes, and H. R. Lewis
Los Alamos National Laboratory, Los Alamos, NM 87545

Introduction

It has been suggested[1] that a small fraction of non-axis encircling high energy ions may be sufficient to stabilize the tilt mode in a large s FRC. Experimental alteration of the ion distribution function in this manner might be achieved by rf heating the tail of the distribution function or by neutral beam injection. A linear Vlasov-fluid eigenfunction-eigenfrequency approach was used to investigate possible stabilization of the tilt mode by a high energy component. The ion distribution function is modelled as the sum of two Maxwellians with separate temperatures and no ion flow velocity. The cold component has a thermal s=7, where s is the approximate number of ion gyroradii contained between the field null and the separatrix. The temperature ratio of the hot component to the cold component (T_H/T_T) was varied from 2 to 100. Global hot particle fractions (n_H) up to ≈.5 were used in the computations.

Two Component Equilibria

Self-consistent, Vlasov-fluid equilibria are needed for the stability calculations. One attractive feature of the Vlasov-fluid model is that any MHD equilibrium can be used to generate an infinite number of Vlasov-fluid equilibria. This allows direct comparison of the results of the two models. The magnetic field of Vlasov fluid equilibrium is identical to the MHD equilibrium magnetic field. The electric potential $\Phi(r,z)=\Phi[\Psi(r,z)]$ for a distribution function consisting of two Maxwellians is determined by the solving the equation

$$P(\Psi) = P_T e^{\frac{-q\Phi(\Psi)}{T_T}} + P_H e^{\frac{-q\Phi(\Psi)}{T_H}} \qquad (1)$$

for $\Phi(\Psi)$, where $P(\Psi)$ is the pressure funtion used in computing the MHD equilibrium. For convenience Φ can be chosen to be zero at the field null. Then P_T and P_H are the hot and thermal particle pressures at the field null. Since the ions are electrostatically confined the potential difference between the field null and the plasma edge scales linearly with T_H/T_T.

Stability Results

The addition of the hot component to the distribution function changes both the MHD and the kinetic stability of the equilibrium. In MHD the addition of the hot component (without changing the total pressure) does not change the potential energy δW, but changes in the shape and magnitude of the density profile reduce the kinetic energy term K. This results in an increased MHD growth rate. The MHD growth rate scales almost linearly with $n_H(T_H/T_T)$ over the parameter range that was studied.

Kinetic growth rates were calulated for various combinations of n_H and (T_H/T_T). The kinetic growth rates normalized to their corresponding MHD growth rates are shown in Figure 1.The normalized growth rate behaves as expected when n_H and (T_H/T_T) are varied. A closer examination of the computed results revealed that the normalized growth rate seemed to depend only on the hot particle pressure. This observation was confirmed when the growth rate was plotted against the parameter $n_H(T_H/T_T)$ and the separate curves for each temperature all collapsed to one curve.

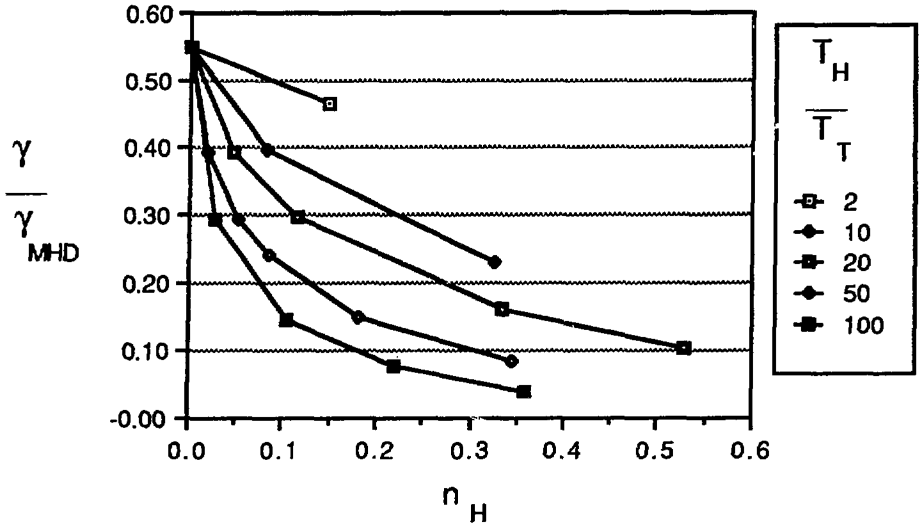

Figure 1. Plot of normalized growth rate vs. n_H

Figure 2 has the normalized growth rate plotted against $\sqrt{n_H(T_H/T_T)}$ and clearly shows how all of the computed points seem to lie on a single curve.

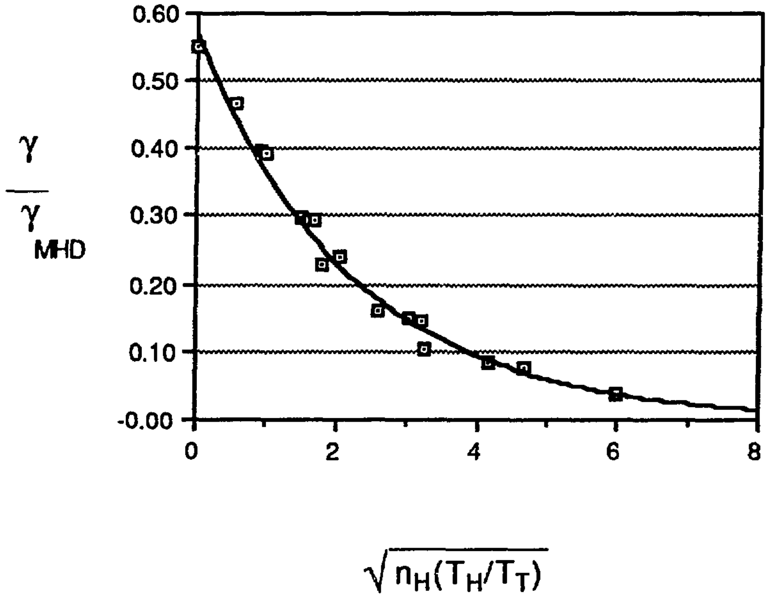

Figure 2. Plot of normalized growth rate vs. $\sqrt{n_H(T_H/T_T)}$

The smooth curve in Figure 2 is an exponential fit to the computed normalized growth rates and it seems to be a very good representation of the computed points. It should be noted that the four points with the lowest normalized growth rates in Figure 2 all have more than 95% of the total plasma energy in the hot particle population. Also remember that the MHD growth rate increases when the hot particle fraction is increased so the unnormalized or true growth rate is decreased less than the normalized growth rate.

Discussion and Conclusions

The calculations show that a hot ion component added to a large s FRC plasma affects both the MHD and kinetic stability of the tilt mode. The MHD growth rate of the tilt increases when the energetic component is added due to a reduction in plasma inertia. Both the normalized and true growth rates of the tilt decrease when an energetic component is present but almost all of the energy must reside in the hot component to get a significant reduction in growth rate. This method of enhancing stability of large s plasmas does not seem to hold much promise and probably does not warrant further study or experimental investigation.

---

* Work supported by USDOE

† Also Dept. of Nuclear Engineering, Penn State University

[1] D. C. Barnes, J. L. Schwarzmeier, H. R. Lewis, and C. E. Seyler, *Physics of Fluids* **29**, 2616 (1986)

EFFECTS OF BEAM IONS ON THE FRC TILT MODE

D. C. Barnes
Los Alamos National Laboratory

Z. Mikic
Science Applications International Corporation

In this paper, we present new theoretical results on stabilizing the internal tilting mode in a FRC which contains a minority energetic ion component. In contrast to previous results obtained in various asymptotic limits of geometry, mode structure, or beam parameters, the present results include all magnetoinductive effects self-consistently in a 3-D calculation representing a realistic FRC.

The model developed here and implemented computationally is similar to previous models. Namely, the plasma is considered to consist of three components; thermal electrons, thermal ions, and energetic (beam) ions. The first two of these components are treated by fluid equations, while the energetic ions are treated as a collisionless Vlasov species. As far as the fluid equations are concerned, this model is a straightforward extension of earlier two-fluid calculations[1] which include the Hall term in Ohm's law.

The describing equations are,

$$\frac{\partial \mathbf{B}}{\partial t} = -c\nabla \times \mathbf{E}, \tag{1}$$

$$\nabla \times \mathbf{B} = \frac{4\pi}{c}(\mathbf{J}_e + \mathbf{J}_i + \mathbf{J}_B), \tag{2}$$

$$\mathbf{J}_i = en\mathbf{u}, \tag{3}$$

$$0 = -\nabla P - en\mathbf{E} + \frac{1}{c}\mathbf{J}_e \times \mathbf{B} + \ldots, \tag{4}$$

$$Mn\frac{D\mathbf{u}}{Dt} = -\nabla P + \frac{1}{c}\mathbf{J}' \times \mathbf{B} - en_B\mathbf{E} + \ldots, \tag{5}$$

where the variables have the same meaning as in Ref. 1, with the additional distinction that $\mathbf{J}_e, \mathbf{J}_i, \mathbf{J}_B$ represent the electron, thermal ion, and beam ion current density, where n_B represents the beam ion number density, where $\mathbf{J}' = \mathbf{J}_e + \mathbf{J}_i$ is the total thermal plasma current, and where the terms omitted in (4) and (5) are those associated with resistivity and viscosity. An additional assumption made in the calculations presented here is the neglect of the last displayed term in (5) for $n_B/n \ll 1$.

---

[1] R. D. Milroy, D. C. Barnes, R. C. Bishop, and R. B. Webster, *Phys. Fluids* **B1**, 1225 (1989).

To close the set (1) - (5) as a time-evolution system, the equations of Ref. 1 are used to advance n and P. The beam current $\mathbf{J}_B$ is obtained treating the beam ions as a collisionless Vlasov species using a particle-in-cell (PIC) method. Thus, for a finite set of beam ions indexed by j, the full Lorentz force equations of motion are used to follow the orbits;

$$M\dot{\mathbf{v}}_j = e(\mathbf{E} + \frac{1}{c}\mathbf{v}_j \times \mathbf{B})_{\mathbf{r}j}, \tag{6}$$

$$\dot{\mathbf{r}}_j = \mathbf{v}_j. \tag{7}$$

The current density is obtained at each grid point by weighing the discrete particle currents to nearby grid points:

$$\mathbf{J}_B(\mathbf{r}_g) = \frac{f}{\nabla V_g} e \sum_j \mathbf{v}_j s(\mathbf{r}_g - \mathbf{r}_j) \tag{8}$$

for each grid point $\mathbf{r}_g$ with associated volume ∇V_g. In (8), f is a normalization determined by the number of simulation particles and the physical inventory of beam ions, and s is a weighing function.

Consistent with the differencing of Ref. 1, (6)–(8) are advanced in a cylindrical coordinate system represented by a finite difference mesh in r and z and a few Fourier harmonics in θ. To resolve the disparity of the orbit and fluid time scales, the particles are advanced with a substep which is a fraction of the fluid time step, and $\mathbf{J}_B$ averaged over the resulting number of substeps. Fluid equations are advanced semi-implicitly, while all coupling between the fluid and the particles is treated explicitly, with resulting first-order accuracy in time.

One natural advantage of the time-dependent approach taken here is the ease with which equilibria are computed. To obtain an equilibrium with an energetic component, a MHD equilibrium is chosen as the initial state. Then, a few beam particles are added at each fluid time step until the desired beam inventory is represented. After a few Alfvén times, the resulting configuration relaxes to a new equilibrium consistent with the added beam diamagnetic current.

Figure 1 shows equilibria obtained with f_B = beam inventory/plasma inventory $= 3.2 \cdot 10^{-3}$, and $6.4 \cdot 10^{-3}$. These equilibria were obtained by adding ions randomly within the volume of the initial separatrix with zero poloidal velocity and with toroidal velocity left-handed relative to the external field corresponding to a fixed energy of 50 keV. The background plasma initially had a total temperature of 300 eV. An increasing beam diamagnetism is evident as f_B is increased.

Tilting stability of these beam/plasma equilibria was investigated by following the evolution of an initial tilt-like velocity perturbation of 1% of the mean Alfvén velocity. Figure 2 summarizes the results for the equilibria of Fig. 1. The logarithmic evolution of the $n = 1$ component of kinetic energy is displayed for each configuration. Linear growth is indicated for the cases with $f_B = 0$ and $f_B = 3.2 \cdot 10^{-3}$. The growth rate obtained for these two cases are $\gamma = 8.4 \cdot 10^4\ s^{-1}$, and $\gamma = 4.7 \cdot 10^4\ s^{-1}$, respectively. In the case $f_B = 6.4 \cdot 10^{-3}$, no growing mode is observed during the time represented by the calculation, either in the kinetic energy history displayed in Fig. 2 or in other diagnostics, such as late-time density and flux contour plots.

These results indicate the possibility of stabilizing the FRC internal tilt in a configuration containing energetic ions. The required energetic energy is apparently a fraction of the total plasma energy. For the two cases with energetic ions considered here, this energy fraction is 36%-72%. This fraction may be reduced by optimizing the fast ion energy and distribution. In fact a third calculation with $f_B = 3.2 \cdot 10^{-3}$ but with the energetic ions more concentrated near the midplane shows that the tilt is suppressed for the same equilibrium studied in this paper. Thus, it seems possible to produce a tilt stable FRC containing an energetic ion species with an inventory fraction about 10^{-3} and an energy fraction about 0.1. Continuing calculations will identify the optimum energetic ion distribution and consider practical issues associated with generation and trapping of the ions in a FRC during formation or subsequently.

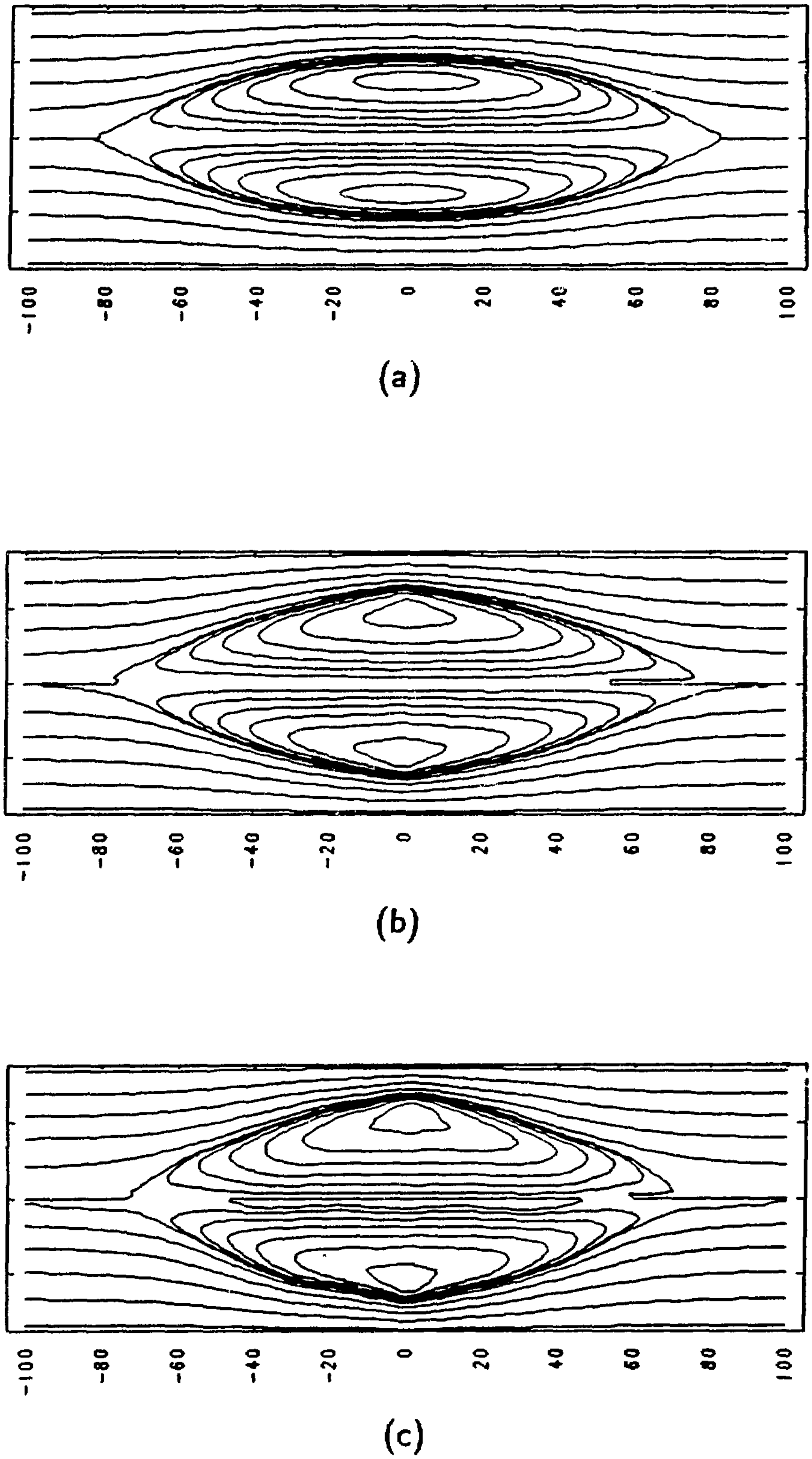

Fig. 1. Equilibria of beam/plasma configurations: (a) $f_B = 0$ (MHD), (b) $f_B = 3.2 \cdot 10^{-3}$, (c) $f_B = 6.4 \cdot 10^{-3}$.

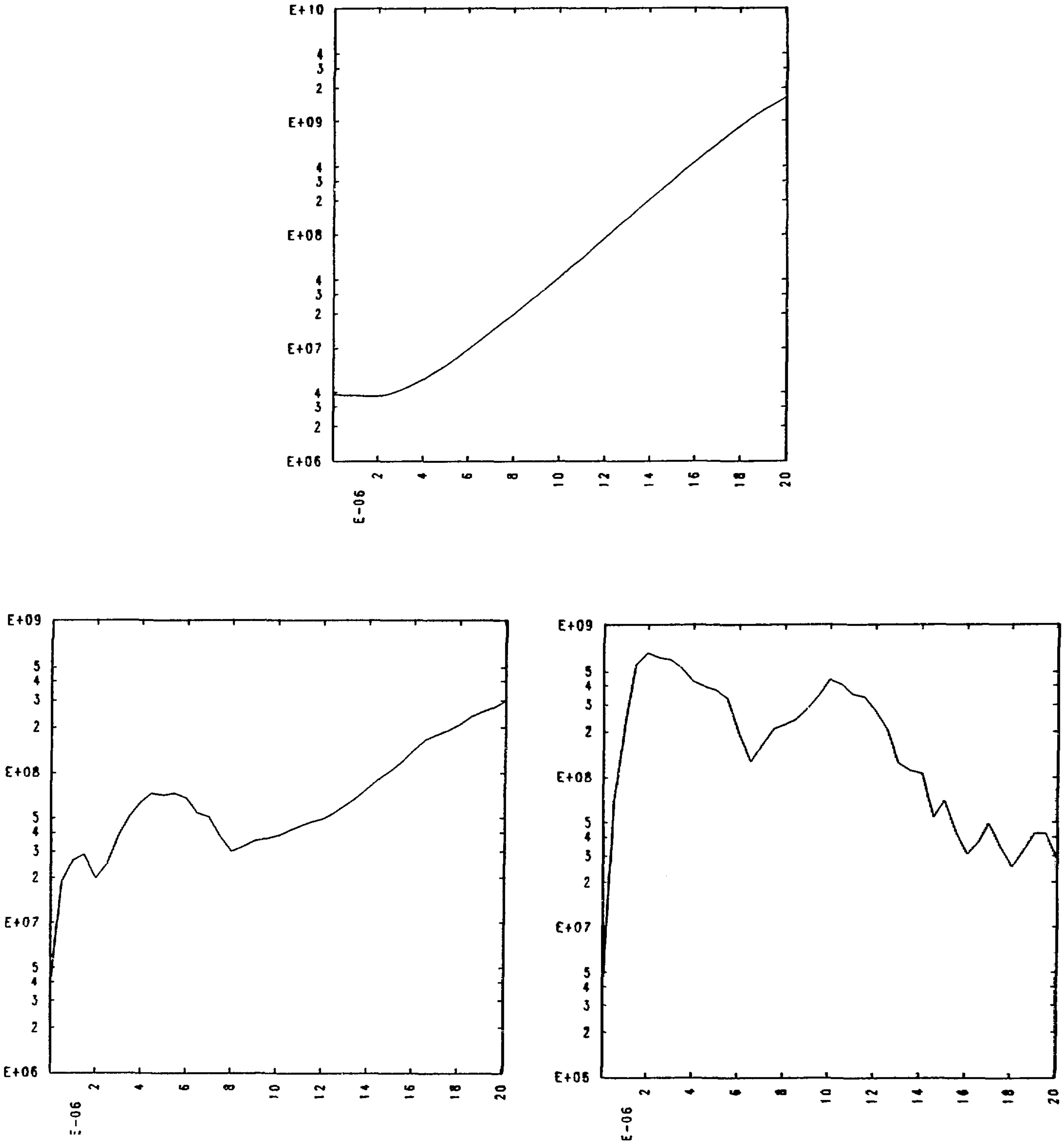

Fig. 2. Evolution of $n = 1$ (tilt) kinetic energy for configurations pictured in Fig. 1.

Microinstability Thresholds of an Axially Focused Neutralized Ion Beam

H.L. Berk, H.V. Wong, and O. Ågren
Institute for Fusion Studies
The University of Texas at Austin
Austin, Texas 78712

Blewett has recently proposed a modification of the coil configuration for the generation of the magnetic field in migma systems. He showed that one can design vacuum magnetic field coils where the magnetic field is low on axis and large at the plasma edge, R_0. As in the original migma concept, the intention with this so-called Migma Exyder is to create a plasma which is a self-colliding beam where the ions pass close to the axis in each radial bounce. Besides the possible relevance in fusion research, the Migma Exyder also has interest as a storage ring for high energy particles, provided good axial confinement and a high luminosity can be created near the axis.

In any migma system with convergent beams, there may be a potential danger for onset of microinstability, which would broaden the distribution of impact parameters. We develop a kinetic theory for small but finite angular momentum P_θ and consider a configuration where the axial extent is much less than the radial extent. We derive and analyze a quadratic dispersion functional for the low frequency ion-ion streaming instability and then extend the analysis to include electron-ion interactions and finite frequency instabilities.

A disk-shaped plasma where relativistic ions are axially focused but otherwise have negligible axial velocity is considered. To model the two-stream effect in the Migma Exyder, the ion orbits are approximated with straight lines in the weak field region $r < R_0$. By assuming that the reflection region $r \gtrsim R_0$ is not essential for the description of instability, it is appropriate to model the system with $B = 0$ for $r < R_0$ and $B \rightarrow \infty$ for $r > R_0$, in other words instantaneous reflection is assumed when the ions reach $r = R_0$. Inside the containment region, the magnetic field is considered negligible for the ions. However, the B-field can still be large enough to be important for the electron dynamics. We shall consider the electron Larmor radius much less than the system size.

The energy $H = \gamma m_i c^2$ and the canonical momentum $P_\theta = \gamma m_i r v_\theta$ are constants of motion. It is convenient to express the ion equilibrium distribution function in terms of γ and the impact parameter b, the distance of closest approach to the axis. Then $f(\mathbf{r}, \mathbf{v}) =$

$F(\gamma, b)\delta(v_z)$ where

$$f(\mathbf{r},\mathbf{v}) = F(\gamma, b)\delta(v_z) \ , \ \gamma = \frac{1}{m_i c^2}\sqrt{m_i^2 c^4 + c^2 P_r^2 + c^2 \frac{P_\theta^2}{r^2}} \ , \ b = \frac{P_\theta}{m_i c\sqrt{\gamma^2 - 1}} \ . \tag{1}$$

For electrostatic perturbations we take the perturbed potential in the plasma to be of the form

$$\phi = \hat{\phi}(r)\exp[i(\ell\theta - \omega t)]$$

with the equilibrium distribution function F_0 a function of the constants of motion. The perturbed distribution is integrated to give

$$\hat{f}_1 = \frac{q_i}{m_i c^2}\left(\frac{\partial F}{\partial \gamma} - \frac{\gamma b}{\gamma^2 - 1}\frac{\partial F}{\partial b}\right)(\hat{\phi} + i\omega\hat{\Gamma}) + i\ell\frac{q_i}{m_i c\sqrt{\gamma^2 - 1}}\frac{\partial F}{\partial b}\hat{\Gamma}$$

$$\hat{\Gamma}(\mathbf{r},\mathbf{v}) = \int_{-\infty}^{t} d\tau\hat{\phi}[r(\tau)]\exp\{i\ell[\theta(\tau) - \theta] - i\omega(\tau - t)\} \tag{2}$$

where the orbits are over unperturbed trajectories. Integrating $\hat{f}_1$ over velocity gives the perturbed ion density n_{i1}. The electron equation is obtained from the cold plasma equation which gives for the perturbed electron n_{e1}.

$$n_{e,1} = \frac{e}{m_e}\left\{\frac{1}{r}\frac{\partial}{\partial r}\left[rn(r)\frac{\frac{d\hat{\phi}}{dr} + \frac{\ell}{r}\frac{\omega_{ce}}{\omega}\hat{\phi}}{\omega^2 - \omega_{ce}^2(r)}\right] - n(r)\frac{\frac{\ell^2}{r^2}\hat{\phi} + \frac{\ell}{r}\frac{\omega_{ce}}{\omega}\frac{d\hat{\phi}}{dr}}{\omega^2 - \omega_{ce}^2(r)}\right\} \ . \tag{3}$$

The Poisson equation for ϕ, if the axial length of the disk approaches zero, is

$$\varepsilon_0 \nabla^2\phi = -(q_i n_{i,1} - e n_{e,1}\delta(z) \ . \tag{4}$$

Multiplying (4) with the adjoint function $\phi^\dagger = \hat{\phi}(r,z)\exp[-i(\ell\theta - \omega t)]$, gives after integration over vacuum and plasma regions the quadratic form

$$L(\phi, \phi^\dagger) = L_f + L_e + L_i \equiv 0$$

where

$$L_f = \epsilon_0\int_0^\infty dr\, 2\pi r\int_{-\infty}^\infty dz\, \nabla\left[\hat{\phi}(r,z)e^{-i\ell\theta}\right]\cdot\nabla\left[\hat{\phi}(r,z)e^{i\ell\theta}\right] \tag{5}$$

$$L_e = -\frac{e^2}{m_e}\int_0^{R_0}\frac{dr\, 2\pi r\, n(r)}{\omega^2 - \omega_{ce}^2(r)}\left[\left(\frac{d\hat{\phi}}{dr}\right)^2 + \frac{\ell^2}{r^2}\hat{\phi} + \frac{\ell}{r}\frac{\omega_{ce}}{\omega}\frac{d}{dr}(\hat{\phi}^2)\right] \tag{6}$$

$$L_i = -4\pi \frac{q_i^2}{m_i} \int_{-R_0}^{R_0} db \int_1^{\infty} \left\{ \gamma \left(\frac{\partial F}{\partial \gamma} - \frac{\gamma b}{\gamma^2 - 1} \frac{\partial F}{\partial b} \right) \right.$$

$$\left[\int_{|b|}^{R_0} \frac{r \widehat{\phi}^2 dr}{\sqrt{r^2 - b^2}} - \sqrt{R_0^2 - b^2} \sum_{n=-\infty}^{\infty} \frac{\omega [G_n(b)]^2}{\omega - \ell \omega_D - n\omega_b} \right]$$

$$\left. - \ell \sqrt{r^2 - b^2} \frac{\gamma c}{\sqrt{\gamma^2 - 1}} \frac{\partial F}{\partial b} \sum_{n=-\infty}^{\infty} \frac{[G_n(b)]^2}{\omega - \ell \omega_D - n\omega_b} \right\} \tag{7}$$

For even and odd n $G_n(b)$ is found to be

$$G_{2n}(b) = \frac{1 + (-1)^{\ell}}{2} \frac{(-1)^n}{\sqrt{R_0^2 - b^2}} \int_{|b|}^{R_0} \frac{r \widehat{\phi}(r)}{\sqrt{r^2 - b^2}} \cos \left[n\pi \sqrt{\frac{r^2 - b^2}{R_0^2 - b^2}} \right.$$

$$\left. + \ell \left(\sin^{-1} \frac{b}{r} - \sqrt{\frac{r^2 - b^2}{R_0^2 - b^2}} \sin^{-1} \frac{b}{R_0} \right) \right] dr$$

$$G_{2n+1}(b) = \frac{1 + (-1)^{\ell}}{2} \frac{(-1)^n}{\sqrt{R_0^2 - b^2}} \int_{|b|}^{R_0} \frac{r \widehat{\phi}(r)}{\sqrt{r^2 - b^2}} \sin \left[(2n+1) \frac{\pi}{2} \sqrt{\frac{r^2 - b^2}{R_0^2 - b^2}} \right.$$

$$\left. + \ell \left(\sin^{-1} \frac{b}{r} - \sqrt{\frac{r^2 - b^2}{R_0^2 - b^2}} \sin^{-1} \frac{b}{R_0} \right) \right] dr\,. \tag{8}$$

We have investigated the stability of the Exyder configuration. We have found a robust stability threshold at relatively high particle storage number due to the $\ell = 0$ two-stream instability. This threshold is insensitive to the sharpness of focusing of the orbits at the center. The limiting particle storage number is roughly given by

$$N_0 = 4\epsilon_0 (\pi - 2) \gamma (r + 1) R_0 E_{k,n} / q_i^2 \tag{9}$$

where $E_{k,n} = m_i c^2 (\gamma - 1)$. For the relativistic case this limit is less stringent than the equilibrium limits that have been previously calculated due to overfocusing. Thus, the low frequency two-stream instability does place any practical limit on the luminosity that can be achieved.

Considerably lower instability thresholds are found due to the excitation of finite frequency modes. We have studied finite frequency, $\ell = 0$, ion-ion modes and found that the critical particle storage number can be considerably reduced by at least an order of magnitude from Eq. (9).

The modes that produce instabilities at the lowest densities are due to finite ℓ-modes that arise when there is a small magnetic field near the center of the device. In this case the lowest particle storage number, $N_1 \simeq 4b\, R_0\, \Delta z\, \tilde{n}_0$, ($\tilde{n}_0$ is the central density and Δz the axial extent) that gives instability for $\ell = 2$ is

$$N_1 \approx \frac{\lambda N_0}{\gamma^3} \frac{b^2\, \Delta z}{R_0^2\, R_L}$$

where λ is a numerical factor of order unity, and R_L is the ion Larmor radius magnetic field near the axis. Thus the limiting particle storage number can have a very reduced bound to the particle storage number (by the factor $b^2 \Delta z/\gamma^3 R_0^2 R_L$) if the $\ell = 2$ instabilities limits the particle storage number. However, it is worth noting that the finite ℓ-modes we have described are highly resonant and small dissipative effects on electrons or feedback methods may stabilize these modes. Further work in this area is needed to understand how to establish stabilizing methods that will operate effectively in the narrow instability bands. Further, our analysis is far from complete, and modes with structure not considered here are possible.

Finally, we note that we have not found a low frequency $\ell = 1$ interchange mode like the one that was found for the "classical" migma, which is predicted to be unstable above a relatively low particle storage number. This is probably due to the intrinsically different nature of the confining magnetic field. Both systems have strong finite Larmor radius effects that stabilize the MHD flute perturbation except for a displacement mode. In the "classical" migma the magnetic field does not change appreciably along the orbit of the particles. Thus, to lowest order there is a no preferred direction and a rigid displacement, which is immune to finite Larmor radius stabilization is an allowed eigenfunction. To next order the radially decreasing magnetic field allows an MHD flute instability to arise in the rigidly displacing system. In Exyder, the magnetic field has a large variation over the particles' orbit, and a rigid displacement is not an accurate eigenfunction. Apparently, the allowed perturbations couple to finite Larmor radius stabilizing effects. In any event an MHD flute-like instability has not been found in our analysis.

1.4D Quasistatic Profile Model of Transport in a Field-Reversed Configuration (FRC)

L.C. Steinhauer
Spectra Technology, Inc.

Global confinement models are useful for determining how a given transport mechanism (dependent on local parameters) translates into global confinement times. Such models are also useful for inferring the overall magnitudes of transport rates, and limited information about their spatial profiles. They are especially important in a field reversed configuration (FRC) where the equilibrium and transport rates are so intimately coupled, and where the flux loss time is such an important factor.

An earlier global FRC confinement model, sometimes called "QUASI", was based on the assumption of a quasi-steady equilibrium.[1] This reduced the transport problem essentially to a similarity problem; the consequent second-order ordinary differential equation could be solved on a PC class computer. The equilibrium was assumed to have "square-ends" (axially uniform between the ends of the FRC) with some features of 2D equilibria: (1) equal pressure on inner and outer branches of the flux lines; and (2) average-beta relation.[2] Models of this type have been called "1-1/4D" transport models.[3] QUASI was used to discover that the poloidal flux loss time was anomalous[4], and that the particle loss time was in significant disagreement with the predictions of lower-hybrid-drift theory.[1]

The same general approach has now been applied in a straightforward way to an equilibrium with realistic axial structure. This might be called a "1.4D quasisteady transport" model. The assumed axial structure can be that of an analytic equilibrium, or a more complicated computed equilibrium as desired. The example used here is an elongated Hill's vortex equilibrium. As will be shown later, the equilibrium is reflected by two integral quantities that appear in the quasistatic diffusion equation.

I. Equations of the 1.4D QUASI Model

Rather than using the local flux, ψ, as the spatial variable, it is convenient to an equivalent the variable, $u = r^2/R^2-1$ where r is the radius of the flux surface ψ at the midplane, and R is the radius of the O-point. It is convenient to define a normalized variables for the magnetic field (at the midplane), a flux variable, and an inventory variable as follows,

$$b(u) \equiv B(r,o)/B_e, \tag{1a}$$

$$F(u) \equiv (1-\psi/\psi_p)F_1, \tag{1b}$$

$$G(u) \equiv N(u)/n_m 2\pi R^2 \ell_s \tag{1c}$$

respectively. Here B_e is the reference magnetic field (taken to be the external magnetic field at the midplane); ψ_p is the poloidal flux (i.e. the maximum value of ψ, which occurs at the O-point); N(u) is the total ion inventory inside the flux surface designated by u; n_m is the ion density at the O-point, and ℓ_s is the length of the FRC (x-point to x-point). Note that b represents the magnetic field at the midplane only; the two-dimensional equilibrium can be used to determine its structure elsewhere.

The factor F_1 is simply F(1); the poloidal flux is given in terms of it,

$$\psi_p = F_1 B_e R^2/2 \tag{2}$$

One more variable is needed which is related to the integral which gives the average beta across the midplane,

$$H(u) \equiv \int_o^u (1-\beta)\,du \tag{3}$$

The surface quantities (through which the system depends on the equilibrium) are given by,

$$U(u) \equiv \frac{B_e}{2\ell_s} \oint \frac{d\ell}{B} \quad ; \tag{4a}$$

$$W(u) \equiv \frac{B_e}{2\ell_s} \oint \left(\frac{r}{R}\right)^2 \frac{\eta_\perp}{\eta_o} \frac{d\ell}{B} \tag{4b}$$

where η_o is the reference resistivity (taken to be that at the midplane). The complete system then reduces to a set of four first order ordinary differential equations,

$$\frac{dF}{du} = b \quad , \tag{5}$$

$$\frac{dG}{du} = b\,\frac{n}{n_m}\,U \quad , \tag{6}$$

$$\frac{dH}{du} = b^2 \quad , \tag{7}$$

$$W\,\frac{db}{du} = \frac{\tau_o}{\tau_N}\,G\,\frac{n_m}{n} + \frac{\tau_o}{\tau_\psi}\,(F_1 - F)U \ . \tag{8}$$

Here, $\tau_N \equiv -N(dN/dt)^{-1}$ and $\tau_\psi \equiv -\psi_p(d\psi_p/dt)^{-1}$ are the particle and flux confinement times respectively. These four equations represent the flux-magnetic field relation, the inventory integral, the average-beta integral, and the diffusion equation. The boundary conditions are

$$b(0) = F(0) = G(0) = H(0) = 0 \tag{9}$$

at the O-point (u=0), and

$$\frac{\sqrt{2}}{1-b^2} \left. \frac{db}{du} \right|_{u=1} = \frac{S}{4w_s} \tag{10}$$

$$H(1) = x_s^2 /2 \tag{11}$$

at the separatrix (u=1).

Here $S \equiv R/\rho_{io}$ is the usual normalized FRC radius parameter, (ρ_{io} is the ion gyroradius in the external magnetic field), and $w_s \equiv n/|\nabla n|\rho_{io}$ is the normalized edge-layer thickness. Equation (11) is the average-beta condition. The system includes four first order differential equations and six boundary conditions. The two additional boundary conditions are needed because τ_N and τ_ϕ are not predetermined. This system is essentially the same as the previous QUASI model except generalized to arbitrary equilibrium through the integrals U and W.

II. Application of the Model

The new global confinement model has been applied to the case of a Hill's vortex equilibrium and an ad hoc flux-dependent resistivity. For a Hill's vortex, the two surface integrals are given approximately by

$$U \cong 1.039 + 0.072(1-u^2) - \frac{1}{4}\ln(1-u^2) \quad , \tag{12a}$$

$$W \cong \left[1 + 0.111(1-u^2)\right] \frac{\eta_\perp(u)}{\eta_o} \quad . \tag{12b}$$

Incidently, the square-ends case is quite different: $U = 1/u$; $W = \eta_\perp(u)/(u\ \eta_o)$. The square ends case has a strong algebraic singularity at the O-point whereas the Hill's vortex case has completely regular behavior there but a weak, logarithmic singularity at the separatrix (u=1). The ad hoc resistivity is given by

$$\eta_\perp(u) = \eta_o\left[1 + (f_o-1)F(u)/F_1\right]^{-1} \quad , \tag{13}$$

i.e. two parameters are used, η_o, the value of the resistivity at the O-point, and $f_o \equiv \eta_o/\eta_\perp(r_s)$, which represents the resistivity profile.

Figures 1 and 2 show the flux (τ_ϕ) and particle (τ_N) confinement times for both square-ends and Hill's vortex equilibria. The normalizing time in each case is the resistive time

$$\tau_o \equiv \mu R^2/4\eta_o \tag{14}$$

Despite substantial differences in U and W, the confinement times are remarkably similar. The confinement times are shorter for the more realistic equilibrium: by 0 to 20 percent for flux; and by 20 to 50 percent for particles. Familiar trends observed in Ref. 1 reappear. These can be approximately quantified by the relations,

$$\tau_\phi \cong 1.2 \frac{\mu R^2}{4\eta_o} \left(\frac{S}{w_s}\right)^{\frac{1}{4}} \quad ; \tag{15a}$$

$$\tau_N \cong 2.3 \frac{\mu R^2}{4\eta_s} \left(\frac{S}{w_s}\right)^{-\frac{4}{5}} \quad \text{for } S/w_s \lesssim 10 \quad , \tag{15b}$$

where $\eta_s \equiv \eta_\perp(r_s)$. The trend toward poorer particle confinement at larger S/w_s reflects the relative steepness of the density gradient near the edge layer in this case. However, as seen in Fig. 2, this trend weakens toward larger S/w_s where the simple dependence $\tau_N \propto \tau_o$ is recovered.

Future work will apply this model to potential transport mechanisms, such as lower-hybrid-drift and low-frequency-drift transport, and make the appropriate comparisons with experimental data.

References

1. L.C. Steinhauer et al., Phys. Fluids **28**, 888 (1985).
2. W.T. Armstrong et al., Phys. Fluids **24**, 2068 (1981).
3. S. Hamasaki, and D.L. Book, Nucl. Fusion **20**, 289 (1980).
4. A.L. Hoffman et al., Appl. Phys. Lett. **41**, 31 (1982).

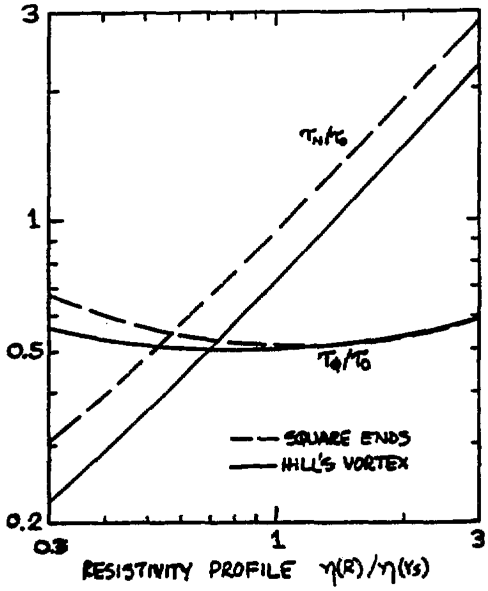

Fig. 1 Dependence of confinement time on resistivity profile for $S=12$, $x_s=0.4$, and $w_s=3$.

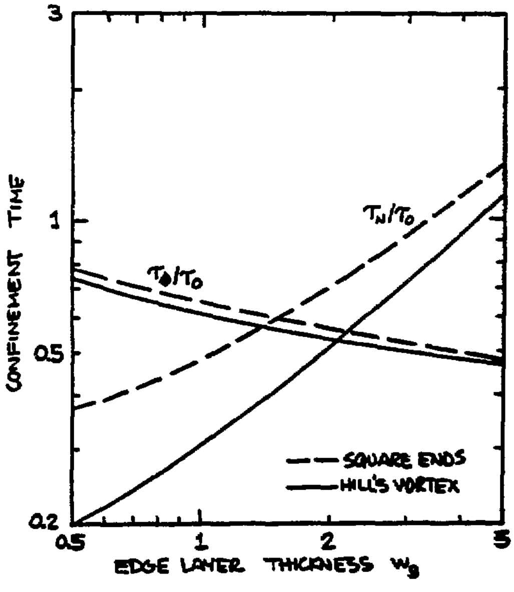

Fig. 2 Dependence of confinement time on edge-layer thickness $S=12$, $x_s=0.4$, and $f_o=1$.

Effects of Turbulent Transport on FRC Equilibrium with External Momentum Input

Masami Ohnishi and Hiromu Momota*
Institute of Atomic Energy, Kyoto University
*National Institute for Fusion Science

§1. Introduction

It is indispensable to keep an FRC in a steady state for offering a prospect of a fusion reactor. A current may be sustained by neutral beam injection (NBI) at a field null to drive Ohkawa current, and bootstrap (diamagnetic) current inside and outside a field null.(1) Fortunately for a D-^{3}He fuel FRC reactor, 15 MeV protons may play a role of driving Ohkawa current since a prompt loss of protons produced by D-^{3}He reactions results in a beam like distribution of energetic protons.(2) The rotating equilibrium of an FRC with externally applied momentum input is studied by solving analytically the momentum balance equations of two fluids for ions and electrons. The theory is applied for a D-^{3}He FRC reactor to evaluate the proton current, the NBI power needed for current sustenance, and the speed of the rotation induced by proton loss and neutral beam injection.

§2. Basic Equations

The momentum balance equations for ions and electrons are written by

$$n_j m_j \frac{\partial \vec{v}_j}{\partial t} + n_j m_j (\vec{v}_j \cdot \nabla)\vec{v}_j = -\vec{\nabla} p_j + eZ_j n_j (\vec{E} + \vec{v}_j x \vec{B}) - S_j m_j \vec{v}_j + \vec{R}_j + \vec{M}_j - \nabla \cdot \overleftrightarrow{\Pi}_j \qquad (1)$$

where j stands for ions(i) and electrons(e), S_j is a particle source, and $\vec{R}_j$ and $\vec{M}_j$ are the ion-electron drag force and the drag force between energetic ions and field ions and electrons, respectively. The collision frequency ν is taken as a small parameter. Substituting the variables divided into stationary and fluctuated parts, i.e. $n_j = \langle n_j \rangle + \tilde{n}_j$, $v_{jr} = \langle v_{jr} \rangle + \tilde{v}_{jr}$ etc. into Eq.(1) and solving for the velocity, $\vec{v}_j$, we obtain

$$\langle v_{j\theta} \rangle = -\frac{\langle E_r \rangle}{\langle B_z \rangle} + \frac{1}{eZ_j \langle n_j \rangle \langle B_z \rangle} \frac{\partial \langle p_j \rangle}{\partial r} \qquad (2)$$

$$\tilde{v}_{j\theta} = -\frac{\langle v_{j\theta} \rangle^2}{r\Omega_j} \frac{\tilde{n}_j}{\langle n_j \rangle} + \frac{1}{m_j \langle n_j \rangle \Omega_j} \frac{\partial \tilde{p}_j}{\partial r} - \frac{\tilde{E}_r}{\langle B_z \rangle} - \frac{\langle E_r \rangle}{\langle B_z \rangle} \frac{\tilde{n}_j}{\langle n_j \rangle} - \langle v_{j\theta} \rangle \frac{\tilde{n}_j}{\langle n_j \rangle} \qquad (3)$$

$$\langle v_{jr}\rangle = \frac{R_{j\theta}+M_{j\theta}}{m_j\langle n_j\rangle\Omega_j} \Big/ \left(1+\frac{1}{\Omega_j}\frac{1}{r}\frac{\partial r\langle v_{j\theta}\rangle}{\partial r}\right) \tag{4}$$

and

$$\tilde{v}_{jr} = \frac{\tilde{E}_\theta}{\langle B_z\rangle} \Big/ \left(1+\frac{1}{\Omega_j}\frac{1}{r}\frac{\partial r\langle v_{j\theta}\rangle}{\partial r}\right) \tag{5}$$

where the fluctuations are assumed for simplicity to be electrostatic and of low frequency. Using the steady state condition, $\nabla\cdot\vec{j}=0$ which is reduced to be $j_r=0$ in the case with a cylindrical symmetry, we obtain the equation

which gives the speed of a plasma rotation $\langle v_{i\theta}\rangle$,

$$\frac{1}{\Omega_i}\frac{1}{r}\frac{\partial r\langle v_{i\theta}\rangle}{\partial r} = \sum \frac{M_{e\theta}{}^{b}+M_{i\theta}{}^{b}}{\langle B_z\rangle}\left(1+\frac{\Omega_b{}^2}{\Omega_\beta{}^2}\right) \Big/ eZ_i\langle\tilde{n}_i\frac{\tilde{E}_\theta}{\langle B_z\rangle}\rangle \tag{6}$$

The numerator of the right hand side of Eq.(6) stands for the momentum transfer density from energetic beam ions and the denominator is the radial particle transport caused by turbulence. The classical diffusion is neglected since it is far smaller than the anomalous one.

Using Eqs.(2) and (3), the current in the θ-direction is given by

$$j_\theta = \frac{1}{\langle B_z\rangle}\frac{d(\langle p_i\rangle+\langle p_e\rangle)}{dr} + \sum eZ_b n_b v_{b\theta} \tag{7}$$

The current produced by turbulence, so-called 'anomalous bootstrap currnt', can be so small as to be safely neglected. Note that no diamagnetic currents exist in a field null point. Then, instead of Eq.(7), the equation

$$j_\theta = \sum eZ_b\left(1-\frac{Z_b}{Z_{eff}}\right) n_b v_{b\theta} \tag{8}$$

should be applied at a field null.

§3. Application to D^{3}He Steady State Reactor

The theory described in §2 is employed for a D-^{3}He fuel FRC reactor with 1 GW electrical output power. The equilibrium profiles of ion and electron densities and magnetic field are assumed to be $\langle n_j\rangle = n_{j0}\mathrm{sech}^2[K(r^2/R_0{}^2-1)]$ and $\langle B_z\rangle = -B_e\tanh[K(r^2/R_0{}^2-1)]$, where K and R_0 are the field reversal factor and field null radius. Based upon the condition for the confinement of 15 MeV protons within a separatrix the proton current is given by $j_p = \frac{eS_p v_0}{8\nu_{sp}}\{1-\frac{(\tilde{U}-1)^2}{x^2}\}H(x^2-(\tilde{U}-1)^2)$, where S_p and v_0 are the rate of proton production and the speed of 15 MeV protons, ν_{sp} is the proton-electron collision frequency, $\tilde{U}$ is the normalized flux function, and H is Heviside step function.

Figure 1 shows the dependence of proton current on the field reversal factor. When a field reversal factor is greater than 0.8, the proton current has the profile hollowed near a field null point. The property is more conspicuous as a field reversal factor increases. The proton current density at a field null gets very small for a field reversal factor of 1.2, and is no use of keeping a plasma in a steady state. The current needed for a steady state is supplied by neutral beam injection. Table 1 shows the proton current density at a field null j_p, injection power for a steady sate W_{inj}, and plasma rotation induced by proton loss and neutarl beam injection $v_{i\theta}$. We pressumed that the fast deuterium ions produced by neutral beam injection at 1 MeV are uniformly distributed in the region of 0.1 m outside/inside of field null surface. An anomalous transport is also assumed to be thousand times as large as the classical value.

§4. Conclusions

The steady state may be attained in a D-^{3}He FRC reactor by the bootstrap (diamagnetic) current drived by the currents due to proton loss and neutral beam injection. Since the proton current, for a high β equilibrium ($\langle\beta\rangle\sim0.9$), contributes greatly to sustain the equilibrium, the power of NBI needed for a steady state is as small as 3 MW. Althogh a turbulent transport produces the anomalous bootstrap current, it is too small to have any influence on the equilibrium. The rotation accompanied with proton loss and neutral beam injection is greatly suppressed by radial anomalous particle diffusion to be a little larger than the speed of the ion diamagnetic drift.

[REFERENCES]

(1) M.Okamoto, H.L.Berk and J.H.Hammer, IFSR#335 (1988).

(2) H.L.Berk,H.Momota and T.Tajima, Physics Fluids, 30 (1987) 3548.

Table 1 Steady Burning Equilibrium for Reversal Factor

$K(\langle\beta\rangle)$	0.6 (0.895)	0.8 (0.830)	1.0 (0.726)	1.2(0.695)
$j_\theta(R_0)$ (MA/m^2)	11.5	15.4	19.2	23.1
j_p (MA/m^2)	16.9	12.2	3.0	~0
j_b (MA/m^2)	9.3	28.8	53.1	69.2
W_{inj} (MW)	3.0	9.1	17.4	22.6
$v_{i\theta}$ (m/s)	1.69×10^5	5.75×10^5	1.28×10^6	2.70×10^6
$v_{i\theta}/v_{ith}$	0.06	0.21	0.46	0.96
$v_{i\theta}/v_{id}$	3.0	7.6	13.6	23.9

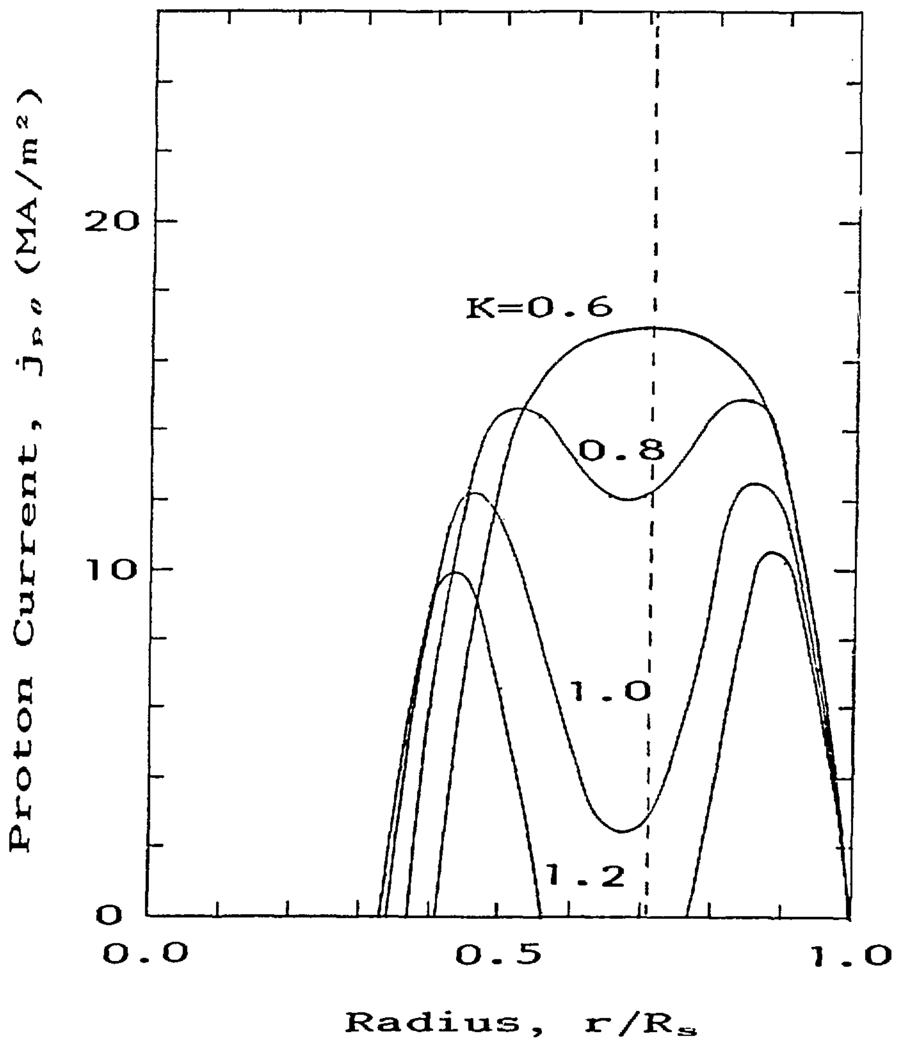

Fig.1 Dependence of proton current profile on field reversal factor.

AMBIPOLAR DIFFUSION OF PLASMAS IN STEADY-STATE FRC's

Hiromu Momota

National Institute for Fusion Science, Nagoya 464-01, Japan

Plasmas in a field-reversed configuration are often described by the MHD equations with a negligibly small azimuthal plasma rotation.[1] This assumes that an $E \times B$ drift due to a radial electric field compensates the diamagnetic drift of plasma ions. The validity of this assumption is, however, unclear because an electric field disappears and no information can be obtained in the framework of the MHD equations. On the other side, one observes rotations of laboratory plasma whose speed is as large as the ion diamagnetic drift velocity.[2] At the early phase of FRC plasma production, a difference of loss rate between ions and electrons may produce a radial electric field and ultimately bring about a plasma rotation.[3] In a steady-state FRC plasma, however, those phenomena are still unclear. It is, therefore, needed to analyze radial electric field or associated plasma rotations of a steady-state high beta plasma in a field-reversed configuration.

In the present analyses, we assume, for the simplicity, an axi-symmetric plasma in an extremely elongated field-reversed configuration. Since we are interested in macroscopic behavior of the plasma, we employ a set of continuity equations and the equations of motion in the cylindrical coordinates system:

$$\frac{1}{r}\frac{d}{dr}(rNV_r) = S_i \qquad (1)$$

$$\frac{1}{r}\frac{d}{dr}(rnv_r) = S_e \qquad (2)$$

$$-\frac{V_\theta^2}{r} = \frac{Ze}{M}(E + V_\theta B) - \frac{1}{MN}\frac{d}{dr}(NT) - \nu_{ie}(V_r - v_r) - \frac{S_i}{N}V_r \qquad (3)$$

$$V_r\frac{d}{dr}(rV_\theta) = -\frac{Ze}{M}V_rB - \nu_{ie}(V_\theta - v_\theta) - \frac{S_i}{N}V_\theta \qquad (4)$$

$$0 = -\frac{e}{m}(E + v_\theta B) - \frac{1}{mn}\frac{d}{dr}(nT) - \nu_{ei}(v_r - V_r) \tag{5}$$

and

$$0 = \frac{e}{m}v_r B - \nu_{ei}(v_\theta - V_\theta) - \nu_{eb}(v_\theta - U) \tag{6}$$

for respective species of plasma particles in a steady-state equilibrium. We have ignored equations of heat for both ions and electrons, for the simplicity of the problems, and the temperatures are assumed to be a given quantities.

E and B denote the radial electric field and the axial magnetic field, respectively. Quantities represented by capital letters refer to plasma ions and small letters to electrons. The collision frequency of i -species colliding with j -species is denoted by ν_{ij} . Quantity S stands for particle's source densities per unit time.

The radial and azimuthal velocities of ions and electrons are obtained from eqs.(1)-(4), provided that the angular ~~velocity~~ frequency of the ion rotation is much smaller than the ion gyro-frequency:

$$V_\theta = \left[\frac{-E}{B} + \frac{1}{ZeN}\frac{1}{B}\frac{d}{dr}(NT) \right] \left[1 - \frac{1}{r\Omega_i} \left\{ \frac{-E}{B} + \frac{1}{ZeN}\frac{1}{B}\frac{d}{dr}(NT) \right\} \right] \tag{7}$$

$$V_r = -\left[\nu_{ie}(V_\theta - v_\theta) + \frac{S_i V_\theta}{N} \right] / \left[\Omega_i + \frac{1}{r}\frac{d}{dr}(rV_\theta) \right] \tag{8}$$

$$v_\theta = \frac{-E}{B} - \frac{1}{en}\frac{1}{B}\frac{d}{dr}(nT) \tag{9}$$

$$v_r = \frac{1}{\Omega_e}\left[\nu_{ei}(v_\theta - V_\theta) + \nu_{eb}(v_\theta - U) \right] \tag{10}$$

Here Z is the effective charge number of plasma ions. Taking into account the definition:

$$V_\theta - v_\theta = \frac{1}{ne}(j_\theta - J^*) \tag{11}$$

and subtracting eq.(9) from eq.(7), we have a generalization of pressure balance equation:

$$B(j_\theta - J^*) = \frac{dP}{dr} + \frac{n - ZN}{n}\frac{d}{dr}(NT) - \frac{MN}{Z}\frac{V_\theta^2}{r} \tag{12}$$

where J^* is the seed current density defined by $J^* = N_bZ_be(U-V_\theta)$.

The radial flow of electrons is obtained by substituting eq.(12) into eq.(10), that is

$$v_r = -\frac{\eta}{B^2}\left(1 + \frac{N_bZ_b^2}{NZ^2}\right)\left[\frac{dP}{dr} + \frac{n-ZN}{n}\frac{d}{dr}(NT) - \frac{MNV_\theta^2}{Z\,r}\right] - \frac{n}{NZ}\frac{Z_b}{Z}\frac{\eta}{B}J^* \quad (13)$$

This equation can be rewritten as:

$$j_\theta = -\frac{1}{\eta}v_rB\frac{NZ^2}{NZ^2+N_bZ_b^2} + \left(1 - \frac{nZ_b}{NZ^2+N_bZ_b^2}\right)J^* \quad (14)$$

or approximately

$$-\frac{1}{\mu_0}\frac{dB}{dr} \sim -\frac{1}{\eta}v_rB + \left(1 - \frac{Z_b}{Z}\right)J^* \quad (15)$$

The first and the second terms on the rhs in this equation are respectively the bootstrap current and Ohkawa current driven by a seed current J^* . It is obvious in this equation that the presence of Ohkawa current at the field-null point of an FRC is indispensable to keep an FRC in a steady-state equilibrium, Without Ohkawa current at field null, we have a magnetic field whose magnitude is zero everywhere.

Defining the velocity

$$V_R = -\frac{\eta}{B^2}\left(\frac{dP}{dr} + \frac{n-ZN}{n}\frac{d}{dr}(NT) - \frac{Mn}{Z}\frac{V_\theta^2}{r}\right)$$

we obtain the radial flux of ions from eqs.(8) and (12)

$$ZNV_r = \left[nV_R - \frac{M}{eB}S_iV_\theta\right] \Big/ \left[1 + \frac{1}{\Omega_i}\frac{1}{r}\frac{d}{dr}(rV_\theta)\right] \quad (16)$$

and the radial flux of electrons from eqs.(10) and (12)

$$nv_r = n\left(1 + \frac{N_bZ_b^2}{NZ^2}\right)V_R - \frac{n^2}{NZ}\frac{Z_b}{Z}\frac{\eta J^*}{B} \quad (17)$$

It may be natural to assume that total charge of particle sources in the continuity equations (1) and (2) is zero. Then the absolute values of radial ion current and electron current must be the same ($0 = (ZNV_r - nv_r)e$) in a steady-state equilibrium. This condition yields immediately from eqs.(16) and (17)

$$\frac{1}{r}\frac{d}{dr}(rV_\theta) = \Omega_i \frac{\eta}{B}\frac{1}{V_R}\left(\frac{n}{ZN}\frac{Z_b}{Z}J^* - \frac{MS_iV_\theta}{\eta en} \right)$$

$$= - \Omega_i \left[\frac{n}{ZN} \frac{Z_b}{Z} J^* - \frac{1}{\eta} \frac{MS_iV_\theta}{en} \right] / \left[j_\theta - J^* \right] \qquad (18)$$

Equation (18) determines the azimuthal rotation of plasma ions so as to adjust the radial flow of ions to an ambipolar diffusion.

The mechanism of the ambipolar diffusion can be understood as follows: Let the seed current increases by an amount $\delta J^* > 0$ at the position where magnetic field is negative. The seed current causes a frictional force on the electrons in the azimuthal direction and change of the radial velocity of electrons

$$\delta v_r \sim - \frac{Z_b}{Z} \frac{\eta \delta J^*}{B} > 0$$

is also positive. Equivalently a decrease in the electron density is associated. The increase of the charge density brings an increase of the radial electric field or equivalently of the azimuthal velocity of ions

$$\frac{1}{r}\frac{d}{dr}(r\delta E) = - B \frac{1}{r} \frac{d}{dr}(r\delta V_\theta) > 0$$

As an ion is flowing in the radial direction it suffers an additional inertial force in the azimuthal direction, if the azimuthal velocity is changed, and consequently it changes the radial velocity

$$\delta V_r \sim - V_R \frac{1}{\Omega_i} \frac{d}{dr}(r\delta V_\theta) > 0$$

Taking into account the change of the ion density, one is able to calculate the change in ion's radial velocity as

$$\delta V_r \sim \frac{c^2}{c^2+V_A^2} \delta v_r \sim \delta v_r$$

So far we studied the equations of motion for respective species of plasma particles. We found in eq.(15) that an seed current at the field null is indispensable to keep an FRC plasma in a steady-state equilibrium. The applied seed current, however, kicks electrons and ultimately enhances radial loss flux of electrons. This enhanced loss of electrons produces radial electric field and equivalently an azimuthal ion rotation to satisfy ambipolar condition (18). The physics quantities: velocities and densities of ions and electrons can be determined respectively on the bases of eqs.(1), (2), (7), (12), (17), and (18); as functions of particle's sources and the seed current. The field quantities E and B are to be obtained with the maxwell equations.

For a practical use of the theory, an approximation $N_b \ll N$ simplifies the problems. Quantities characterizing an equilibrium B , V_θ , and n are related by the force force balance equation:

$$B\ (j_\theta - J^*) = \frac{dP}{dr} - MN\,\frac{V_\theta^2}{r} = \left(\frac{1+Z}{Z}\right) \frac{d}{dr}(nT) - \frac{1}{Z}\, Mn\, \frac{V_\theta^2}{r} \tag{12}$$

This equation is supplemented by the condition of ambipolar diffusions

$$\frac{1}{r}\frac{d}{dr}(rV_\theta) = -\ \Omega_i\ \left[\ \frac{Z_b}{Z}\ J^* - \frac{1}{\eta}\ \frac{1}{en}\ MS_i\ V_\theta\ \right] \Big/ \left[\ j_\theta - J^*\ \right] \tag{18}$$

and the continuity condition in the form

$$n = -\ \frac{B}{\eta}\ \left[\ \frac{1}{r}\int^r rS_e\, dr\ \right] \Big/ \left[\ j_\theta - \left(\ 1 - \frac{Z_b}{Z}\ \right)\ J^*\ \right] \tag{19}$$

then the above quantities can be obtainable as a function of applied particle's sources and a seed current respectively.

In our discussions, we postulated the temperatures of ions and electrons. Viscosities are also ignored in equations of motions. Those have to be justified in practical use of the theory.

REFERENCES

1) M.Tuszewski; Nucl.Fusion 28(1988) 2033

2) S.Ohi, T.Minato, et al.; Phys. Rev. Lett. 51(1983) 1042
R.E.Siemon, W.T.Armstrong, D.C.Barnes, et al.; Fusion Technol.9(1986)13

3) M.Y.Hsiao and P.R.Chiang; to be published in "Phys.Fluids"

Velocity-Space Particle Loss in Field-Reversed Configurations

Pi-Ren Chiang and Ming-Yuan Hsiao

Department of Nuclear Engineering, 231 Sackett Building
The Pennsylvania State University, University Park, PA 16802

The classical transport assumes that the entire velocity space is for particle confinement. However, in reality, there are unconfined regions in velocity space, which introduces the velocity space particle loss (VSPL).[1-4] Due to the magnetic structure in FRCs, the VSPL is significant in the separatrix and small-r regions. Under the fast-loss assumption, i.e., the unconfined particles escape from the system immediately, Hsiao and Miley's result[2] showed that the particle loss rate due to the collisional VSPL was much higher than the experimental values. In reality, particles tend to fill in the loss region via collisions (classically or anomalously); and the unconfined particles stay in the system for a finite period of time. If these two effects are considered, the particle loss rate may be significantly reduced. In this paper, a finite-loss-time model, which incorporates these two effects, is used to modify the loss boundaries in velocity space. Both the open-field and closed-field confinement criteria are used to calculate the particle confinement times for FRCs.

Following Hsiao and Miley's approach, the open-field confinement criteria can be transformed to (r,v) space. The transformation yields

$$v_r^2 + (v_\theta - v_{\theta 0})^2 + v_z^2 < v_{c0}^2 , \tag{1}$$

where

$$v_{c0} = \left(\frac{|q|B_0 r}{mc}\right)\left(1 - \frac{2\Psi}{B_0 r^2} + \frac{2q\Delta\Phi_w}{m\omega_{c0}^2 r^2}\right)^{1/2} , \tag{2}$$

$v_{\theta 0} = - qB_0 r/mc$, $\Delta\Phi_w = \Phi(r_w) - \Phi(r)$, and $\omega_{c0} = (|q|B_0/mc)$ is the cyclotron frequency. Here, as in Ref. 2, the boundary of confinement region is approximated by the entire sphere as described by Eq.(1), instead of a cut-off sphere. The closed-field confinement criteria can be expressed in (r,v) space as

$$v_r^2 + a^2(v_\theta - v_{\theta 1})^2 + v_z^2 \le v_{c1}^2 , \tag{3}$$

where

$$v_{c1} = \left(\frac{q^2\Psi^2}{m^2c^2r_s^2a^2} + \frac{2q\Delta\Phi_s}{m}\right)^{1/2} , \tag{4}$$

$v_{\theta 1} = qr\Psi/mca^2r_s^2$, $a = (1-r^2/r_s^2)^{1/2}$ and $\Delta\Phi_s = \Phi(r_s)-\Phi(r)$. Note that the confinement region in velocity space for the closed-field confinement is an ellipsoid with a minor radius of

v_{c1} in the v_r and v_z directions, and a major radius of $v_{c1}/a(r)$ in the v_θ direction. To simplify the calculation and have a conservative estimation of the particle confinement times, the ellipsoid is approximated by a sphere with radius v_{c1}.

In essence, collisions tend to fill the loss region in velocity space, thus relaxing the distribution function toward a Maxwellian. The relaxation time τ_r is usually approximated by like-particle collision time $\tau_c = m^2\langle v\rangle^3/(8\pi e^4 L n(r))$, where L is the coulomb logarithm, $\langle v\rangle$ is the average velocity of the unescaped particles. In the mean while, unconfined particles continue escaping from the system. The escape time of the unconfined particles can be given as $l/2v_{esc}$, where l is the system length and v_{esc} is the average velocity of the escaped particles. Accordingly, a fraction $f_u= \exp(-\tau_c/\tau_{esc})$ of the unconfined particles may remain in the system. The exponential form comes from the fact that both terms are the e-folding times of the particle density. Therefore the particle density n(r) can be written as

$$
\begin{aligned}
n(r) &= n_c + f_u \times n_u \\
&= \int_{V_c} f(\mathbf{r},v)\, dv + \left(\int_{V_L} f(\mathbf{r},v)\, dv\right)\exp\!\left(-\frac{\tau_r}{\tau_{esc}}\right)
\end{aligned} \qquad (5)
$$

where $f(\mathbf{r},v)$ is the particle distribution function, V_C and V_L are, respectively, the confinement and the loss regions in velocity space. Equation (5) has the following features. First, as τ_c approaches to zero, which is equivalent to an infinite collision frequency, the density is exactly the same as the integration of the $f(\mathbf{r},v)$ over the whole velocity space. Second, as τ_{esc} approaches to zero, n(r) is the integration of $f(\mathbf{r},v)$ over the confinement velocity space only, since $\tau_{esc}=0$ implies that the unconfined particles are lost immediately.

Next we want to modify the loss boundary v_c by Eq. (5). Physically, it is reasonable to assume that the unconfined particles with higher energy escape earlier. The 'effective' confinement region then will be increased by changing the loss boundary v_c due to the unconfined particles remaining in the system. From Eq.(5), a new loss boundary v_c' should satisfy

$$
\begin{aligned}
n(r) = n(r,v_c') &= n_c(r,v_c) + n_u(r,v_c)\exp(-\tau_c/\tau_{esc}) \\
&= n_c(r,v_c) + [n_c(r,\infty) - n_c(r,v_c)]\exp(-\tau_c/\tau_{esc})
\end{aligned} \qquad (6)
$$

where v_c is determined from Eqs. (1) or (3). Once v_c' is obtained, the local particle loss rate $\langle\tau_p\rangle$ can be calculated by replacing v_c with v_c' in Ref. 2.

A calculation of a self-consistent ambipolar electric field in the radial direction was attempted. However, the calculation failed in the region near r=0, and the magnitude of the electric field was not realistic because the loss rate of electrons is several orders lower than that of ions. A more realistic electric field should be calculated combining the classical transport and the collisional VSPL together. Therefore, in this study the radial electric potential profile is assumed to be flat in the radial direction. Table I shows the experimental and the calculated particle confinement times for the present major experiments. The calculated confinement times using the open-field confinement criteria are about 2 to 5 times the experimental values, while the ones using the closed-field confinement criteria are two orders lower than the experimental values. These results are expected since both the criteria represent the extreme cases in FRCs. A sequence of cases with parameters varied from the parameters in the experiments shown in Table I are run to find the scaling of the particle confinement time. The confinement time scaling for the open-field confinement is $\tau_p \approx l_s^{0.6} x_s^3 r_c^2 n^{0.6} T_i^{0.3}$, while for the closed-field confinement, τ_p scales as $l_s^{0.6} x_s^3 r_c^{1.6} n^{0.4} T_i^{0.1}$. The calculated power laws of scaling are almost the same for these experiments. It is important to note that the scalings are obtained for the present experimental parameters. Since the expression of τ_p is nonlinear, the scalings may not be applied to the parameters significantly different from those of these experiments. In reactor regime, a simple power law may not be appropriate for a prediction of the confinement time. A comparison between the scaling of the collisional VSPL model and other empirical and theoretical scalings is made in Table II. As shown in Table II, the VSPL scaling agrees well with empirical scaling. It is noted that, for the scaling on the temperature, the VSPL model has the best prediction among the theoretical scalings. Therefore, the collisional VSPL appears to be one important contributing factor to the anomalous transport observed in the present experiments.

References

1. M. Y. Hsiao and G. H. Miley, "Particle Confinement Criteria for Axisymmetric Field-Reversed Configurations," Nuclear Fusion **24**, 1029(1984).
2. M. Y. Hsiao and G. H. Miley, " Velocity-Space Particle Loss in Field Reversed Configurations," Phys. Fluids **28**, 1440(1985).
3. M. Y. Hsiao, J. L. Staudenmeier, and P. R. Chiang, "Electric Field due to Velocity Space Particle Loss in Field-Reversed Configurations," Phys. Fluids B **1**, 375(1989).
4. M. Tuszewski, "Field Reversed Configurations," Nuclear Fusion **28**, 2033(1988).

Table I. Comparison of the confinement times between experimental and VSPL results. τ_p(EXP) is the experimentally observed particle confinement time; τ_p (OF) is the collisional VSPL result for the open-field confinement criteria; τ_p (CF) is for the closed-field confinement criteria.

Device	τ_p (EXP)	τ_p (OF)	τ_p (CF)
FRX-A	35 μs	63 μs	0.56 μs
FRX-B	39 μs	70 μs	0.57 μs
FRX-C (5 mtorr)	68 μs	312 μs	2.05 μs
FRX-C (20 mtorr)	154 μs	749 μs	3.43 μs
TRX-2	126 μs	501 μs	2.86 μs

Table II[4]. Particle Confinement Time Scaling: $\tau_p \approx l_s^a x_s^b r_c^c n^d T_i^e$

Scaling	a	b	c	d	e
A. Empirical					
R^2/ρ_{ie}	0	2	2	0.5	0
$x_s R^2/\rho_{ie}(l_s/r_c)^{3/4}$	0.75	3	1.25	0.5	0
ϕ	0	3	2	0.5	0.5
TRX-1	0	2.2	2.2	0.6	0.3
FRX-C/T	0.2	1.4	1.4	0.5	0.4
TRX	0	3.6	3.6	0.9	0
B. Theoretical					
LHD	0.6	3.3	2	0.5	-0.7
Bohm	0	2	2	0.5	-0.5
Krall	0	2	2	0.5	-0.5
Classical	0	2	2	0	1.5
VSPL (Open-Field)	**0.6**	**3**	**2**	**0.6**	**0.3**
(Closed-Field)	**0.6**	**3**	**1.6**	**0.4**	**0.1**

Resistivity at the Field Null of the FRC Plasma

Richard A. Gerwin, *CTR-6*
Los Alamos National Laboratory

I. SYNOPSIS

In the absence of major destructive instabilities, the configuration time is ultimately determined by particle and flux containment. If the profiles are "gentle," then the anomalous flux-loss rate depends essentially on the anomalous resistivity at the field null.

Conventional electrostatic quasi-linear models of anomalous cross-field resistive diffusivity are based upon the use of $\vec{E} \times \vec{B}$ drift velocities, and hence break down at the magnetic field null. In this paper, an electromagnetic treatment valid at the field null is developed, based upon the presence of flute-parity perturbations. An expression for anomalous resistivity at the field null in the quasi-linear approximation is derived by averaging in the ignorable direction over the random phases of the perturbations. The expression is valid for arbitrary (non-local) radial shapes of the perturbing modes (for example, the eigenfunctions need not be centered at the field null), and for an arbitrary ratio of real frequency to growth rate. The effective resistivity due to flute perturbations of the MHD type will be considered.

II. THE MODEL

Consider a quasi-1D model of the FRC. Revert to a slab model with "radial" direction x, "azimuthal" direction y (periodic), and axial direction z. The zero-order magnetic field is along the z-direction. We seek flute-type perturbations independent of z in a model in which the equilibrium has only an x-dependence. We neglect electron inertia, so Ohm's law reads

$$\vec{E} + \vec{u} \times \vec{B} = D_\eta \nabla \times \vec{B} - \frac{1}{ne} \nabla P_e \quad , \tag{1}$$

where $D_\eta = \eta/\mu_0$ is the resistive diffusivity of the plasma, $\vec{E}$ and $\vec{B}$ are electric and magnetic field vectors, P_e is electron pressure, n is electron number density, and u is the electron fluid velocity. (Thus, the Hall term is included.)

There are two types of modes independent of z. One has perturbation components δB_x, δB_y, and δE_z. The other has perturbation components δE_x, δE_y, and δB_z. It can be shown, by using potentials for $\vec{E}$ and $\vec{B}$ in Eq. (1), that modes of the former type always die away resistively as the perturbations are convected with the electron fluid. Consequently, we restrict attention to modes of the latter type. They have the form of interchanges.

III. ELECTROSTATIC PERTURBATIONS

The conventional approach is to examine the effect of cross-field electrostatic perturbations, δE_y, on the cross-field (radial) particle flux, nu_x. One takes the cross-product of Eq. (1) with $\vec{B}$, multiplies by n and divides by B^2, and invokes radial pressure balance to find

$$n\vec{u} = n\frac{\vec{E} \times \vec{B}}{B^2} - \eta\frac{n\nabla P}{B^2} + \frac{\nabla P_e \times \vec{B}}{eB^2} \quad , \tag{2}$$

where P is the total plasma pressure. The second term on the rhs constitutes the classical contribution to the radial flux due to resistivity intrinsic to a quiescent plasma. It can be thought of as allowing a resistive slippage between the plasma velocity and the velocity of magnetic field lines, $n(\vec{u} - \vec{V}_E)_x$, where $\vec{V}_E = \frac{\vec{E}\times\vec{B}}{B^2}$. The third term has no zero-order radial (x) component because ∇P_e itself is x-directed. Also, in a purely electrostatic model in which perturbations of $\vec{B}$ are suppressed, $(\nabla \delta P_e)_y$ perturbations (with δP_e periodic in y) will contribute no net effect to the radial particle flux when averaged over the y-direction.

The first term on the rhs can produce a nonlinear electrostatic contribution to the radial particle flux, of the form

$$(nu_x)_{NL} = \frac{\langle \delta n \delta E_y \rangle}{B_{z0}} \quad , \tag{3}$$

in which perturbations of magnetic field are again suppressed in the electrostatic model. From this term, one could construct an equivalent anomalous resistivity from

$$\frac{\langle \delta n \delta E_y \rangle}{B_{z0}} = -D^*_{part.} \frac{\partial n}{\partial x} \tag{4}$$

where the anomalous particle diffusivity is given by

$$D^*_{part.} = (D^*_\eta)\left(\frac{1}{2}\beta\right) = r_{ce}^2 \nu_e^* , \tag{5}$$

wherein we have assumed uniform and equal temperatures for simplicity. Here, $\beta = P/(B^2/2\mu_0)$, ν_e^* is the anomalous electron collision frequency, and r_{ce} is the electron gyro-radius. Eq. (3) breaks down at or near the magnetic field null.

IV. ELECTROMAGNETIC PERTURBATIONS AT THE FIELD NULL

Write Eq. (1) as

$$ne\vec{E} + ne\vec{u} \times \vec{B} = \eta ne\vec{J} - \nabla P_e \quad , \tag{6}$$

split into mean values depending only upon the x-coordinate and fluctuations depending upon the x-coordinate and also periodic in the y direction,

$$n = n_0 + \delta n, \qquad \vec{E} = \vec{E}_0 + \delta\vec{E}, \qquad \vec{u} = \vec{u}_0 + \delta\vec{u}$$

$$\vec{B} = \vec{B}_0 + \delta\vec{B}, \qquad P_e = P_{eo} + \delta P_e \quad , \tag{7}$$

take the y-component, average over the y direction, $\langle \ldots \rangle$, and neglect the explicit resistive term (in order to concentrate on anomalous resistivity due to the fluctuations). Note that $\vec{u}_0 = u_{0y}(x)\hat{y}$, and $\partial P_{e0}/\partial y = 0$. After dividing through by $(n_0 e)$, one finds

$$E_{0y} = \eta^* J_{0y} \equiv -\langle \frac{\delta n}{n_0}(\delta E_y - \delta u_x B_{0z}) \rangle + \langle \delta u_x \delta B_z \rangle \equiv (\eta^* J_{0y})_1 + (\eta^* J_{0y})_2 \quad , \tag{8}$$

which defines the anomalous resistivity η^*. Henceforth, we shall refer to the two terms on the rhs of Eq. (8) as $(\eta^* J_{0y})_1 + (\eta^* J_{0y})_2$.

Now, the y-component of Eq. (1) for the fluctuations/reads

$$\delta E_y - \delta u_x B_{z0} = -\frac{\partial}{\partial y}\left(\frac{\delta P_e}{n_0 e}\right) \tag{9}$$

where we note that $u_{x0} \equiv 0$ and $\partial P_{e0}/\partial y = 0$. Substitution of (9) into (8) yields, for the first term on the rhs,

$$(\eta^* J_{0y})_1 = \langle \frac{\delta n}{n_0^2 e}\frac{\partial}{\partial y}\delta P_e \rangle. \tag{10}$$

We next assume that the adiabatic law governs the electron fluid.

$$\left(\frac{\partial}{\partial t} + \vec{u}\cdot\nabla\right)(P_e \rho^{-\gamma}) = 0 \tag{11}$$

where the plasma mass density is $\rho \equiv m_i n$ and γ is the adiabatic index. This equation linearizes to

$$\left(\frac{\partial}{\partial t} + u_{0y}\frac{\partial}{\partial y}\right)(\delta P_e - C_s^2 \delta\rho) + \delta u_x \left(\frac{\partial P_{e0}}{\partial x} - C_s^2 \frac{\partial \rho_0}{\partial x}\right) = 0 \tag{12}$$

where $C_s^2 \equiv \gamma P_{e0}/\rho_0 \equiv \gamma T_{e0}/m_i$. Note that $\partial P_{e0}/\partial x$ and $\partial \rho_0/\partial x$ vanish at the field null. Therefore, at the field null,

$$\delta P_e - C_s^2 \delta\rho = f(y - u_{0y} t). \tag{13}$$

Since f is periodic in y, f must vanish identically for unstable perturbations. Therefore, at the field null,

$$\delta P_e = C_s^2 \delta\rho = \gamma T_{e0} \delta n \tag{14}$$

Substitution of (14) into (10) yields $(\eta^* J_{0y})_1 = 0$ at the field null. Therefore, we turn to the second term on the rhs of Eq. (8), namely

$$(\eta^* J_{0y})_2 = \langle \delta u_x \delta B_z \rangle \tag{15}$$

To examine this term, we take the z-component of the curl of Eq. (1), linearized in the fluctuations, and evaluated at the field null. Noting that $\nabla\cdot\vec{B} = 0$, $\nabla\cdot\vec{u}_0 = 0$, $\vec{B}\cdot\nabla\vec{u} = 0$ for flute perturbations, and that n_0 and P_{e0} are independent of y, with $\partial n_0/\partial x = 0$ and $\partial P_{e0}/\partial x = 0$ at the field null, we find

$$\left(\frac{\partial}{\partial t} + u_{0y}\frac{\partial}{\partial y}\right)(\delta B_z) + \delta u_x \left(\frac{d}{dx} B_{z0}\right) = 0. \tag{16}$$

Thus, Eq. (16) determines δu_x in terms of δB_z, which, upon inserting into Eq. (15) yields, at the field null,

$$(\eta^* J_{0y})_2 = -\left(\frac{dB_{z0}}{dx}\right)^{-1} \left\langle \delta B_z \left(\frac{\partial}{\partial t} + u_{0y}\frac{\partial}{\partial y}\right)\delta B_z \right\rangle. \tag{17}$$

The final term clearly vanishes upon averaging periodic perturbations over the y direction. Hence, Eq. (17) reduces to, at the field null,

$$\frac{\eta^*}{\mu_0} = \left(\frac{dB_{z0}}{dx}\right)^{-2} \left\langle \delta B_z \frac{\partial}{\partial t} \delta B_z \right\rangle . \tag{18}$$

In general, a growing mode, periodic in y, can be written as

$$\delta B_z = (a e^{i\psi} + a^* e^{-i\psi}) e^{\Gamma t}; \quad (\psi = ky - \omega t), \tag{19}$$

where Γ is the growth rate and ω is the real frequency of the mode. Upon use of this form in Eq. (18), the final result for η^* can be obtained by averaging over y. No time-average is required. The result is

$$\frac{\eta^*}{\mu_0} = \left(\frac{dB_{z0}}{dx}\right)^{-2} (2\Gamma |a|^2 e^{2\Gamma t}) = \left(\frac{dB_{z0}}{dx}\right)^{-2} (\Gamma |\delta B_z(t)|^2) , \tag{20}$$

where the growing rms (with respect to y) amplitude $|\delta B_z(t)|$ must be assigned a saturated value from some nonlinear model or from experimental observations. Eq. (20) is the general quasilinear expression for the anomalous resistive diffusivity at the field null due to interchange-like modes. In general, one will sum such contributions over all active modes.

V. ANOMALOUS RESISTIVITY AT THE FIELD NULL FROM INTERCHANGE-TYPE INSTABILITIES

For a growth rate that scales (for interchange or co-interchange ideal modes) as[1]

$$\Gamma \sim V_A / (\frac{1}{2} \ell_z) \tag{21}$$

where ℓ_z is the length of a representative flux surface and V_A is a representative Alfvèn speed on that surface, with $(dB_{z0}/dx) \approx B_{ex}/(\frac{1}{2} r_s)$, the anomalous resistive diffusivity at the field null becomes

$$\frac{\eta^*}{\mu_0} \sim \frac{1}{4} \left| \frac{\delta B}{B_{ex}} \right|^2 \frac{r_s V_A}{\epsilon} \quad . \tag{22}$$

Here, ϵ defines (non-standardly) the elongation $(\frac{1}{2} \ell_z / r_s)$ of the unstable flux surface, the field at the separatrix radius r_s is B_{ex}, and $|\delta B|$ is the magnetic perturbation at the field null. This result suggests that larger radius and smaller elongation are detrimental to the effective resistivity at the field null. As a numerical example, we take $B = 5 \times 10^3$ Gauss, $n = 10^{15}\ cm^{-3}$, $r_s = 15\ cm$, $\epsilon = 7$, $V_A \approx 2 \times 10^7\ cm/s$ (deuterium), $|\frac{\delta B}{B_{ex}}| \sim 0.1$, and we then find $(\eta^*/\mu_0) \sim 10^5\ cm^2/s$, compared to a classical resistive diffusivity of $\eta/\mu_0 \sim 10^4\ cm^2/s$ for $T_e = 100\ eV$.

1. D. C. Barnes, "Stability of Tilting Modes in Field-Reversed Configurations," Document EUR 11335 EN, International School of Plasma Physics (Piero Caldirola) edited by S. Ortolani and E. Sindoni, Varenna, Italy (Sept. 1987).

FRC Collisionless Resistivity*

T. Tajima and W. Horton (Institute for Fusion Studies, The University of Texas at Austin)

Ions in the field reversed congifuration (FRC) exhibit stochastic orbits due to the field null and the curvature of poloidal field lines. Velocity correlations of these particles decay in a power law fashion t^{-m} where $1 \leq m \leq 2$. This decay of the single particle correlation function is characteristic of the long tail correlations of strongly chaotic or nonlinear systems found in other problems of statistical physics. This decay of correlations gives rise to a collisionless resistivity that can far exceed the collisional resistivity in an FRC plasma. The finite correlation time τ_c of a single particle limits the acceleration in the electric field producing the finite resistivity. Maxwellian test particle distributions are integrated to find the measure of the set of stochastic ions that contribute to the collisionless resistivity. The computed conductivity is proportional to the square root of the characteristic ion gyroradius in both simulation and theory.

---

*Work Supported by USDoE

SCALING LAWS OF TOROIDALLY COUPLED RF DRIVEN FIELD-REVERSED CONFIGURATIONS

ANDRAS KUTHI
University of California, Los Angeles, CA 90024

ABSTRACT

The RACETRACK reactor concept of two toroidally coupled RF driven FRC-s is examined and scaling laws governing the equilibrium are derived. Radial force balance of the rigidly rotating electron fluid leads to a characteristic plasma radius which is independent of the density, $R^2 = 4T_e/\Omega B_a$. Particle and force balances of the nutral gas lead to a scaling relation between the density of the neutral gas outside the plasma and the peak plasma density. An important characteristic of the rigid-rotor FRC is that fully developed gas blankets are possible, thus eliminating wall effects and greatly reducing the problem of impurities.

Introduction

Field-Reversed-Configurations leek. Mostly because the separatrix maps to the axis and along the associated magnetic field null the pressure gradient cannot be balanced without axial flow. The pressure on axis is quite large, about 30 % of the peak pressure in present day FRC experiments. Reducing the separatrix pressure is not altogether good because then the volume average beta drops and magnetic field utilization becomes inefficient.

To address this issue of axial loss from FRC-s the concept of RACETRACK[1] was developed. RACETRACK consists of two identical long FRC-s side by side connected at the ends by toroidal high-field sections. The beta in the toroidal sections is low, about $1/R_nR_m^2$, where R_n is the pressure ratio - separatrix to peak - and R_m is the mirror ratio, (B_{tor}/B_a) = (toroidal field / straight section field), so the toroidal sections can confine this low beta plasma effectively using traditional stellarator techniques. Most of the plasma, however, is in the high-beta straight FRC-s, so the volume average beta is high and the field utilization is effective. Since we assume recirculation of the axial losses only the radial losses are addressed in this paper.

Assuming the above ideas underlying the concept are correct we proceed to examine the steady-state FRC equilibrium as generated by rotating magnetic fields[2]. The main effect of the rotating transverse field is to establish the form of the diamagnetic current as that due to a rigid rotor plasma,

$$J_d = -enr\Omega(s_i - s_e). \qquad (1)$$

The angular frequency of field rotation is Ω, e is the magnitude of the unit charge, n is the plasma density, and the constant ion and electron slip factors are s_i and s_e, respectively. In addition, we will be using Ampere's law which has the form

$$dB_z/dr = -\mu_0 J_d \qquad (2)$$

in the long cylinder approximation.

The Plasma Momentum Balance

In equilibrium the forces must balance, thus

$$eT(dn/dr) = J_d(B_z - B_c), \qquad (3)$$

where the magnetic field necessary to balance the centrifugal force is B_c. It is given by the formula $B_c = m_i\Omega(s_i - 1)^2/e(s_i - s_e)$. The temperature is assumed constant, $T = T_e + T_i$, which is a good assumption since it has been observed in our experiments[3].

An important difference between inductively generated FRC such as a theta pinch and our rotating field driven FRC is the amount of ion rotation and consequently the magnitude of the centrifugal field. In our case it is quite small, although measurable, while in theta pinch generated FRC-s it is a significant fraction of the total field and therefore less field is available to balance the kinetic pressure.

Eliminating the density from (1), (2), and (3) and solving the resulting second order nonlinear differential equation for $B_z - B_c$ we get the profiles,

$$B_z - B_c = (B_a - B_c)\tanh[(r^2 - r_0^2)/R^2] \qquad (4)$$

and

$$n = n_0 \,\mathrm{sech}^2[(r^2 - r_0^2)/R^2]. \qquad (5)$$

Here B_a is the constant axial magnetic field generated by the external straight section coils, n_0 is the density corresponding to a beta of unity in the field $B_a - B_c$, that is, $n_0 = (B_a - B_c)^2/2\mu_0 eT$. The interesting scaling relation is given by the normalizing radius,

$$R^2 = 4T/(B_a - B_c)\Omega(s_i - s_e), \qquad (6)$$

characterizing the plasma size. The density peak occurs at the radius r_0 when this quantity is real, and on axis when it is imaginary. In the latter case the peak beta is less than one. When the beta is much less than one the density profile tends to a Gaussian[4].

The scaling relation (6) is independent of the density. This means, that we can fix the plasma size by the proper choice of the field rotation frequency! The temperature, magnetic field, and the density tend to be fixed by fusion reaction rate considerations. In another form equation (6) gives a relation for an "effective" S number,

$$R^2/l_i^2 = 2\Omega_i(1 + T_i/T_e)/\Omega(s_i - s_e)(1 - B_c/B_a), \qquad (6a)$$

connecting the number of ion Larmor radii, l_i, inside the plasma with the cyclotron and rotation frequencies. Observe, that this is not the same as the number of Larmor orbits within the separatrix, which would be related to r_0 instead of R, but this distinction is not important for present day configurations with r_0/R of the order of unity.

A whole set of engineering relations between global configuration parameters can now be derived. Let's call the normalized peak radius squared $x_0 = (r_0/R)^2$, then we have the total plasma current

$$I = B_a L[1 + \tanh(x_0)]/\mu_0, \qquad (7)$$

the line density

$$N = I/ef(s_i - s_e)L, \qquad (8)$$

where f is the RF frequency and L is the length of the straight FRC; the stored magnetic energy

$$W_B = IT\ln[1 + \exp(2x_0)]/f, \qquad (9)$$

and the power dissipated by the diamagnetic current

$$P_d = 4\pi\eta L B_a^2 F(x_0)/\mu_0^2, \qquad (10)$$

where the function $F(x_0)$ is given by the formula

$$F(x_0) = (2/3)\ln[1 + \exp(2x_0)] - \mathrm{sech}^2(x_0)/6. \qquad (11)$$

$F(x_0)$ tends to $4x_0/3$ for large x_0, and $F(0) = 0.3$.

The Neutral Gas Balance

In our present low power experiment the peak density is about 10^{12} cm^{-3}, thus it is fully permeable to neutral gas. The neutral density is independent of the radius and so is the ionization frequency, $f_i = n_n\langle sv\rangle_i$. The dominant power requirement is not the one balancing the dissipation of the diamagnetic current but enthalpy lost by the plasma particles,

$$P_H = [3T/2 + W_i]I(f_i/f). \qquad (12)$$

W_i is the ionization potential, possibly including some excitation loss, in which case the power includes radiative losses in addition to the enthalpy loss. However, a high beta fusion plasma is expected to have a density of 10^{15} cm^{-3} which will completely exclude the neutrals. The neutral pressure gradient is then balanced by collisions with the plasma ions and this results in a diffusive scale-length of penetration[5],

$$L_n^2 = eT/m_n n^2 \langle sv\rangle_i \langle sv\rangle_c, \tag{13}$$

where the ionization rate is $\langle sv\rangle_i$, the charge-exchange rate is $\langle sv\rangle_c$, and the neutral mass is denoted m_n. At the boundary layer between the neutral gas and the fully ionized plasma the temperature rapidly drops to a few eV and the electron fluid rotation comes to a halt. In this gas blanket interface the dominant term of the diamagnetic current balance,

$$\eta J_d = \langle v_{ez} B_r\rangle - v_r B_z, \tag{14}$$

is the radial particle flux. If very high rotating field is used, the RF drive term can be dominant all the way to the wall, and then the plasma density profile is unaffected by the gas blanket. However, in the most probable case the rotating field is limited and then the plasma flux outward becomes diffusive instead of convective. Assuming classical cross-field diffusion in the gas blanket balancing the inward gas flux with the outward plasma flux,

$$-(eT/m_n n\langle sv\rangle_c)\ dn_n/dr = (\eta eTn/B_z^2)\ dn/dr, \tag{15}$$

the scaling relation connecting the plasma density entering the blanket, n_b, with the neutral density at the wall is obtained:

$$n_n(\text{wall}) = n_b^3\ (m_n\langle sv\rangle_c\langle\eta\rangle/B_a^2). \tag{16}$$

The heat flux entering the blanket, Q, must be within limits for the blanket to exist. A simple model for the heat balance of the blanket is the following,

$$K\ dT/dr = nv_r(W_i + 3eT) + Q_{rad} - Q, \tag{17}$$

where the classical cross-field heat conductivity is K. This leads to the condition on the maximum heat flux,

$$Q_{max} = eTn_n(\text{wall})v_{ith}(\langle sv\rangle_i/\langle sv\rangle_c)^{1/2}. \tag{18}$$

If the heat flux is larger than this then the blanket will be burned away. Introducing impurities into the blanket on purpose can extend this maximum. The minimum heat flux is given by the enthalpy transport term in eq.(17). For heat flux less than that the blanket will quench the plasma temperature.

[*] Work supported by DOE.

References:

[1] A.Kuthi et al, Rev. Sci. Instrum. **57**, 2720 (1986).
[2] W.N.Hugrass et al, Phys. Rev. Lett. **44**, 1676 (1980).
[3] A.Kuthi et al, Phys. Fluids **B1**, 2054 (1989).
[4] A.Kuthi, Physics Letters **A 127**, 431 (1988).
[5] A.Kuthi, Physica Scripta **26**, 27 (1982).

THE LOWER HYBRID DRIFT INSTABILITY AND THE EVOLUTION OF PLASMA GRADIENTS

A. G. Sgro and S. Peter Gary
Los Alamos National Laboratory

The evolution of plasma gradients is studied with hybrid computer simulations (particle ions, fluid electrons with nonzero mass) carried out in the x-y plane of a plasma with a modest density gradient in the x direction and a magnetic field $\mathbf{B} = B_z(x)\hat{\mathbf{z}}$. These initial density and magnetic field profiles represent a one-dimensional equilibrium of the sheath region of a Field Reversed Configuration (FRC) near the separatrix, and are plotted versus x in the top panel of Fig. 1. All variables are initially uniform in y.

The one-dimensional equilibrium is unstable to the growth of various instabilities. The fastest growing and the first to appear is the lower hybrid drift instability. Initially, the simulation exhibits rapid growth of the fluctuating electric fields. The average growth rate at early times is in good agreement with the maximum growth rate predicted by $\beta = 0$ linear stability theory. By $\Omega_i t \simeq 1.5$, the fluctuating fields have attained their maximum energy density and the initially uniform (in y) density contours, shown in the top panel of Fig. 2 (at $t = 0$), have developed a large amplitude wave as shown in the next panel of Fig. 2. At these early times there are four or five wavelengths in the box, implying a wave number of $ka_i \simeq 8$, fairly close to the wavenumber at maximum growth of $k_m a_i = 10$ predicted by the $\beta = 0$ linear theory. This behavior, and a corresponding response by the B_z contours, not shown here, is quite similar to that found at comparable times in previous simulations of a plasma sheath unstable to the lower hybrid drift instability. These earlier results have led to the general perception that while the y averaged magnetic field and density profiles show an apparent broadening due to these waves, there is no real transport across the sheath since the sheath region, although perturbed, still has about the same thickness locally as it had at $t = 0$.

Our simulations, done with a hybrid code which allows larger time steps and therefore longer runs, are distinguished from these other such computations in several ways but especially in their duration; we have run to many ion gyroperiods to examine the late time fluctuation spectra and density profiles. In this late time regime, localized spreading develops over much of the sheath region. This is illustrated in successive panels of Fig. 2, which shows that the early time, short wavelength density fluctuations coalesce toward longer wavelength structure as time progresses.

The lower panels of Fig. 1 plot $n(x)$ at several different y-values. In some regions the sheath remains relatively narrow in x, while in other regions it becomes much broader. At some y-values the density falls to a low value monotonically, while in others a plateau develops in $n(x)$ at intermediate x, and only at larger x does the density fall to the lowest value. Thus, although the density and field contours spread and the sheath becomes broader at local values of y as well as on average, the process is much more in the nature of a turbulent evolution of the sheath and does not exhibit the monotonically decreasing profile in x at many values of y, nor the homogeneous character in y, expected of a diffusive process.

In conclusion, we have obtained two new results which we believe have important implications for further studies of wave-particle transport across plasma gradients in general and across the FRC separatrix in particular. First, we find that the lower hybrid drift instability exhibits a shift to longer wavelength fluctuations as time progresses. Second, relatively flat density plateaus are observed in the simulation results.

Our simulations show results which violate two important assumptions usually made for quasilinear theories of transport by the lower hybrid drift instability: first, that the instability retains the relatively short wavelength of its linear growth phase and, second, that these short wavelength fluctuations stochastically scatter plasma particles to yield cross-field diffusion.

From the progressive broadening of the sheath as the simulation progresses, it might be concluded that the influence of the enhanced fluctuations weakens as the sheath broadens. However, it may be seen that this is not true by recalling that the combined effect of plasma transport from the interior of the FRC toward the sheath, and the loss of plasma along open field lines, will act to steepen the gradient. On time scales of interest, the plasma gradient will broaden until the two effects balance and plasma loss will proceed as part of this quasi-steady condition at the sheath.

SC025281-2.BA

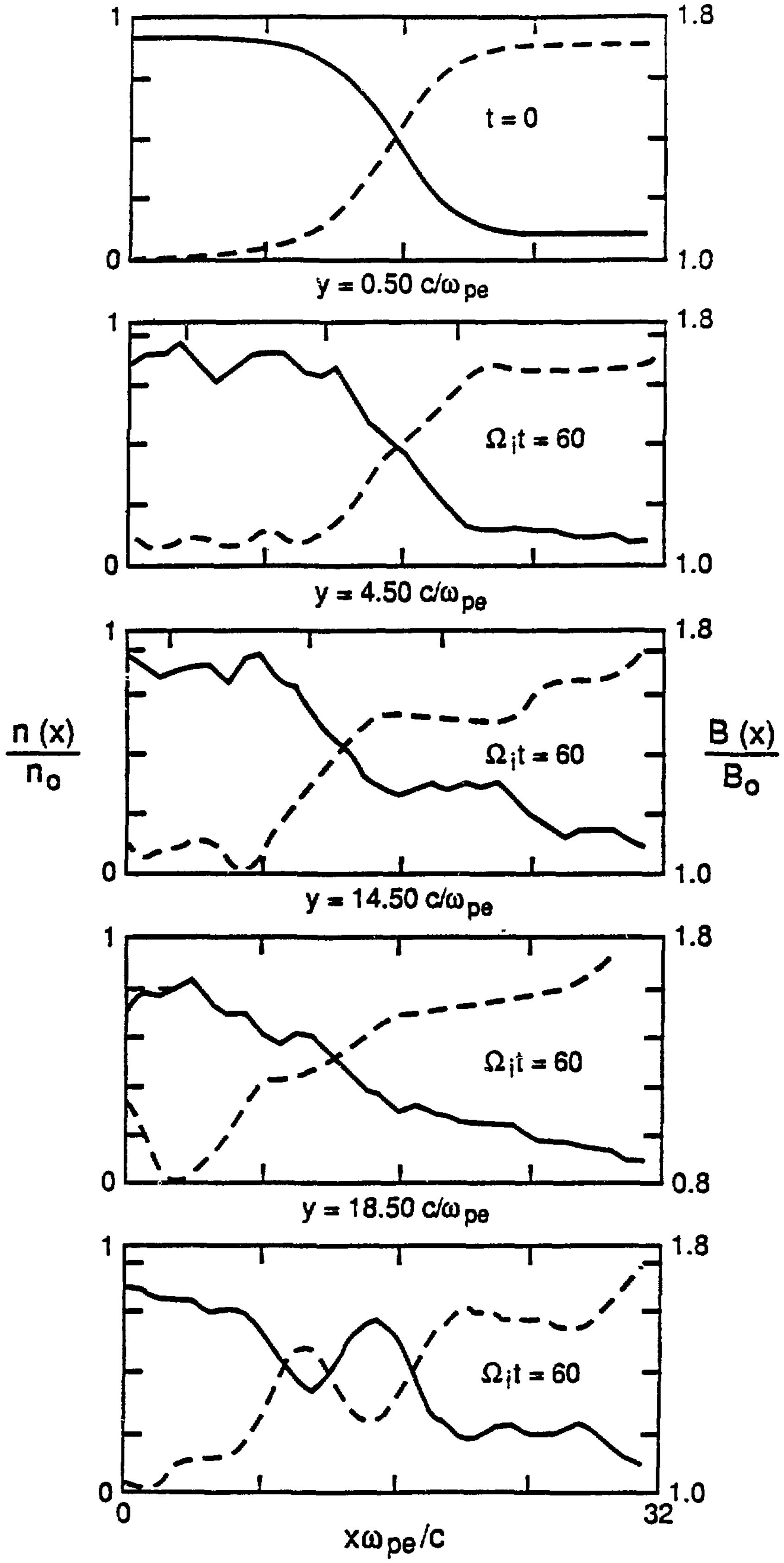

Figure 1

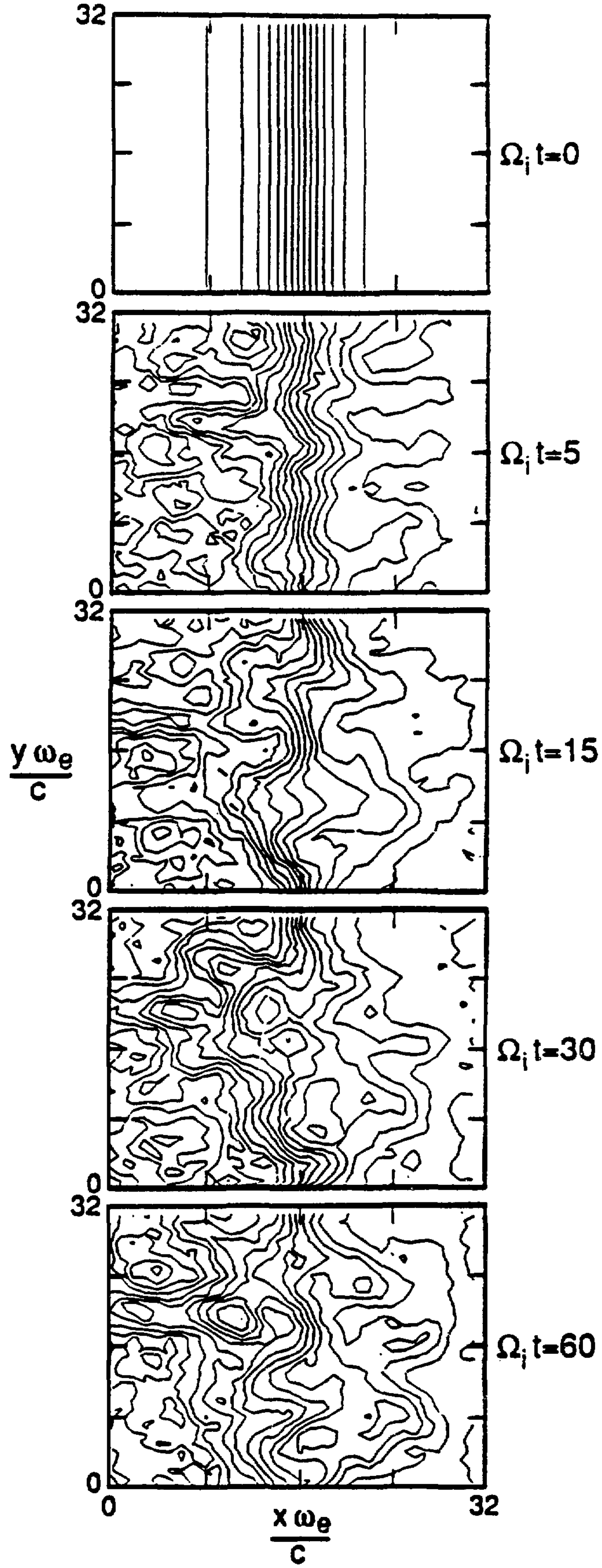
32
0
$\Omega_i t=0$
32
0
$\Omega_i t=5$
32
0
$\Omega_i t=15$
32
0
$\Omega_i t=30$
32
0
$\Omega_i t=60$
$\frac{y\,\omega_e}{c}$
0
32
$\frac{x\,\omega_e}{c}$

Anomalous Heat Transport Caused by Ion Temperature Gradient Driven Turbulence

SATOSHI HAMAGUCHI
Institute for Fusion Studies
The University of Texas at Austin
Austin, Texas 78712

Abstract

The ion temperature gradient driven mode or η_i-mode turbulence is discussed as a source of anomalous heat transport. The scaling of the anomalous ion heat conductivity with magnetic shear $s = L_n/L_s$ and the excess of $\eta_i (= L_n/L_{T_i})$ over the critical value $\eta_{i,c}$ for marginal stability is found to vary as $\chi_i = g\,(\rho_s/L_n)\,(cT_i/eB)\,(\eta_i - \eta_{i,c})\exp(-\alpha s)$, where $g = O(1)$ and $\alpha \simeq 5$.

1. Introduction

From the numerous results of experiments, it is known that the transport observed in Field Reversed Configurations (FRC) is anomalous or significantly larger than classical diffusion.[1] It is generally considered that this anomalous transport is due to turbulence of the plasma excited by various microinstabilities. For the current FRC experimental devices, where the typical ion-drift parameter $v_D/v_i = \rho_i/L_n$ ($v_D = v_i^2/\omega_{ci}L_n$, $v_i^2 = T_i/m_i$, $\rho_i = v_i/\omega_{ci}$, and $L_n = -(\partial \ln n/\partial r)^{-1}$) is of $0.2 \sim 0.8$ and the density gradient is generally much larger than the ion temperature gradient ($\eta_i = L_n/L_{T_i} \ll 1$, $L_{T_i} = -(\partial(\ln T_i)/\partial r)$), the lower hybrid drift (LHD) instability is unstable and believed to produce the anomalous transport.[2] The LHD instability is mainly driven by the density gradient and has a real frequency and a growth rate near the lower hybrid frequency $\omega_{LH} = (\omega_{ce}\omega_{ci})^{1/2}$. This fast growing instability is also known to be stabilized by temperature gradients[3,4] although current experiments do not seem to produce large enough temperature gradients to completely stabilize the LHD mode.[2] In future experiments of the FRC, where the temperature will be significantly higher and the duration of discharges will be significantly longer, however, one could expect that the microinstabilities with low frequencies $\left(\omega_{ci} \lesssim \omega \lesssim \omega_e^* = (cT_e/eB)(ky/L_n)\right)$ play more important roles in anomalous transport of FRC plasmas.

From this point of view, we discuss the microinstability caused by the ion temperature gradient and the associated heat transport in the present work. There are two different branches of the ion temperature gradient driven mode (or the η_i-mode): one is the interchange-like mode driven by the field curvature and the ion temperature gradient and the other is the slab mode driven by the coupling of the drift wave to the ion acoustic wave destabilized by the ion temperature gradient. In this work, we only consider the latter one or the slab η_i-mode, which is expected to be important in the long central region of a high-temperature FRC plasma.

2. Dynamical Equations

The dynamical equations of the slab ion temperature gradient driven mode are derived from the two fluid equations with the assumptions of the electrostatic mode and adiabatic electrons.[5] In the central region of a FRC plasma, the magnetic field configuration may be modelled as $\mathbf{B} = B(\hat{\mathbf{z}} + (x/L_s)\hat{\mathbf{y}})$, where B is the constant poloidal field, Bx/L_s is the weak toroidal field and x is the position in the radial direction measured from a particular radius r_0. Here L_s denotes the scale length of the magnetic shear. Using the standard notations of physical quantities,[6] we define the following characteristic velocity and space scales

$$c_s = \left(\frac{T_e}{m_i}\right)^{1/2}, \qquad \rho_s = \frac{c_s}{\omega_{ci}} = \frac{c(m_i T_e)^{1/2}}{eB},$$

the nondimensional parameters

$$K = \frac{T_i}{T_e}(1+\eta_i), \qquad \Gamma = \frac{\gamma T_i}{T_e},$$

and space-time variables

$$\tilde{x} = \frac{x}{\rho_s}, \qquad \tilde{y} = \frac{y}{\rho_s}, \qquad \tilde{z} = \frac{z}{L_n}, \qquad \tau = \frac{tc_s}{L_n}.$$

Here the subscript 0 denotes the unperturbed quantities which are assumed to be functions of only x, and the tilde denotes the fluctuating quantities. We also assumed that the unperturbed parts of the velocity field $\mathbf{v}$ and the potential Φ be zero and the adiabatic elections, i.e., $\tilde{n} = e\Phi/T_e$. In the FRC, where the ion temperature T_i tends to be higher than the electron temperature T_e, it is reasonable to assume that $\rho_s/L_n = c(m_i T_e)^{1/2}/eB\,(< v_D/v_i)$ be a typical small scale. Therefore, with the assumption that the fluctuation level be of order ρ_s/L_n, the evolution equations of the slab η_i-mode are given by

$$\left(1-\nabla_\perp^2\right)\frac{\partial\phi}{\partial\tau} = -\left(1+K\nabla_\perp^2\right)\frac{\partial\phi}{\partial\tilde{y}} - \nabla_\parallel v + \left\{\phi, \nabla_\perp^2\phi\right\} - \mu_\perp\nabla_\perp^4\phi \tag{1}$$

$$\frac{\partial v}{\partial\tau} = -\nabla_\parallel(\phi+p) - \{\phi, v\} + \mu_\perp\nabla_\perp^2 v + \mu_\parallel\nabla_\parallel^2 v \tag{2}$$

$$\frac{\partial p}{\partial\tau} = -K\frac{\partial\phi}{\partial\tilde{y}} - \Gamma\nabla_\parallel v - \{\phi, p\} + \chi_\perp\nabla_\perp^2 p + \chi_\parallel\nabla_\parallel^2 p, \tag{3}$$

where only the $\mathbf{E}\times\mathbf{B}$ convective nonlinear terms are retained as nonlinearity. Here, $\phi = \left(e\tilde{\Phi}/T_e\right)(L_n/\rho_s)$, $v = \left(\tilde{v}_\parallel/c_s\right)(L_n/\rho_s)$, $p = (\tilde{p}_i T_i/p_{i0}T_e)(L_n/\rho_s)$, $\{f, g\} = \hat{z}\cdot\nabla_\perp f\times\nabla_\perp g$, and $\nabla_\parallel = \partial/\partial\tilde{z} + s\tilde{x}\partial/\partial\tilde{y}$.

3. Linear Stability Analysis

Linear stability properties are briefly discussed in this section with a special emphasis on the shear stabilization effect. Assuming the $\tilde{y}$ and τ dependence of the dependent variables

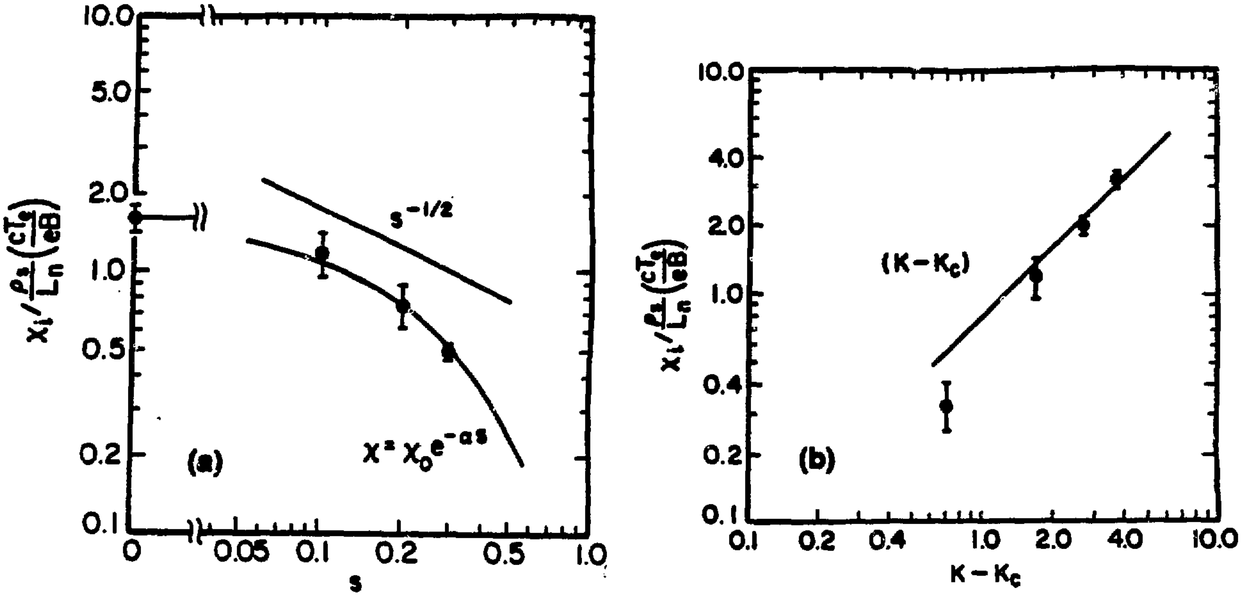

Figure 1. Dependence of the anomalous ion heat conductivity χ_i on shear s (a) and $K\,(T_i/T_e)\,(1+\eta_i)$ (b).

as $\exp ik\,(\tilde{y} - \Omega\tau)$ in Eqs. (1)–(3), where $k = k_y\rho_s$ is the normalized wavenumber in the y direction and $\omega = k\Omega$ is the normalized complex frequency we linearize Eqs. (1)–(3):

$$\frac{d^2}{d\tilde{x}^2}\tilde{\phi} + \left(-k^2 + \frac{1-\Omega}{\Omega+K} + \frac{B+K}{\Omega+K}\cdot\frac{s^2\tilde{x}^2}{AB - s^2\tilde{x}^2\Gamma}\right)\tilde{\phi} = 0, \qquad (4)$$

where $A = \Omega + i\mu_{\|}ks^2\tilde{x}^2$ and $B = \Omega + i\chi_{\|}ks^2\tilde{x}^2$. Here we set $\mu_\perp = x_\perp = 0$, considering a collisionless plasma. It is known[5] that, in the case where $\mu_{\|} = \chi_{\|} = \Gamma = 0$, Eq. (4) gives the following eigenvalue $\Omega = \Omega_{\ell k}$ and the eigenfunction ϕ:

$$\Omega_{\ell k} = \frac{1}{2\,(1+k^2)}\left[\left(1 - k^2K - is(2\ell+1)\right) \pm \sqrt{\left(1 - k^2K - is(2\ell+1)\right)^2 - 4is\,(1+k^2)\,(2\ell+1)K}\right] \qquad (5)$$

and

$$\tilde{\phi} = e^{-\sigma\tilde{x}^2/2}H_\ell\left(\sigma^{1/2}\tilde{x}\right), \qquad (6)$$

where $\sigma = is/\Omega$, $\ell(\ell \geq 0)$ is the radial mode number associated with the ℓth eigenvalue of the Weber equation, and $H_\ell(z)$ is the ℓth-order Hermitian function of the complex variable z. We note from Eq. (5) that the shear and radial eigenmode number dependence of $\Omega_{\ell k}$ enter the formula as the term $s(2\ell+1)$. As shown in Ref. 6, the maximum growth rate $\gamma_{\max} =$

$\max_{k,\ell}(k\,\mathrm{Im}\,\Omega_{\ell k})$ is a function of only K, not of shear s, since $\gamma_{\max}$ may be obtained by varying $\bar{s} = s(2\ell + 1)$ (rather than just ℓ) as well as k. Therefore, the growth rate of the most unstable slab η_i-mode is independent of the shear s. With the effects of finite dissipation and compressibility (i.e., $\Gamma \neq 0$), it has been shown[6] that γ is a decreasing function of the shear s. In particular, compressibility shows a strong stabilization effect when the shear s is large.

4. Numerical Results and Conclusions

Equations (1)–(3) are solved numerically and the anomalous ion heat conductivity $\chi_i = \langle \tilde{p}_i \tilde{v}_{ix} \rangle / (-p'_{i0})$ is estimated.[6] Figure 1(a) and (b) show the dependence of χ_i on s (with fixed $K = 3.0$) and $K - K_c = (\eta_i - \eta_{i,c})T_i/T_e$ (with fixed $s = 0.1$), respectively. Here, $\mu_\perp = x_\perp = 0.1$, $\mu_\| = x_\| = 1.0$, $\Gamma = 2$ and the domain $L_x \times L_y \times L_z = 40\rho_s \times 10\pi\rho_s \times 7L_n$. From the nonlinear analysis in Ref. 6 and these numerical simulations, we obtain the scaling of χ_i as

$$\chi_i = g\frac{\rho_s}{L_n}\left(\frac{cT_i}{eB}\right)(\eta_i - \eta_{i,c})\exp(-\alpha s),$$

where $\alpha \simeq 5$ and $g = O(1)$.

Acknowledgements

The author wishes to thank W. Horton and A. Ishida for helpful discussions. The work was supported by U. S. Department of Energy Contract No. DE-FG05-80ET-53088.

References

1. M. Tuszewski, Nucl. Fusion **28**, 2033 (1988).
2. A. W. Carlson, Phys. Fluids **30**, 1497 (1987).
3. J. B. McBride and S. Hamasaki, Phys. Fluids **21**, 1979 (1978).
4. S. P. Gary and J. J. Sanderson, Phys. Fluids **21**, 1181 (1978); **22**, 338(E) (1979).
5. W. Horton, R. D. Estes, and D. Biskamp, Plasma Physics **22**, 663 (1980).
6. S. Hamaguchi and W. Horton, IFSR #383, The University of Texas at Austin (1989), submitted to Phys. Fluids **B**.

FORMATION OF FRCs WITH LARGE BIAS FIELDS

John T. Slough
Spectra Technology, Inc.
Bellevue, WA

Operation of field reversed theta pinches (FRTP) at high bias fields is desirable for forming high flux FRCs. However, at high bias fields radial shock heating becomes ineffective, and the resulting high flux and low plasma energy results in strong axial implosions. This is especially true for large devices where ohmic losses may be expected to be small. These strong axial implosions have either prevented long lived FRCs from being formed, or have resulted in large flux losses during and immediately following the axial implosion. By employing new formation methodologies, which emphasize initial plasma uniformity, high bias field operation with good flux retention was obtained on the TRX[1] device.

The strength of the axial contraction, which occurs sometime after field reversal, can be crudely evaluated by comparing the plasma heating before the axial contraction with that which would be required to produce a given equilibrium FRC length. The pre-axial contraction heating comes from the two sources listed below:

$$\text{radial shock:}\quad E_r = 0.4 f_s B_*^{6/5} B_c^{4/5}\, \pi r_w^2 L_c/\mu_o \qquad [1]$$

$$\text{ohmic heating:}\quad E_j = (1-f_\phi^2)\, B_{1o} B_c\, \pi r_w^2 L_c/\mu_o \quad . \qquad [2]$$

f_ϕ is the fraction of initial lift-off flux, $\Phi_{1o} = \pi r_w^2 B_{1o}$, retained, and $f_s = 1/(1 + 1.7(B_{1o}/B_*)^{3/2})$ is the reduction in radial shock heating effectiveness due to the presence of a bias field. B_{1o} is the lift-off field, B_c is the field (assumed constant) at which the axial contraction occurs, and B_* is the characteristic field defined by Green and Newton,[2] $B_*(\text{kG}) = 2.26 E_\theta^{1/2}(\text{kV/cm})\, p_o^{1/4}(\text{mTorr})$ for deuterium. These energies must be compared with the required plasma energy for an equilibrium FRC:

$$\text{equilibrium:}\quad E_p = 1.5\langle\beta\rangle B_c^2\, \pi r_s^2 L_s/2\mu_o \qquad [3]$$

where r_s is dependent on the field profile which, for simplicity, can be taken as a rigid rotor with $r_s = (\pi f_\phi B_{1o} r_c/r_w B_c)^{1/3} r_w$. Ignoring radial shock heating, and equating Eqs. (1) and (3) yields an expression for the minimum length to diameter ratio, ϵ_{min} (using $r_w/r_c = 0.9$, $\langle\beta\rangle = 0.9$).

$$\epsilon_{min} = \frac{L_s}{2r_s} \simeq 0.5\, \epsilon_c \frac{(1 - f_\phi^2)}{f_\phi} \qquad [4]$$

where ϵ_c is the ratio of the coil length to tube diameter.

In the absence of radial shock heating, the minimum transient elongation, ϵ_{min}, is seen to depend only on the flux loss during formation - not explicitly on B_{1o} or B_c. The predicted ϵ_{min} for FRC-C/LSM and TRX is shown in Figure 1. The ϵ_{min} for LSX would be the same as TRX if the formation flux loss were similar since ϵ_c is the same for the two devices. The minimum elongation for FRX-C/LSM is found to be smaller for the same flux loss due to the shorter coil. It can be seen that the observed flux loss and ϵ_{min} for both FRC-C/LSM and TRX are in good agreement with this rather crude analysis. The inclusion of the complete thermalization of the radial shock energy implied by eq. (1) significantly changes the predicted ϵ_{min} during formation. For a B_{1o}/B_* of 0.1 to 0.2, characteristic of the experiments on FRX-C/LSM, it can be seen from Fig. 1 that ϵ_{min} would never be less than 4. The observation of much smaller elongations on LSM[3] indicates that thermalization of the radial shock energy is not complete at the time of the axial implosion, and that eq. (1) considerably overestimates the amount of radial shock heating in a large radius device such as LSM. It would appear from the LSM data that for a large device, radial shock heating is minimal, even though E_θ is maintained at a large value.

It is also clear from Fig. 1 that flux retention from lift-off into the equilibrium does not increase with increased size. This is contrary to what one would expect if plasma turbulence, responsible for the anomolous flux loss during formation, scaled independent of radius. The increased resistivity during formation with size, implied by the LSM results, is not necessarily bad. It allows for greater preheating of the plasma prior to the peak axial implosion and therefore avoids very short ϵ_{min}. The value of f_ϕ was similar for both LSM and TRX, which also had similar formation times. Since the extrapolation from LSM to LSX is small compared to TRX, a similar value of f_ϕ can be expected. In that case the ϵ_{min} should be no worse than that experienced on either TRX or LSM.

The relatively large values of f_ϕ observed on TRX, particularly at large B_{1o}, were achieved only when barrier fields were employed during both preionization and field reversal. A drawing of the barrier field rods, attached directly to the outside of the plasma tube, is shown on Figure 2. Application of the short range barrier fields (generally at a level of about 1.5 kG at the wall) during field reversal reduced the overall impurity level, but the most dramatic effect occurred when the barrier fields were also on during preionization. Optimum timing of the barrier fields with the main fields and ionization currents are shown on Figure 3 for both I_z and slow ringing I_θ preionization. A much more symmetric ionization distribution (as inferred from visible photography and the symmetry of the radial and axial implosions) was then achieved, which resulted in high levels of flux retention at values of B_{1o} approaching B_*, even though the axial implosions were then so strong that minimum transient FRC elongations ($L_s/2r_s$) as low as 1.5 were seen.

Flux retention data for TRX, operated both with and without barrier fields, is shown on Figure 4. All data represent discharges where a stable FRC was formed with an equilibrium flux confinement time greater than 50 µsec. The barrier field data at 5 and 10 mTorr fill pressures were taken with both I_z and ringing I_θ inductive preionization. The calculated maximum 65% flux retention was obtained for both forms of preionization although, at high flux, the results were less reproducible when using I_z preionization. Without barrier fields, FRCs could be formed only sporadically for lift-off fields above 1 kG, and when they could be formed the flux retention was poor. At lift-off fields above 1.2 kG, the barrier field - I_z preionization results also tended to become much more erratic. 1.2 kG, however, was the maximum lift-off field which could be obtained using ringing I_θ preionization and the 3-turn TRX-2 coils. The higher lift-off field data at 15 mTorr fill pressures was obtained with ringing I_θ preionization and the old single turn TRX-1 coils (with a degraded E_θ of only 0.22 kV/cm and $B_* = 2.1$ kG). Reproducible 65% flux retention was extended up to lift-off fields of 1.5 kG, which was the maximum lift-off field that could be trapped using that magnet and preionization configuration. This produced record (for TRX) equilibrium fluxes of 3 mWb, and permitted FRC lifetime measurements to be made at s values above 3.[5]

The results shown on Figure 4 are a considerable improvement over previously reported flux retention, which tended to fall within the cross hatched area. Operation in other experiments at f_ϕ values above 0.65 (since some flux loss must also occur during the axial implosion), is well into the region shown on Figure 1 where strong axial implosions would be expected to occur, and where transient elongations as low as 1.5 were indeed measured. Prior to the use of barrier fields, formation at such high B_{lo}/B_* values was always very irreproducible, and always involved very poor flux retention.

An indication of the improvement in formation performance is shown on Figure 5 which, except for the new data, is a reproduction from Reference 4. Previously, obtainable equilibrium fluxes for long lived FRCs fell in the range of 0.1 to 0.2 of $\Phi_* = \pi r_w^2 B_*$. Using barrier fields, Φ_e/Φ_* values of 0.5 could be obtained. As shown on Figure 1, this high a lift-off field operation will become more difficult in larger devices as f_ϕ increases. The large s experiment (LSX) presently under construction at Spectra Technology (r_w = 40 cm) needs to operate at a lift-off field of 1 kG to meet its design goal of s = 8 (30 mWb equilibrium flux), and its B_* is only about 1.2 kG. Methods of delaying the axial contraction until more flux loss can occur will be utilized, but it will still be impossible to avoid strong axial implosions at such high ratios of B_{lo}/B_*. The ability of the barrier field assisted preionization to provide the initial plasma uniformity needed to survive the expected strong axial dynamics will be a rigorous test of this new technique.

REFERENCES

1. J.T. SLOUGH, A.L. HOFFMAN, R.D. MILROY, Phys. Fluids B 1, 840 (1989).
2. T.S. GREEN, and A.A. NEWTON, Phys. Fluids 9, 1386 (1966).
3. M. TUSZEWSKI, et al., Proceedings of the 8th Compact Toroid Symposium, University of Maryland, June 4-5, 1987, pg. 191.
4. M. TUSZEWSKI, Phys. Fluids 31, 3754 (1988).
5. J.T. SLOUGH and A.L. HOFFMAN, Nuclear Fusion 28, 1121 (1988).

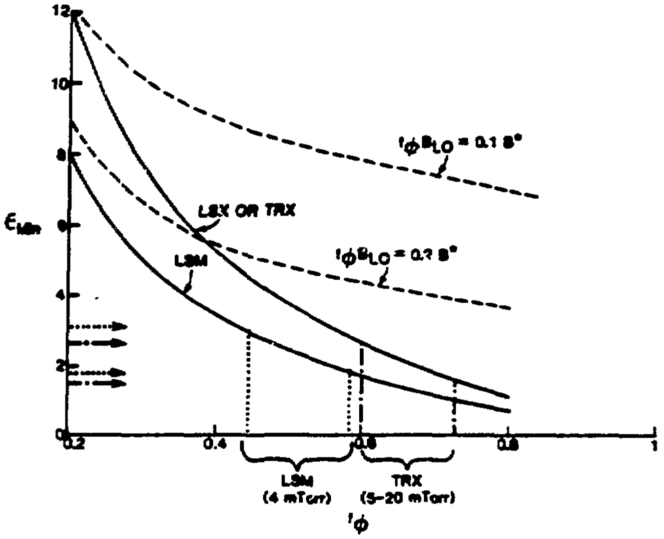

Figure 1. ϵ_{min} predicted by Eq. (4). Dashed curves assume additional radial shock heating as in Eq. (2) over range of lift-off fields used on LSM.

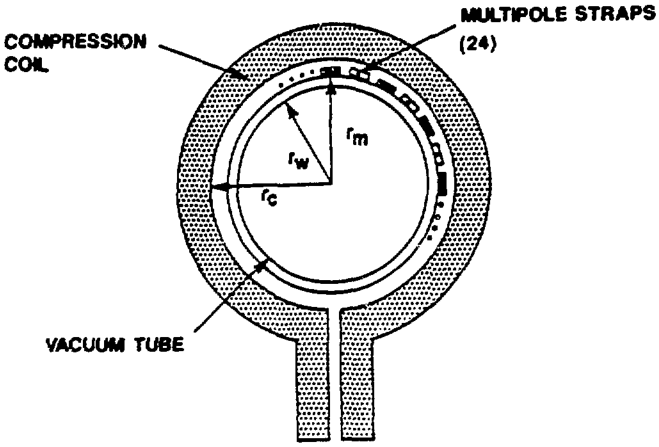

Figure 2. Barrier Strip Geometry on TRX-2 (r_w = 10cm, r_m = 10.5cm, r_c = 12.5cm).

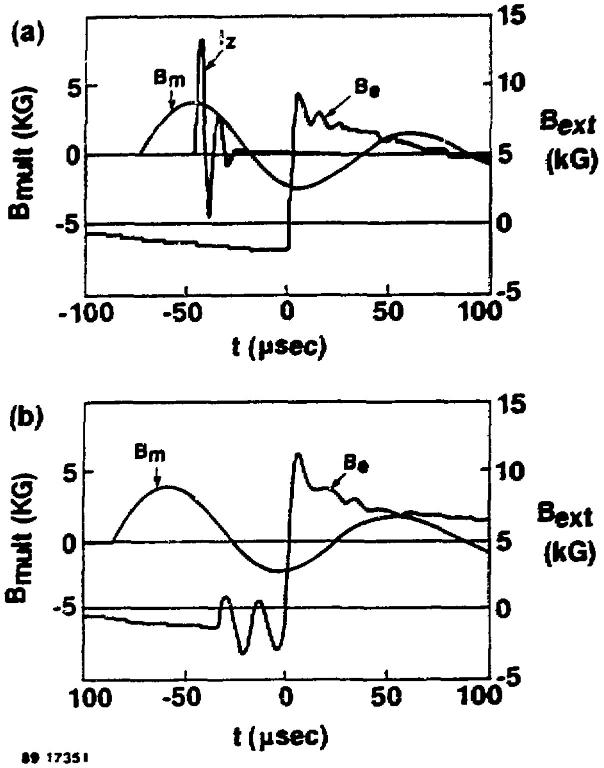

Figure 3. Time Histories of Various Fields and Currents for
(a) Axial Discharge Preionization, and
(b) Inductive Preionization.

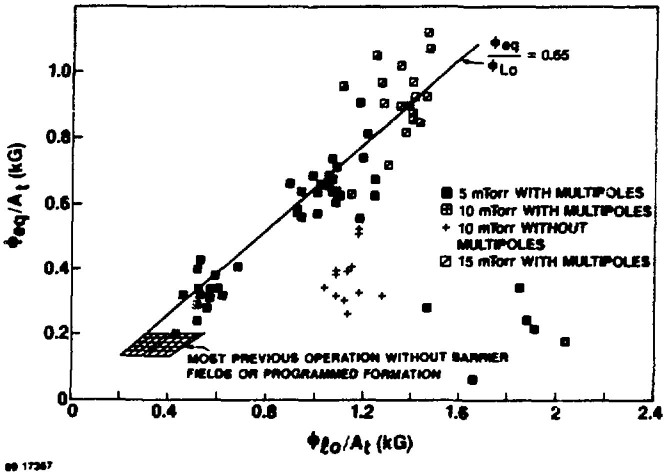

Figure 4. Poloidal Flux in the Equilibrium FRC as a Function of Lift-Off Flux (Normalized to Tube Area).

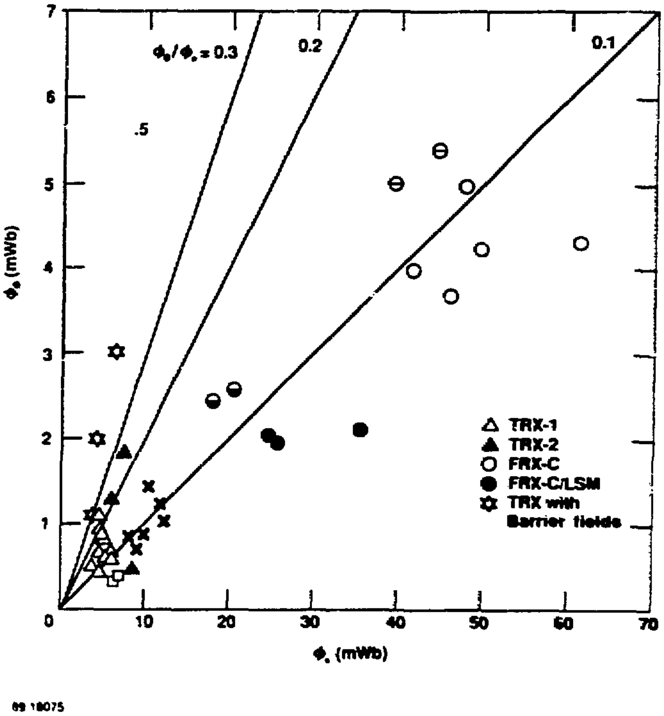

Figure 5. Equilibrium Flux Data from Ref. 4 with New Barrier Field Data.

Stabilization of Rotational Instability in FRC by an Axial Current

Y.Nogi, M.Ooi, Ta.Takahashi, T.Saito.
Y.Maruyama, T.Takahashi, S.Shimamura
College of Science and Technology, Nihon University
1-8 Kanda Surugadai, Chiyoda-ku, Tokyo 101, Japan

1. Introduction

Most dangerous macroscopic instability in Field-Reversed Configuration(FRC) plasma is known as an $n=2$ rotational instability which deforms elliptically the cross section of the plasma column. The growth of the instability, however, could be suppressed by multipole field[1]. We found that the instability was also stabilized by another method. The stabilizing effect of this method comes from tension of the azimuthal field line which is produced by axial current flowing on the separatrix. Frequency and amplitude of the axial current were varied to know the threshold value of the stability. Preliminary results of the present experiment are given and the stability condition is compared with Ishimura's theory[2].

2. Observation of Rotational Instability

The FRCs produced by two devices NUCTE-2 and 3 are discussed in this paper. The plasma was observed by an excluded-flux array, a single-chorded interferometer at the axial midplane of the coil $z=0$, an optical fiber array to measure plasma light in visible range at $z=-5$cm and a B_θ probe array at $z=\pm 19$cm. Each fiber has a collimator to detect the light emitted from narrow region. The arrangement of these diagnostics without the excluded-flux array is shown in Fig.1. Typical behavior of the FRC at 6mtorr fill pressure without the stabilizing current is seen in Fig.2. The rotational instability is shown as out of phase in the visible lights, which corresponds to the modulation of $\int n_e dl$ signal. Figure 3 includes one of B_θ signals on the same experimental condition as Fig.2 and a result of Fourier analysis of them. The n-th mode amplitude is defined here as $\sqrt{(a_n^2+b_n^2)}$ which can be obtained from the coefficients in Fourier series $B_\theta = a_0/2+\Sigma(a_n \cos n\theta + b_n \sin n\theta)$. The $n=1$ mode keeps small level through the discharge, but the $n=2$ mode grows with onset of the rotational instability. This result predicts that a quadrupole current is induced near the plasma column. We can construct the current channel from the B_θ signals as Fig.4. The mechanism of the current generation is attempted to explain from both effects of charge separation near the separatrix by centrifugal force and end shorting of the created charges.

3. Limit of Applied Current

There existed the critical amplitude of the current to apply the FRC. Above the value the FRC was destroyed by the growth of kink instability. Experiment showed that the applied current must satisfy the following condition[3]

$$q = \frac{2\pi r_s B_e}{l_s \mu_0 I_z / 2\pi r_s} > 1 \qquad (1)$$

where B_e, r_s and l_s are the external field, the separatrix radius and the separatrix length, respectively.

4. Stabilizing Experiment

The stabilizing current was applied to the FRC at about t=30 μs which was almost onset time of the rotational instability. The current ranged in amplitude I_z=26-56kA and in frequency ω=0-4.5x10^5rad/s. The q value is very close to unity at I_z=56kA. The stabilizing effect became clear with increasing the amplitude and the frequency of the current. The modulation in $\int n_e dl$ is lowered by this effect as seen in Figs.5(a) and (b) where the currents of I_z=47kA with ω=4.3x10^5rad/s and I_z=56kA with ω=4.5x10^5rad/s are applied. It was known from the excluded-flux signal that the termination time was prolonged to 100-110μs by the axial current. There was no much difference in the separatrix length between the FRCs with and without the current.

Kink instability was frequently excited by the high current. The abrupt decrease of $\int n_e dl$ in Fig.5(c) results from the movement of the plasma column to the tube wall. This behavior was pursued by the B_θ probe array. Figure 6 shows two cases of the n=1 mode in high and low currents. The mode grows rapidly in the high current case as soon as the current starts.

4. Discussion

Ishimura derived the critical current to stabilize the rotational instability from linear MHD equations[2]. The stabilizing effect of the current is not expected in the frequency range of $\omega \lesssim \Omega$ where Ω is angular velocity of rotation of the plasma column around z-axis, but the FRC is stabilized in $\omega \gg \Omega$ by the following condition

$$\frac{B_a^2}{\overline{B}_a^2} > \frac{1-x_s^4}{1+3x_s^4} - \left(\frac{1+x_s^4}{1+3x_s^4} + \frac{x_s^2(1-x_s^4)}{2(1+3x_s^4)}\right) \frac{\overline{q}_1^2}{\overline{B}_a^2} \qquad (2)$$

where $B_\theta = (r_s/r) B_a \cos(\omega t + \delta)$, $\overline{B_a} = r_s \Omega \sqrt{(\mu_0 \rho)}$, $\overline{q}_1 = \pi r_s B_e / (l_s \overline{B_a})$ and ρ =mass density. The present experiment is limited in the range of $\omega \lesssim 2\Omega$. The onset of the kink instability might be explained by the theory. The n=2 mode, however, is always stabilized in the experiment, though the stability region of the theory is very narrow in this frequency range. The square of azimuthal field at the separatrix B_a^2 to stabilize the rotational instability was needed 3-10 times larger than that expected from the theory. Since the current has damping wave form with e-folding time $\tau \sim 20\mu$s in the experiment, the effective value of B_a^2 during the current pulse approaches to the theory.

The experiments are summarized as follows. The rotational instability is stabilized by high frequency axial current, but the kink mode can't be suppressed at present. The current with much higher frequency will be applied to the FRC to control the kink motion.

References

[1] S.Ohi et al., Phy. Rev. Lett. 51 (1983) 1042

[2] T.Ishimura, Proceeding of 10th US-Japan Workshop on Compact Toroids, Hakone, Nov.14-16 (1988) page 84

[3] S.Okada et al., Plasma Physics and Controlled Nuclear Fusion Research 1986, 2 (1987) 551

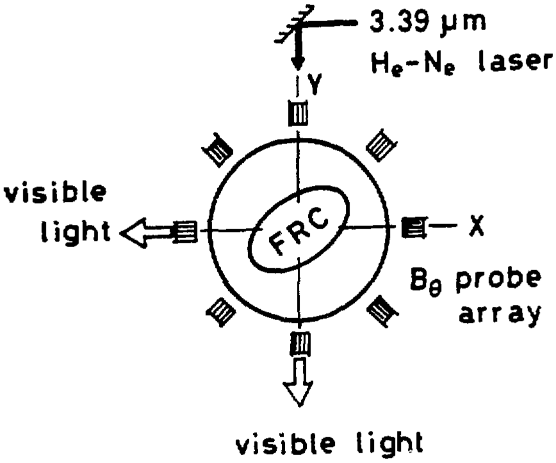

Fig.1
Schematic of diagnostics

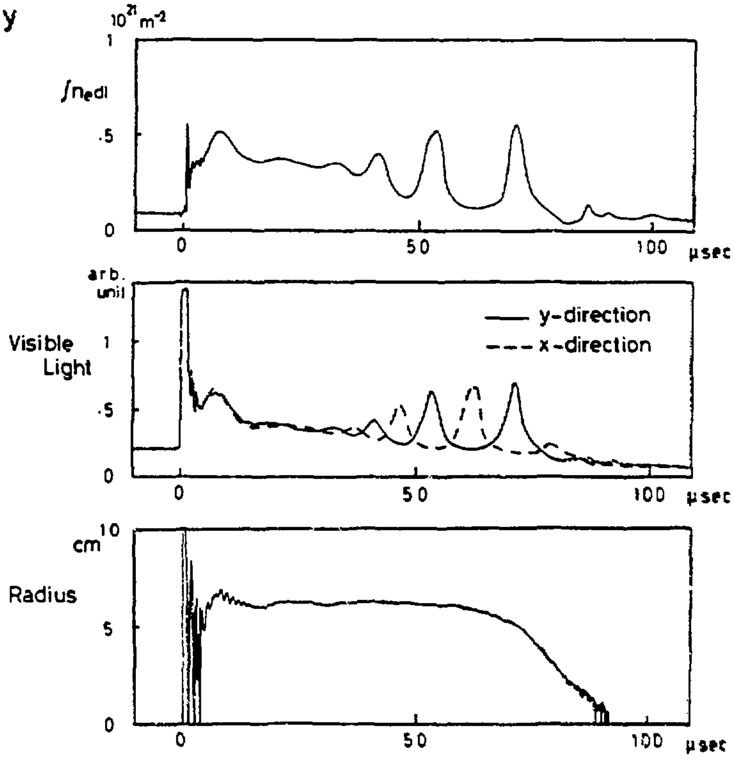

Fig.2
Time evolutions of $\int n_e dl$, visible lights and r_s of FRC without stabilizing current

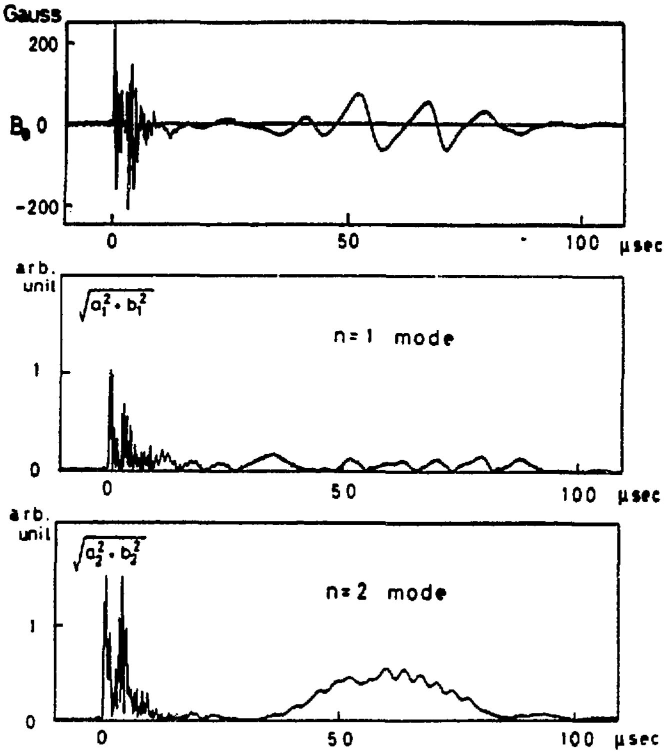

Fig.3 Typical B_θ signal and growth of n=2 mode

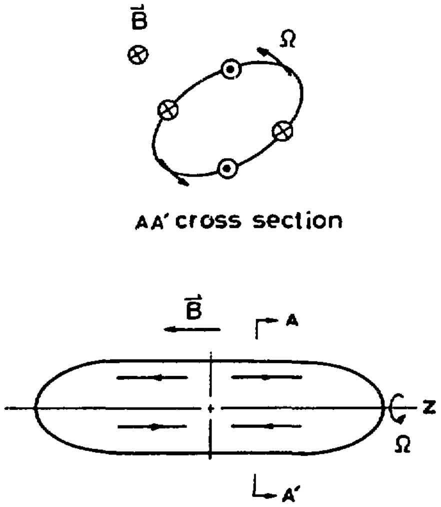

Fig.4 Current channels predicted from B_θ fields

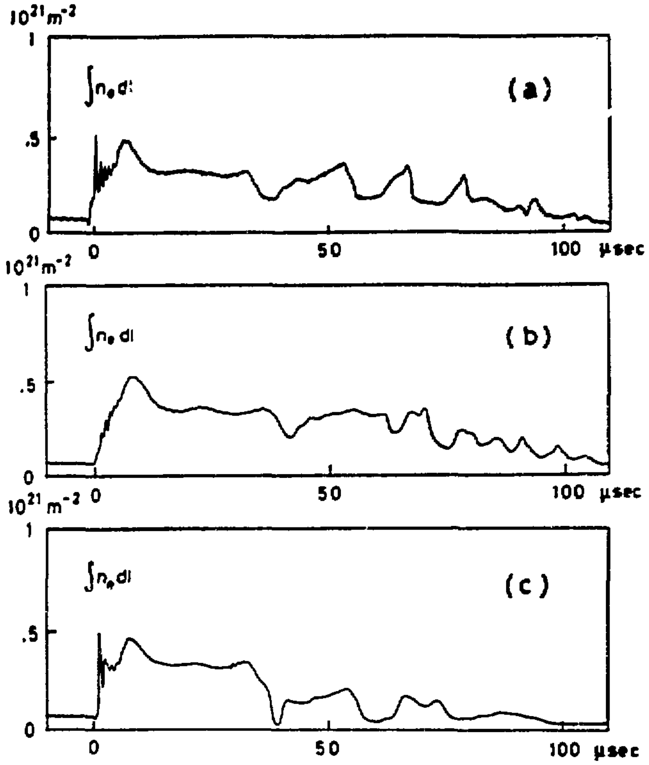

Fig.5 Behaviors of FRC with axial current of (a) I_z=47kA, (b)and(c)I_z=56kA

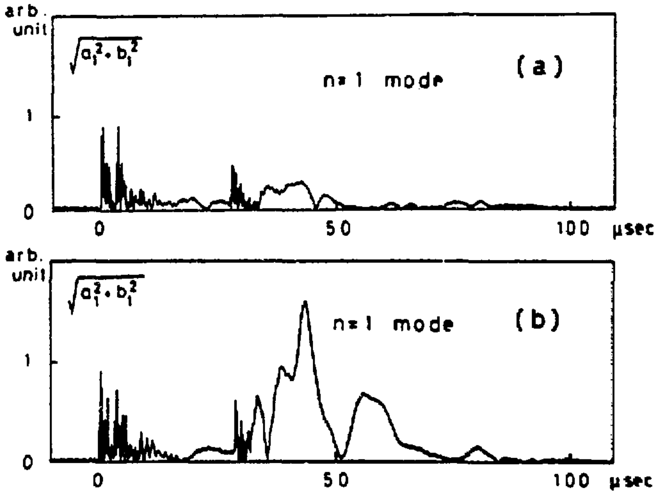

Fig.6 Current dependence of n=1 mode (a)I_z=47kA,(b) I_z=56kA

OBSERVATION OF TILT ASYMMETRIES IN FIELD-REVERSED CONFIGURATIONS[*]

M. Tuszewski, D.C. Barnes, P. Klingner, C. Ng[+],

and the FRX-C Team

Los Alamos National Laboratory, Los Alamos NM 87545, USA

1. Introduction: In recent years, part of the experimental effort on the FRX-C/LSM device has been devoted to understanding why good FRC confinement is observed only in a narrow window of the operating parameter space (fill pressures less than 5 mtorr and bias fields less than 0.8-0.9 kG). The transition from good to bad confinement has been shown for some time to correlate with strong axial shocks,[1] suggesting a formation or stability problem. More recently, FRC magnetic asymmetries have been observed whenever the confinement was poor.[2] To gain further understanding, a 64-coil probe array was built, and data from over 700 discharges were collected during the summer of 1989. We summarize in this paper the results of a preliminary analysis of these data.

2. The probe array: B_θ is chosen over B_r to increase sensitivity near the straight conducting boundary and because of simpler data analysis (no n = 0 component). The array consists of 8 axial x 8 toroidal B_θ coils located at about 33 cm radius, between coil (35 cm) and quartz tube (30 cm). The axial locations are $z = \pm10, \pm30, \pm50$, and ±70 cm, which allows separation of axially even and odd components by subtracting and adding signals at given $\pm z$. In this paper, even and odd refer to the axial symmetry of flux surfaces. The axial parity of B_θ is opposite to that of flux surface displacement (i.e. an even mode has odd B_θ and vice-versa). At each axial location, 8 coils are placed at equal 45° toroidal intervals, permitting Fourier analysis for the n = 0, 1, 2, and 3 toroidal symmetries. Each probe is mounted within a Newport Corporation RSA-1 rotary stage, which is adequate to null-out B_z pick-up to within a few Gauss. Epoxy casting provides high voltage insulation. A complete electrical shield (0.2 μs around the coil) yields essentially noise-free signals. The probe signals are integrated passively (RC = 200 μs) and digitized every μs (12-bit Lecroy 6810). The residual B_z pick-up is removed numerically by using, at a given axial location, a B_z probe from the excluded flux array (similar digitization). Then, a numerical procedure allows (optional) signal separation into even and odd components and toroidal Fourier analysis. The B_θ array is quite reliable (over 99% of usable data) and relatively maintenance-free.

3. Experimental results: The data generally confirm results[2] obtained with a limited number of probes. Good FRCs (i.e. flux anomalies less than 10 compared with classical) are mostly axisymmetric during their stable period, except for n = 1 and 2 axially-even modes (the wobble and elliptical rotational instabilities). The axially-odd signals of good FRCs are consistently observed to be less than a few Gauss, as illustrated in Fig. 1. Bad FRCs (i.e. anomalies greater than 100) also have even n = 1 and 2 asymmetries. However, in contrast with good FRCs, they show substantial odd asymmetries, as in the example of Fig. 2.

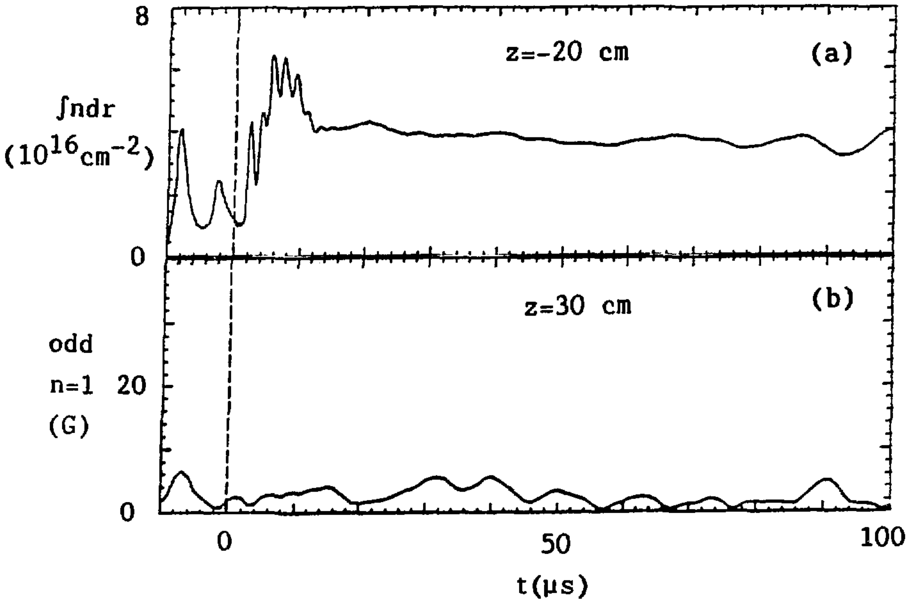

Fig.1 Time histories of (a) density and (b) odd n=1 amplitude for a good 3 mtorr FRC with 0.7 kG bias.

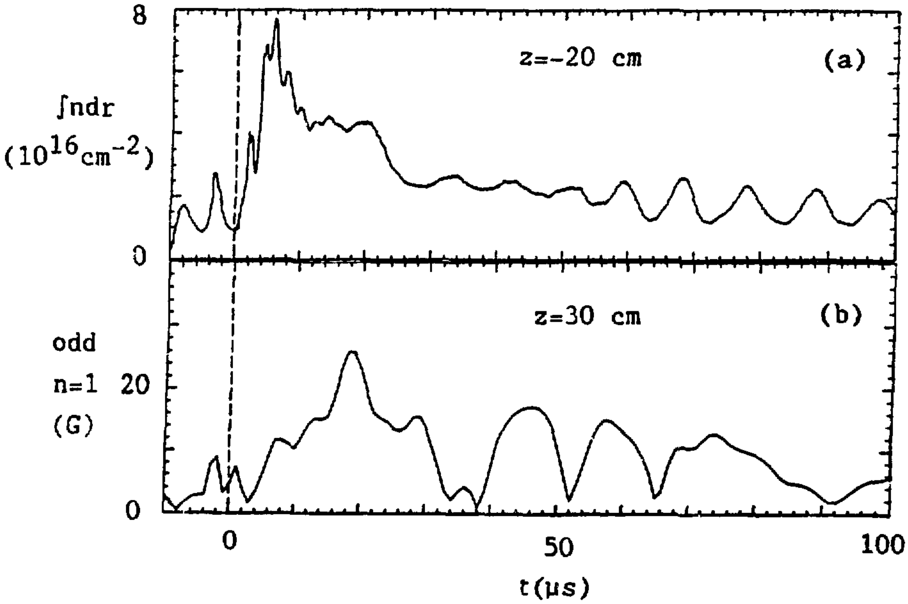

Fig.2 Time histories of (a) density and (b) odd n=1 amplitude for a bad 3 mtorr FRC with 1 kG bias.

FRCs with intermediate confinement show a level of odd asymmetries in between those of Figs. 1 and 2. The odd asymmetries are mostly $n = 1$, but substantial $n = 2$ is also present on average at all fill pressures. For fills greater than 5 mtorr, the $n = 3$ relative amplitudes increase on average, indicating contribution from higher-order components.

During preionization, transient B_θ signals in the range 10-20 G are observed in all cases, suggesting initial perturbations of a few percent. The odd asymmetries of bad FRCs begin to grow soon after field reversal as seen in Fig. 2. The amplitude of the $n = 1$ asymmetry peaks around 20 µs, and then suddenly decreases in coincidence with density and diamagnetism. Thereafter, the amplitude has a fluctuating time history. For fill pressures greater than 4 mtorr, one observes in addition flute-like (mostly even and spread over the FRC length) asymmetries during the axial shock. These transient flutes are better resolved with end-on X-ray images.[3]

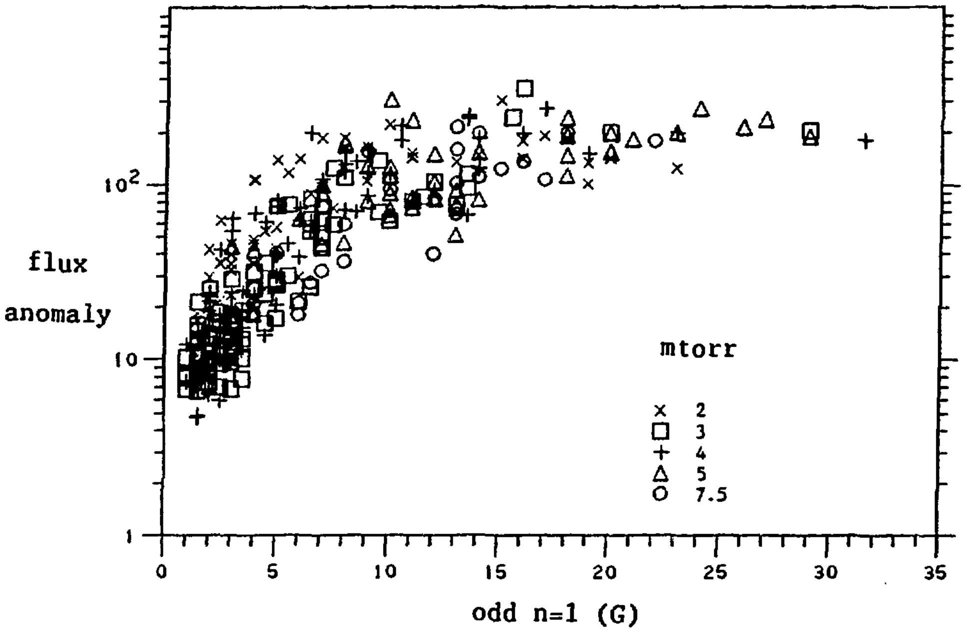

Fig.3 Correlation between flux confinement and odd n=1 amplitude for all available discharges.

We consider an average amplitude (15-20 µs located at $z = 10$-30 cm) as a preliminary measure of the odd $n = 1$ asymmetry. These amplitudes are compared to the corresponding inferred flux anomalies in Fig. 3. Good FRCs have consistently low odd amplitudes (1-4 Gauss). A smooth but rapid transition to poor confinement is observed for amplitudes around 5 Gauss. Bad FRCs have amplitudes greater than 10 Gauss. Anomalies saturate around 200 because flux decay times cannot be much less than 10-20 µs. The correlation between odd $n = 1$ amplitude and FRC confinement shown in Fig. 3 is the strongest identified so far. The data show weaker correlations with $n > 1$ odd asymmetries and much weaker or no correlations with even asymmetries, plasma radius, and asymmetries during preionization.

4. Simulation: The observed odd $n = 1$ asymmetries could be associated with the theoretically predicted internal tilt instabilities. Hence, a preliminary comparison with a 3-D simulation (resistive-MHD including Hall effects[4]) is made. A 2-D FRC equilibrium similar to 5-mtorr high-bias LSM data just after formation ($B_e = 4$ kG, $r_s = 22$ cm, $\ell_s = 150$cm, $T_e = 100$ eV, $T_i = 300$ eV, $s = 4$) is given a tilt perturbation and B_θ at $r = 33$ cm is monitored as the $n = 1$ mode develops. High-bias FRCs were chosen for this comparison because one could most often observe a well-defined growth up to 15-20 µs (i.e. Fig. 2) and because they are more MHD-like (i.e. higher s values).

The calculated B_θ show qualitative (factor of two) agreement with the initial evolution of the observed odd $n = 1$ asymmetries in several respects. First, growth rates γ (normalized to MHD values $2v_A/\ell_s$) are compared. The experimental γ is estimated by fitting an exponential to the initial growth of the $n = 1$ odd asymmetry (up to 15-20 µs and averaged over 10-30 cm for all high-bias discharges). This procedure yields $\gamma = 0.7 \pm 0.3$ (2-5 mtorr) while the code gives $\gamma = 0.8$. Second, the B_θ magnitudes are compared. The experimental growth times are 4-5 µs, so that odd $n = 1$ amplitudes (peak values around 30 G) at 15-20 µs roughly correspond to 3-4 growth times. The code gives 30-80 G central amplitudes at 3-4 growth times. This comparison is qualitative because initial experimental perturbations are unknown and may vary appreciably from that (1%) of the simulation. However, the calculated flux surfaces at 3 growth times shown in Fig. 4(a) present a tilt level possibly consistent with experimental data.

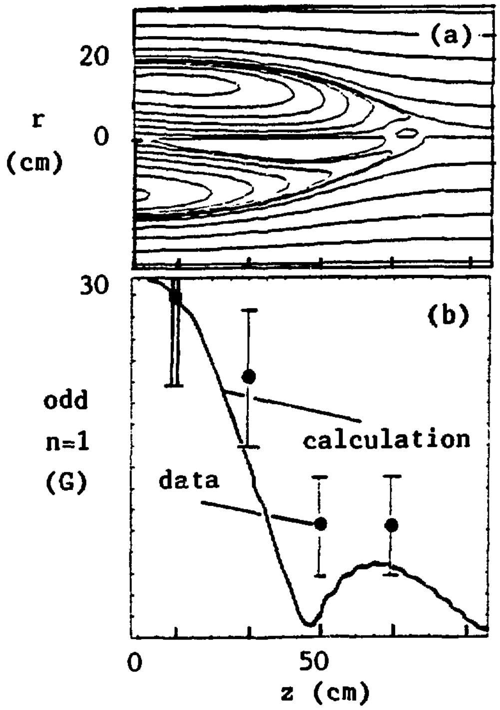

Fig.4 Comparison of experimental and calculated axial distributions of odd n=1 amplitudes.

Finally, the axial distributions of B_θ are compared in Fig. 4(b). The calculated $B_\theta(z)$ at 3 growth times is shown with a solid line. The data normalized to values at 10 cm are given with solid circles. The (single) error bars are standard deviations that indicate uncertainties in axial distribution. The (double) error bar at $z = 10$ cm indicates uncertainty in profile magnitude.

One should note a significant difference between data and simulation after about 20 μs. The data show B_θ saturation and subsequent collapse as density and diamagnetism rapidly fall. Then, a low-flux FRC configuration often survives while reduced odd $n = 1$ amplitudes with fluctuating time histories are observed. This contrasts with the calculation where B_θ increases monotonically until FRC destruction. Further work is needed to understand this difference between data and simulation.

5. <u>Discussion</u>: The above preliminary comparison shows that the early development of the observed $n = 1$ odd asymmetries is consistent with internal tilt instabilities. One could expect such modes to start growing from initial perturbations as soon as the (bad-curvature) FRC configuration is formed when field-line connection is completed (onset of axial shock). The odd $n = 1$ amplitudes show some correlation with both increased s parameter (up to 4 for the LSM data) and decreased FRC elongation (down to 1-2 during axial shock) as bias and fill pressure are increased. Further work is needed to uncover the detailed factors that govern the growth of the observed odd asymmetries. The estimated $\gamma \sim 0.7$ for the LSM data with $s \sim 2$-4 is consistent with present theoretical understanding of the FRC internal tilt mode. In particular, the small FRC elongations after formation (typically 2-4) presumably explain why γ remains close to unity instead of being strongly suppressed[5] for low s values.

6. <u>Conclusions</u>: The data presented in this paper clearly show that external probe arrays provide simple, nondisturbing, reliable diagnostics that can yield much useful information in FRC research. The most important result from the above preliminary data analysis is the observation of an axially-odd $n = 1$ asymmetry whenever the FRC confinement is degraded. Comparison of the data with a numerical calculation suggests that this asymmetry is qualitatively consistent with an internal tilt instability. Although preliminary in nature, these results constitute a significant step in resolving the well-known discrepancy between experiment and theory where FRC stability is concerned.

* work supported by the U.S.D.O.E.
+ New Mexico State University

1. M. Tuszewski et al., Proceedings 8th CT Symposium, Maryland, 1987, p. 191.
2. M. Tuszewski et al., Proceedings 9th CT Symposium, Union, 1989, p. 123.
3. D. Taggart et al., these Proceedings.
4. R.D. Milroy et al., Phys. Fluids B <u>1</u>, 1225 (1989).
5. D.C. Barnes et al., Phys. Fluids <u>29</u>, 2616 (1986).

End on Soft X-ray Imaging of FRCs on the FRX-C/LSM Experiment*

D.P.Taggart, R.J.Gribble, A.D.Bailey III[1], and S.Sugimoto[2]

Los Alamos National Laboratory

Introduction

Recently [1], a prototype soft X-ray pinhole camera was fielded on FRX-C/LSM at Los Alamos and TRX at Spectra Technology. The soft X-ray FRC images obtained using this camera stand out in high contrast to their surroundings (unlike the images from visible light framing cameras which are often obscured by light emission from sources outside the FRC). It was particularly useful for studying the FRC during and shortly after formation when, at certain operating conditions, flute-like structures at the edge and internal structures of the FRC were observed which other diagnostics could not resolve.

Building on this early experience, a new soft X-ray pinhole camera has been installed on FRX-C/LSM, which permits more rapid data acquisition and briefer exposures. It will be used to continue studying FRC formation and to look for internal structure later in time which could be a signature of instability. This paper summarizes the initial operation of this camera.

As of this writing, the camera has been used primarily in conjunction with measurements of external magnetic field asymmetries of FRCs. Some of the images obtained during the bias and pressure scans of this series of measurements are included to indicate the effect of varying source conditions on formation. Additionally, a series of shots at optimum operating conditions was taken to document the appearance of the best FRCs which we can form on FRX-C/LSM and to establish analysis procedures which would be applied to all of the data at various pressures and biases. Preliminary analysis of this data shows good agreement between the FRC radius determined from the X-ray image and the excluded flux array. It also indicates that relative density values (maximum density vs. density in "hole") inferred from the data are reasonable.

Experimental Apparatus and Procedure

A diagram of the new soft X-ray pinhole camera is shown in Figure 1. The camera uses a vacuum flange mounted Galileo 3075-FM Chevron MCP with a phosphor/fiberoptic output. The vacuum flange mounting allows the image recording medium (film or CID camera) to be outside the vacuum chamber, which eliminates the prototype camera requirement of vacuum openings between shots to retrieve exposed film. A 0.25-μ Be foil blocks visible and UV light. This plus a 300-nm CsI coating on the input side of the MCP should ensure that the camera's response is peaked near 10 nm. The input side of the MCP is gated once per discharge with a flat-top pulse of 1 μs duration (the prototype camera had an exposure time of 2 μs). The output of the MCP is at ground and the phosphor bias is typically +2.5 kV. For this first series of experiments, images were recorded as contact prints on Polaroid Type 52 sheet film. These images were subsequently digitized and analyzed using a G.E. 4TN2507A CID surveillance camera and Imaging Technology FG-100-AT image processing board with the ITEX 100 library of image processing subroutines (both PC based). Pinhole diameters of 0.5-1.0 mm were used, permitting spatial resolution at the plasma on the order of 0.8-1.6 cm. This resolution plus the short (~1 μs) exposures allows us to detect fine scale features at the plasmas edge (Fig. 2).

Discussion of Results

To document the appearance of the FRC in our optimum operating regime, a time series of photos was taken at a fill pressure of 3 mTorr with a 570 gauss bias. The outstanding characteristic of these FRCs (up to their n=2 instability at about 80 μs) is their nearly circular, smooth edge profile. These images have been used to compare the radius determined from the excluded flux array with the radius determined from the X-ray image. The radius of the plasma in the X-ray image is taken to be the point at which the density drops to $n_{max}/2$. The density is assumed to be related to the reflected light intensity from the contact print image of the FRC by $I_R \propto (n^2)^\gamma$, where I_R is the reflected light intensity from the contact print image and γ is the slope of the characteristic curve of the film (γ for our film is 1.35). The results (Fig. 3) show that from about 10 μs after formation begins to the onset of the n=2 instability, the two methods agree to within 4%. At earlier times the plasma is too dynamic and at later times the plasma is too deformed to expect good agreement. Because of point and line defects (bright spots) in the images as well as moire' type patterns cutting across the field of view, not much effort has been devoted to trying to quantify internal structures seen within the separatrix. Nevertheless, a crude analysis of how n_{hole}/n_{max} varies with x_{sep} has been made. Restricting the analysis to shots with exposure levels which should be in the most linear region of that curve, the correct trend is seen in the data (Fig.4) when compared to a rigid rotor model, but with considerable scatter. Using the same scaling, a contour plot is shown for a shot with a particularly deep center hole (Fig.5).

As Fig. 1 shows, not all FRCs are as symmetric as our optimized 3 mTorr shots are. As an example of one trend which is evident in our data, Fig.6 shows how, at constant bias, FRC symmetry deteriorates as fill pressure increases.

Summary and Future Plans

In summary, a new soft X-ray pinhole camera has been constructed and used successfully. Image processing software has been developed to analyze the resulting images. We are continuing to analyze our data to:

i) determine if the azimuthal asymmetries seen at high fill pressures during formation can be explained by consideration of the radial dynamics[2] of the plasma,

ii) correlate the measured shifts of the plasma away from the geometric axis with magnetic field asymmetries measured at the wall,

iii) develop software to analyze images for evidence of asymmetries inside the plasma separatrix.

We have completed preparations to eliminate the use of film all together and record the image directly using the CID camera. Finally, a 4-frame system is being built (in collaboration with Spectra Technology,Inc.) for use early next year.

*-Work supported by U.S.D.O.E.

1-Caltech
2-Osaka University

References:

[1] E.Crawford,Proceedings 9th U.S. Compact Toroid Symposium (Union, WA, 1989),pp.138-141
[2] A.Sgro,*ibid.*,pp.91-94

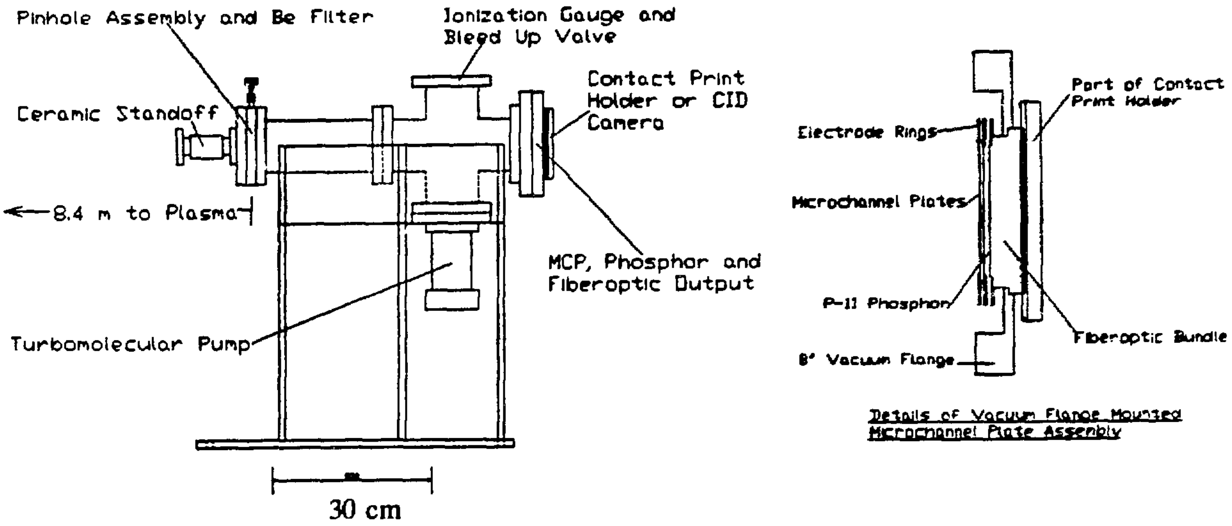

Principal Features of X-ray Pinhole Camera

Details of Vacuum Flange Mounted Microchannel Plate Assembly

Figure 1-Schematic Diagram of New Soft X-ray Pinhole Camera

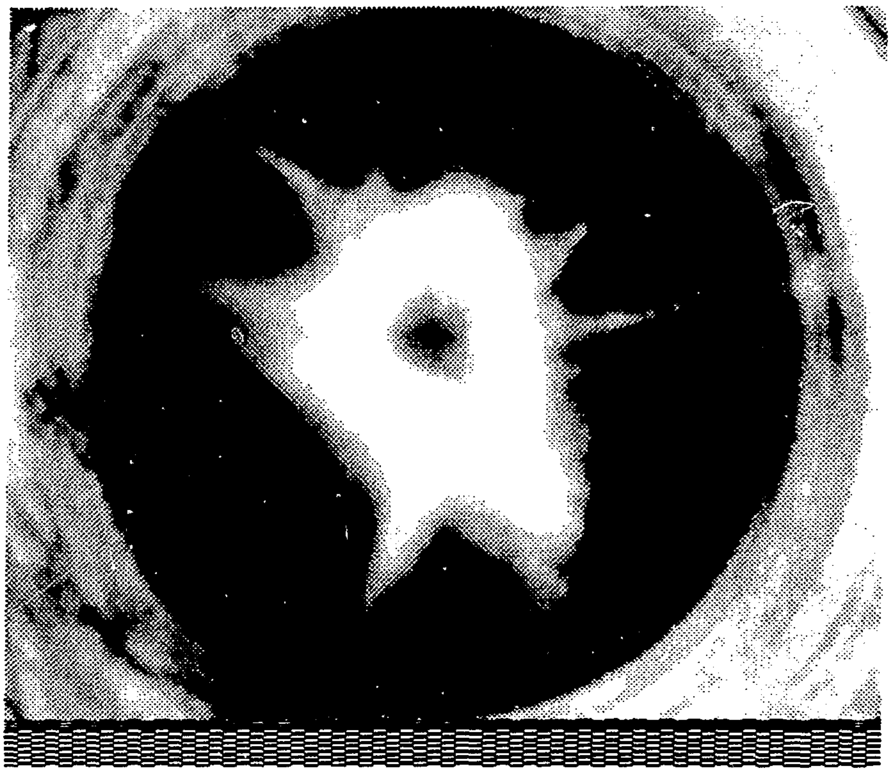

Figure 2- The severely deformed FRC shown above was photographed 5 μs after firing the theta pinch. It was formed at a bias magnetic field of 290 gauss and a deuterium fill pressure of 12.7 mTorr. It is not a typical FRC but demonstrates the capabilities of the soft X-ray imaging system. The FRC stands out in high contrast to its surroundings. The bright circular area at the perimeter of the photo is the quartz tube in the compressor (40 cm dia., 6.4 m from pinhole). The pinhole diameter for this photo was 0.5 mm, giving spatial resolution of 0.8 cm at the FRC, which is 8.4 m from the pinhole.

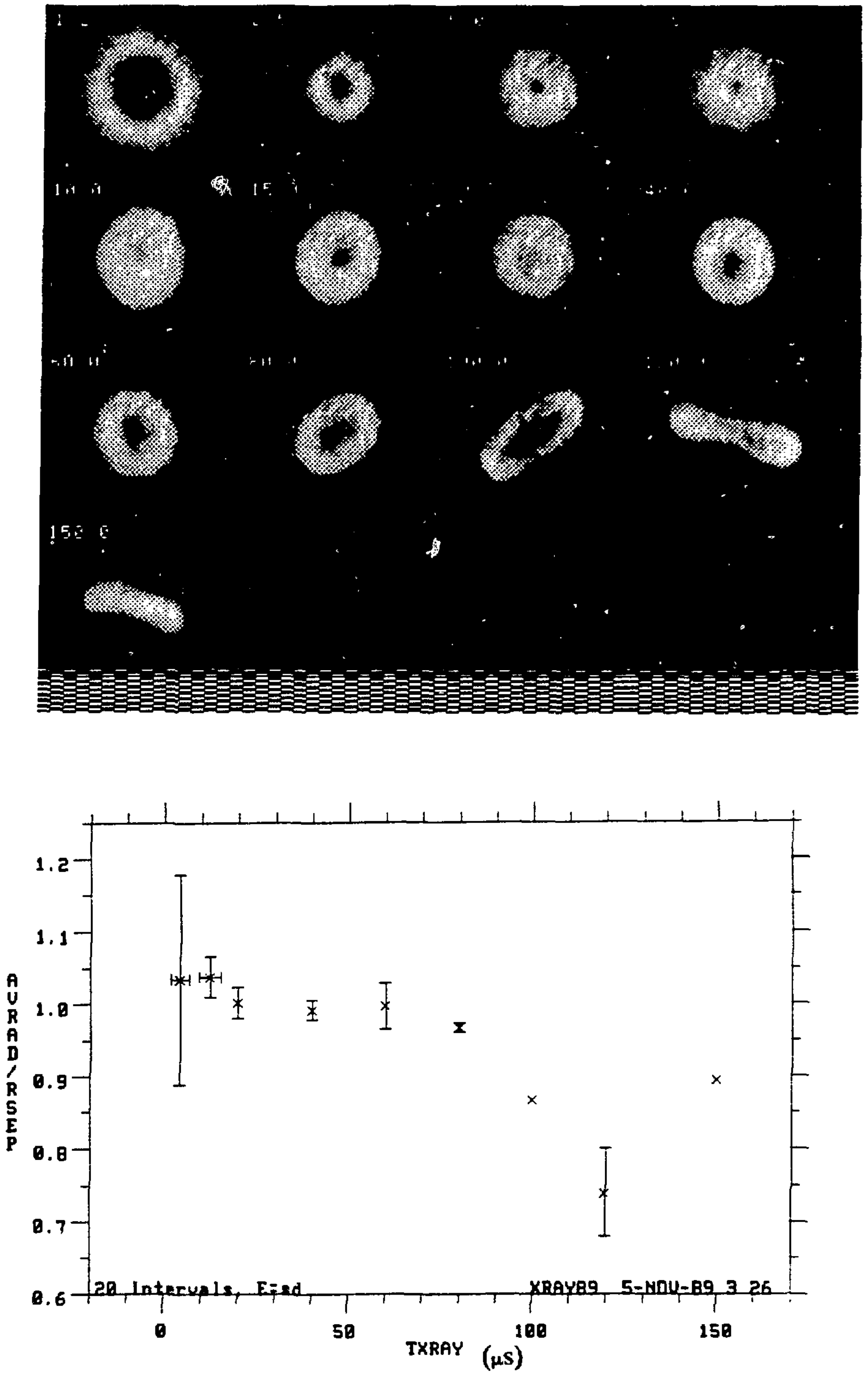

Figure 3- *The time sequence of photos above is typical of FRCs formed at the* optimum operating regime (fill pressure= 3 mTorr deuterium, bias field= 570 gauss, B_{wall}=4 kG, τ_ϕ= 270 (+/- 70) μs). The time of the photo (in μs) is listed in the upper left hand corner of each frame and there is one exposure per discharge. The plot below *compares the plasma radius determined from the X-ray image (AVRAD) with the* radius determined from the excluded flux array (RSEP) at various times.

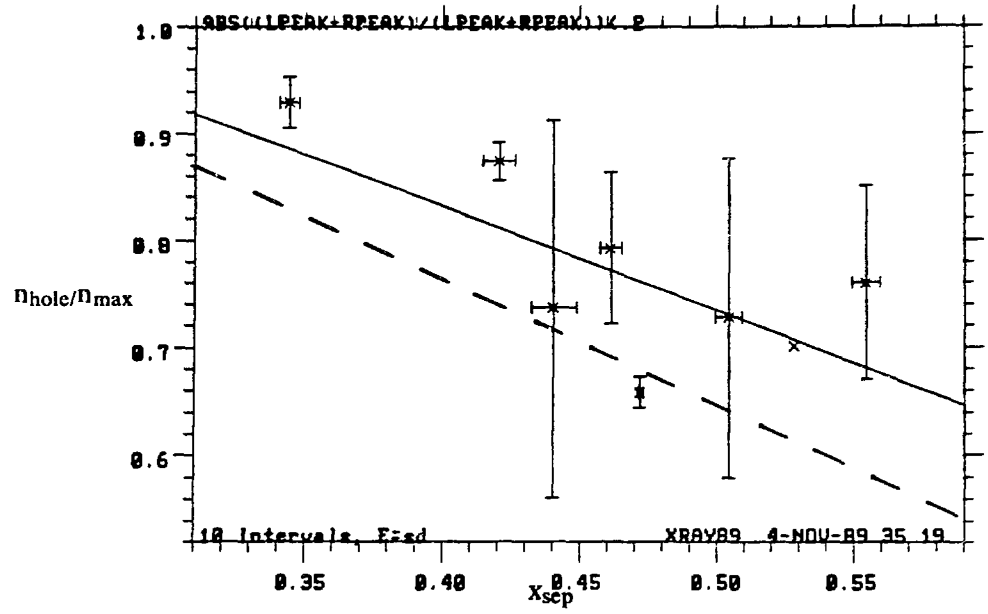

Figure 4- In the figure above the ordinate n_{hole}/n_{max} is the ratio of the density at the "hole" of the FRC (central density minimum) to the maximum density (which occurs somewhere between the hole and the FRC edge). The relative density values are inferred from the reflected light intensity using the same relationship which was used to determine the FRC radius from the soft X-ray images. The abscissa x_{sep} is the excluded flux radius normalized to the radius of the field coils. The solid line is a linear least squares fit to the experimental data and the dashed line is what one would expect for a rigid rotor.

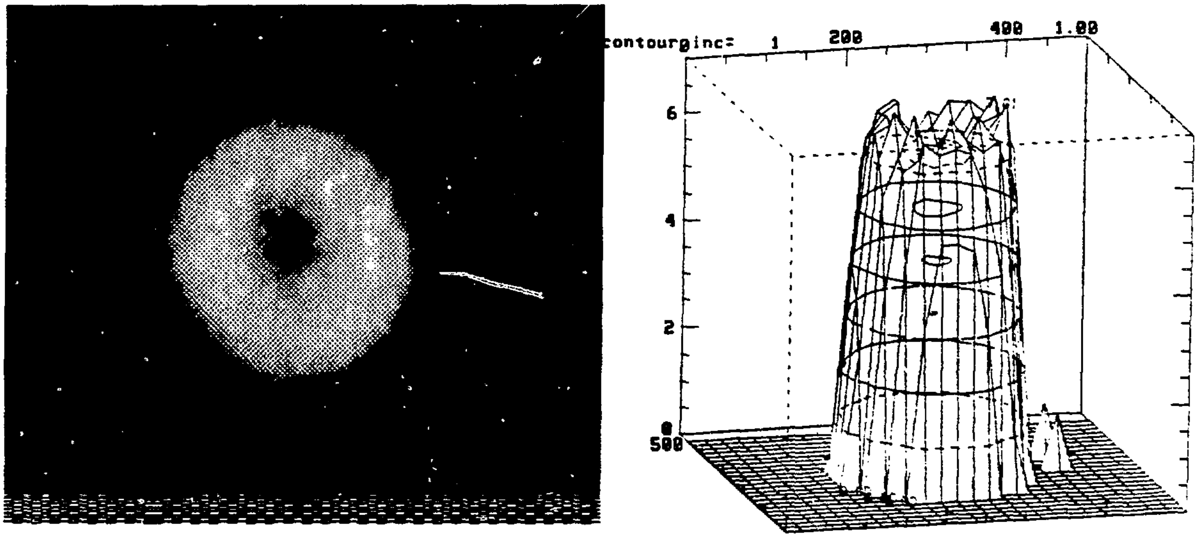

Figure 5- The above photo of an optimized 3 mTorr FRC was taken 60 μs after firing the theta pinch coil. Because it is very symmetric and has a particularly deep hole, it was chosen as an interesting example of how the density as a function of position can be unfolded from the photos. Using the same relationship between reflected light intensity and density mentioned above, the contour plot at the right was obtained. The vertical axis represents the density and the horizontal axes position.

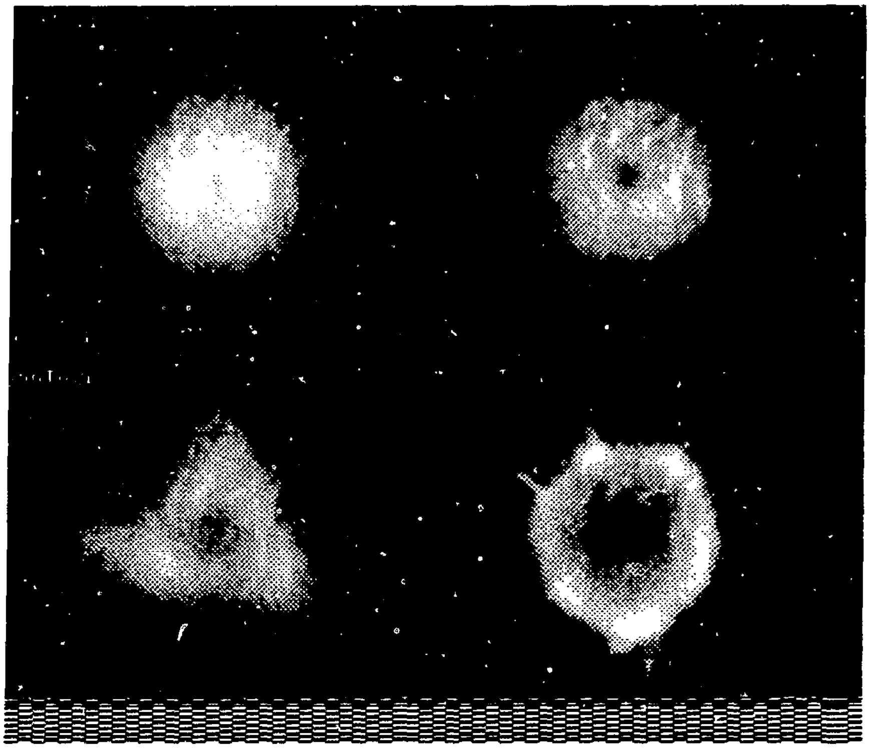

Figure 6- The figure above demonstrates how, at constant bias, FRC symmetry and confinement deteriorates as we increase fill pressure. Each of the photos above was taken 5 μs after firing the theta pinch at a bias field of 570 gauss. The fill pressure is listed in the upper left hand corner of each frame. The flux confinement times for these shots are listed below.

Fill Pressure (mTorr)	Flux Confinement Time τ_Φ (μs)
2	168
3	470
5	14
12.5	17

Doppler Broadening Measurements in FRX-C/LSM[1]

M. H. BARON[2], R. E. CHRIEN
Los Alamos National Laboratory
Los Alamos, New Mexico, United States of America

1. Abstract

Measurements obtained *in situ* during field reversed configuration (FRC) formation show that the Doppler broadening ion temperature T_{CV} is larger by a factor of two or more than the ion temperature T_i derived from pressure balance and Thomson scattering. After a time comparable to an ion-ion equilibration time, T_{CV} and T_i come into agreement with each other. An exception to this picture occurs in the lowest fill pressure condition (2 mtorr), for which $T_{CV} > T_i$ is maintained throughout the FRC lifetime. Earlier Doppler broadening measurements in FRX-B [1] and FRX-C [2,3] also showed persistent, anomalously high T_{CV} at low fill pressure. The initially high values of T_{CV} are probably caused by convective motion generated by the radial implosion. The low fill pressure results suggest an enhanced ohmic power input to the carbon ions.

2. Apparatus

A seven-channel polychromator has been used to study the Doppler broadening of CV emission from FRCs. The polychromator consists of a Jarrell-Ash 0.5 meter Ebert scanning spectrometer with a quartz fiber at the exit slit to disperse 2.4 Å over 24° to a seven channel photomultiplier array. The polychromator has a resolution of 0.53 Å, a wavelength range of 1900-4600 Å, and a time response of 0.5 MHz. The polychromator was initially situated to view the FRC radially through a zero impact parameter and at $z = -20$ cm. The range of view was generally limited to 6 cm radially by masking the coils. The reason for looking from +3 cm to −3 cm was to minimize the effect of the FRC rotation on the broadening of the CV line. In a later run the polychromator was situated to view axially through the center of the FRC. The entire radial extent of the FRC was viewed. In both cases a single lens was used to match the f-number of the polychromator. The polychromator was calibrated in two steps. First, the 3610.51 Å and the 3612.88 Å lines of a Cd lamp were used to calibrate the motor driven scan speed to wavelength. Then, the 2537 Å line of a Hg lamp was used to do a relative calibration of the seven channels to each other and, coupled with the first calibration, to determine the instrument resolution and channel separation.

3. Measurements

During *in situ* operations of FRX-C/LSM Doppler broadening measurements of the helium-like carbon impurity line (2271 Å) were obtained for 2, 3, 4, and 5 mtorr fill pressures. For the 2 and 3 mtorr conditions a detailed scan of the bias field was made for both a degraded main bank and a full main bank configuration (6 and 8 kG peak magnetic field, respectively). In the 4 and 5 mtorr cases only a rough scan of the bias field was made using a degraded main bank.

The pressure balance temperature was obtained by application of radial pressure balance. The magnetic field, the excluded flux radius, and the line integral density were all measured with at least a 1 MHz time response. Only times when the FRC was in radial equilibrium (after 10 μs) were used. The electron temperature was measured

---

[1] Work supported by the United States Department of Energy

[2] Auburn University, Auburn, Alabama

by single point Thomson scattering. [4] A good data base exists for the electron temperature at a variety of operating conditions thus permitting, by cross referencing, an electron temperature to be assigned.

For all the conditions, T_{CV} was 2 to 5 times larger than T_i from pressure balance and Thomson scattering. In the 3, 4, and 5 mtorr cases T_{CV} and T_i came into agreement in typically 30, 25, and 18 μs, respectively. Only in the 2 mtorr case did the two temperatures not come into agreement during the stable lifetime of the FRC. In all cases good Gaussian fits (Fig. 1) were obtained from approximately 3 μs until the FRC went n = 2 unstable.

4. Discussion

For the 3 mtorr case it is clearly evident that from 10 to 20 μs the temperature derived from CV Doppler broadening is not in agreement with the temperature inferred from pressure balance (Fig. 2a). This discrepancy implies that there is a mechanism which preferentially heats the carbon ions more efficiently than the deuterium ions. There are two obvious mechanisms which could alter the Doppler broadening profiles. The first is that a Maxwellian has not yet been established. The fits to the data show that the CV line can be fit with a Gaussian typically 3 μs after the main bank fires. This is an indication that the carbon may have a Maxwellian velocity distribution, but this is not sufficient evidence in itself. The second mechanism which could alter the Doppler broadening profile is convective motion. In the future it is planned that several different impurity lines will be observed to determine the dependence on the charge-to-mass ratio and thus if convective cells are present [5].

The presence of a preferential heating mechanism seems likely. If, during the radial implosion, both the carbon and deuterium ions are given the same radial velocity then the energy the two ion species acquire will differ by a factor of six. If this is the case, then the carbon ions acquire a directed velocity which will have to relax into a Maxwellian before the Doppler broadening data can be accurately used. The question then arises as to the time required for the carbon to come into thermal equilibrium with itself. It was seen experimentally that good Gaussian fits were obtained, looking both radial and axially, from 3 μs until the plasma went unstable. This suggests that the carbon ions came into thermal equilibrium in 2 μs or less. Classically this would not be expected. Possibly an anomalous equilibration mechanism is present or the profile is being broadened by convective motion within the FRC. From the data the ratio of T_{CV} to T_i is seen to vary from a factor of 2 to 3 in the 3 mtorr case, at 10 μs. Assuming a factor of six temperature difference immediately after the radial implosion, then the carbon-deuterium equilibration time is approximately 25 μs. [6] Then, 10 μs after the radial implosion the temperature difference would be expected to fall to a factor of 4. This is approximately the value seen experimentally.

The carbon-deuterium equilibration time was compared with the classical prediction. The classical carbon-deuterium equilibration time [6]

$$\tau^{C/D} = \left[1.8 \times 10^{-19} \left\{ \frac{(m_C m_D)^{1/2} Z_C^2 Z_D^2 n_D \lambda_{CD}}{(m_C T_D + m_D T_C)^{3/2}} \right\} \right]^{-1} \tag{1}$$

was evaluated using the density and temperature values for the specific time of interest. The experimental equilibration time was obtained by using

$$\tau^{C/D} \cong \frac{T_D - T_C}{\frac{d(T_C - T_D)}{dt}} \tag{2}$$

evaluated with the observed temperature difference and the slope of that difference. The only restriction placed on the time that this value could be obtained was that no radial oscillation were present for within 5 μs. The two values were compared for identical times at various operating conditions and good agreement was seen in almost every case, except in later times at 2 mtorr (Fig. 3). It should be emphasized that in the 2 mtorr case, after typically 25 μs, the experimental equilibration time did not agree with the theoretical equilibration time. This disagreement was not plotted in Figure 3 because the experimental equilibration times were exceedingly large.

Only in the 2 mtorr case did T_{CV} and T_i not come into agreement during the stable lifetime of the FRC. The carbon-deuterium equilibration times were always shorter than the stable lifetime of the FRC by a factor of two or more. Thus the two temperatures would be expected to come into agreement unless some post-formation mechanism was present to preferentially heat the carbon ions. The only obvious mechanism is an enhanced ohmic power to the carbon ions. The power needed to sustain the temperature difference between carbon and deuterium

$$P_{C/D} = 1.5(Vol)(n_C)\left[\frac{(T_D - T_C)}{\tau^{C/D}}\right] \tag{3}$$

is found to be typically 0.6 MW (60 eV/μs/particle). This is approximately ten percent of the total ohmic power dissipated.[7] Small scale convective motion is again a candidate for preferentially heating the carbon.

High T_{CV} was also investigated by positioning the polychromator to view the FRC axially. Conditions for maximum axial contraction (2 mtorr, high bias, and high main magnetic field) were chosen. Interferometer and magnetic probe data indicated an axial contraction speed of 30 cm/μs. The axially directed velocity that the carbon ions would receive from the axial contraction was expected to be from 30 to 60 cm/μs depending on whether the axial shock was fluid, kinetic, or some combination of the two. These velocities correspond to a doppler shift of up to 4 Å to either side of the main Gaussian peak. No evidence of this shift was observed. One possible reason for the shift not being observed is that not enough CV was present in the area being swept up by the axial contraction to produce a detectable signal. In contrast, recent translation experiments clearly show a total shift of the Gaussian during the translation period. The Doppler shift seen experimentally is typically 0.8 Å, which corresponds to a 12 cm/μs gross plasma motion. The velocity observed experimentally with the magnetic probes is 10 cm/μs which is in agreement with the velocity from the observed Doppler shift.

References

[1] W. T. Armstrong, et al., Phys. Fluids 24, 2068 (1981).

[2] R. E. Siemon, W. T. Armstrong, R. R. Bartsch, et al., Plasma Phys. and Controlled Nuc. Fusion Research (Proc. 9th Int. Conf. Baltimore, 1982), Vol. 2, IAEA, Vienna 283 (1983).

[3] R. E. Chrien, W. T. Armstrong, Bull. Am. Phys. Soc. 27, 928 (1982).

[4] D. J. Rej, 9th U. S. Compact Toroid Symposium, Union WA, (1989).

[5] P. C. Thonemann, Optical Spectrometric Measurements of High Temperatures(P. J. Dickerman, ed.), p. 56. Univ. of Chicago Press, Chicago, Illinois, 1961.

[6] David L. Book, NRL Publication 0084-4040 (1987).

[7] D. J. Rej, M. Tuszewski, Phys. Fluids 27, 1514 (1984).

5. Figures

1. Gaussian fits to polychromator data at $t = 5, 10, 20,$ and $30\ \mu s$.
2a. T_{CV} and T_i versus time at 2 mtorr fill pressure.
2b. T_{CV} and T_i versus time at 3 mtorr fill pressure.
3. Experimental equilibration time versus theoretical equilibration time.

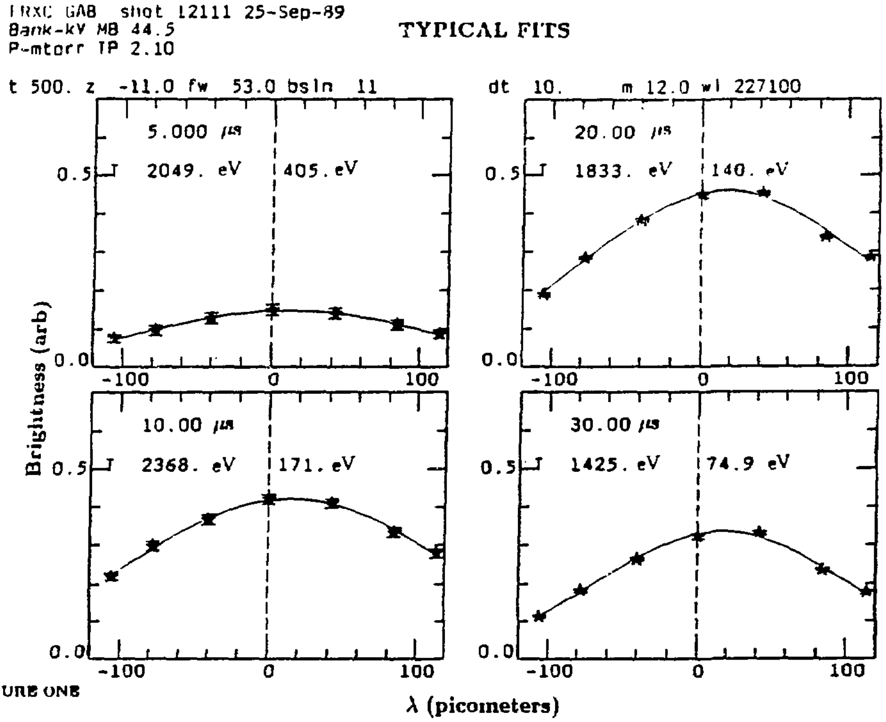

FIGURE ONE

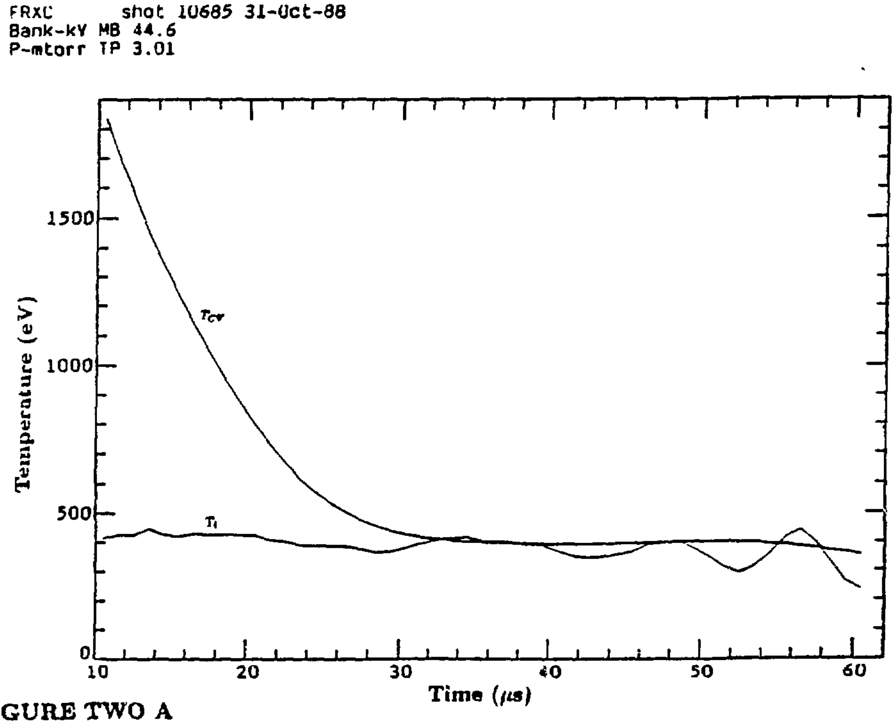

FIGURE TWO A

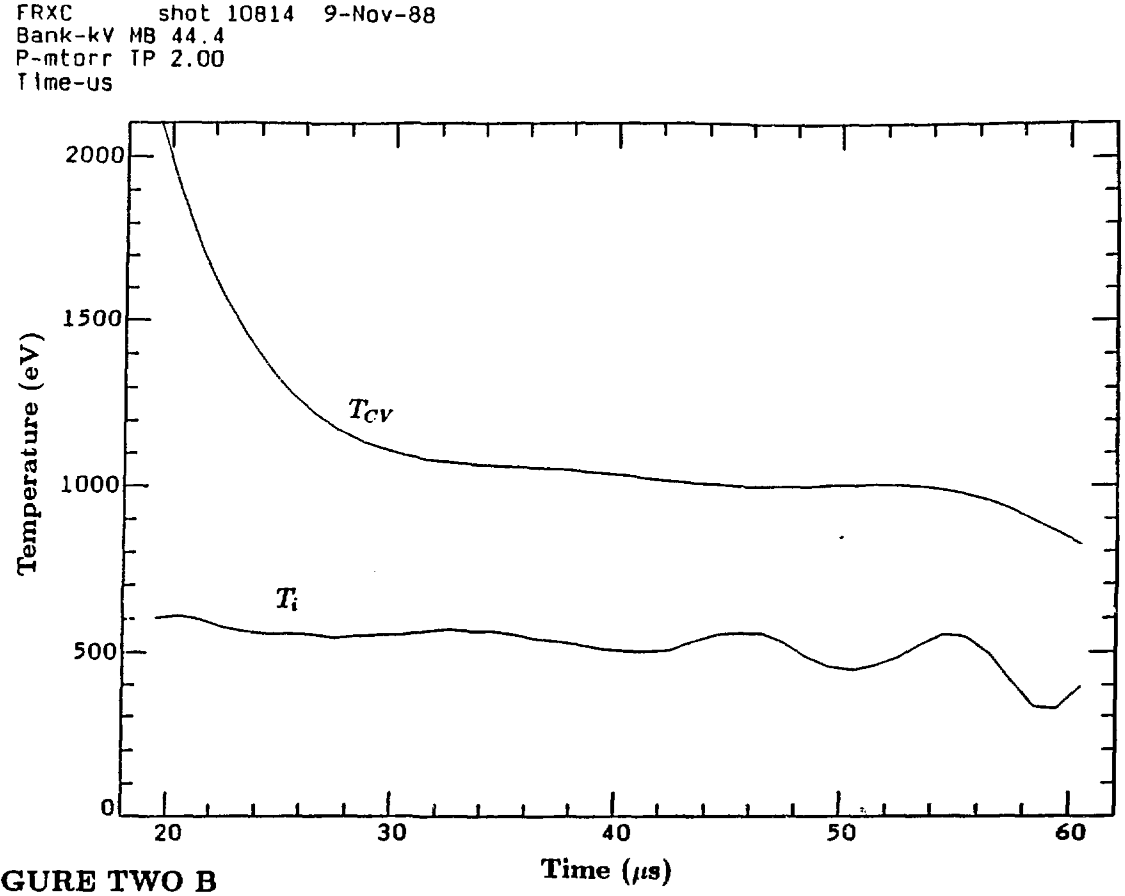

FIGURE TWO B

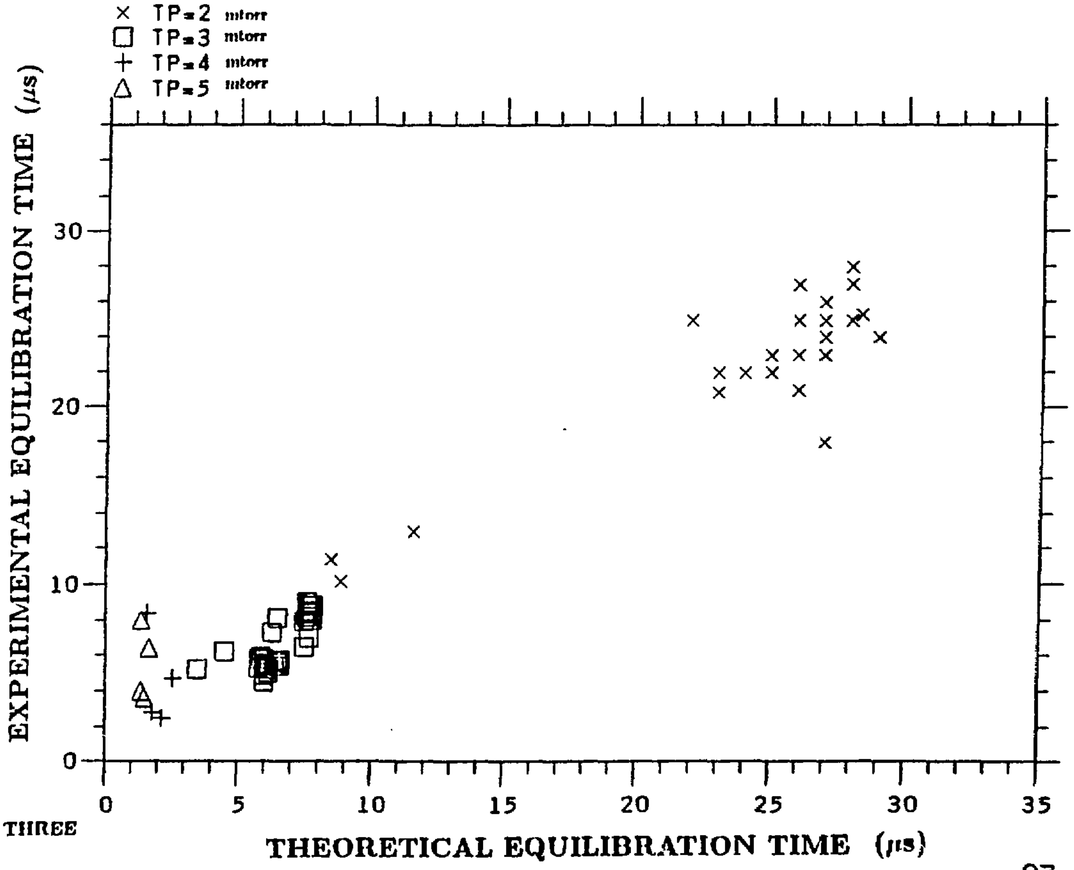

FIGURE THREE

INITIAL RESULTS FROM FRC COMPRESSION EXPERIMENTS ON FRX-C/LSM

D. J. Rej, G. A. Barnes, M. H. Baron*, R. E. Chrien, R. E. Siemon,
J. T. Slough†, D. P. Taggart, T. Takahashi‡, M. Tuszewski, and B. L. Wright

Los Alamos National Laboratory, Los Alamos NM 87545

I. **INTRODUCTION**: After more than two years of preparation, high-power FRC compression heating studies are now underway on the Los Alamos *FRX-C/LSM* facility. Field-reversed configuration plasmas are formed and translated out of the θ-pinch source, and into a compressor where the external B-field can be increased from 0.4 to 2 T in 55 μs. A principal experimental goal is to study FRC confinement at the high energy density, $n(T_e+T_i) \leq 1.0\times10^{22}$ keV/m^3, associated with the large external field. In this paper, we report on the first experiments which were performed between April and July, 1989.

II. **APPARATUS**: A photograph of the *LSM Compression Experiment* is shown in Figure 1. Engineering details about the device and the associated pulsed-power systems have been reviewed elsewhere.[1-3] The magnet configuration used in these initial experiments is schematically shown in Figure 2. The θ-pinch source is centered at axial position z=0. The θ-pinch coil consists of a straight 1.5-m-long, 0.70-m-i.d. central region, with a 0.25-m-long, 0.66-m-i.d. mirror at the upstream end. The coil is enlarged to a 0.76 m i.d. at the downstream end in order to compensate penetrating dc magnetic fields. A transition region, consisting of a 0.5-m-long, 0.4-m-i.d. stainless chamber and dc magnets, links the θ-pinch and compressor. The compression coil is symmetric, consisting of a 2.8-m-long, 0.46-m-i.d. central region with 0.15-m-long, 0.44-m-i.d. passive end mirrors. The compressor is placed colinearly between the *FRX-C/LSM* source and a shortened version of the *FRX-C/T* translation stage. DC magnets in this third stage provide a mirror field to the pre-compressed FRC; however, the compressed plasma has not been translated into this stage during these first

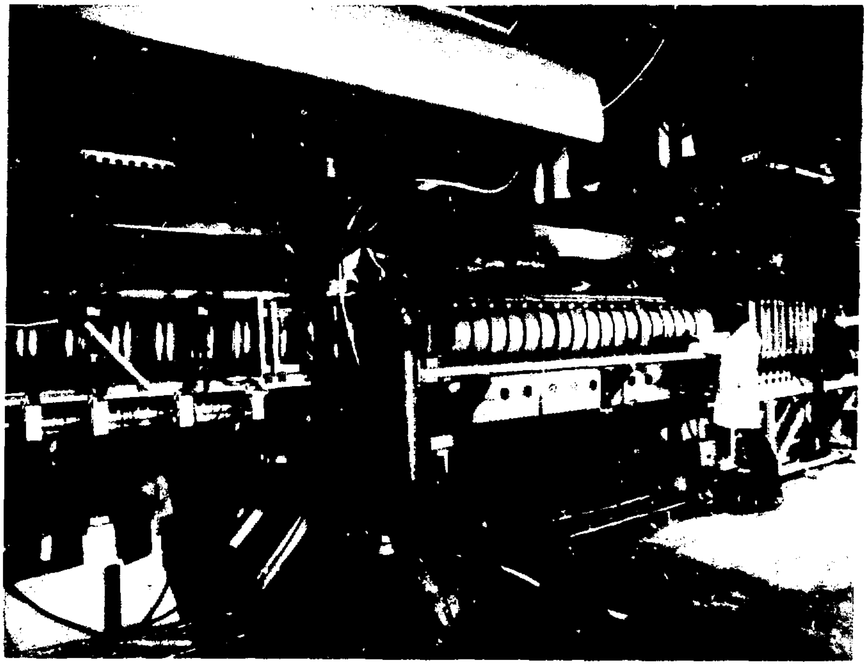

Fig. 1: Photograph of the LSM Compression Experiment.

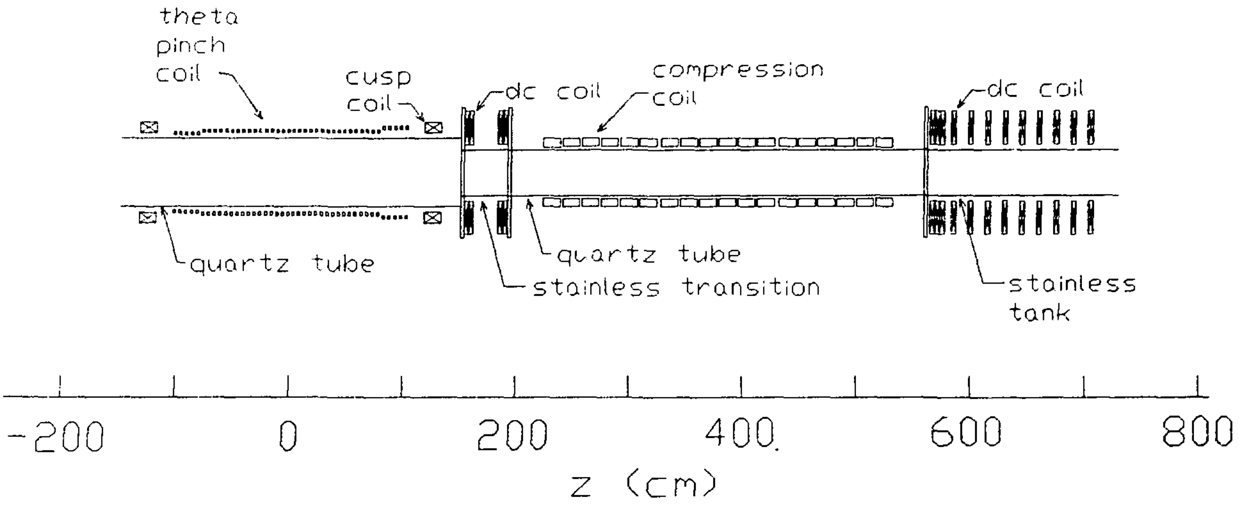

Fig. 2: Magnet configuration used in initial compression experiments.

experiments. A straight quadrupole magnet is mounted outside the compression coil to control the $n=2$ rotational instability. The quadrupole field (up to 47 mT vacuum B_0 at $r = 0.10$ m) is pulsed with a waveform similar to that of the main compression field. A 3-mtorr initial D_2 fill is introduced either by static or puff fill (at 4 ms before the discharge). Experiments have been performed at relatively weak bias fields $B_b \simeq 65$ mT and θ-pinch fields $B \simeq 0.4$ T, conditions where FRCs with sufficiently long confinement have been formed and translated.[4]

Plasma diagnostics include: (1) a 29-station excluded flux array to determine the separatrix profile $r_s(z)$; (2) 4 side-on chords of interferometry to measure plasma density; (3) single-point Thomson scattering aligned to measure T_e at the geometric axis near the center of the compressor; (4) a polychromator to measure Doppler-broadened temperatures of impurity ions;[5] (5) time-resolving and time-integrating neutron detectors;[6] (6) an 11-chord prototype tomography system aligned for side-on measurements in the compressor.

III. <u>OBSERVATIONS</u>: FRC formation, translation, and compression in a single discharge are illustrated by the representative excluded flux data in Fig. 3. Time is referenced to the discharging of the main θ-pinch capacitor bank at t=0. Formation took place during the first 10 μs. The FRC dwelled in the source for approximately 20 μs as it responded to modest accelerating forces from the upstream passive mirror. The plasma slowly drifted out of the θ-pinch until it received a stronger accelerating force from a magnetic field gradient under the cusp coil at the entrance of the transition region (see Fig. 2). The FRC entered the compressor at time $t \simeq 30$ μs traveling with axial speed 1.3×10^5 m/s ($\simeq 2/3$ of the ion thermal speed).

The compression field was usually initiated at time $t \simeq 65$ μs, during the FRCs first transit through the compressor (see Fig. 3). Average plasma parameters just before compression were: $B_o = 0.28 \pm 0.02$ T, $n_o = (0.5 \pm 0.1) \times 10^{21}$ m^{-3}, $T_o = T_{eo} + T_{io} = 335 \pm 85$ eV, $T_{eo} = 76 \pm 10$ eV, $r_{so} = 137 \pm 8$ mm, $V_{so} = 125 \pm 19$ liter. For the discharge shown in Fig. 2, B rose to 1.7 T at t = 120 μs. The separatrix volume V_s steadily decreased to 10 liter at t = 95 μs, when the FRC became $n \simeq 2$ unstable. During this interval, the line-average density increased to 3×10^{21}m^{-3}, the pressure balance temperature to 1.4 keV, the plasma kinetic energy from 5 to 15 kJ, while the the particle inventory dropped by approximately 1/3. Preliminary 0-D analysis of this discharge yielded an energy confinement time of approximately 45 μs. The variations in r_s, V_s, n and T with compression field are plotted in Fig. 4. Each data point in any given graph corresponds to a separate discharge. These data,

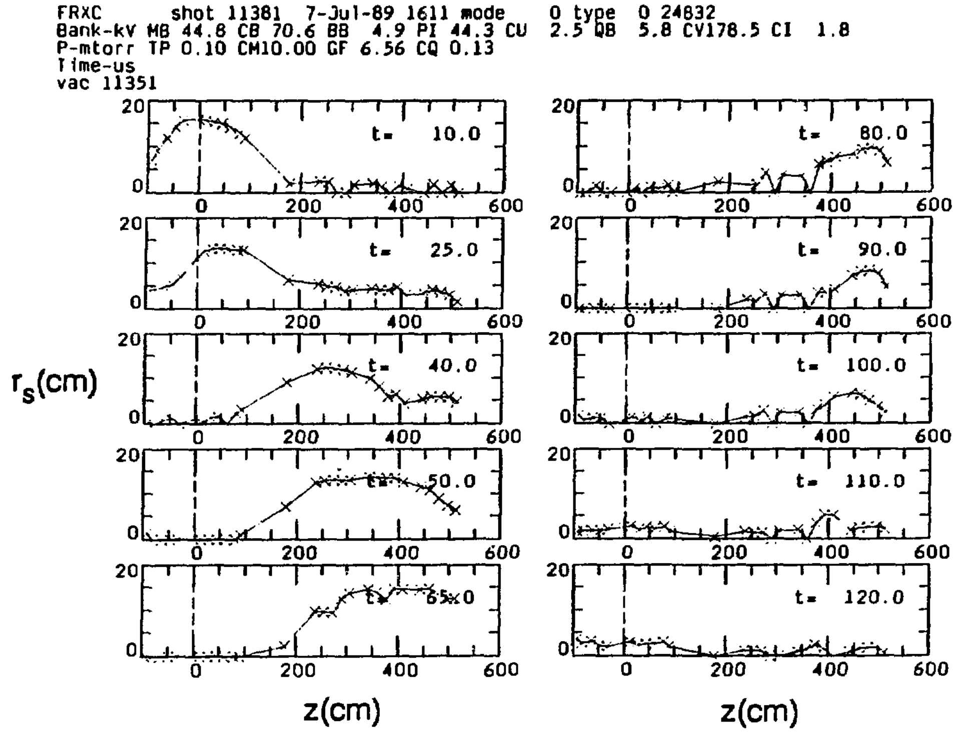

Fig. 3: Time-evolution of the separatrix radius profile measured during a single compression discharge.

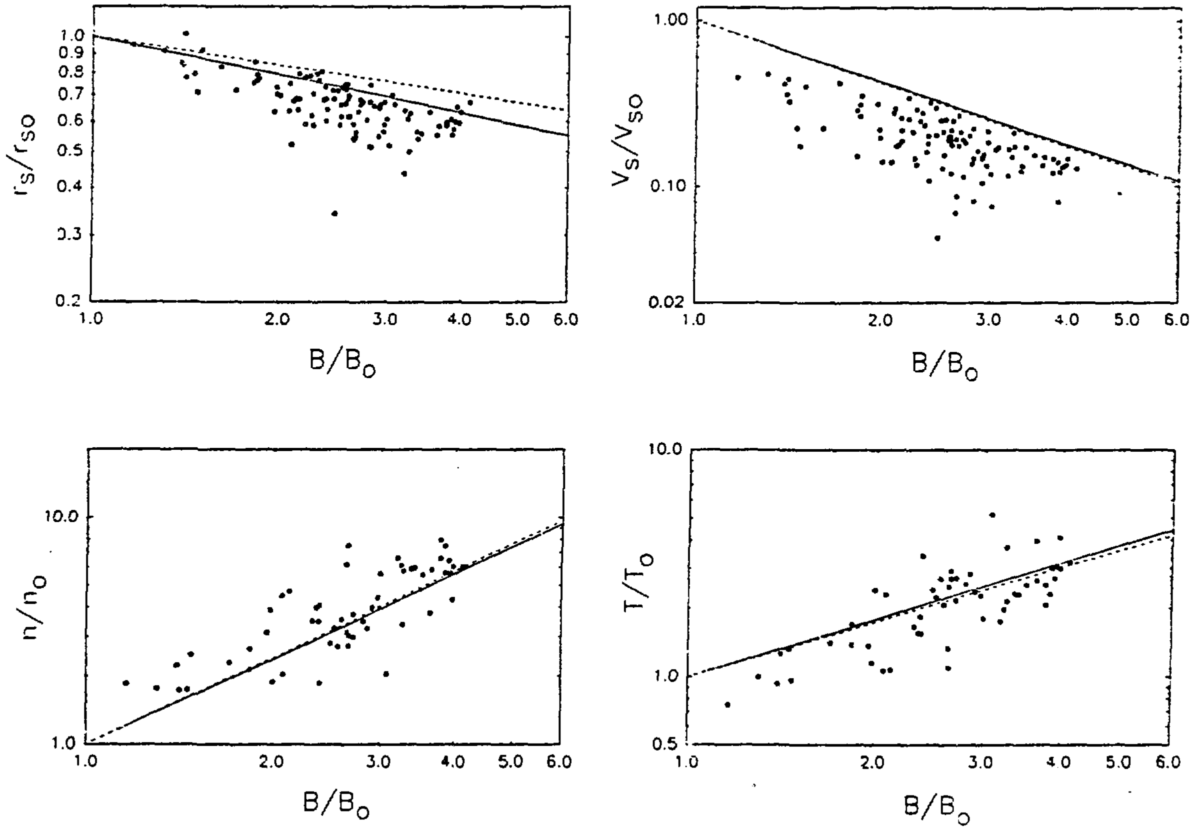

Fig. 4: Variations in the normalized separatrix radius and volume, average density, and pressure balance temperature with the compression magnetic field. The dashed and solid lines denote the predictions of adiabatic theory for the low and high-flux sharp boundary equilibria, respectively.

measured 20 μs into the compression phase, are normalized to their precompression values, while the lines denote the predictions of adiabatic theory.[7]

FRC lifetimes were limited by the $n=2$ rotational instability. Without stabilizing quadrupole fields, the $n=2$ mode frequently disrupted the plasma well before the maximum compression field was reached. With quadrupoles, the stable period was often extended so that substantial compression heating occurred before the instability terminated the discharge.

Significant electron heating was observed during compression. T_e data are plotted in Fig. 4. Each data point corresponds to a separate discharge, while the error bars denote the uncertainty in the Gaussian fit to the 9 spectroscopic channels of the Thomson scattering detector. Because of translation, the axial position of the FRC varied during compression. In addition, there were shot-to-shot variations in the trajectory; consequently, the Thomson scattering measurements were performed over a variety of axial locations relative to the FRC both inside the separatrix (*i.e.*, at different locations between the two x-points), and outside in the open-field-line jet. Only T_e data from inside the separatrix are plotted in Fig. 5. Unfortunately, there are no data for the largest compression fields, $B \geq 1.2$ T, since FRCs were too short and were axially displaced sufficiently away from the scattering region at high fields. During compression, T_e rose steadily from 76 eV to approximately 300 eV at $B \simeq 1.1$ T. These temperatures are considerably larger than the highest T_e measured in the *FRX-C*[8] and *FRX-C/LSM* sources.[4,9] A logarithmic least-squares fit to these data yielded the empirical scaling $T_e \simeq 225 \times B^{0.86}$ which is similar to the $T \sim B^{4/5}$ scaling predicted from adiabatic theory.[7] The ion temperature also increased with the compression field, as evidenced by increased impurity Doppler broadening[5] and neutron emission.[6] Deuteron temperatures as high as 1 keV may be inferred from the pressure balance and Thomson scattering data.

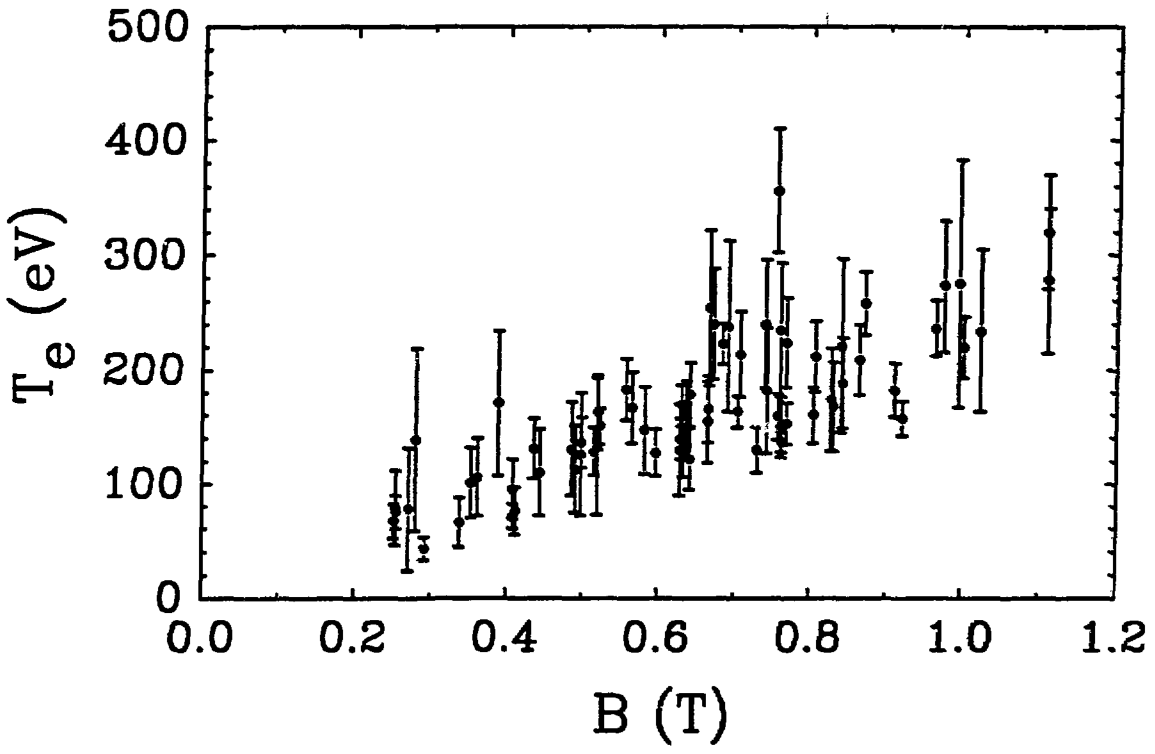

Fig. 5: Electron temperatures measured at the geometric axis during compression.

ACKNOWLEDGMENT: FRC research at Los Alamos is performed under the auspices of the USDOE.

[*] Auburn University, Auburn AL 36849, USA
[†] Spectra Technology, Inc., Bellevue WA 98004, USA
[‡] Nihon University, Tokyo 101, JAPAN

REFERENCES:

[1] D. Rej, R. Siemon, D. Taggart, *Proc. 9th US CT Symp.*, March 1989 (Spectra Tech., 1989) p. 118.
[2] D. Rej *et al.,* Los Alamos Report *LA-11519-MS* (1989).
[3] D. Rej and W. Waganaar, *Proc. 7th IEEE Pulsed-Power Conf.* (Monterey, June 1989), in press.
[4] R. Siemon, *et al., Proc. 1988 IAEA Conf.* (Nice), in press.
[5] M. H. Baron and R. E. Chrien, these proceedings.
[6] R. E. Chrien and M. H. Baron, these proceedings.
[7] R. Spencer, M. Tuszewski, R. Linford, *Phys Fluids* **26**, 1564 (1983).
[8] D. Rej and W. T. Armstrong, *Nuclear Fusion* **24**, 177 (1984).
[9] D. Rej, *op cit.* Ref 1, p. 114; and Los Alamos Report *LA-11622-MS* (1989).

Neutron Measurements in the FRX-C/LSM Magnetic Compression Experiment*

Robert E. Chrien and Miles H. Baron**
Los Alamos National Laboratory, Los Alamos, NM 87545

Introduction

Neutron measurements are being pursued as an ion temperature diagnostic in the FRX-C/LSM Magnetic Compression Experiment. One can easily see that the d-d neutron emission is a sensitive measure of ion heating during adiabatic magnetic compression of FRCs. The reaction rate may be written as $R = (1/2)\, n\, N \langle\sigma v\rangle$, where n and N are the deuterium density and inventory. The fusion reactivity varies as $\langle\sigma v\rangle \propto T^{5.6}$ for $T \approx 1$ keV. For adiabatic compression, $n \propto B^{1.2}$ and $T \propto B^{0.8}$ so $R \propto B^{5.7}$ in the absence of losses. The neutron yield is also sensitive to the time duration that the plasma remains near its peak temperature.

Neutron Detectors

We have tried two types of neutron activation detectors to measure the yield in FRX-C/LSM. The first consists of a 0.25 mm rhodium foil wrapped around a geiger tube and located inside a Cd-shielded moderator.[1] The rhodium is activated by thermal or epithermal neutrons and then β-decays with a 42.3 s half-life. The decays are counted for 60 s starting 0.1 s after a compression shot. The second is based on the ^{75}As(n,n')^{75m}As(0.304 MeV) reaction and consists of an epoxy casting of arsenic powder surrounding a plastic scintillator.[2] The arsenic metastable state decays through gamma emission with a 17 ms half-life. The gammas are detected by a large plastic scintillator (20 cm $\phi \times 10$ cm) and photomultiplier tube (12.7 cm ϕ) and counted for 50 ms starting 5 ms after compression. The time-resolved neutron emission is measured by viewing the plastic scintillator with a second smaller photomultiplier tube operated in current mode.

The rhodium counter was located 1 m from the axis of the compression coil at z=4.3 m. It was calibrated in situ by activating it to steady state with a ^{252}Cf neutron source (2 MeV average energy) placed inside the compression coil and then counting the decays after the source was quickly removed. This calibration indicated that the rhodium counter is about 3.3 times more sensitive than expected from the original d-d neutron calibration performed by Ekdahl.[1] Based on the results of other tests performed in a variety of scattering geometries, we can attribute about a factor of two sensitivity enhancement to the scattering and/or partial moderation caused by the massive aluminum compression coils. The remaining sensitivity enhancement may be caused by the difference in the neutron spectrum or by other unknown effects. The coils are also expected to modify the spatial distribution of the neutron source to resemble a diffuse source with the dimensions of the coil itself. Based on a calculation of detector response to such a diffuse source (including the angular sensitivity of the detector), the rhodium counts were systematically increased by 6%. An additional correction is needed whenever the FRC is not axially centered in front of the rhodium counter. The estimated uncertainty in the neutron yield measurement is a factor of two.

The arsenic counter was placed about 4 m from the compression coil to avoid interference by the dc magnetic field. The calibration technique used for the rhodium could not be used for the arsenic because of its short half-life; instead the original published calibration has been tentatively used. Multichannel scaler analysis of the arsenic count rate showed an

---

*Work supported by US Department of Energy

**Auburn University

initial rapid decay with about a 5 ms time constant and which contributed to the counts in the nominal counting interval. These early counts can be attributed to room-scattered neutrons.[3] When the delay before counting was increased to 10 ms, the neutron yield estimated from the arsenic and rhodium counters were in approximate agreement. Since the net counts obtained from the arsenic counter were three times smaller than from the rhodium counter, we have not made further use of the arsenic data.

Results

The measurements reported here were obtained using target plasma formed under reduced-field source conditions.[4] The initial FRC parameters at the start of compression were $r_s = 14.0\pm0.8$ cm, $B_w = 2.83\pm0.20$ kG, $\bar{n} = (0.48\pm0.07)\times10^{15}$ cm^{-3}, $T_i+T_e = 348\pm85$ eV, and $T_e = 76\pm10$ eV.

The neutron yield was observed to increase rapidly with compression field (Fig. 1). The scaling is $Y \propto B^4$, which is less rapid than that predicted for the neutron rate during adiabatic compression. The maximum neutron yield was about 2.5×10^8 for 15.5 kG field.

The integrated plastic scintillator signal was compared with neutron yield on a shot-by-shot basis (Fig. 2). The linear relationship shows that the plastic scintillator is primarily observing neutrons and is used to calibrate the scintillator output for neutron rate (3.0×10^{16} neutrons/s/A).

The time evolution of compression field and neutron rate are shown in Fig. 3. The neutron rate increases rapidly with magnetic field until the FRC is disrupted near peak field by the n=2 rotational instability.

Together with density and volume, the neutron rate at various times during compression can be used to infer the ion temperature. This neutron ion temperature T_n can be compared with the ion temperature T_i inferred from pressure balance and Thomson scattering measurements (Fig. 4). For the purpose of this comparison the electron temperature is estimated from the empirical scaling $T_e(eV) = 32B^{0.86}$ obtained from Thomson scattering measurements during compression.[4] This comparison shows that there is reasonable agreement between T_n and T_i. However there is a tendency for T_n to exceed T_i when T_i is less than 0.8 keV, which needs further study. Nevertheless, these measurements show that substantial ion heating up to 1 keV has been obtained during magnetic compression experiments.

REFERENCES

[1] C.A.Ekdahl, Rev.Sci.Instr.50 (1979) 941.
[2] E.L.Jacobs,S.D.Bonaparte,P.D.Thacher,Nucl.Instr.and Meth.213 (1983) 387.
[3] P.D.Thacher, private communication.
[4] D.J.Rej, et al., these proceedings.

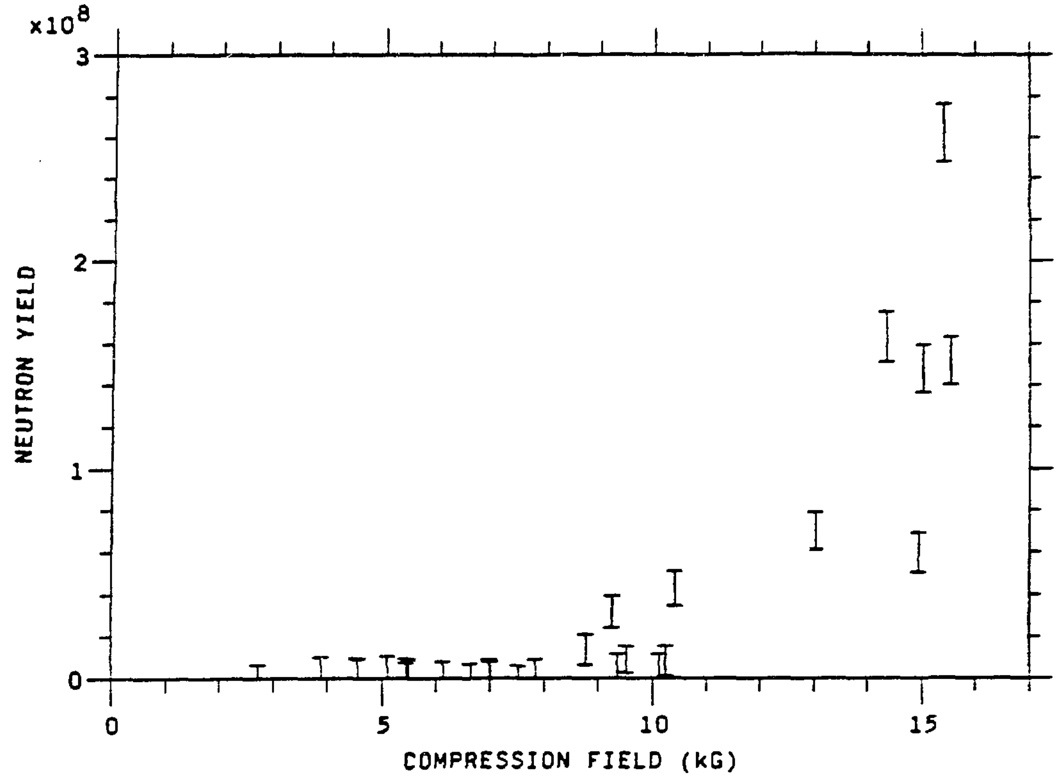

Fig. 1 Variation of neutron yield with magnetic field measured 40 μs after the start of compression.

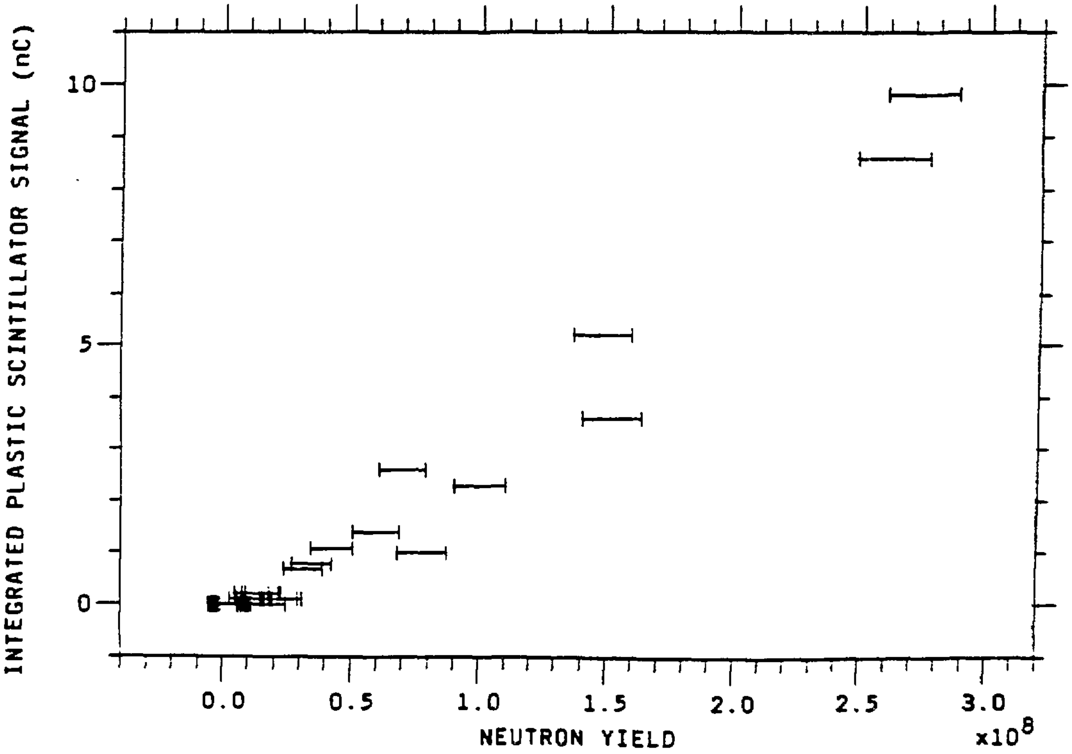

Fig. 2 Variation of integrated plastic scintillator signal with neutron yield.

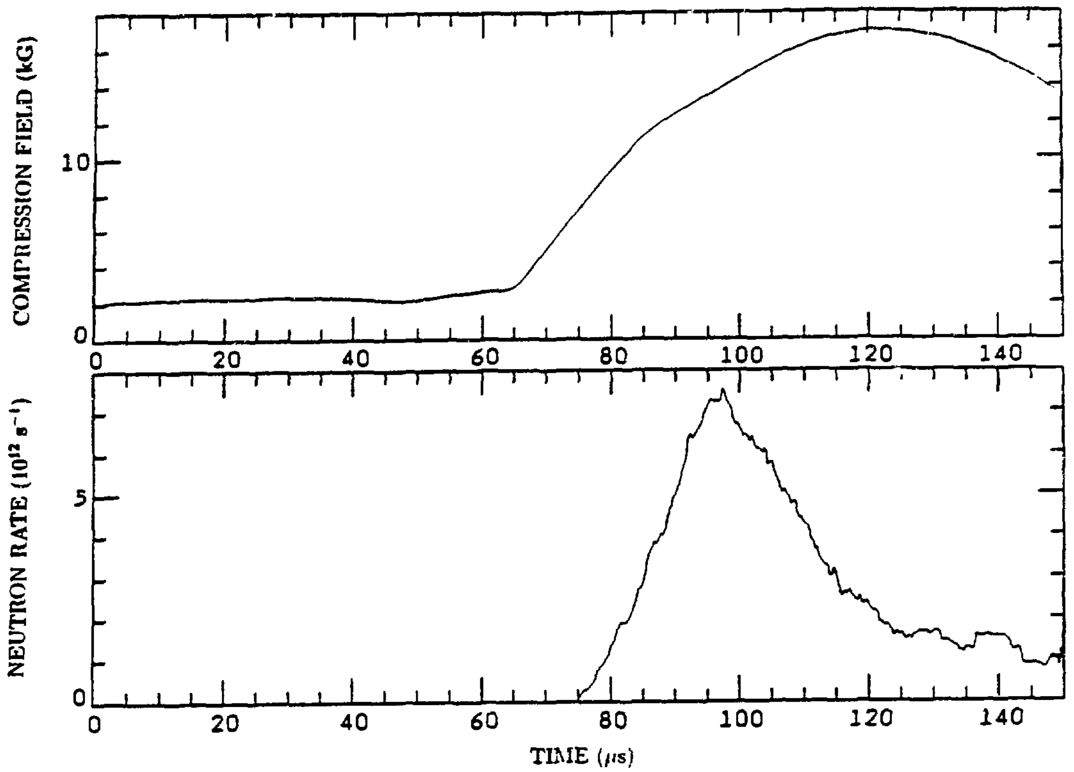

Fig. 3 Time evolution of compression magnetic field and neutron rate.

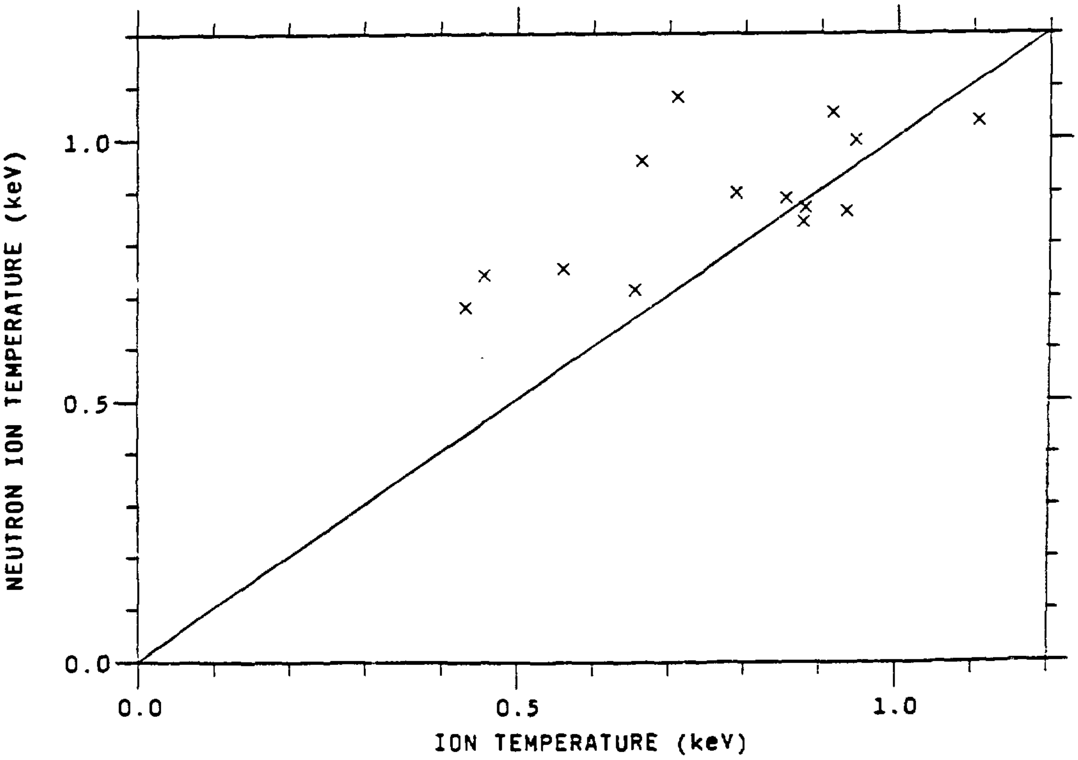

Fig. 4 Comparison of ion temperature inferred from neutron emission with T_i inferred from pressure balance and Thomson scattering measurements.

Large Volume FRC Plasma Production and High Energy Particle Injection Experiments in FIX machine

Seiichi GOTO, Yoshikazu YANO, Akira SHIOKAWA, Yoshio UEDA,
Satoshi SUGIMOTO, Shigefumi OKADA, Yoshifumi ITO,
Shoichi OHI and Tsutomu ISHIMURA
Plasma Physics Laboratory, Faculty of Engineering,
Osaka University
Yamada-oka 2-1, Suita, Osaka 565, Japan

Abstract: By the translation technique in FIX experiments a large FRC plasma of about 3m length and 0.4m diameter has been confined for 400~500μs in the quasi-static mirror field of 0.5kG. The plasma parameters are typically the following ; $x_s\sim0.5$ for $r_w=0.40$m, $2l_s\sim3$m, $n\sim5\times10^{-19}\,m^{-3}$, $2T=100\sim150$eV, $T_i=50\sim80$eV, $T_e=30\sim60$eV and $\Phi_i\sim1$ mWb. Here T_i and T_e are independently estimated from fast neutral energy analysis and injected helium beam attenuation, respectively. It is noted, in the behaviors of interferometric and probed beam signals, that the appearance of the usual $n=2$ rotational instability has not been observed during plasma life.

1. Introduction

As the first step toward the future FRC sustainment technology based on high power neutral beam injecion, we had constructed an FRC machine FIX last year [1], having capability of installing one to three injectors with the power of 50 kW class at 10~15 kV. The conditioning of plasma production has been continued to make two different modes of operation possible, that is, the usual theta-pinch FRC formation and the FRC translation. A weak power nuetral beam injector has been also installed this summer and tried to make injection experiments for developments of handling tenchnique and new diagnostics.

This paper presents an outline of the machine FIX together with representative plasma parameters in the formation part, the characteristic behavior of the translated plasma in the quasi-static mirror field for confinement, and the hydrogen and the helium beam probing results.

2. Experimental set-up.

A side-view drawing of the machine FIX is shown in Fig.1, where one can find the fomation part at the lefthand followed by a large-scale confinement vessel with five circular ports for beam injection. An injector of maximum power 30 kW at 10 kV is already mounted at the midport. Other various machine parameters are given in the reference [2].

In Fig.2 typical time behaviors of interferometric line density and diamagnetic signals in the usual FRC production mode is presented. In this case we can derive the following plasma parameters ; x_S~0.3 for $2r_W$=0.31m, $2l_S$~0.6m, 2T=150~200eV, and Φ_i=0.4~0.6 mWb.

3. Plasma behavior in translation experiment

By control of charging voltage and firing time of driven mirror coils at both ends of the compression coil, the FRC plasma can be translated into the quasi-static long mirror field of 0.5 kG with the mirror ratio of 3 to 4, and lasts beyond 400 μs as presented in Fig.3, where 9 loops in the pinch region and 18 pick-up coils inside the stainless vessel are used. Combining this data with the interferometric nl measurement for the translated plasma we obtain the following parameters : x_S= 0.4~0.5 for r_W=0.4m, $2l_S$=2.5~3.0m, $n \lesssim 5 \times 10^{19} m^{-3}$,2T=100~150eV, Φ_i~1 mWb and s~1. This experimental result indicates that the translation method provides the techinique of a large volume and fairly fat FRC production in the steady mirror field beyond an estimate for the translation relation [3] based on the conservation relation and the Barns' equilibrium condition.

An example of the nl signal is shown in Fig.4 (b),where it is noted that very small fringe shift of λ=3.39μm for the low density of the order of $10^{19} m^{-3}$ could be influenced by vibrations of components and thus the base line of the signal is not clearly determined. Then, we could not reduce the nominal confinement constants τ_N and τ_E. Another remark to be pointed out is that we have not obseved the indication of n=2 deformation during the plasma life in all the shots up to now although the growth time ranges in several tenth of microseconds under the MHD rigid rotor assumption.

As the first trial of neutral beam injection into the FRC plasma, hydrogen neutral H^0 of 3keV energy and helium neural He^0 of 1keV were probed in order to confirm the reliability of the nl waveform from H^0 beam attenuation, and also for estimation of average electron temperature T_e from He^0 probing. The beam detection of H^0 and He^0 after passing through the plasma is performed by a neutral particle energy analyzer to eliminate parasitic components of beams. Typical results are shown in Fig.5 and 6. Here again we have no indication of n=2 rotational instablity. From Fig.5 (b) the similar $n_i l$ waveform as that of the interferometer is found except its final part though the measuring place of interferometer is apart 0.6m from the midplane where the beam injector is mounted. The He^0 beam attenuation signal in Fig.6 (b) can give the average electron temperature by using the formula $I/I_0 = \exp(-\langle \sigma v_e \rangle n_e l / v_b)$ where σ is the electron impact ionization cross-section of He^0 and v_b the beam particle velocity. The estimated electron temperatures T_e are 45eV, 45eV and 60eV at the time point ①, ② and ③ on Fig.6, respectively. In addition we could have the average ion temperature T_i to be 60~80eV by using the neutral particle energy analyzer mentioned above. The total temperature (T_e+T_i) obtained here gibes fairly good consistency with that from the diamagnetic temperature 2T.

In order to look for the reason why we observe no elliptical deformation in FIX plasma, we should get the informations on plasma rotation and internal azimuthal magnetic field at least. As the initial measurement on rotation the spectral line profile of He II (4686Å) from the helium mingled into the working gas D_2 were observed by a multichannel spectrometer. The result shows that the spectral line shift could not be observable, while the broadening gives the ion temperature 60~80eV. This means that the rotation speed of He may be less than 1×10^4 m/s which is low compared to the value 3×10^4 m/s expected by $\Omega^* = T_i(dn_i/dr)/enBr$. As for the azimuthal field B_θ the internal probe measurement has been tried and the field B_θ around 100 G is observed in the straight field (~500 G) during the movement of the translated plasma. However, many problems on inserting the probe should be overcome to make the measurement approved.

4. Summary

The large bore FRC plasma is successfully confined in the quasi-static mirror field for about 500 μs. There is no indication of n=2 rotational instability over the plasma life. The neutral beam injection experiment starts as the new diagnostics development and will go to the high energy particle study in FRC.

Reliable measurements on density, rotation and internal magnetic field are required to study the new regime of FIX translated plasma. The plasma parameters should be also improved for research of high energy particle-plasma interaction in future.

References

[1] S. Goto et.al, Proc.of 10th US-Japan Workshop on Compact Toroids (Nihon Univ.), pp.71 (1988).

[2] S. Goto et.al, Technol. Repts. Osaka Univ. 39, 129 (1989).

[3] M. Tanjo et.al, Technol. Repts. Osaka Univ. 34, 201 (1984).

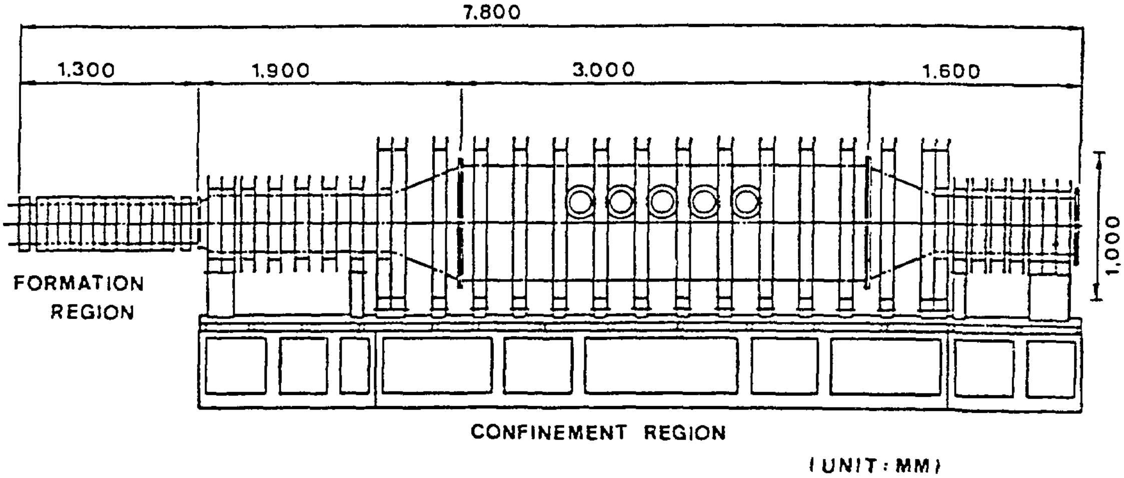

Fig.1. Side view drawing of FIX.

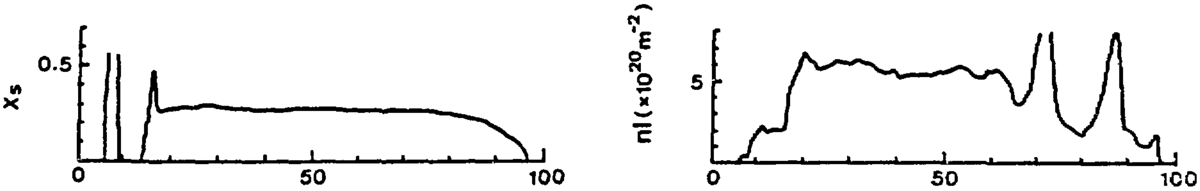

Fig.2. FRC plasma behavior in the formation region.

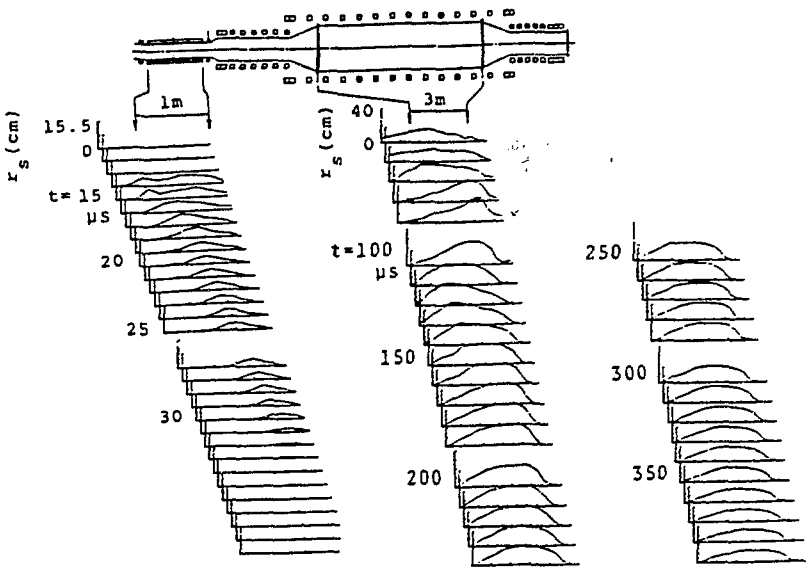

Fig.3. Time change of axial x_s profile in translation.

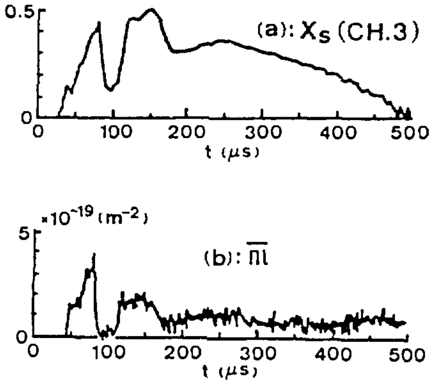

Fig.4. Diagnetic (a) and interferometric (b) signals at the off-midplane.

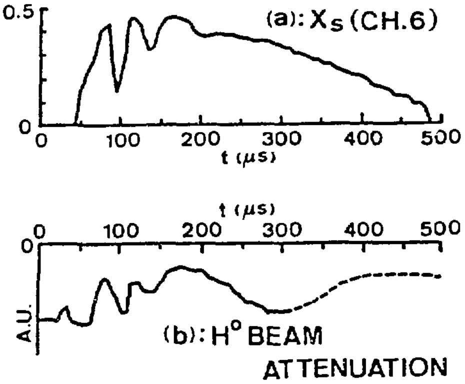

Fig.5. Diamagnetic (a) and beam attenuation (b) signals at the midplane.

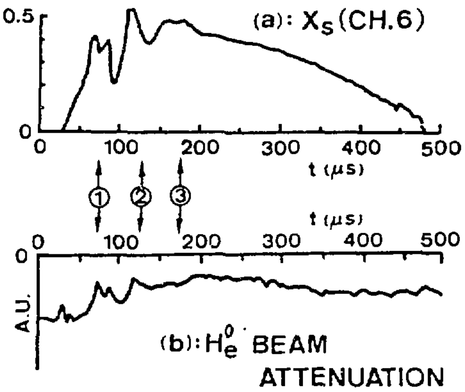

Fig.6. Diamagnetic (a) and beam attenuation (b) signals at the midplane.

Tomographic Observation of Two-Dimensional Profile of FIX Plasma

S.Sugimoto, Y.Nishizawa, and S.Goto

Plasma Physics Laboratory, Faculty of Engineering
Osaka University
2-1 Yamada-oka, Suita-city
Osaka 565, Japan

A two-dimensional(2D) measurement system for FRC plasmas based on spectroscopy and computed tomography has been developed. The features of this system as follows: (1) fifty chord signals of plasma emission are collected using five ten-channel fiber optic arrays; (2) 2D emission intensity profiles can be reconstructed as a function of time with up to a 0.25 μs resolution; (3) the result has explicit physical meaning with the help of five grating monochromators; (4) the measurement wavelength is tunable over visible and ultraviolet regions, and the bandwidth is also variable (0.2-2nm).

Figure 1 shows a block diagram of the system. This system is composed of five photocollector arrays, five grating monochromators, fifty photomultipliers, and fifty-channel transient memory. We have reported the preliminary measurement on the PIACE-II machine.[1,2] After this experiment, the optical system of the measurement system was improved to allow a more optimum alignment of the fifty chords (see Fig.2). The distance between each photocollector array and the center of the coils should be adjusted according to the radius of plasma. The new optical system has a circuler guide rail and five linear ones along which the photocollector arrays are movable. The observing angle of each photocollector array was also adjustable. This was useful to avoid various obstacles, such as ports for other measurements and coils parallel to the quartz discharge tube.

We first measured a translated plasma at the outlet of the source region in the FIX machine.[3,4] Figure 3 shows a schematic diagram of the FIX machine and the location of the tomographic measurement. Typical plasma parameters of the source plasma produced on the FIX machine were total temperature ~200eV, electron density ~6.4×10^{15}cm^{-3}, and a lifetime ~80μs. The separatrix radius and the length of the plasma were about 4.5 and 70cm, respectively. Five photocollector arrays were placed azimuthally around the z-axis at interval angles of 55~65°. The distance between the center of the coils and the pinhole of each photocollector array was 300mm and the diameter of each pinhole was 3.0 mm.

Figure 4 shows ten chord signals acquired with photocollector array 1 for a typical plasma shot. The sampling frequency was 4MHz, and the wavelength and bandwidth of the emission were 497.6 nm and 1.0 nm, respectively. This wavelength is appropriate to the detection of bremsstrahlung. The signals have been moving-averaged by 5 sampling points (±500ns) for noise supression. The primary signal of each chord was detected after firing the main field (t>20μs). The other diagnostics were an array of diamagnetic probes and two chords of interferometry. The data showed that the plasma was confined in the source region for about 20 μs after formation, and moved into the confinement region with a velocity of more than 1×10^5m/s. Accordingly, the peak of the chord signals near the time of 50μs must be due to the translated FRC plasma.

The result of reconstructing a set of 2D and time-resolved profiles is given in Fig.5. The height of a 2D plot represents the emission intensity. The reconstruction was performed by the ART method$^{5)}$ without the assumptions of plasma rotation or point symmetry. The reconstruction space was divided by 7×7 area cells. Therefore, the plotted profiles have been interpolated smoothly. The spatial shift which is observed in this sequence of plasma profiles is due to the disagreement between the center of the coils and that of optical system. The reconstructed profiles clearly have some artifacts in the plasma as well as in the surrounding area. The causes of these artifacts seem to be nonuniformity of the alignment of the fifty chords and an error of the relative sensitivity calibration. Using the above results, we can obtain a time sequence of FRC plasma cross-sections perpendicular to the z-axis. Hence, a 3D profile of the translated FRC plasma may be obtained using this measurement method.

Since the major aim of this measurement, however, is observation of equilibrium profiles, formation, gross instability, plasma end profiles, we are now trying to measure the 2D bremsstrahlung profile at the midplane in the source region. At the same time, we are improving the optical system to increase the sensitivity for future measurements in the confinement region where the plasma density will be at least 100 times lower than in the source. Additionally, a reconstruction technique for a 2D H_β emission profile is being developed.

1) S.Sugimoto, T.Niina, and S.Goto, J. Appl. Phys., to be published.
2) S.Sugimoto and S.Goto, Proceedings of the 10th US-Japan workshop on compact toriods, Nov.14-16,1988, Hakone, 59(1988).
3) S.Goto, Y.Yano, A.Shiokawa, S.Sugimoto, S.Okada, Y.Ito, S.Ohi, and T.Ishimura, Technology reports of the Osaka University 39,129(1989).
4) Y.Ito, S.Sugimoto, Y.Ueda, S.Okada, S.Ohi, S.Goto and T.Ishimura, Proceedings of the 9th U.S. compact toroid symposium, Mar.14-15,1989, Washington,103(1989).
5) S.Kawata and O.Nalcioglu, IEEE Trans. Med. Imaging MI-4, 65(1985).

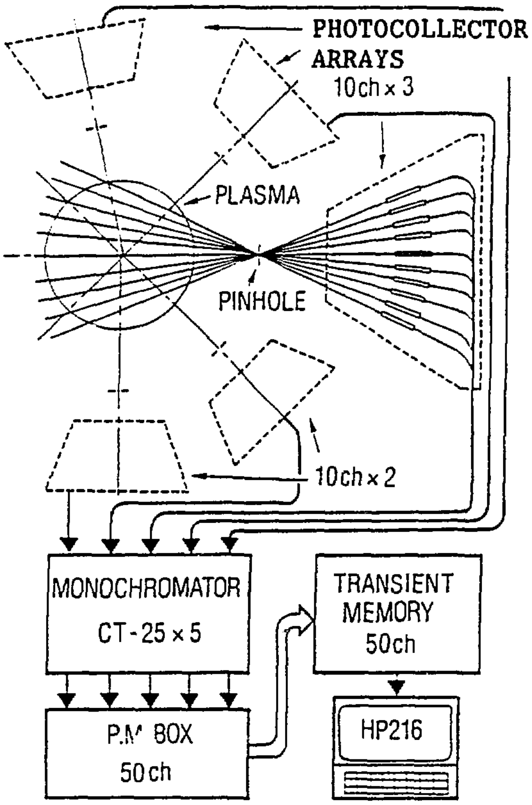

Fig.1
Block diagram of the spectroscopic plasma tomography measurement system.

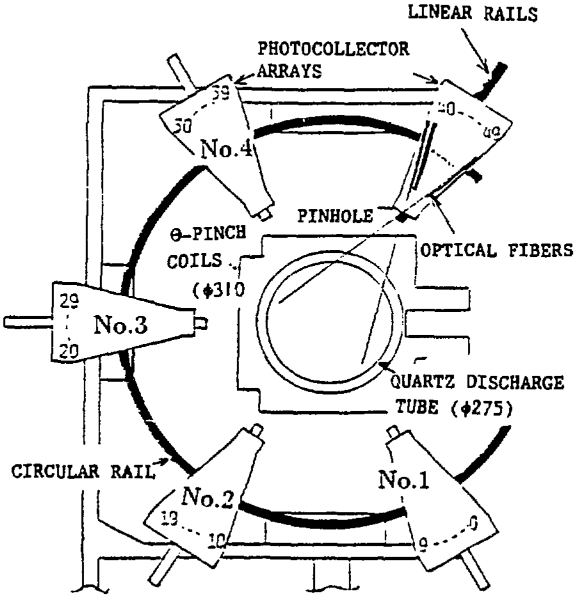

Fig.2
Optical system in the developed system.

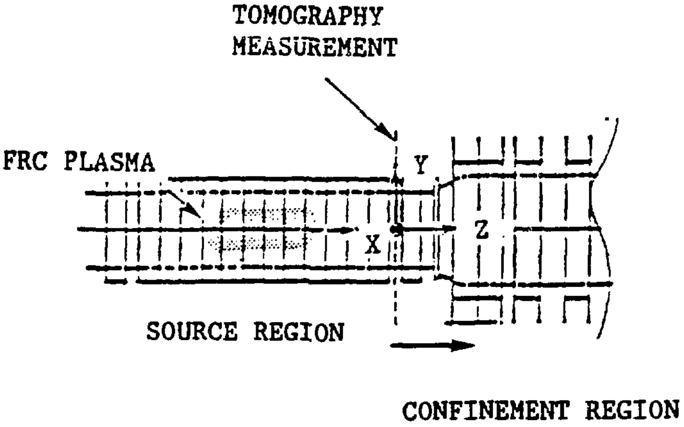

Fig.3
Schematic diagram of the source region in the FIX machine and the location of the tomography measurement.

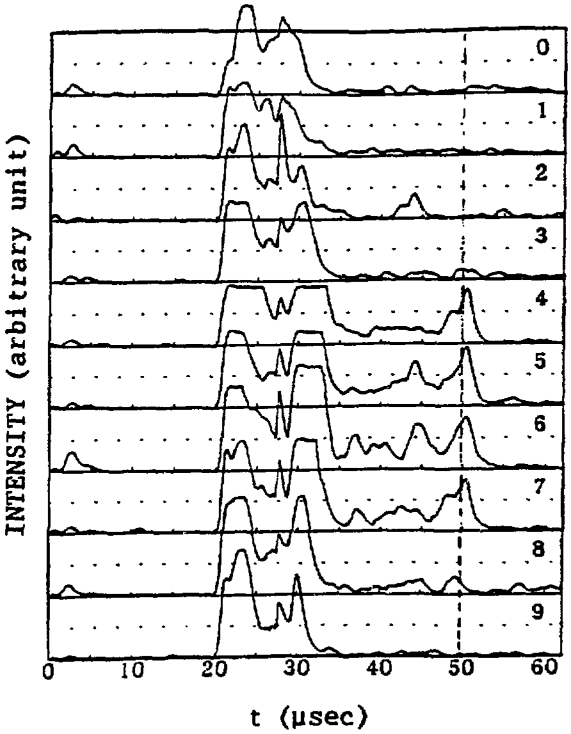

Fig.4
Ten chord signals acquired with photocollector array 1 for a typical plama shot. The measurement wavelength and bandwidh were 497.6nm and 1.0nm.

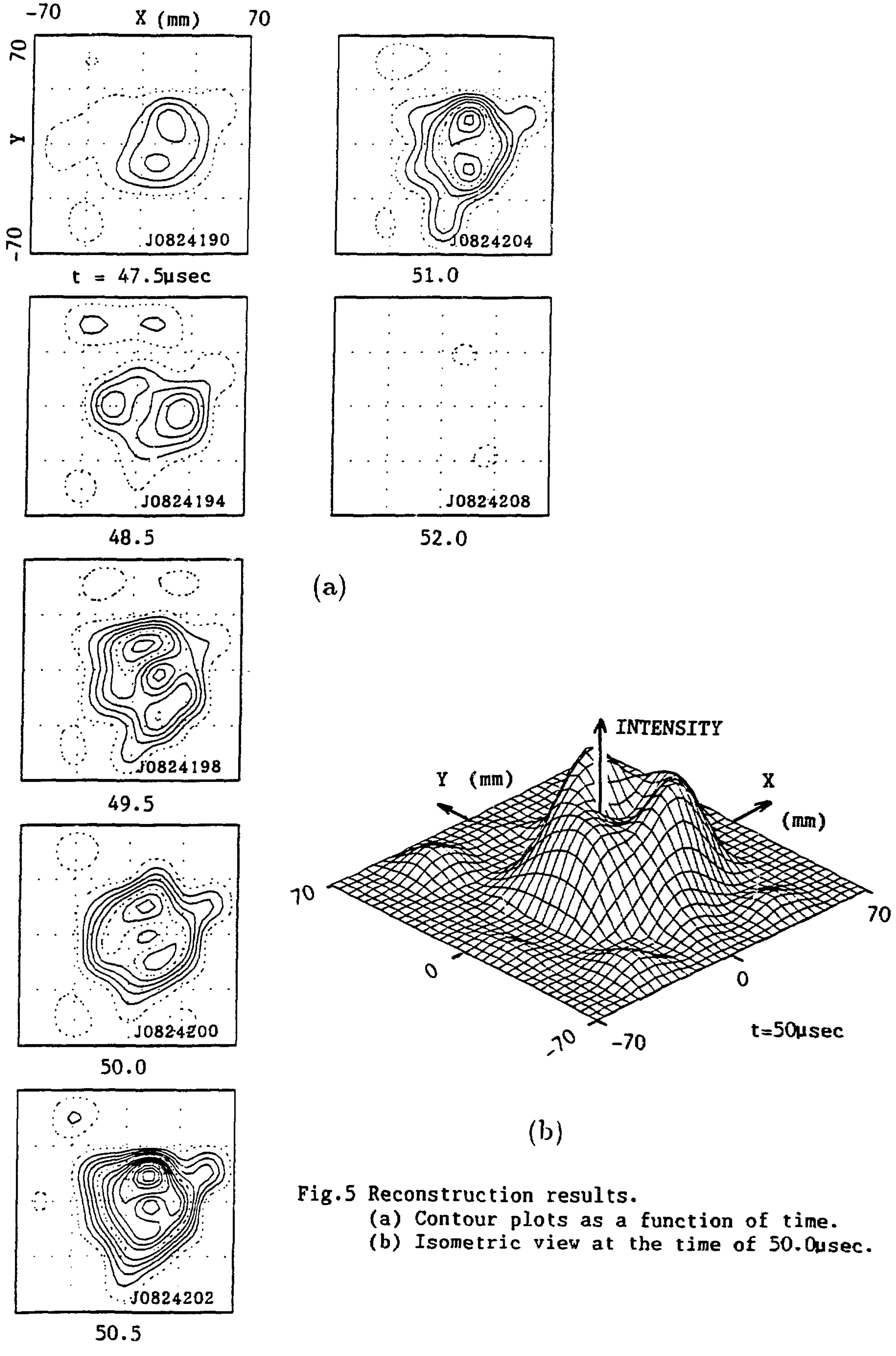

Fig.5 Reconstruction results.
(a) Contour plots as a function of time.
(b) Isometric view at the time of 50.0μsec.

DESIGN AND STATUS OF THE LARGE s EXPERIMENT

Alan L. Hoffman
Spectra Technology, Inc.
Bellevue, WA

The large s experiment (LSX) is being constructed at STI with the design goal of producing s = 8 FRCs, with temperatures sufficient that the ion mean free path exceeds typical device dimensions. The device dimensions have been chosen based on analytic expressions for plasma heating and s.

$$\frac{1}{2}\left(T_e + T_i\right) = 300\left(B_{lo}^{6/5} + 0.3 f_s B_*^{6/5}\right) B_e^{4/5}/p_o \quad \text{eV} \qquad [1]$$

B_{lo} is the lift-off field, B_* is the characteristic field given by Green and Newton[1], and B_e is the external field (all in kG). p_o is the deuterium fill pressure in mTorr and f_s is a parameter which reflects the reduction in radial shock heating effectiveness as B_{lo} approaches B_*. Using a rigid rotor expression for the poloidal flux, Φ_e, of an FRC in a flux conserver of radius r_c, the effective number of internal ion gyroradii, s, is given by

$$s = 35 \left(\frac{B_e(T)}{r_c(m)}\right)^{1/3} \frac{\Phi_e^{2/3}(Wb)}{T_i^{1/2}(keV)} \quad . \qquad [2]$$

The physical parameters of the LSX device are listed on Table 1.

TABLE 1
LSX PHYSICAL PARAMETERS

Coil Diameter (ID)	$2r_c$	= 0.9 m
Plasma Tube Diameter (ID)	$2r_w$	= 0.8 m
Fast Coil Length	L_c	= 4.5 m
Total Magnet Length		5.0 m
Total Plasma Tube Length		6.3 m
Peak External Field	B_e	= 7.5 kG
Maximum Bias Field	B_o	= 2.0 kG
B_* Field (at 5 mTorr)	B_*	= 1.2 kG
Energy ($\pi r_c^2 L_c B_e^2/2\mu_o$)		650 kJ

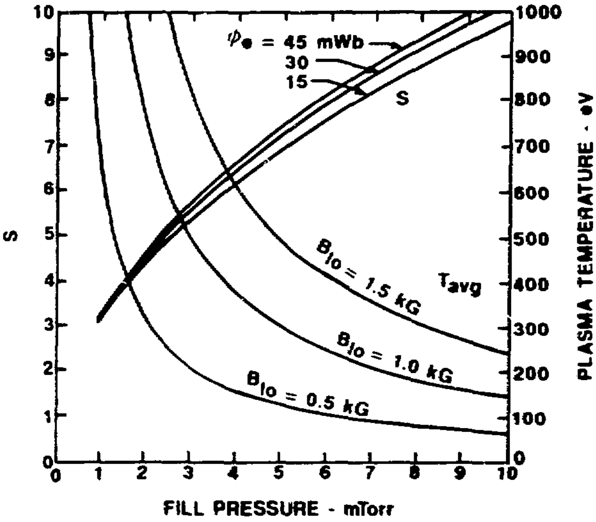

89 :8162

Fig. 1. Anticipated temperatures and s values for LSX as a function of D_2 fill pressure and lift-off field. (B_e = 7.5 kG, f_ϕ = 0.65)

The temperatures and s values achievable in LSX (based on equations 1 and 2, with the radial shock heating contribution ignored) are shown on Figure 1 as a function of fill pressure and B_{lo}. It was assumed that 65% of the lift-off flux was retained into equilibrium. In order to produce s = 8 FRCs, and still satisfy the mean free path requirement ($T_i \geq 250$ eV), an equilibrium flux of 30 mWb (B_{lo} = 1 kG) is required at a fill pressure of 6 mTorr. The previous small 20 cm diameter TRX device has been operated at lift-off fields above 1 kG and, by making use of recent formation advances, has produced 'long lived' FRCs with 65% flux retention. However, as evidenced by the experience on the 60 cm diameter FRX C/LSM, where long lived plasmas could only be formed at B_{lo} values below about 0.3 kG (based on Φ_e = 5 mWb and 65% flux retention),[2] operation at high B_{lo} is expected to become more difficult as the device size increases.

There are several reasons why FRC formation is expected to get more difficult in larger devices. Firstly, the magnetic field gradients will be lower during the anti-parallel phase, and less flux will be dissipated. The reduced plasma heating will result in more dynamic axial contractions, which will make the formation process more susceptible to disruption from initial non-uniformities. FRX C/LSM operated well only at a flux level low enough that the radial shock heating term in Eq. 1 was significant, and strong axial contractions were avoided. However, this limited the equilibrium flux to some small percentage (~10%) of $\pi r_w^2 B_*$. The second reason why formation may be more difficult at large sizes is that kinetic effects are reduced, and instabilities may grow more rapidly. On the small TRX device, operation at low fill pressures was always easier, but this was attributed to increases in axial viscosity, which damped out plasma oscillations after the axial contraction.

LSX is a relatively low E_θ device, and radial shock heating will be negligible for all conditions. However, it has been built with two features to enhance the ability to operate at high lift-off fluxes. It has special control coils at the ends to allow for a type of programmed formation termed 'bubble mode',[3] whereby the axial contraction is delayed to permit more ohmic heating to occur. It also has barrier rods to produce a short range multipole field at the tube wall during preionization and field reversal. This has been demonstrated on TRX to provide for better initial uniformity, and to produce much better flux retention at high lift-off fields, even with extremely dynamic axial contractions.[4]

A drawing of the LSX device is shown on Figure 2. Three 25-cm long coils at each end can be individually energized, or they can be bussed together in various arrangements between themselves or with the central 3 meters. Different electrical connections and triggering sequences allow for operation in various modes of programmed formation, ranging from the most rapid driven contraction in 'slingshot' mode, to the delayed contraction in 'bubble' mode.[3] Quasi steady multi-turn plug coils are also located at each end, which form the basis of the programmed formation method. Twenty-four barrier strips are attached directly to the plasma tube, and can produce 3 kG multipole fields at the tube wall. Octopole rods are located outside the main coils, and can be run either straight or helical.

The plasma tube consists of five 1.25-m long, 80-cm ID quartz tube sections. Both clear quartz and opaque (Rotosil) sections have been purchased and vacuum tested. They can be sealed with dry "O"-rings, using shielded polypropalene joining rings and axial compression seals. The less expensive opaque tube sections will be used at the ends. The main coils are attached in two halves after the plasma tube is put in place, so that radial vacuum penetrations are possible for diagnostics.

The main coils are driven by ±25 kV capacitor bank modules in a flexible arrangement to permit individual energizing of the various coils. A drawing of the complete LSX facility is shown on Figure 3. A ±5 kV bias bank, isolated by bias inductors, supplies up to a 2 kG bias field. Separate banks power the plugs, barriers, and octopole rods. All the capacitor banks have been built and are presently being wired for control monitoring and triggering. The magnets are also complete and will be connected to the capacitor banks in the next few months.

The main capacitor bank has several additional features to affect the above mentioned formation enhancements. Several of the modules powering the end coils have insertable PFNs which can produce a delay in the current rise. Use of these PFN modules is illustrated in the MOQUI (2D MHD) calculation on Figure 4 of bubble mode formation. All three end coils are connected together in this simulation, which has been found numerically to produce the greatest delay in the axial contraction. The PFN end modules are fired at the same time as the modules powering the central three meters, and the remaining end modules are fired close to the peak of the main field. Also indicated on the figure by the dashed lines is possible operation with an oscillation in the bias field. This oscillation is much slower than the normal 'ringing I_θ' preionization used in many theta pinch devices, but has been found to produce very uniform preionization on TRX-2 when used in conjunction with ringing barrier fields.[4] The ringing B_z field is produced using several of the main capacitor bank modules in a ringing mode. Accommodation has been made in the control system for this mode of operation.

LSX is scheduled for plasma tube assembly next February, and initial shakedown testing sometime in May. The complete facility is scheduled to begin experimental operation on 16 July, 1990.

REFERENCES

1. T.S. GREEN and A.A. NEWTON, Phys. Fluids 9, 1386 (1966).
2. M. TUSZEWSKI, Phys. Fluids 31, 3754 (1988).
3. J.T. SLOUGH et. al., Phys. Fluids B 1, 840 (1989).
4. J.T. SLOUGH and A.L. HOFFMAN, "Experimental Study of the Formation of FRCs Employing High Order Multipole Fields", to be published.

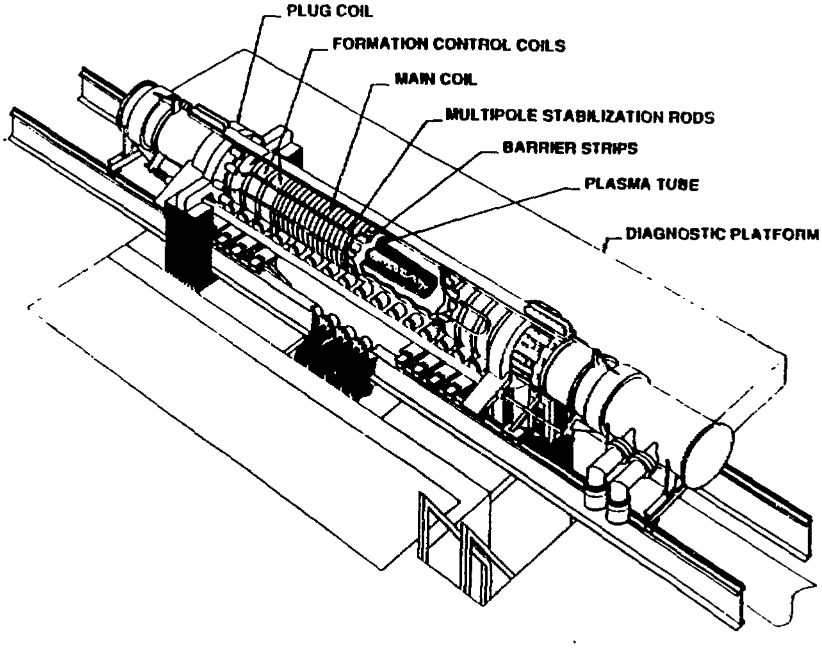

Figure 2. LSX Experiment Layout.

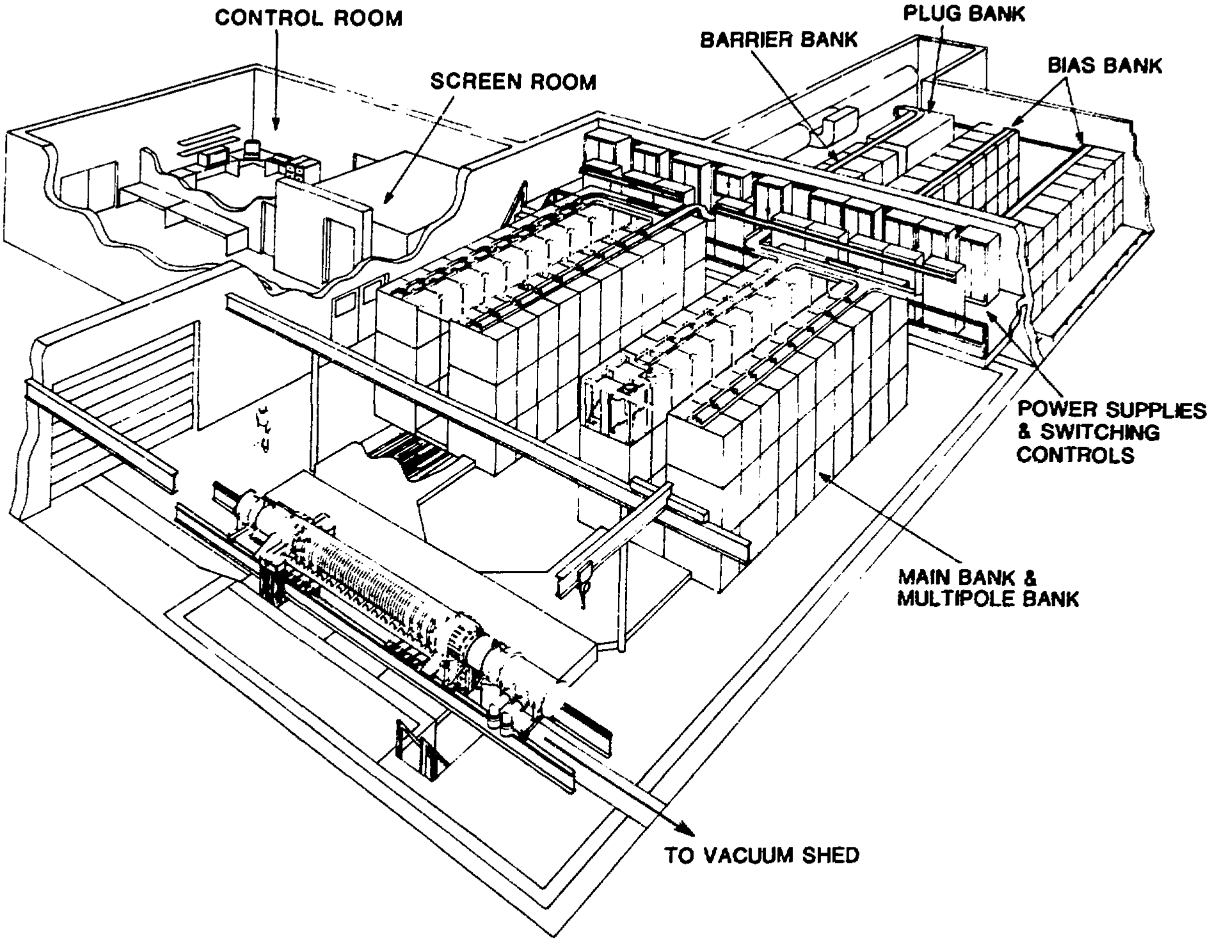

Figure 3. LSX Facility Layout Drawing.

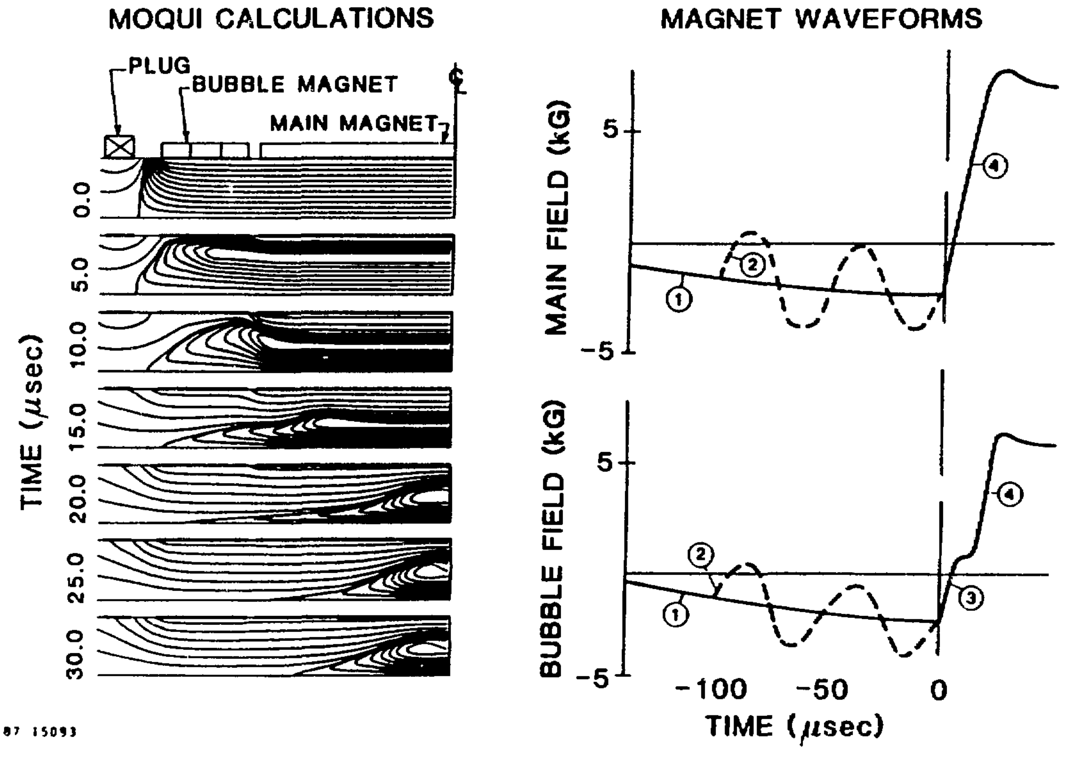

Figure 4. Bubble Mode Formation on LSX.

The Coaxial Slow Source: Parallel Operation and The Radiation Barrier

R. D. Brooks, R. Farengo, T. R. Jarboe, G. C. Vlases,
R. J. Maqueda, R. J. Smith, R. Raman, R. G. Berger & W. F. Pierce
AERB FL-10 University of Washington, Seattle, WA 98195 U.S.A

I. INTRODUCTION

The Coaxial Slow Source (CSS) has previously been reported[1] to produce "annular FRCs" on a slow time scale and at low voltages. We report here preliminary results from 2 aspects of the ongoing CSS research. The first is experimental results from the CSS operated in the parallel mode, CSS-P. The second topic involves analytical work on ohmic heating of a high $<\beta>$ plasma with and without impurity radiation losses.

II. PARALLEL OPERATION

The CSS has been modified to operate in the "parallel mode." To accomplish this the outer single turn theta pinch coil has been modified to have four turns, the same as the inner coil. The coils are wired in parallel to the same capacitor bank so that the space between them is a flux conserver if the external inductance is negligible. Thus the total flux in the annulus between the two coils must always remain zero. If an additional flux conserving ring (plasma) is created between these coils, equal and opposite fluxes will build up on either side of it when the circuit is energized. This results in the plasma being centered between the coils without the radial dynamics associated with formation in the independent coil mode.

The CSS-P can be operated in two different regimes. In the first the capacitor bank is energized before forming the plasma. This leads to the inner coil filling with flux while the space between the coils remains flux free. At the time of peak current (end of first quarter cycle) the filling gas is preionized and current begins to flow in the outer coil. As the current in the inner coil decreases, flux is transferred from the inner coil out and the outer coil in maintaining the total flux in the space between the coils and between the plasma and the axis of the device constant. We refer to this stage as programmed formation because the flux does not need to tear to wrap the plasma. At the end of the second quarter cycle, all of the flux initially stored in the inner coil has been delivered. This marks the end of the programmed formation phase. Flux will continue to be delivered for another quarter cycle but, since this flux did not initially wrap the plasma, a reconnection process is necessary for it to do so. We refer to this as tearing formation.

In the second mode of operation, the plasma is produced before the coils are energized and involves only tearing formation. One of the major differences between programmed and tearing formation is that during programmed formation the separatrices are on both coils. If an axial equilibrium is established within the coil length, a midplane average beta between the coils of 0.5 and thus a "fat" plasma results. During tearing formation it is possible for the separatrices to be away from both coils and to have an arbitrarily "thin" plasma.

One of the aspects of the CSS-P which is most noteworthy is the ability to form a field reversed plasma at very low loop voltages. This has resulted in the tearing formation of a plasma at the beginning of the discharge, when the loop voltage is at its peak, for a wide range of operating conditions. For 10 mT of D_2 and significant preionization a field reversed plasma with reasonable flux confinement properties was produced with a loop voltage below 100 volts. We believe that this formation occurs so easily because any conducting plasma will be forced away from both coils and thus will not be quenched by a wall as it would be during independent operation. Because of the ease of formation during the first quarter cycle, even without preionization, it is difficult to form in the programmed formation mode. We do have preliminary results of such formation, where an energetic PI is employed, indicating a short configuration is formed. Since for most operating conditions breakdown occurs during the first quarter cycle, the remainder of the results discussed here are for that mode.

Though visible light photography must be interpreted carefully, streaks of the CSS-P plasma give results consistent with other diagnostics. A thin annular plasma can be seen to form at the appropriate radius. This thin plasma can either gradually become thicker or rapidly disappear in a bright flash. The bright flash, which can appear at different times at different azimuthal locations, is associated with a rapid loss of flux and the appearance of transient B_θ signals adjacent to the outer coil. The cause of this is presently unknown but it may be related to impurity radiation effects.[2]

One characteristic of the plasma produced by the CSS in the independent mode was a short flux decay time. The CSS-P has been able to produce plasmas with significantly longer flux decay times. If we assume that the field is uniform between the coils and the null location, the field adjacent to the coils represents the flux between the coil and the null. This field normalized to the charging voltage of the capacitor bank does not depend on charging voltage if there is a thin plasma at the null location with a resistance which does not depend on charging voltage. This normalized field is plotted in Fig. 1 versus time. It can be seen that for all of the discharges the fields track very well for the first 15 μsec. Starting around this time, depending on charging voltage, significant flux loss as described above occurs. For the 1.5 kV case no rapid flux loss appears and, again assuming a thin plasma, the loss of flux is consistent with a flux confinement time of about 150 μs. It should be pointed out that though we are in first quarter cycle tearing formation mode, significant <β> and a "fat" plasma may exist. (An axial probe array indicates that the plasma was long.) Depending on the ratio of specific heats, γ, and axial dynamics the plasma energy represented by this <β> must have come from ohmic heating. The 150 μs time would then represent a time for loss of energy from the plasma and field configuration. If we take the flux confinement time to be 150 μs and assume a plasma thickness of 4 cm, classical resistivity is consistent with a temperature of $T_e = 21$ eV.

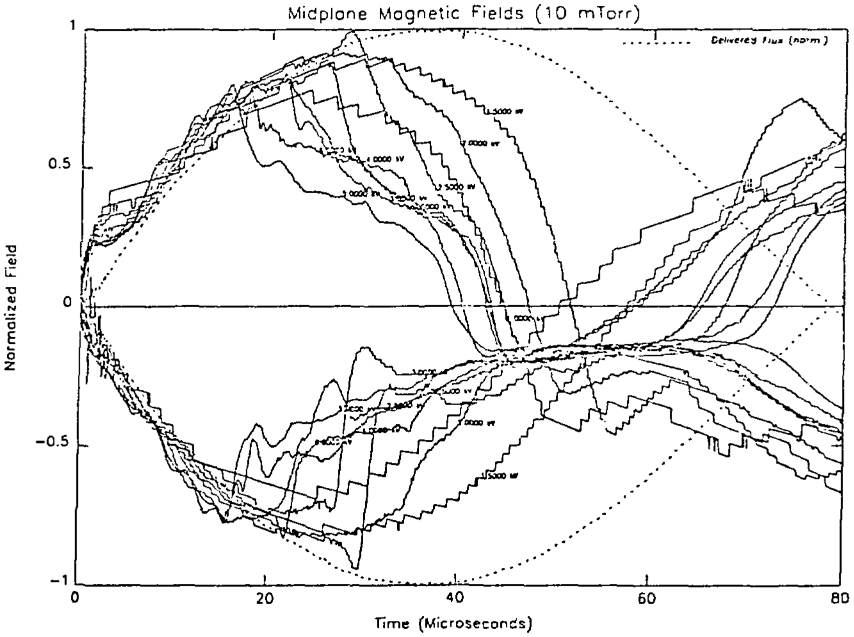

Figure 1. Magnetic field normalized to the flux addition rate adjacent to the inner and outer coils versus time for discharges at various voltages. (10 mT D_2)

III. RADIATION AND OHMIC HEATING

The long time scales on which the CSS operates and the lack of an initial bias field make it difficult to increase the plasma temperature. Results reported in the past are consistent with a cool, radiation dominated, plasma with fairly high density. In order to overcome this problem a better understanding of the physical mechanisms responsible for this behavior is necessary. As a first step simple models have been developed to study the effect of line radiation from impurities and ohmic heating on the energy balance. The work follows the same ideas as previous calculations carried out for z-pinches[3] but using a 2D MHD equilibrium calculated by solving the Grad-Shafranov equation. Two problems have been addressed using this model. The first is to simply calculate under what conditions the ohmic power equals the radiated power and the second is to determine the time evolution of the temperature, assuming there is no radiation.

Equilibrium The solution of the Grad-Shafranov equation we will consider was first discussed by Maschke[4] and Herrnegger[5] and describes a plasma inside a toroidal chamber with rectangular cross section. As a model for the CSS this is clearly an approximation because it assumes that the flux inside the inner and outer coils is the same and there are end caps connecting both coils. The first assumption is well justified, at least in the parallel mode, because ideally there should be no net flux between the coils and the second one is justified because $L >> r_o - r_i$ so that end effects will not be important.

Assuming $p = p_1\psi^2$, where p is the plasma pressure and ψ the flux function we obtain

$$\psi = A\cos\left(\frac{\pi z}{L}\right)\left[F_o(\eta, \alpha r^2) + \gamma G_o(\eta, \alpha r^2)\right]$$

where F_o and G_o are the regular and irregular Coulomb wave functions of order zero, parameter η and argument αr^2, L is the length of the separatrix,

$$A = \frac{B_z(r=r_i,\ z=0)\pi}{\alpha\left[F'_o(\eta, \alpha r^2) + G'_o(\eta, \alpha r^2)\right]}, \qquad \alpha = \frac{\pi^2}{L^2\, 8\eta}$$

where $r_i(r_o)$ is the inner (outer) separatrix radius and η and γ are determined by requesting ψ to be zero at both separatrices.

Ohmic heating and line radiation A necessary condition to increase the plasma temperature is that the ohmic power has to be greater than the radiated power. If this is satisfied and there are no other important energy losses the temperature (and probably the size) of the plasma will increase. At low temperatures the most important contribution to radiation losses is due to line radiation from impurities. We will assume that both C and O are present and that an equilibrium coronal model (with Post's rates^6) applies (equal electron and ion temperatures will be assumed throughout this paper). The radiated power is then $P_R = f\, n_e^2\, L_z(T_e)$ where f is the impurity concentration and L_z is the cooling rate. The ohmic power is simply $P_\Omega = \eta(T_e)\, j^2$. A very simple model can be used to illustrate the basic physics of the problem. Considering a plasma slab of thickness a and uniform current density and temperature we have

$$J \propto \frac{B_o}{a}\ (B_o : \text{external field}) \Rightarrow P_\Omega \propto \eta(T_e)\,\frac{B_o^2}{a^2}$$

$$n_e \propto \frac{B_o^2}{T_e} \Rightarrow P_R \propto \frac{f\, B_o^4}{T_e^2} L_z(T_e)$$

The condition $P_\Omega > P_R$ then gives $$B_o \leq \frac{C_1}{a\, f^{1/2}}\left[\frac{\ln\Lambda\ T_e^{1/2}}{L_z(T_e)}\right]^{1/2}$$

where C_1 is a numerical constant and classical resistivity has been assumed. The important point to note here is that there is an upper limit on the value of the magnetic field and that this value increases as the thickness and the impurity fraction decrease. In a regular FRC, a thin plasma sheath is produced after field reversal. Since ohmic heating is very efficient in the sheath, its temperature increases rapidly. As the sheath implodes radially, it heats the bulk of the plasma raising the temperature above the radiation barrier.

Using our solution of the Grad-Shafranov equation it is possible to write both the toroidal current density and the particle density in terms of the flux function (assuming uniform T_e)

$$j = 4\pi c p_1 r\psi \qquad n_e = p_1\,\frac{\psi^2}{2T_e}$$

The condition for plasma heating can then be written as

$$\int_{vol} \eta(T_e)\,(4\pi c p_1)^2\, r^2\, \psi^2\, dV \geq \int_{vol} \frac{f\, p_1^2\, \psi^4\, L_z(T_e)}{4\, T_e^2} dV$$

where the integrals extend to the volume occupied by the plasma. After some straightforward algebra we obtain the condition

$$f^{1/2} B_o \leq C_2\left(\frac{S_\Omega}{S_r}\right)^{1/2}\left[\frac{\ln\Lambda\ T_e^{1/2}}{L_z(T_e)}\right]^{1/2}$$

where C_2 is another numerical constant and S_Ω and S_R are given by

$$S_\Omega = \int_{r_i}^{r_o} dr\, r^3 \left[F_o(\eta, \alpha r^2) + \gamma G_o(\eta, \alpha r^2)\right]^2 \qquad S_R = \int_{r_i}^{r_o} dr\, r \left[F_o(\eta, \alpha r^2) + \gamma G_o(\eta, \alpha r^2)\right]^4$$

This condition has the same dependence with temperature and impurity fraction as the simple model. It turns out that, although not clear from the equation, the dependence upon plasma thickness remains basically the same replacing a by $a_* = (r_o^2 - r_i^2) / (r_o^2 + r_i^2)^{1/2}$. Specifying the external field it is very simple to calculate the maximum density from the pressure balance condition and therefore the condition $P_\Omega > P_R$ can also be expressed as a constraint on the maximum density. We plot in Fig. 2, the critical magnetic field times $f^{1/2}$ (for which $P_\Omega = P_R$) as a function of temperature for three values of r_o/r_i, (21.3/5.3, 17.3/9.3, 15.3/11.3) with equal amounts of C and O present. Above the curve the radiated power exceeds the ohmic power and below the opposite is true.

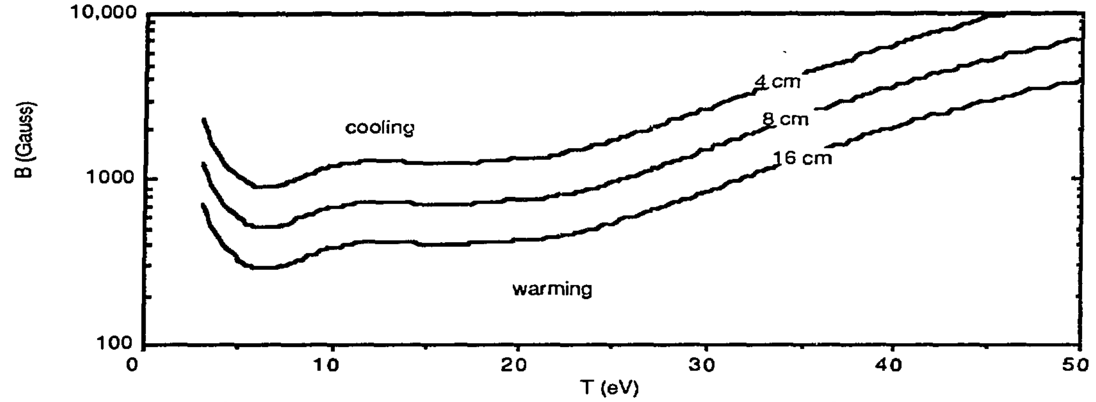

Figure 2. Magnetic field at the midplane adjacent to the outer coil for which ohmic heating is balanced by radiative cooling for various plasma thicknesses. (1% O, 1% C)

Temperature evolution A very simple energy balance equation can be obtained by assuming the particle inventory remains constant and neglecting the work term. With these assumptions we get

$$3\, N_e \frac{d}{dt}(T_e) = \int P_\Omega dV - \int P_R dV$$

The fastest temperature increase is clearly obtained when there are no radiation losses. Assuming uniform density and current, and neglecting radiation we can write

$$3\, n_e \frac{d}{dt}(T_e) = \eta J^2 \propto T_e^{-3/2} \frac{B_o^2}{a^2} \Rightarrow 3\, n_e T_e \dot{T}_e \propto T_e^{-1/2} \frac{B_o^2}{a^2}$$

but

$$n_e\, T_e \propto B_o^2 \Rightarrow \dot{T}_e \propto \frac{T_e^{-1/2}}{a^2} \text{ or } T_e^{1/2} \frac{d}{dt}(T_e) \propto \frac{1}{a^2}$$

integrating this we get $T_e \propto \frac{t^{2/3}}{a^{4/3}}$. This shows that the thinner the plasma the faster the temperature will increase and also that the magnetic field does not appear. A similar procedure can be followed using the solution of the Grad-Shafranov equation and writing

$$N = \int n\, dV = \int \frac{p}{2T_e} dV = \int p_1 \frac{\psi^2}{2T_e} dV$$

The time dependence is the same as in the simple model and the dependence upon plasma thickness is also maintained if we replace a by a_* In Fig. 3 we plotted the temperature as a function of time for the same values of r_i and r_o as in Fig. 2. It is clear that as the temperature increases its time derivative decreases due to the decrease in the classical resistivity. In an actual experimental situation this may not be the case, however, because as the temperature increases, anomalous effects can become important increasing the resistivity well above its classical value.

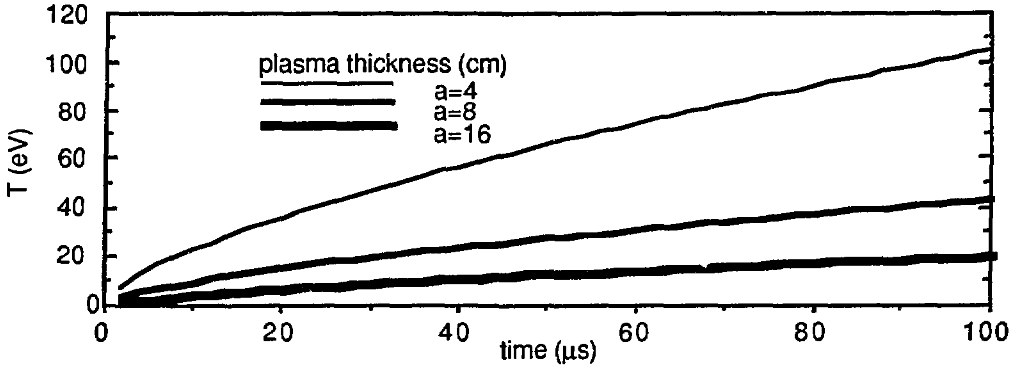

Figure 3. Plasma temperature for ohmic heating with no losses versus time for various plasma thicknesses.

Although very simple models have been used the results presented above give some indications as to the requirements to increase the plasma temperature above the radiation barriers.

- In order for radiation losses not to dominate, $f^{1/2}B_0a^*$ must be small.
- Even if radiation is negligible, a^* must be small for ohmic heating to quickly raise T_e unless anomalous processes become important.

IV. CONCLUSIONS/PLANS

The CSS-P in tearing formation mode has produced field reversed plasmas with flux and/or energy loss times considerably longer than past configurations. Since a thin plasma is possible in the tearing mode but not with the programmed formation mode with an axial equilibrium, this is consistent with both expected increased ohmic heating and reduced radiation losses. Because of the long times predicted for ohmic heating, radiation dominance may not be needed to explain past CSS results. However the presence of MHD activity and associated flux loss at higher charging voltages and thus applied fields may indicate a threshold for radiation dominance.

Future plans for the CSS include:

- Continued modeling including time dependant radiation.
- Improved PI to allow formation at reduced fill pressure. This should facilitate programmed formation and result in a thinner plasma in the tearing mode.
- Evaluation of modifications to the parallel mode (e.g. cusps) which will allow a thin plasma until the radiation barrier is exceeded at which time axial equilibrium could be established.
- Consideration of a longer rise time or staged bank to allow temperatures to rise above the regime dominated by radiation before imposing high magnetic fields.
- Reinstallation of the crowbar and mirrors (or trigger coils) to force reconnection and form an axial equilibrium after the temperature has risen.
- Use of bolometry and possibly impurity doping to assess the conditions where radiation dominates the plasma.

1. Z. A. Pietrzyk, et al, Nuclear Fusion, **27**, No. 9, 1478(1988).
2. L. C. Steinhauer, Proceedings of the Ninth U. S. Compact Toroid Symposium, Union Washington, 146(1989).
3. J. W. Shearer, Phys. Fluids **19**, 1426(1976).
4. E. K. Maschke, Plasma Phys. **15**, 535(1973).
5. F. Herrnegger, Proceedings of V European Conference on Controlled Fusion and Plasma Physics, Grenoble, 1972, Vol I p.26.
6. D. E. Post, et al, Atomic Data and Nuclear Data Tables, **20**, 397(1977).

TSX - A POTENTIAL EXPERIMENT ON TILT-STABILIZATION OF FRX-RINGS USING LARGE-ORBIT ION RINGS

(SYSTEMS ANALYSIS)

H.H. Fleischmann, W. Podulka and S. Jones

MICE-Group, Applied and Engineering Physics
Cornell University, Ithaca, NY 14853

Based on the good stability characteristics of large-orbit rings observed in various electron ring experiments[1,2], one of us several years ago proposed[3] to use high energy large-orbit ion rings for stabilizing - if needed - compact toroid rings against tilt motion. In view of the closely approaching capability to generate potentially unstable large-s FRX rings in the new LSM and LSX devices, this paper presents a systems-type analysis of potential experiments for testing this idea, including a review of various aspects important for the selection and design of such an experiment, a critical discussion of relevant recent results from IREX and the present status of the new MICE device.

Fig. 1 shows the basic arrangement envisioned for FRX stabilization with a ring of axis-encircling, high-energy ions embedded within or possibly also reaching partially outside the actual FRX ring. Unfortunately, presently existing theoretical treatments[4-6] or experiments[7] do not permit definitive conclusions regarding the required optimal current, energy and angular spread of the ion ring. Various, rather coarse model calculations[4-6] estimate that ion ring currents equal to about 10-50% of the total ring current may be sufficient for stabilization. Conceptually, one might expect that an ion ring be optimal when covering regions near the separatrix, both inside and outside the FRX: the proximity of the (parallel) diamagnetic plasma currents and the ion currents can provide for the stabilization of the plasma while the direct coupling to the outer filled lines might help to anker the ion ring itself, i.e., prevent a simultaneous tilt of plasma and ion ring together. No predictions exist concerning the best angular spread of the ions.

In view of this uncertainty regarding the required/optimal fast-ion parameters we will use in our analysis the following assumptions as "standard":

(i) Fast-Ion Energy:

$$E_f = (1/2)\, m v^2_f \text{ with } R_{Larmor,\, f} = (eB_{wall}/mv_f) = R_{separatrix}$$

(ii) Fast-Ion Current in Ring:

$$\varepsilon_f = I_f/I_{tot} = 30\%$$

(iii) Angular Distribution:

$$<\theta> = 30\text{-}50^\circ \text{ i.e. } <v_{\theta,f}>/v_f = .8$$

Concerning the selection of the FRX device to be used for a tilt-stabilization experiment (TSX), the following requirements apply:

(i) The FRX rings by themselves clearly have to be tilt unstable in order to demonstrate stabilization by the fast ions; in particular, it would be very useful if the FRX rings would show a clear stability threshold either in parameter space or - even better - in time (being initially stable and then becoming unstable).

(ii) The slowdown time τ_f of the fast ions by electron drag has to be sizably longer than the axial Alfvén time $\tau_{A,L}$ of the plasma, i.e.

$$\tau_f = E_f/(dE_f/dt) > 10L/v_A = 10\tau_{A,L}$$

Condition (i) clearly excludes smaller FRX devices like FRX-A and FRX-B and FRX-C. Following the recent indications[8] of some tilt motions, certain LSM (source) rings may be sufficient; beyond that, we have to look for LSX and/or LSM-compr. as basis for TSX studies. Similarly, all analyses[9] of (ii) show the smaller FRX rings to be insufficient and the LSM(source) rings being somewhat borderline, but LSM-comp. and LSX being well suitable.

The approximate plasma and ring parameters relevant to the latter three devices are summarized in Table I assuming the use of protons as fast ions. In this, τ_L denotes the longitudinal bounce time of the trapped protons, Q_p the total amount of trapped protons (in mAsec), E_t the total energy, in kJ, of the fast protons trapped in the ring, E_{source} the total fast-pulse energy in the diode (assuming a proton generation efficiency somewhat optimistic of 1/3 and a proton trapping efficiency of 1/2).

TABLE I Parameters of Potential TSX Experiments

	LSM (source)	LSM (compr.)	LSX
B_W (kG)	4.1	19	7.5
R_S (cm)	15	8.5	25
L (cm)	200	100	200
n (cm^{-3})	8 (14)	7 (15)	2 (15)
T_e (eV)	150	600	300
T_i (eV)	400	800	400
v_A (cm/sec)	3.2 (7)	5 (7)	3.7 (7)
$\tau_{A,L}$ (μs)(long.)	6	2	5.4
$\tau_{A,r}$ (μs)(radial)	.45	.17	.68
E_p (MeV)	.19	1.3	1.7
v_p (cm/sec)	.6 (9)	1.6 (9)	1.8 (9)
$\tau_L = L\sqrt{2}/v_p$ (μs)	.45	.09	.16
Q_p (mAsec) (trapped)	30	15	33
τ_f (μs)	59	80	260
E_f (kJ)	5.7	20	56
E_{source} (kJ) ($\eta_{tot} = 1/6$)	34	120	340

The latter numbers can be compared with presently available pulse drivers: "Longshot" (about 100 kV, 1-2 kJ), IREX (600 (?) kV, about 15 kJ) and MICE (1MV, about 80 kJ), with the latter being easily expandable by about a factor of 2-3). Of these, MICE clearly is sufficient for performing physics and development studies close to the parameter range needed for TSX although it may still be somewhat marginal for a full-scale TSX or LSX.

Assuming that the fast protons are injected axially through a cusp arrangement (e.g. as in MICE) and making the assumptions, $R_{diode} = R_{separ.}$, $(\Delta R/R)_{source} = 0.2$, pulse time $\tau_p = 100$ nsec, ion trapping efficiency $\eta_{tr} = 50\%$, we obtain ion current densities in the diode of about 3 kA/cm^2 for LSM (comp) and 1 kA/cm^2 for LSX, respectively. These numbers are somewhat high in comparison with densities available in present magnetically insulated ring diodes (300 A/cm^2)

but comparable with those in reflex diodes [10], however, these requirements can be sufficiently relaxed by increasing the pulse length τ_p (to about 2-300 nsec) and/or the diode radius (to about $2xR_{separ}$), with both of these increases also being helpful otherwise. Similarly, the beam generated toroidal magnetic field B_{tor} (along the ring plane) within the diode (i.e. generated by axial proton current plus electron leakage current) would be larger than the axial field B_w for τ_p = 100 nsec and $R_d = R_{sep}$, but again could be relaxed to a manageable level $B_{tor}/B_w \approx .1$-.2 by the mentioned increases in τ_p and R_{diode}, in particular in the ion drift region (protons only). Thus, the source requirements certainly are within obtainable limits even for somewhat reduced trapping efficiencies, although certainly not down to the levels, $\eta_{tr} = .05$, observed in our electron ring experiments.[1,2] For LSM (source), a standard current density of about 2 kA/cm^2 would be needed, which appears hard to obtain at the low voltages of only 100-200 kV; clearly, a very sizable increase in pulse time and/or diode radius will be needed in this case. Recent single-particle orbit calculations (see below) indicate that angular spreads of the ion beam in the diode equal to a few degrees; i.e. comparable to already observed spreads, are permissible

Regarding the choice of injection strategy, tangential neutral-atom injection will require neutral-atom beams of about 250A, 400A, 1 kA (equivalent) for LSX, LSM (comp), and LSM (source), respectively, when considering maximum pulse times $\tau_p = (1/2)\, t_f$. Such beams clearly are beyond reach (at least economically) for the expected MeV-type beams of LSM (comp) and LSX. A more detailed analysis may be needed for LSX (source)[11].

For cusp-type injection into LSX or LSM (comp), we consider the two extreme cases of either direct beam injection into the FRX ring or the formation of an intermediate stationary ion ring with a subsequently slow (Alfvén velocity) merging of this ring with the FRX. Considering direct injection first, the beam will create Alfvén waves in the FRX, but due to $v_p \gg v_A$ the fast ions, to first order, still will move in an essentially constant magnetic field. This can be seen in Table I where the fast-ion bounce times t_L are sizably shorter than the radial Alfvén times $\tau_{A,r}$, for LSX and LSM (comp). For this reason, we calculated an extensive number of injection orbits for test particles having only a small axial energy (at most few percent of E_p) before encountering the FRX field (The latter configuration was taken from LANL equilibrium calculations[12]). Results (see Fig. 2) indicate that the injected protons generally will bounce only once or twice before reemerging from the FRX; up to 20 bounces have been found - however, only for very narrowly defined conditions. Collisional drag of the fast protons will help in principle, but actually will be too small to seriously contribute. Any trapped ions will have very large axial velocities $v_z \approx v_p$.

Additional calculations including time-dependent fields modeling the generated Alfvén waves are in progress; also, some MHD calculation of actual beam injection may be performed. Unless these calculations show a strongly improved trapping it appears that direct injection may not be very useful. Instead, we expect that ion ring merging will have to be used. In this case, the effective potential confining the fast protons in the ring and the potential barrier between the ring and the FRX will move and change only on the rather slow Alfvén time scale with the trapped ions pouring into the FRX and remaining trapped (see Fig. 3). We expect that the fast ions finally trapped in the FRX will have sizable axial velocities even in this case.

As additional results, our orbit calculations showed that (i) trapped particle orbits in the FRX generally exhibit pronounced non-ergodic behavior (see i.e. Fig. 4 where orbits are confined to only a part of the related H, P - permissible space in (r,z)) and (ii) collisional drag of the fast ions will lead to a deeper trapping rather than untrapping of the orbits (see Fig. 5)

Additional calculations on the influence of the angular spread of the ion beam in the diode indicate the need of spreads as low as a few degrees.

Discussion of Recent Experiments

(i) IREX: Recently, the achievement of trapped rings with $\delta B/B_0 = 10\%$ was claimed[13]. Unfortunately, this claim appears - at best - badly uncertain. The only proof offered in this talk even under questioning was a single Faraday cup trace showing a fast-ion current density of 60A/cm ^{2} (with all other traces shown being in the range of 10-30A/cm ^{2}). Even taking the "extreme" value[14] of 8 cm for the radial thickness of current layer (instead of the 5cm used in Pedrow original thesis [15] and in other papers of that group), and assuming this current density to be uniform (in spite of its apparently very unusually high value), we obtain a field change of 600 G across the layer corresponding to a beam generated field of about 450G on axis when considering flux conservation within the tank (This latter effect also was not included in the calculated line of Fig. 11 in Ref. 14, i.e. there is a sizable systematic deviation between the "theoretical" calibration and the experiments.), i.e., somewhat more than 5% of the applied 8kG; more realistic appears about +4%. However, we should add that one of us (HHF) was informed more recently[16] that some Faraday cup recordings with larger (first with j=100 A/cm^2 and then j=150A/cm^2)"were just discovered after the meeting talk amongst the earlier recorded results" of the experiment that had been stopped about a year earlier. Obviously, the reliability of this late discovery following the above objections is hard to estimate.

(ii) MICE Experiments: The conversion of the old RECE-Christa pulse driver to the new MICE driver (1 MV, 2 Ohm, 200 nsec, positive) was recently completed. As indicated in Fig. 6, the next water pulse line contains two 2 Ohm, 200 nsec transmission lines connected with a SF_6 switch. For detail parameters see Table II. Due to the unnecessarily large sizes of both the Marx tank and the water tank, the present field stresses only amount to about 65% of the usual Martin limits, and the overall energy level of the driver could be expanded quite easily by a factor 2-3 with the addition of a stronger Marx generator.

The new pulse driver so far has been tested up to actual diode voltages of 800 kV. No breakdown was observed in spite of a presently still missing guard ring. Voltage rise times are about 40-50 nsec. Using a normal magnetically insulated ring diode with flashboard anode, current densities of up to about 200 A/cm^2 were observed with Faraday cups. Some discrepancies, however, presently still exist with the somewhat smaller proton outputs measures with carbon activation. Corresponding investigations are in progress. The MICE tank had been very successfully tested to full specifications earlier.

Using the described ion beam, first fast-pulse injection experiments into the MICE tank were performed, mostly using hydrogen gas fills of 50-150mTorr. Observed transient beam-generated field changes range up to 6% of the applied magnetic field. The beam behavior appears to show some deviations from extensive single-particle orbital calculations performed over the last few months. Related investigations are in progress.

References:

1. e.g. D. A. Phelps et al., Phys. Fluids 17, 2226 (1975).
2. e.g. H. A. Davis et al., Phys. Letters 37, 542 (1976).
3. H. H. Fleischmann, US-Japan Joint Symposium on Compact Toruses, Princeton Dec. 1079, p. 41 and 3rd Symp. on Physics and Technol. of Compact Toroids, Los Alamos, Dec. 1980 p. 31.
4. R. N. Sudan and P. Kaw, Phys. Rev. Lett. 47, 575 (1981) corrected in C. Litwin et al., Phys. Fluids 27, 2791 (1984).
5. Y. Nomura, J. Phys. Soc. Jap.. 54, 1369 (1985).
6. C. Mehanian and R. V. Lovelace, Phys. Fluids 31, 1681 (1988).
7. R. Jayakumar et al., IEEE Trans. PS-117, p. 41 (1989).
8. N. Tuszewski, private communication, and APS-DPP Mettg. Anaheim, Dec. 89.
9. e.g. K. F. McKenna et al., LANL intern. report, 1987.
10. J. Golden et al., NRL report.
11. D. J. Rej, private communication.
12. R. Webster, private communication.
13. D. A. Hammer, 13th Annual APS-DPP Mtg. 10/31-11/4/88 Bull. APS 33, Oct. 88, p. 2041 Talk 7I6.
14. P. D. Pedrow et al., Phys. Fluild B1, 1059 (1989).
15. P. D. Pedrow, Ph.D Thesis, Cornell University.
16. D. A. Hammer, private communication about Nov. 20, 1988.

MICE PULSELINE

MECHANICAL	
· OUTER DIAMETER	2.57m
INNER DIAMETER	1.91m
· PULSELINE LENGTH	3.0m
· TRANSITION SECTION LENGTH	3.0m
MATERIAL:	Stainless Steel surfaces with Aluminum skeleton
· 12 kgallons high purity water	
ELECTRICAL	
· PULSETIME	180 nsec
· IMPEDENCE	2.0 ohms
· MARX	2 parallel halves of 29 .68 uf capacitors each
· PULSELINE CHARGING VOLTAGE	2 MV
· NOMINAL FIELD STRENGTH	71 kV/cm (=65% Charlie Martin)
· MARX CHARGE	105 mC
· PULSELINE CHARGE	90 mC
· SF_6 SWITCH (From HYDRA; courtesy of Sandia)	

Table II. MICE Pulseline Parameters

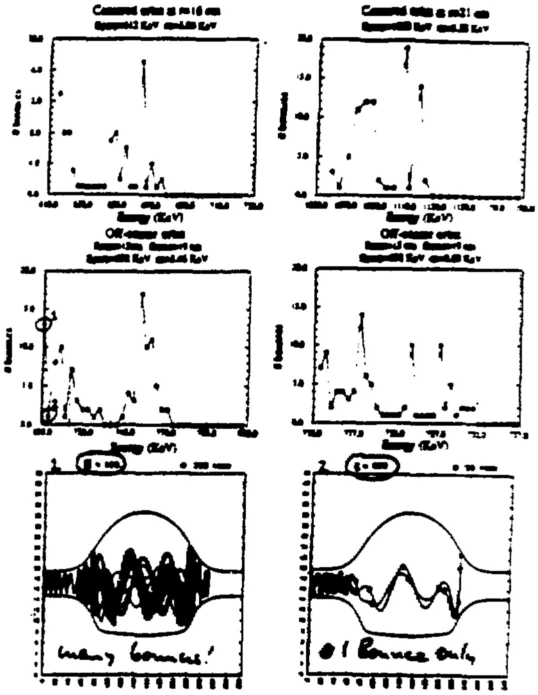

Result: Number of bounces before re-escape very sensitively dependent on conditions

Fig. 2 Trapping of ions in static FRX rings

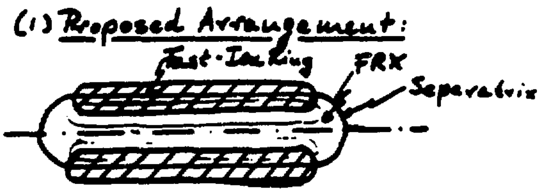

H. Fleischmann, 2nd CT-Symposium, Princeton, 197?

Fig. 1 Basic Configuration

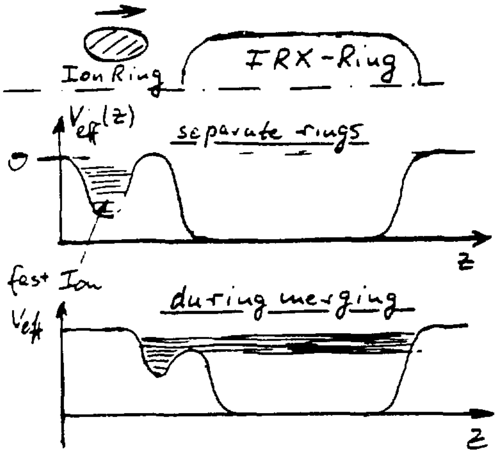

Fig. 3 Development of effective potential and ion filling during merging

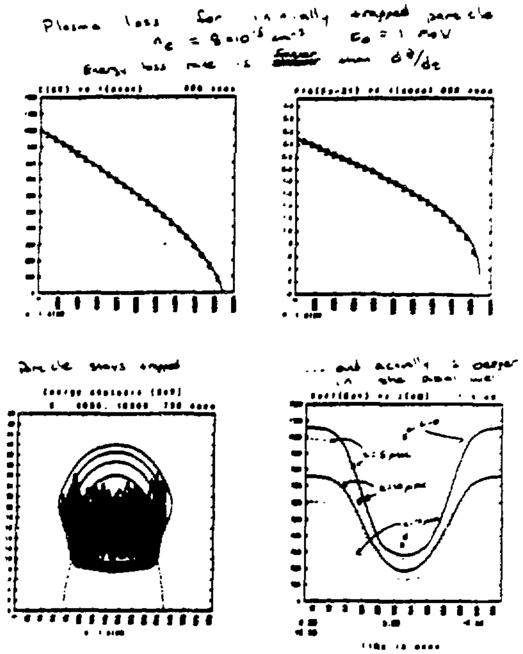

Fig. 5 Untrapping (?) by collisional drag

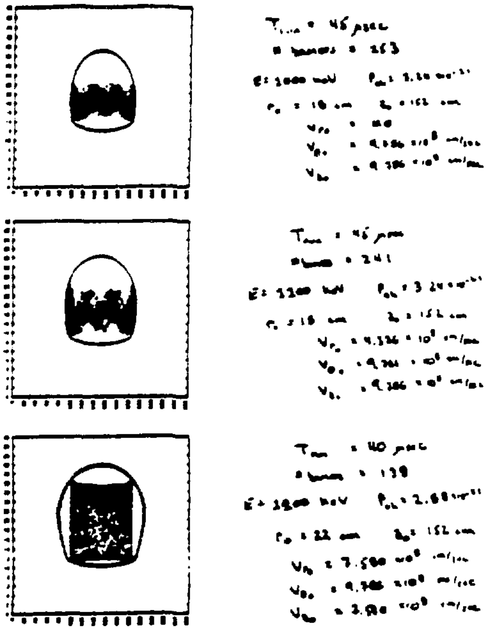

Result: most orbits are non-ergodic

Fig. 4 Ergodicity (?) of trapped ion orbits

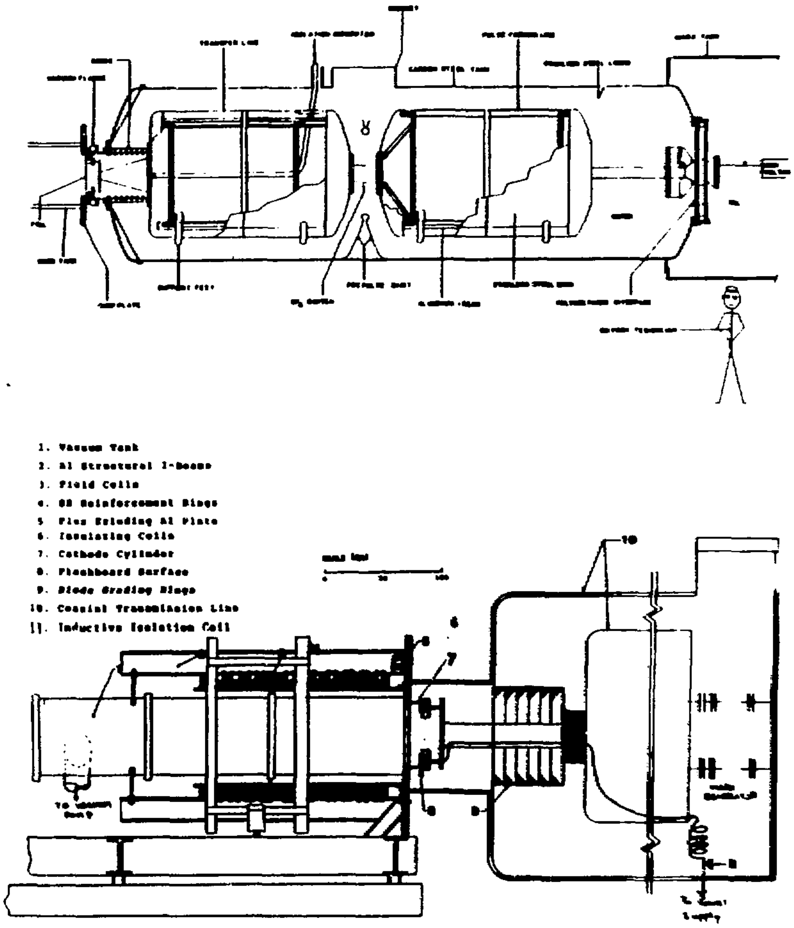

Fig. 6 MICE pulseline and confinement tank

A 0.1 TW Gas-Breakdown Plasma-Anode Ion Diode.*

J. B. Greenly, A. Dunning, and G. D. Rondeau

Laboratory of Plasma Studies, Cornell University

Ithaca, N.Y. 14853

A magnetically-insulated extraction-geometry ion diode using inductive breakdown of a gas layer to produce a magnetically-confined anode plasma has been successfully operated[1] on the LONGSHOT pulser: 120kV, 30kA, $\lesssim\mu s$. This LONGSHOT diode doubled the total ion output compared to a standard dielectric anode, allowed constant impedance for >500ns, and improved upon all other characteristics except beam divergence. The plasma anode has now been integrated into a similar diode to operate on the Neptune pulser: 700kV, 3Ω, 100ns, >0.1 TW. The goal is to investigate the scaling of this diode to the higher voltage, and to current density above 0.5 kA/cm^2. The major scaling issue is whether good control can be maintained of the anode surface shape and position, and the resulting ion canonical momentum and divergence. The beam from this diode will be used to form diamagnetic ion rings, and will allow good diagnosis of beam quality. First experimental results will be presented.

---

* Work supported by DOE Contract DE-FG02-87ER53246.

[1] J.B. Greenly, M. Ueda, G.D. Rondeau, and D.A. Hammer, J. Appl. Phys. 63, 1872 (1988).

PROGRESS WITH ENERGY CONFINEMENT TIME IN THE CTX SPHEROMAK

T. R. Jarboe, J. C. Fernández, F. J. Wysocki, C. W. Barnes
I. Henins, S. O. Knox, G. J. Marklin

Los Alamos National Laboratory, Los Alamos, NM 87545, USA

The 0.67 m radius mesh flux conserver (MFC) in CTX was replaced by a solid flux conserver (SFC), resulting in greatly reduced field errors. Decreased spheromak open flux led to vastly improved decaying discharged, including increased global energy confinement times, τ_E (from 20 to 180 μs), and corresponding magnetic energy decay times, τ_{B^2} (from 0.7 to 2 ms). Improved confinement allowed the observation of the pressure-driven instability (predicted by Mercier) which ejects plasma from the spheromak interior to the wall.[1]

In the CTX 0.67 m radius mesh flux conserver (MFC), ≈1/4 of the spheromak poloidal flux forms the "edge" with open flux intersecting the FC wall. Figure 1 shows one half of a cross section of the MFC, along with the poloidal flux contours for a typical decaying CTX spheromak. $\ell_{eff} \approx 3\,m$ represents the effective length between the effective points where the (poloidal) open field lines intersect the wall.[2] The effective poloidal electric field $E_{eff} = \eta j_{\parallel}$ at the edge is also illustrated. Consistent with the Taylor minimum energy principle relaxation tends to drive current to maintain a uniform j/B. Plasma on the open field lines tends to be cooled and lost rapidly leading to large E_{eff} in this (low j/B) region giving a large helicity dissipation rate $2E_{eff}B$ per unit volume. We found, in the mesh flux conserver, that the lowest E_{eff} can be obtained by maintaining a neutral fill in the edge. The relaxation must now drive a current in the neutral dominated edge and ionization processes must replace carriers as fast as they are lost. Thus the conditions in the edge are similar to Paschen breakdown conditions. $E_{eff}\ell_{eff}$ *versus* the neutral H_2 pressure in the edge agrees with the Paschen voltage[3] for breakdown of neutral hydrogen.[2]

Throughout the plasma, nj is negligible compared to E_{eff} at the edge, so that $dK/dt \approx -2E_{eff}\int_{edge} B\,dvol$. The result is spheromak magnetic-energy decay times τ_{B^2} which are uncorrelated with the electron temperature, but which are correlated with the edge neutral pressure.[2] This model is also consistent with the results in the HBTX1B reversed-field pinch discharges with limiters.[4]

Also, as in HBTX1B, strong relaxation activity needed for edge current-drive seems to heat ions.[2,6] Figure 2 shows selected times for discharge 15805, one of the nearly identical 47 discharges previously studied.[2] The maximum reproducible Thomson scattering T_e ever achieved in the MFC is ≈100 eV. The top curve shows the spheromak toroidal current. The second curve shows the line brightness of the impurity line used, OV at 2781 Å. The third curve is the Doppler broadening temperature T_D. Since the calculated ion equilibration time is much shorter than τ_p and similar to the plasma energy confinement time, τ_E, T_D should reflect the bulk ion temperature, T_i. These high T_D indicating an anomalously high T_i have also been observed in reversed field pinches.[5,6] The oscillations in T_D (Fig. 2) are correlated with the saturated, rotating current driven kink modes (see bottom of Fig. 2). During sustainment the $n = 1$ link is observed while during decay the $n = 2, 3$ are seen.[7]

If the rotation is interperted as being caused by the ion diamagnetic drift then the value of T_i needed for the observed rotation speed is equal to T_D. This correlation further indicates that T_D represents T_i. T_D oscillations are most probably due to the mode exposing the spatial profile of T_i, which we cannot resolve with our single-chord instrument. Accounting for $T_D \gg T_e$, the previously presented[2] energy confinement times $\tau_E \equiv 3/2\langle\beta\rangle_{vol}\tau_{B^2}$ in the MFC should be corrected up to the 50 μs range, and $\langle\beta\rangle_{vol}$ up to $\approx$5%. Still, large charge exchange losses and enhanced transport from excessive relaxation activity almost surely degrade confinement significantly.

A 0.60 m radius solid flux conserver (SFC) has been designed to decrease the relative fraction of open spheromak magnetic flux much below the value in the MFC. Ti gettering of the SFC walls was necessary for density and impurity control. In the SFC, as in the MFC, the spheromak equilibrium is deduced from magnetic field measurements at the FC surface, coupled with a Grad-Shafranov MHD equilibrium solver.[7] The n_e and T_e are diagnosed by an absolutely calibrated multi-point Thomson scattering system. T_e and n_e are combined with the MHD equilibrium calculations to determine the electron β_e and pressure p_e. The result is an accurate calculation of τ_E.

τ_{B^2} in the SFC scales proportionally with T_e at the magnetic axis. See Figure 3. With reproducible $T_e \approx 150 eV$, maximum τ_{B^2} is 2 ms. In the SFC the OV T_D is similar to T_e, and maximum global τ_E = 180 μs (using $T_i = T_e$). Figure 4 shows the increase in τ_E for similar discharges over time as the decaying spheromak plasma heats up. In this figure, only τ_E values measured before the pressure-driven instability (discussed below) are included. These SFC results suggest reduced open magnetic flux resulting in less relaxation activity, which reduces direct ion heating and increases plasma confinement, as also reported for HBTX1B.[8] Because of the superior diagnostics on CTX (due in part to better access of the spheromak) it is not necessary to make "top hat" or "local confinement" assumptions. However, for comparison with RFPs the "local" or "top hat" confinement time is 1.5 ms for the best discharges which is better than obtained in RFPs.

In the SFC, a pressure-driven instability ejects the spheromak plasma in a distinct event.[1] As the maximum electron pressure gradient, ∇p_e, increases, $\langle\beta\rangle_{vol}$ remains at $\approx$3-6% (using $T_i = T_e$). At a threshold ∇p_e, p_e moves toward the outer flux surfaces within 10-20 μs, indicating a flux interchange. No concurrent signature on the magnetic probes at the wall is observed, as normally occurs with current-driven instabilities. Thus, the confinement now appears to be limited by the expected pressure driven mode. The SFC geometry has a Mercier limit of 0.5% for the Taylor state. The spheromak is shear stabilized with q at the wall smaller than q at the magnetic axis. By shortening the flux conserver on the geometric axis the q at the wall can be lowered, increasing the shear. Figure 5 shows a flux conserver shape that has a Mercier volume averaged β-limit of $\sim$5%. It is not clear how much the confinement might be improved due to increasing the Mercier β-limit by a factor of 10. However, even if the β and temperature only increased a factor of two, with classical scaling, the maximum energy confinement time would reach 1.0 ms.

Although the magnetic structure looks more like a standard toroidal confinement geometry, the topology is still simply connected giving it all of the advantages of the stationary spheromak reactor.[8]

REFERENCES

1. F. J. Wysocki, J. C. Fernández, I. Henins, T. R., Jarboe and G. J. Marklin, "Evidence for a Pressure-Driven Instability in the CTX Spheromak," *Physical Review Letters* **61** (1988), 2457.

2. J. C. Fernández, C. W. Barnes, T. R. Jarboe, I. Henins, H. W. Hoida, P. Klingner, S. O. Knox, G. J. Marklin, and B. L. Wright, "Energy Confinement Studies in Spheromaks with Mesh Flux Conservers," *Nuclear Fusion* 28, 9 (1988), 1555.

3. A. Von Engel, "Ionized Gases," Oxford University Press, Oxford, 1955, page 172.

4. T. R. Jarboe and B. Alper, "A Model for the Loop Voltage of Reversed Field Pinches," *Physics of Fluids* 30 (1987) 1177.

5. G. A. Wurden, et al., *Nuclear Fusion* 27 (1987) 857.

6. B. Alper, et al., in *Plasma Physics and Controlled Nuclear Fusion Research* (1986) pp. 399-411, Vienna (1987), IAEA II Kyoto Conference, (1986).

7. S. O. Knox, C. W. Barnes, G. J. Marklin, T. R. Jarboe, I. Henins, H. W. Hoida, and B. L. Wright, "Observations of Spheromak Equilibria Which Differ from the Minimum Energy State and Have Internal Kink Distortions," *Physical Review Letters* **56** (1985) 842.

8. R. L. Hagenson and R. A. Krakowski, "Steady-State Spheromak Reactor Studies," *Nuclear Technology* 8 (1985) 1606.

LIST OF FIGURES

1. One half of the MFC cross-section is shown. Typical normalized spheromak poloidal flux contours (5% increments) during decay are included. The poloidal magnetic field wraps around the magnetic axis in the counter-clockwise direction, while the toroidal field goes into the page.

2. Traces *versus* time for typical MFC discharge 15805: The top figure shows the spheromak toroidal current, increased by helicity injection until 1.2 ms, when the source is turned off (arrow in the bottom figure). The middle figure shows the "brightness" *br*, defined as the area under the gaussian fit. The bottom figure shows the Doppler temperature T_D. Error bars at regular intervals illustrate the uncertainty resulting from the fit.

3. Magnetic energy decay time as a function of Te at the magnetic axis.

4. τ_E from similar spheromak discharges in the solid flux conserver are plotted *versus* time. The helicity source is turned off at 700 μs.

5. Flux conserver shape for a spheromak with Mercier-beta limit $\simeq$5%.

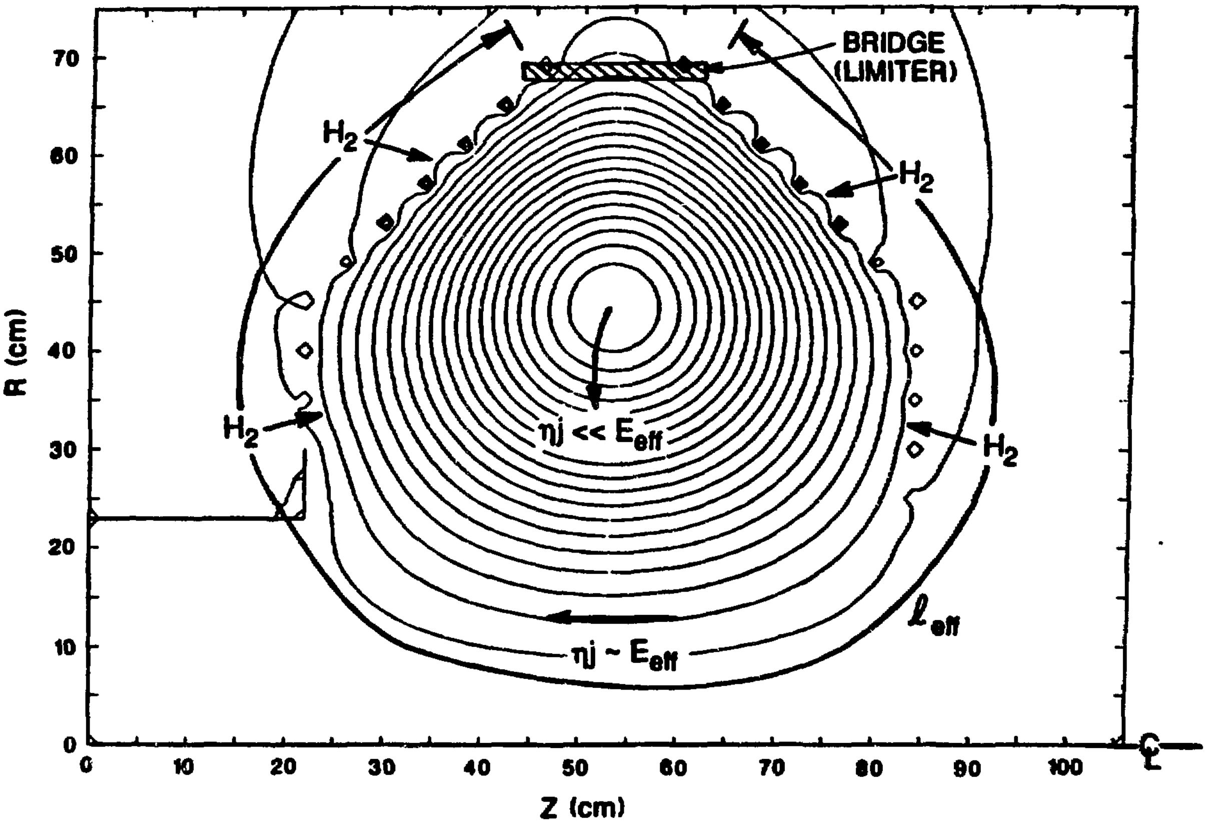

Figure 1

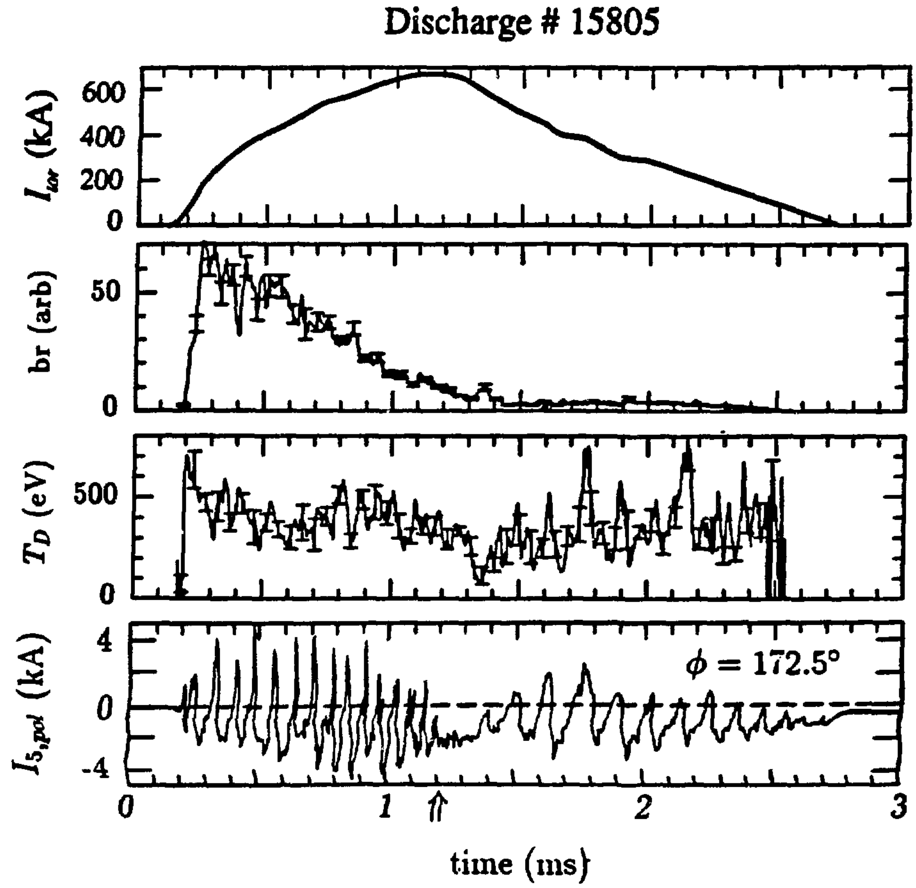

Figure 2

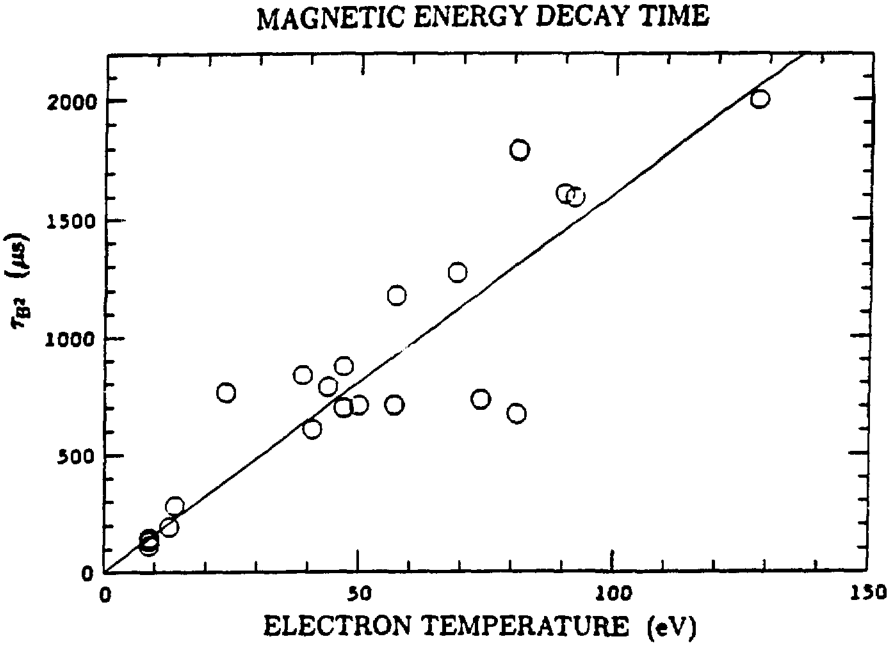

Figure 3

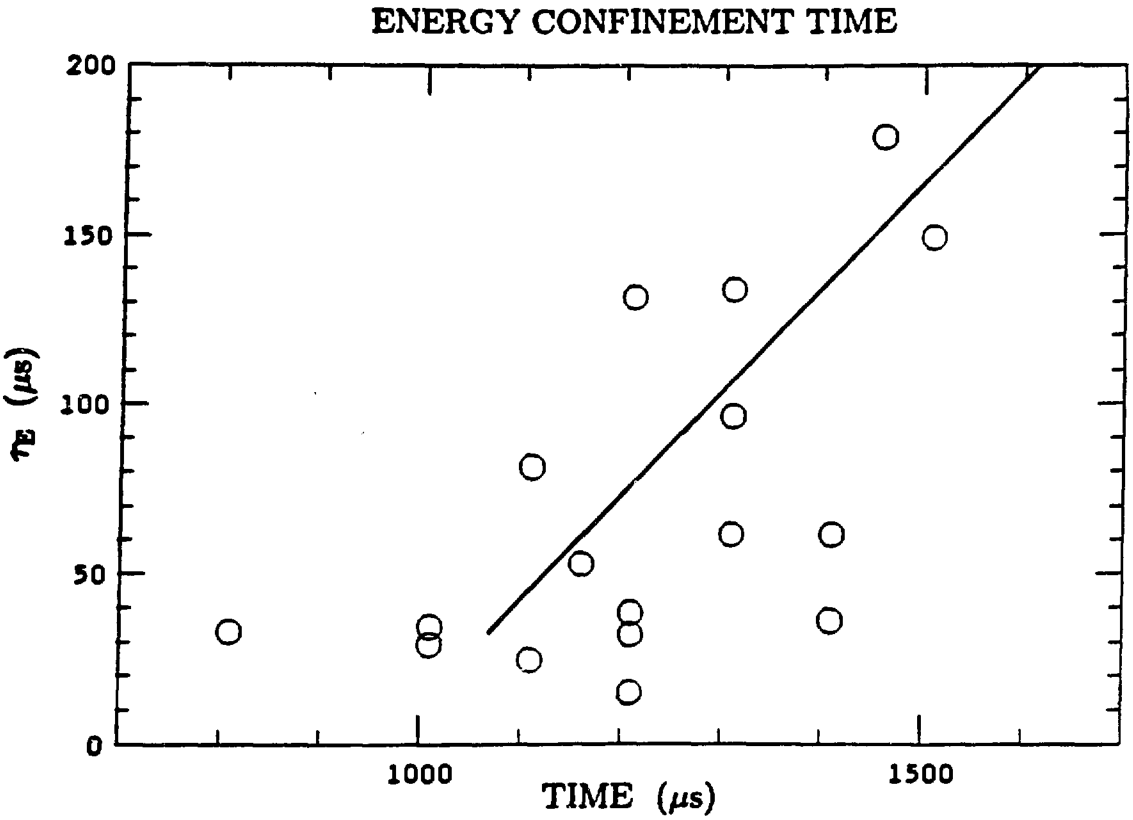

Figure 4

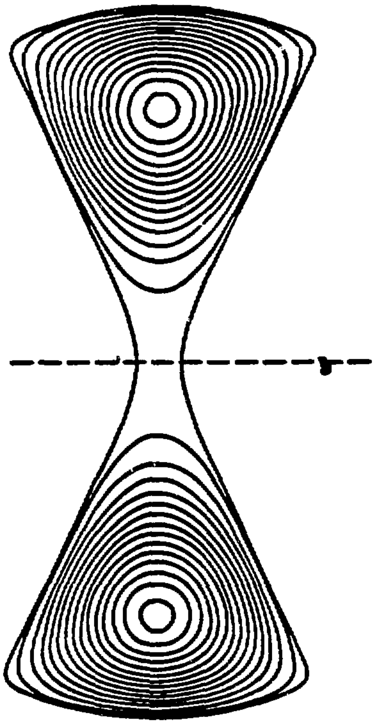

Figure 5

Experimental and theoretical studies on the magnetic configuration of bumpy-z-pinch/flux-core-spheromak.

M.Katsurai, N.Amemiya, A.Hayakawa.

Department of Electrical Engineering, University of Tokyo
Bunkyo-ku, Tokyo 113, JAPAN

I. Introduction

The University of Tokyo spheromak machine, TS-3 [1], was modified and upgraded by the installation of a pair of magnetized coaxial plasma guns on each axial end of the machine. The outer electrodes of the guns have been used for generating an axial discharge along the major axis of the machine. This modification has enabled us to perform experimental studies on the formation and sustainment of bumpy-z-pinch configurations[2] / flux-core-spheromak configurations [3] (in the following description, we call them FCS). On the last workshop(the 10th), we reported successful production of FCSs either by the successive operation of a conventional Z-theta-discharge of TS-3 and an axial discharge between the outer electrodes of the coaxial guns, or by the single operation of the axial discharge in an external field with an appropriate configuration. On the basis of these results, we have extended magnetic measurements of the FCSs in TS-3.

II. Appatarus

Fig.1 shows the modified TS-3 machine with a pair of magnetized coaxial plasma guns on its both axial ends. In the following experiments, single axial discharge between the outer electrodes of the coaxial plasma guns has been used to produce the plasmas. The current waveform for the axial discharge is shown in Fig.2. with a maximum peak value of about 50 kA and a half period of about 160 μs. The dotted curve in the figure is the waveform of the optional current supplied to the internal poloidal coils for compressing the produced plasmas in the center region. One of the most powerful tools for our measurements is a two-dimensional magnetic probe array with 30(5x6) mesh points. This array covers a toroidal plane (normal to the magnetic axis) of the FCSs produced, and gives us the time variation of axial components of the poloidal field. On the assumption of axisymmetry for the produced configuration, we can reproduce the time dependent poloidal flux plot of the configuration. We also has used a cicular toroidal probe arrays with eight points to measure the toroidal mode activities during the formation, sustainment, and termination phases of the FCS.

III. Experimental results

Fig.3 (a) and (b) show exsamples of the poloidal flux plots demonstrating successful productions of FCS during 90 and 140 μs. The figures (a) and (b) are cases without and with the application of the optional compression current, the dotted curve in Fig.2, to the internal poloidal coils, respectively. The application of the compression cuurent enhances the merging speed of two FCSs initially produced at both ends and increases the lifetime of single FCS in the center region. It should be noted that the flux plots in other time periods, namely, in the production and termination phases, loose such physical meaning as poloidal flux surfaces because the plasma configuration has non-axisymmetric motions during these periods. The eight points toroidal probe array has been used to measure the modal behavior of the motions. An example of the measurements is shown in Fig.4. The activities are found to be very strong during the production and termination phases, while it is strongly supressed during the mid phase where a single FCS configuration is foud to be sustained. It has been found that the FCS configuration observed in our experiments is a class of FCS with a pair of X points on the separatrix. Fig.5 shows the operation region for the production of FCS in the Iex vs. Fgun diagram, where Iex is the current in the external field coils, and Fgun is the amount of magnetic flux produced by the bias field coils of the magnetized coaxial plasma guns.

IV. Equilibrium analysis

The experimentally observed configurations are compared to that obtained by theoretical analyses. The Grad-Shafranov equation for the zero-beta Taylor state is analytically solved in a finite length cylindrical vessel as shown in Fig.6. For the boundary condition, we assume the presence of a certain amount of external fluxes that axially penetrate the vessel through holes on the end plates. This solution is an extension of Turner`s solution where the holes are assumed to be infinitesimally small[4]. The solution has been used to survey the q profile and the magnetic hill/well profile of the FCS configuration. Fig.7 shows a diagram presenting a classification of FCS in terms of the appearace and location of X points on the separatrix. Unlike the conventional spheromak configuration with a magnetic hill and a radially decreasing q profile, FCS can be provided with a magnetic well or with a radially increasing q profile like ULQ and tokamak as shown in Fig.8 (a) and (b), respectively.

$$\psi=\rho\frac{J_1(x\rho)}{J_1(x)}-2\sum_{j=1}^{\infty}\left\{\frac{J_1(\lambda_j\rho)}{J_0(\lambda_j)}\cdot\frac{\cos(\chi_j\zeta)}{\cos\left(\frac{\chi_j}{2}\right)}\times\left[\frac{8}{\lambda_j^{2}}\left(\frac{a}{b}\right)^2\frac{J_0(\lambda_j\frac{b}{a})}{J_0(\lambda_j)}-\frac{16}{\lambda_j^{3}}\left(\frac{a}{b}\right)^3\frac{J_1(\lambda_j\frac{b}{a})}{J_0(\lambda_j)}+\frac{1}{1-\left(\frac{\lambda_j}{x}\right)^2}\right]\right\}$$

ρ ; normalized radial position ($\rho\equiv r/a$),

ζ ; normalized axial position ($\zeta\equiv Z/L$),

a ; radius of boundary cylinder,

L ; axial length of boundary cylinder,

X ; eigenvalue of force-free equation ($X\equiv ka$),

λ_j zero of J_1,

$\chi_j\equiv\sqrt{K^2-\lambda_j^2}\cdot\left(\frac{L}{a}\right)$.

<u>Helicity extraction</u>: It is expected that, when FCS plasmas are subjected to certain current driving forces which bring them to a nonequilibrium state, they will be given some relaxation mechanisms which make them stay in an euilibium Taylor state. Future FCS plasmas in a fusion reaction regime may have various such current driving forces as the boot-strap current driving force and the alpha-particle current driving force. These forces generate internal helicity. Therefore, if internally generated hilicity can be extracted by virtue of the relaxation mechanisms through the center electrodes of FCS, FCS may be worked as a direct current generator.

References

[1] M.Katsurai, N.Amemiya, et al.: Proceedings of the 8th, the 9th, and the 10th US-Japan Workshops on Compact Toroids.
[2] T.H.Jensen, M.H.Chu: J. Plasma Phys. 25(1981) 459
[3] J.B.Taylor: Rev. Mod. Phys. 58(1986)741
[4] L.Turner: Phys. Fluids 27(1984)1677

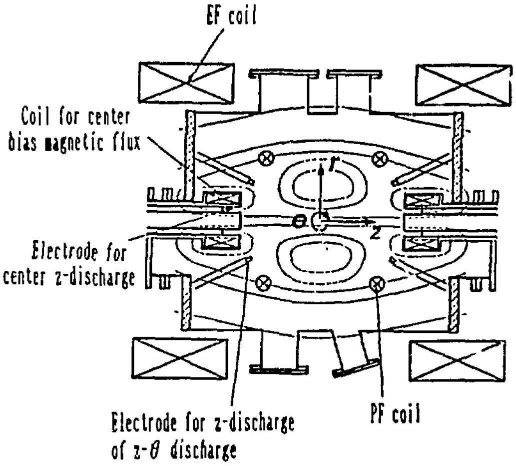

Fig. 1 TS-3 machine.

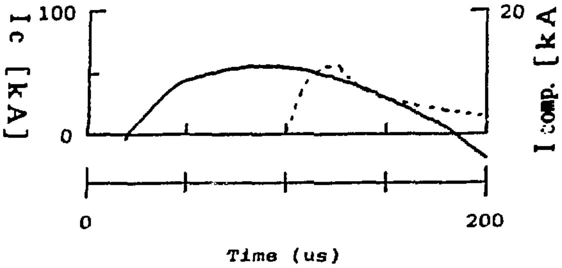

Fig. 2 Dischrge current. (dotted line; compression current)

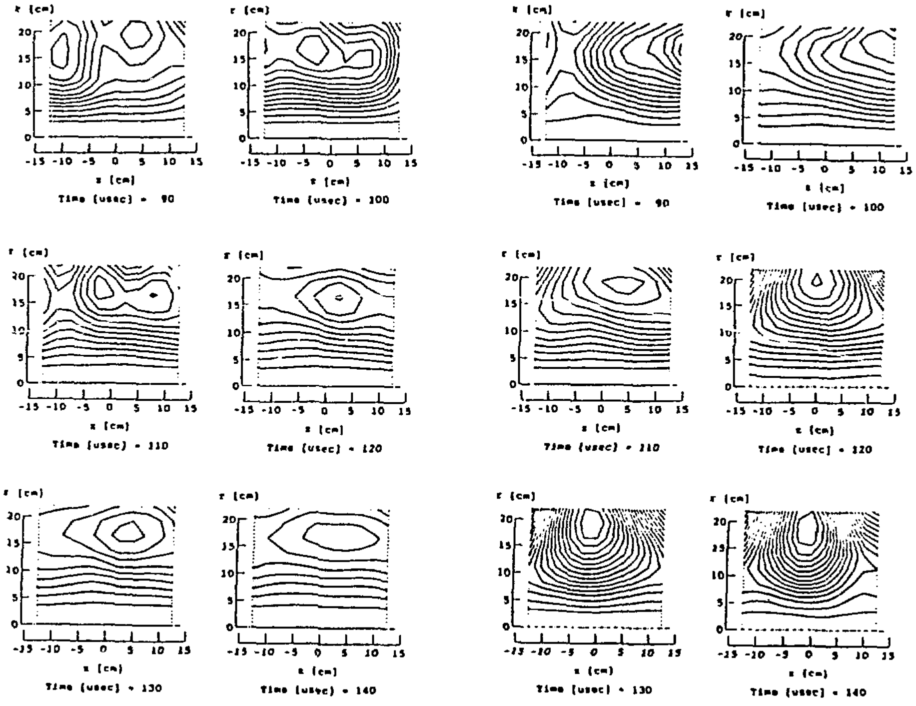

(a) Without compression

(b) With compression

Fig. 3 Poloidal flux plot.

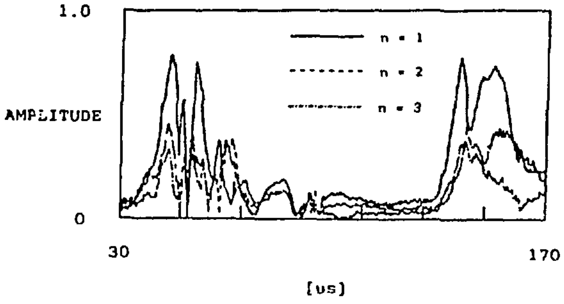

Fig. 4 Toroidal mode amplitude.

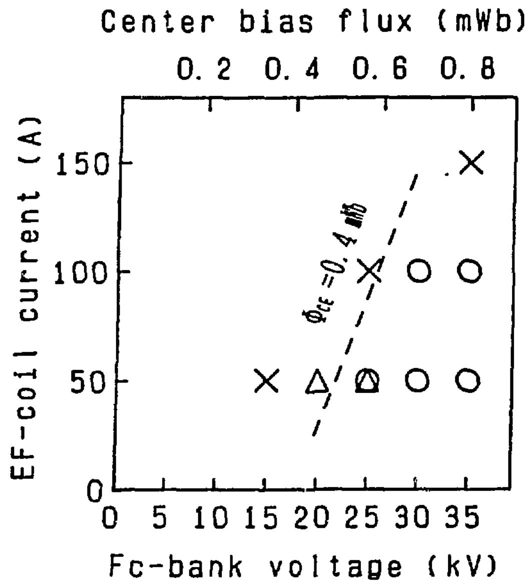

Fig. 5 Operation region for FCS production.

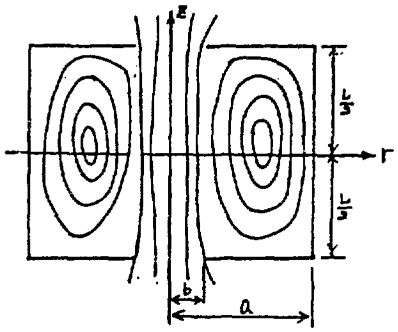

Fig. 6 Boundary condition for equilibrium calculation.

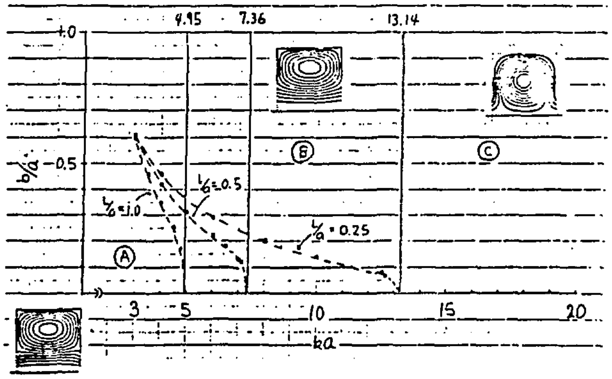

Fig. 7 Cassification of FCS.

A. with flux-core with null-point

B. with flux-core without null-point

C. without flux-core

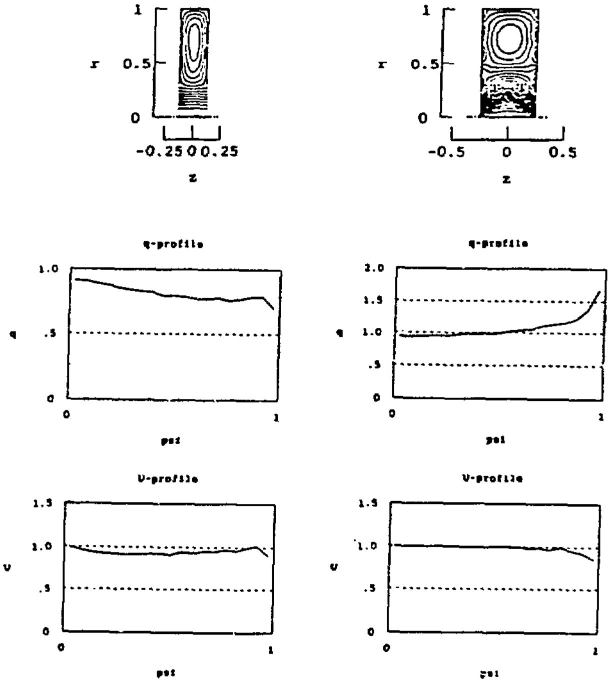

(a) (b)

Fig. 8 Examples of equilibrium.

The Impedance and Energy Efficiency of a Coaxial Magnetized Plasma Source used for Spheromak Formation and Sustainment

Cris W. Barnes, T. R. Jarboe, G. J. Marklin, S. O. Knox, and I. Henins
Los Alamos National Laboratory, Los Alamos, New Mexico 87545

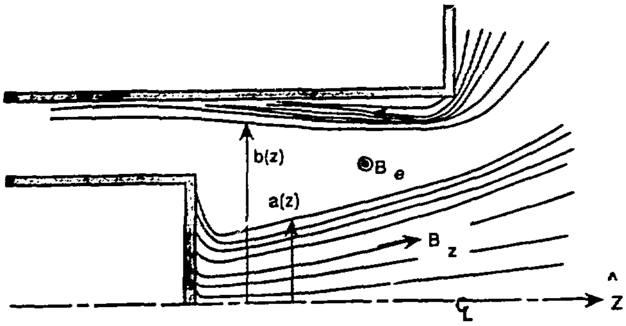

Figure 1: Diagram showing the geometry of the simple coaxial channel flow model. A region of azimuthal field B_θ where the axial flow occurs is bounded by regions of axial field B_z, with separatrices of radius $a(z)$ and $b(z)$.Diagram showing the geometry of the simple coaxial channel flow model. A region of azimuthal field B_θ where the axial flow occurs is bounded by regions of axial field B_z, with separatrices of radius $a(z)$ and $b(z)$.

Electrostatic (dc) helicity injection has previously been shown to successfully sustain the magnetic fields of spheromaks and tokamaks. The magnitude of the injected magnetic helicity balances (within experimental error) the flux lost by resistive decay of the toroidal equilibrium. The problem of optimizing this current drive scheme hence involves maximizing the injected helicity (the voltage-connecting-flux product) while minimizing the current (which multiplied by the voltage represents the energy input and also possible damage to the electrodes).

The impedance (voltage-to-current ratio) and energy efficiency of a dc helicity injection experiment are studied on the CTX spheromak. Over several years changes were made in the physical geometry of the coaxial magnetized plasma source as well as changes in the external electrical circuit. The source could be operated over a wide range of external charging voltage (and hence current), applied axial flux, and source gas flow rate. A database of resulting voltage, helicity injection, efficiency, electron density, and rotation has been created. These experimental results are compared to an ideal magnetohydrodynamic theory of magnetic flux flow. The theory is parameterized by the dimensionless Hall parameter, the ratio of electric to mass current. For a constant Hall parameter the theory explains why the voltage depends quadratically on the current at constant flux. The theory also explains the approximately linear dependence of the impedance-to-current ratio on the current-to-flux ratio of the source. The current-to-flux ratio itself (the energy-per-unit-helicity of the source) is bounded below by considerations of force balance. While the rotation of the flow is not understood, the density of the sustained spheromak is shown to be related to the mass flow in the source, supporting the constant Hall parameter assumption. The overall efficiency of sustainment through dc helicity injection is limited by the usual ohmic resistive decay, by the force-balance limits on the current-to-flux ratio, by the losses of the external electrical circuit, and by the fundamental limitations on the achievable impedance of flux flow in a magnetized plasma. Even so, ratios of spheromak magnetic energy to capacitor bank energy of over 17% have been achieved on CTX. Ignoring external circuit losses the efficiency of electrostatic helicity injection for converting energy received by the coaxial source to the energy of the spheromak magnetic field has exceeded 70%.

Introduction The key to high-field steady-state sustainment of spheromaks by dc helicity injection[1] is to maximize the magnetic helicity injection rate $\dot{K} = 2V\Phi_g$ while minimizing adverse effects due to the current I. (V is the voltage between electrodes which are connected by a magnetic flux Φ_g.) However, in the presence of a magnetized plasma an arbitrary voltage cannot be applied at the electrodes. The flux flowing away from its source is limited by the Alfvén speed of the plasma. The result is that the voltage of the source (the rate of change of flux) is not the charge voltage on the external capacitor bank, but has a very strong dependence on the current of the system[2]. The magnitudes of the magnetic fields of spheromaks[3], reversed-field pinches (RFPs)[4], and tokamaks[5] have been shown to be determined by the balance between the injected magnetic helicity and resistive dissipation. The energy-per-unit-helicity efficiency of the sustainment[3] can be raised by increasing the connecting flux, but such an increase in flux impedes the fluid flow and lowers the electrical impedance (voltage/current ratio).

The problem of maximizing the impedance and efficiency is important for any scheme for sustainment by helicity injection, including spheromaks, RFPs, or tokamaks. Understanding the physical constraints on the flow of flux in a magnetized plasma, and its relation to mass flow, is also important to understanding the physics of "relaxation" phenomena[6]. The observed relationship of mass flow to current is critical in determining the density of the sustained spheromak, which affects its transport properties[7].

Ideal MHD theory of the flow The problem of sustainment by helicity injection can be treated as a "steady-state" problem, where local time derivatives are negligible ($\partial/\partial t = 0$). Single-fluid MHD equations with an ideal Ohm's Law are used to explain the observations. The basic equations include conservation of mass and flux, Ohm's Law, and force balance.[8]

The ideal Ohm's Law may be violated due to the presence of a Hall current. The important parameter is[2, 9]

$$\Xi = \frac{I_g}{I_{\dot{m}}} = \frac{I_g}{e\dot{m}/M} \qquad (1)$$

where $I_{\dot{m}}$ is the flow rate of a material with atomic mass M expressed in units of the current. The Hall parameter Ξ is also called the "replacement factor" since it tells us how many times the electrons that neutralize the space charge of the ions that traverse the accelerator channel are replaced.[2] If $\Xi = 0$ then the electrons and ions move identically together, and there is no current flow at all. As Ξ increases the current carried by the electrons exceeds that carried by the massive ions, resulting in a net current. In the limit where the ions are stationary and the electrons carry all the current the Hall parameter becomes infinite. If $\Xi \ll 1$ then the Hall terms can be ignored. In the CTX case, Ξ ranges between about 0.03 and 0.16.

We consider the flow in a geometry such as Figure 1. The magnetizing axial flux, created by a solenoid inside the inner electrode, emerges from the front region of the inner electrode and returns through the outer electrode of the Marshall gun. Above the lower current sheet [at $a(z)$] there will be plasma flow, electric field, and radial current density. Below $a(z)$ the axial flux (with no flow along it or azimuthal flux in it) will be compressed until radial force balance is satisfied. Only some fraction of the axial flux may be trapped in the axial flow region, and above the upper current sheet [at $b(z)$] is another region of axial flux (of the opposite sign) that is compressed against the entrance region wall. The axial flow channel expands radially against both regions of axial flux until radial force balance is achieved. Our simple model assumes there is no axial flux embedded in the region of axial flow. This approximation is essentially that the effect of the rotational force $E_r B_z$ is small compared to the axial force $E_r B_\theta$.

The force balance along the flow (Bernoulli's equation) determines an energy constant of the motion. Differentiating along the flow leads to the Huginoit equation which determines the acceleration. The acceleration can only take place when the geometry of the channel changes, or at a choke point where the velocity equals the

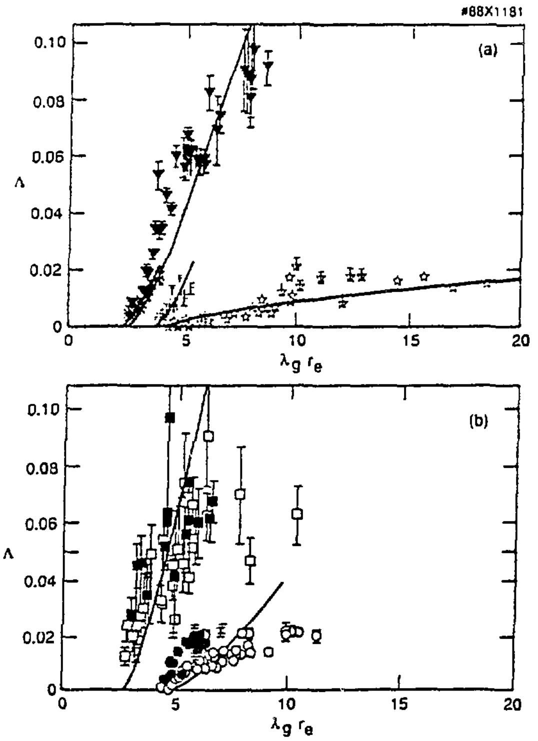

Figure 2: Gun parameter Λ versus $\lambda_g r_e$ for several different conditions.

Alfvén speed. Since the flow accelerates throughout the nozzle, the axial velocity is thus determined at the throat. The geometric shape of the nozzle is determined from radial force balance between the axial and azimuthal magnetic fields. This analysis leads to the following expression for the gun voltage

$$V_g = \frac{e\mu_0^2}{4\pi^2 M} I_g^2 \Xi F(x) \tag{2}$$

where $x = \lambda_g r_e$, $\lambda_g = \mu_0 I_g/\Phi_g$, and $F(x)$ depends on λ_g/λ_{th}.[8] If there is too much axial flux in the gun, the tension in the axial field can exceed the pressure in the toroidal field and the toroidal flux will not be able to emerge from the gun.

The three powers of current in the voltage scaling Eq. (2) can be understood as follows: One power is due to the source current determining directly the toroidal flux magnitude for fixed λ_g. One power comes from the proportional increase in the Alfvén speed with the increase in magnetic field. The final power of current comes *from the necessity of constant mass flow through* the source due to the continuity equation. This results in a rarefaction of the density as the velocity of the flow increases since the velocity goes through the Alfvén speed at the nozzle. Thus at constant mass input the density drops as the velocity increases, further increasing the voltage and adding the final power of current to the voltage. The actual experiment only shows 2 powers of current in the voltage scaling. This is because the amount of mass flow in the experiment generally increases proportionately with the current (the Hall parameter is a constant), and thus one power of the current is canceled by the increase in density.

Experimental results The gun parameter

$$\Lambda \equiv \frac{V_g}{I_g^2}\frac{4\pi^2 M}{e\mu_0^2} = 2.6 \times 10^5 \frac{M}{m_p}\frac{V_g}{I_g^2}$$

can be plotted versus λ_g and compared to $\Xi F(\lambda_g r_e)$ from Eq. (2) (Fig. 2). The comparison with theory is a two parameter fit: first the value of $\lambda_g = \lambda_{th}$ where the voltage limits to zero is found, and then second the Hall parameter Ξ is adjusted to match the magnitude of the impedance/current ratio of the gun parameter Λ. The scaling of voltage with the square of the gun current has removed a large variation in the data, and the theory also predicts the approximate linear increase of V_g/I_g^2 with increasing I_g/Φ_g. When these large variations are removed, the simplified theory does not have the remaining curvature of the experimental data quite right, and the theory tends to underestimate Λ at small λ_g and overestimate Λ at large λ_g.

Using the two parameters λ_{th} and Ξ determined from the data combined with the value of the external circuit impedance, the voltage and current can be uniquely determined given the charging voltage on the main bank and the applied magnetizing flux. Figures 3(a) and (b) show plots of the observed current and voltage versus flux, with the predicted values from the

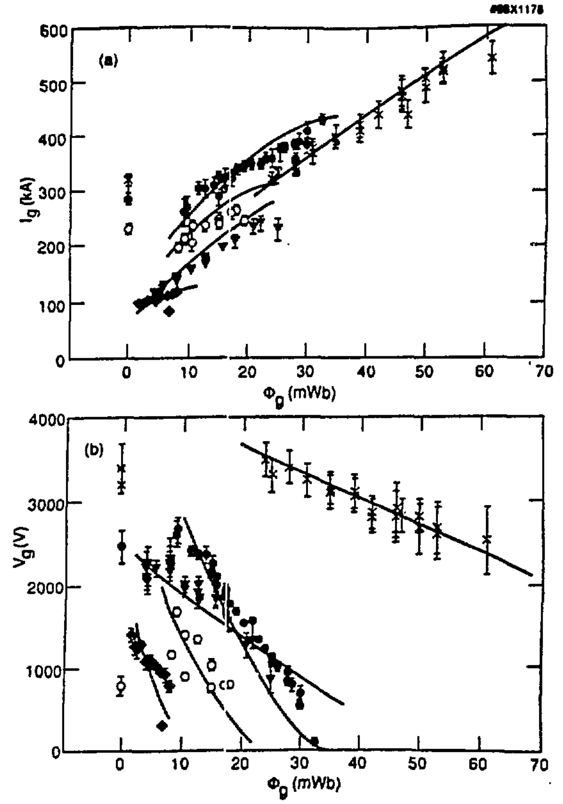

Figure 3: Gun current and voltage versus gun flux, compared to the analytic theory with the two adjustable parameters λ_{th} and Ξ. Each symbol represents a given geometry and circuit type, with the main bank voltage held constant. (a) Gun current. (b) Gun voltage.

gun law fit through the data. When plotted this way one can clearly see the huge differences in the observed voltages and currents at similar connecting flux but for different main bank voltages and circuit types.

Curves may be calculated of the current, voltage, impedance, helicity injection rate, and efficiency versus Φ_g for different main bank voltages for a given circuit. Figure 4 illustrates such a set of calculations. The efficiency η and the helicity injection rate both have maxima versus magnetizing flux, but not at exactly the same value. The maxima occurs because at low flux very little helicity is injected by the low connecting flux, and at high flux very little helicity is injected by the low voltage.

The magnitude of the density in the spheromak during sustainment depends on the gun current. Figure 5 shows how the spheromak density remains approximately proportional to the gun current, despite a significant increase in the magnitude of the "confining" magnetic fields of the spheromak[7]. Usually the amount of gas generated in the source is undetermined and $\dot{m}$ is a free parameter of the operation. In one case [Mode 1984b(5)] a "slow" gas valve was installed on the source which continually fed 10^4 torr-liter sec^{-1} of gas for many milliseconds. Figure 6(a) illustrates the changing proportionality of the spheromak density-to-current ratio as more gas was added to the source. Fig. 6(b) shows how normalizing the gun parameter Λ by the n_e/I_g proportional-estimate of $\dot{m}$ reasonably brings the voltage data together, that is, the drop in voltage as the gas is added is in theoretical agreement with the increase in $\dot{m}$.

Discussion and conclusions In the CTX helicity injection experiment we operated with a wide range of electrode dimensions, external electrical circuits, charging voltages and magnetizing fluxes. The resulting source voltages and helicity injection rates can now be understood for our coaxial source by a simple MHD theory. Previous work on coaxial accelerators had predicted and found that the voltage depended on the square of the current, assuming the the ratio of electrical-to-mass current (the Hall parameter Ξ) remained constant. We have confirmed this result, and further observed the proportional dependence of the spheromak density on source current as expected for constant Ξ. The measurements of the density and gas flow rates are within factors of 2 or 3 from expectations based on the fitted value of Ξ. We also learned that the geometry of the injection should be designed to reduce the value of λ_{th} to as close to the value of the equilibrium to be driven as possible.

This work was supported by U.S. D.O.E. contract No. W7405 ENG-36. One of us (CWB) thanks the Princeton Plasma Physics Laboratory for support under U.S. D.O.E. contract DE-AC02-76-CHO-3073.

[1] T. R. Jarboe, I. Henins, A. R. Sherwood, C. W. Barnes, and H. W. Hoida, Phys. Rev. Lett. **51**, 39 (1983).

[2] A. I. Morozov and L. S. Solov'ev, Steady-state plasma flow in a magnetic field, in *Reviews of Plasma Physics Volume 8*, edited by M. A. Leontovich, page 1, Consultants Bureau, New York, 1980.

[3] C. W. Barnes et al., Phys. Fluids **29**, 3415 (1986).

[4] K. F. Schoenberg, R. W. Moses, Jr., and R. L. Hagenson, Phys. Fluids **27**, 1671 (1984).

[5] M. Ono et al., Phys. Rev. Lett. **59**, 2165 (1987).

[6] J. B. Taylor, Rev. Mod. Phys. **58**, 741 (1986).

[7] J. C. Fernández et al., Nucl. Fusion **28**, 1555 (1988).

[8] C. W. Barnes, T. R. Jarboe, G. J. Marklin, S. O. Knox, and I. Henins, The impedance and energy efficiency of a coaxial magnetized plasma source used for spheromak formation and sustainment, Technical Report LA-UR-89-909, Los Alamos National Laboratory, 1989, Submitted to the Physics of Fluids.

[9] A. I. Morozov and L. S. Solov'ev, Sov. Phys.-Dokl. **10**, 834 (1966).

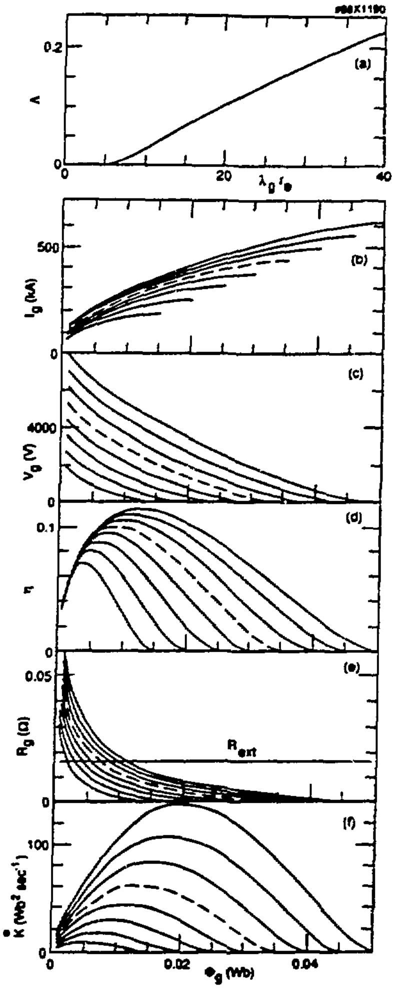

Figure 4: Gun performance versus axial flux, using the analytic theory fit to the data. Using the theory shown in (a) with $R_{ext} = 16\ \mathrm{m}\Omega$, $\lambda_{th} = 15.4\ \mathrm{m}^{-1}$ and $\Xi = 0.05$, the (b) current, (c) voltage, (d) efficiency η, (e) impedance, and (f) helicity injection rate are all plotted versus gun flux for main bank charge voltages from 3 to 10 kV. The curves at 7 kV are dashed.

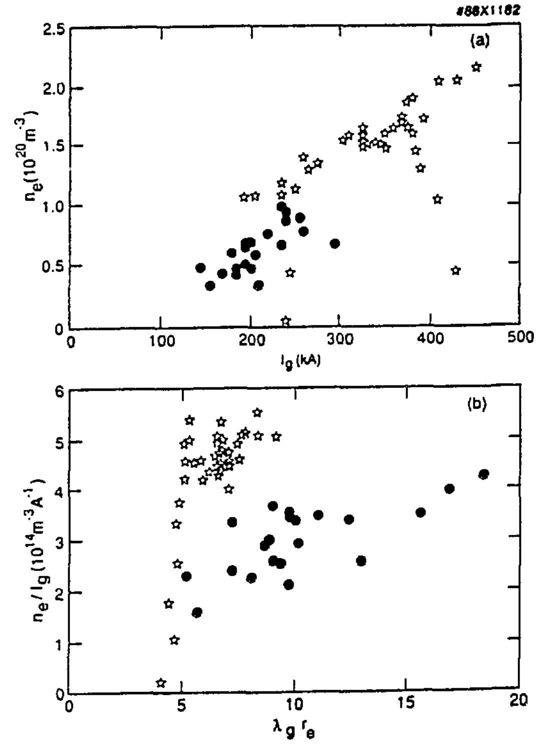

Figure 5: Spheromak volume-average density dependence on source parameters. (a) Density versus source current for two different operating modes. (b) Density divided by current versus λ_g, showing the near constancy of the spheromak density on the source current except near the helicity injection threshold when the density drops.

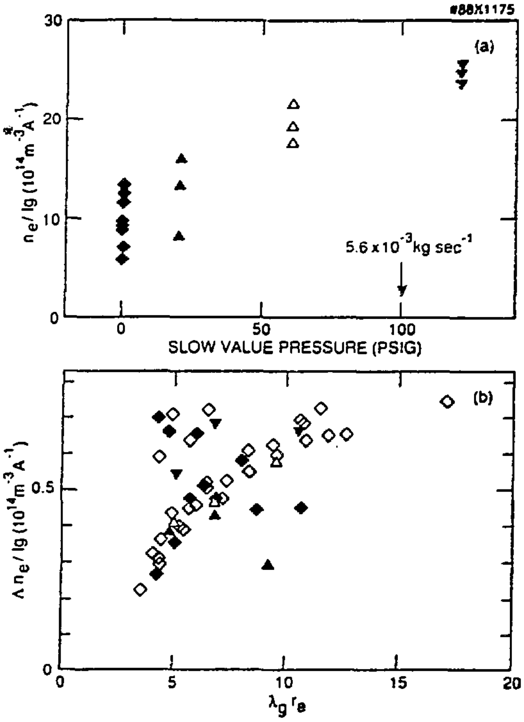

Figure 6: Effect of external changes to gas flow rate. (a) Density divided by current for Mode 1984b(5), versus the amount of pressure in the slow gas valve (in PSIG). The finite y-intercept defines the amount of $\dot{m}$ for the usual uncontrolled case. (b) Gun Parameter Λ normalized by the current-to-density ratio versus $\lambda_g r_\epsilon$ *for the different discharges with the slow valve.* The symbols are the same as (a), with added data from this same mode but with no slow valve and a constant value of $n_e/I_g = 10 \times 10^{14}m^{-3}A^{-1}$ assumed also shown (◇).

Berkeley Compact Toroid Experiment: Experimental Results and Progress

E. C. MORSE, A. KULEWIEC, R. STACHOWSKI, J. S. HARDWICK, AND W. B. KUNKEL

University of California, Berkeley, CA 94720 USA

0. INTRODUCTION

The Berkeley Compact Toroid (BCTX) experiment is a spheromak device with a 70 cm flux conserver and a Marshall-gun generated plasma. This device will be used to test a pulsed radiofrequency (RF) heating scheme operating at the lower hybrid frequency in this device, using a 20 → 40 MW pulsed rf source at 450 MHz. The design of this heating system will be described, and the results of experiments on the currently unheated discharges will be presented.

1. FORMATION AND STABILITY STUDIES

Some effort has been spent in the past year in quantifying the MHD formation and stability characteristics of the spheromak plasmas generated in the BCTX device. The experimental plan has concentrated on studies of the characteristics of the CT plasma without auxiliary heating using information from magnetic probes, Rogowski coils, Langmuir probes, and from radiation detectors. Studies of materials problems are also underway in order to reduce the effects of impurities in the experiments. Since the current experiments use internal probes in the plasma, the plasma temperatures are low, and the lifetimes are rather short, with magnetic decay times on the order of 100μ s.

The basic CT formation can be seen from the internal magnetic field probe data. A sample of such data is shown as Figure 1. These five signals are from B-dot probes spaced 5 cm apart along the midplane of the device. The positions of these stations are at radii of 10 cm, 15 cm, 20 cm, 25 cm, and 30 cm from the midplane, and the outermost station is a few cm from the mesh flux conserver. From this data, one can infer that the poloidal magnetic field reverses across the midplane, which would be required for the presence of closed symmetrical magnetic field lines. Furthermore, one can see that as the discharge progresses, the magnetic null moves outward, and ends somewhere between stations 3 and 4, i. e. at about $r \approx 0.64a$. This is consistent with various low-beta equilibrium models. The magnetic lifetime of this run is particularly short ($\approx 20\mu s$), due to low energy input for this case.

A set of Rogowski coils, fabricated originally by LANSL for use on the CTX experiment, have been installed on the mesh flux conserver. These probes measure the image currents in the 0.5" Cu rods forming the cage. Six such probes were installed, all on mesh sections oriented poloidally, i. e. measuring essentially Z-currents. The probes were arranged at ninety degree intervals around the cage, with a two coils symmetrically placed in Z on opposing sides of the mesh. This placement affords some sensitivity to low-order MHD modes, giving information about azimuthal mode number and the symmetry of the mode in Z. A sample set of data obtained from this set is shown as Figure 2. Here, a rotating m=1 MHD mode can be clearly seen on the four probes with the appropriate phasing. It is interesting to note that the precession rate of this signal, around 100 KHz, indicates the presence of a large amount of bulk flow in the equilibrium, as the temperature of this discharge is low enough to rule out FLR effects. While adjustment of the toroidal-to-poloidal field energy has been seen to make this instability appear or disappear, no other mode number has been seen to date. Output from a single Rogowski coil for a discharge at higher bank energy is shown as Figure 3. In this case, the oscillations seem are not taken as MHD oscillations, as they are seen in phase on all probes. These oscillations are artifacts of the L-C ringing of the Marshall gun bank, which appears to be restriking and sending in plasma with alternating toroidal flux. Notice that the timescale for this discharge is somewhat longer, with a lifetime on the order of 100 μ s.

2. OTHER IMPROVEMENTS

A set of fast ($\tau \approx 2$ ms) piezoelectric valves have been substituted for the pulsed electromagnetic solenoid valves used earlier. These valves have a relatively low gas throughput (1 → 7 torr-l s^{-1} at the manufacturer's nominal voltage rating (100 V) ; but it has been found that increased flowrates at higher voltages without crystal failure is possible. The smaller gas inventory present has resulted in a reduction of the moving mass in the Marshall gun, as seen by a reduction in the L-C oscillations in the gun discharge current. A larger capacitor bank for the Marshall gun discharge current circuit (44 kJ, 20 kV) has replaced an earlier 25 kJ bank, and this in turn affords a higher value of discharge mass for optimal tuning. Whereas earlier experiments could only clamp the L-C ringing oscillation by the addition of an external series resistor, the more recent data show that at the full bank voltage, the ringing is somewhat suppressed.

Poloidal fields in the spheromak plasma are generated in the Marshall gun by a coil mounted outside the gun near the muzzle end. The gas valves are immediately upstream of this coil. A drawback of this design is that a substantial portion of of the magnetic flux is between the inner and outer electrodes, and this flux is less efficiently coupled into the generated spheromak that the flux inside the center electrode. For this reason a magnetic pole piece was fabricated by laminating 600 sheets of 10-mil transformer iron stampings to form a 15 cm diameter cylinder approximately 75 cm in length. This was placed in the center electrode under the PF coil but shifted slightly aft, towards the breech end of the gun, so as to trap the maximum flux in the electrode where the gas is injected. Initial tests show that this is a much more efficient poloidal field circuit than the unloaded case.

After several hundred shots, the machine was taken up to air and the gun and flux conserver materials were examined. The inner electrode was found to have a set of dendritic arc tracks along its length. A great deal of copper was found to be vapor-deposited on all stainless components. Additionally, the copper mesh flux conserver was found to have some iron deposition, preumable from the stainless inner electrode. The tantalum-jacketed Rogowski coils were found to be completely covered with copper from the flux conserver. Surface erosion was most severe around the midplane beltline of the flux conserver, while almost none was seen on the endcap, which indicates that the Marshall gun did not connect elctrically to the endcap during these discharges. Spectroscopic measurements are underway to determine the extent to which these sources of metal vapor affect the impurity balance in the plasma.

3. RF DRIVE SYSTEM

The RF drive components for the lower hybrid heating experiments are now in place. The main RF power components are Varian VA-812D klystrons, which are rated at 20 MW of RF output in pulsed service. The present inventory of parts will allow for operation of two tubes in tandem, and three additional tubes are onsite for use as spares of for possible expansion. The excitation for these tubes is a dual 4 kW traveling wave tube (TWT) amplifier, which in turn is driven by a 0.5 W solid state preamp. The system operates in a nonsaturated regime, and thus RF envelope modulation is possible.

The high voltage power pulse for the klystrons requires a 250 kilovolt pulse of up to 100 μ s length. For this reason, a Blumlein direct feed capacitor bank has been designed, as opposed to a step-up pulse transformer as would be more common in radar service. The relatively long pulse would cause flux-core problems in a step-up design. The line, a Guillemin type-E network, consists of two twelve-element L-C networks with a total of twenty-four 0.02 μF, 250 kV capacitors and a set of coils wound with stripped RG-213 cable for high voltage standoff. The entire line is designed for oil immersion. The line is fired by a triode-stabilized spark gap switch. Arc protection is provide by a series resistor in the cathode circuit.

The RF power output from the klystrons is transmitted to the plasma through approximately 4.5 meters of WR-2100 waveguide. The RF power is coupled into the plasma through a 21" × 10.5" window with the long side of the guide perpendicular to the magnetic axis of the CT plasma. The RF power will be coupled into the plasma through a grill which functions as a phasing structure to couple the TE_{01} mode in the waveguide into a TM-like mode for coupling into the plasma. A $(0, \pi, 0, \pi)$ phasing on the elements on this grill can then couple the RF energy transmitted through the waveguide into a nearly orthogonally directed slow wave in the plasma, which propagates nearly parallel to $\vec{B}$. The phasing structure uses elements which are cut to one-half of a free-space wavelength, staggered axially by one-quarter of a free-space wavelength, and pitched laterally by a half-wavelength for the slow wave in the plasma. The launched wave must have a parallel index greater than that dictated by the Golant condition, $n_{\|} > (1 + (\omega_{pe}/\omega_{ce})^2)^{1/2}$. For BCTX parameters, a choice of $n_{\|} = 10$ is made; this results in a pitch between radiating elements of 3.3 cm. In order that the antenna structure does not form a large break in the flux conserver, the radiative elements are Babinet-type slots in a metal grill rather than floating conductors. Some experimentation will clearly be necessary to avoid breakdown problems and disturbance to the plasma by the antenna structure. The experimental results to date show that plasma erosion of the metal parts of the cage is worst at the midplane, and it might be necessary to stagger the rf entrance or provide a vestigal electrode of some kind.

4. CONCLUSION

Data from the unheated CT plasma shots with internal magnetic probes show that magnetic equilibria are being formed, and that some discharges are susceptible to an m=1 instability at high rotational rate. Some improvements in the poloidal field drive circuit and a more careful attempt to control the gas loading have been shown to improve the overall lifetime and robustness of the formed plasma. A fairly high rate of metal vaporization is seen in the discharges and may lead to the choice of alternate electrode materials, such as tungsten or other refractory metal. Future rf heating experiments will attempt to alleviate the short energy confinement times by burning through the radiation barrier formed by the low-Z impurities. Future diagnostic emphasis will be placed on surface probes, spectroscopy, and laser measurements.

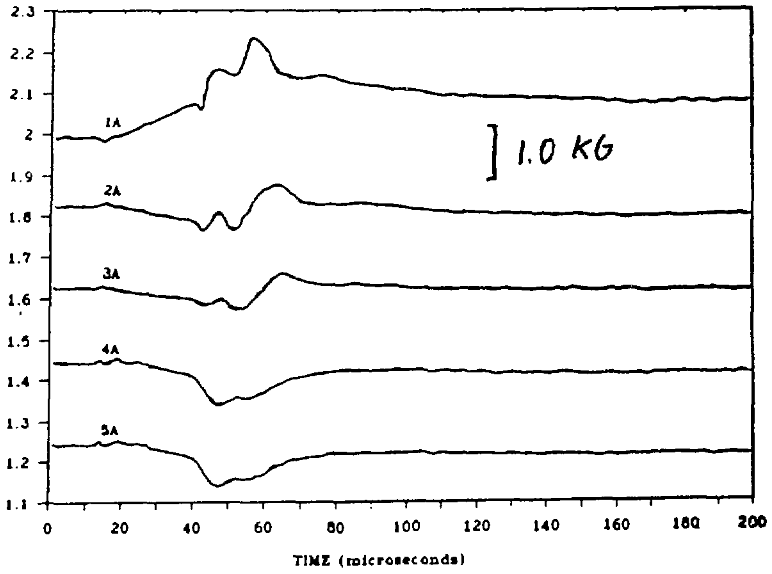

Fig. 1. Poloidal Field Profile from Internal Probes.

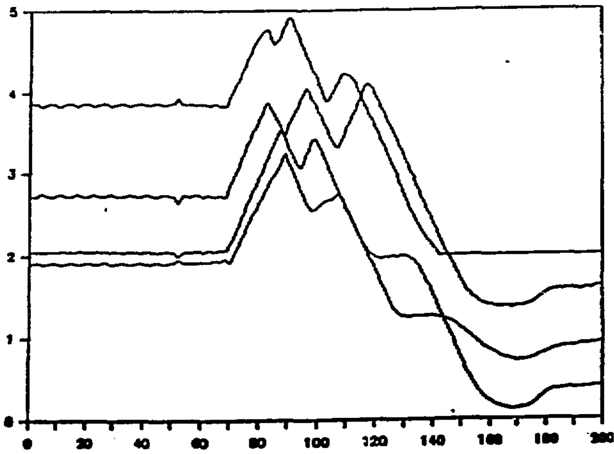

Fig. 2. Rogowski Coil Data Showing $m = 1$ Instability.

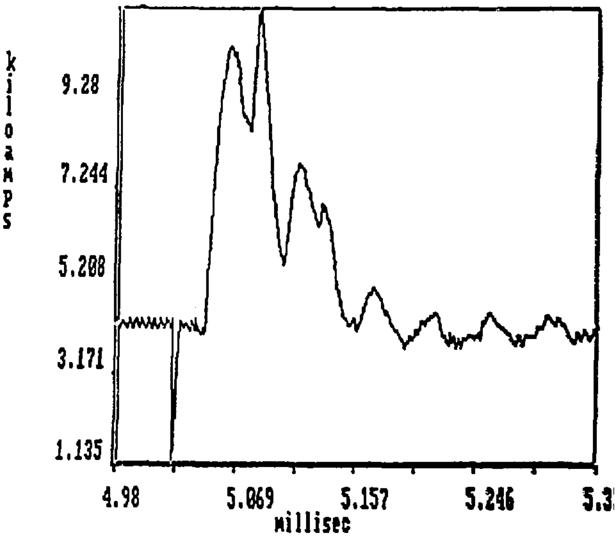

Fig. 3. Rogowski Coil Currents for 44 kJ Discharge.

Progress on SPHEX, the spheromak at Manchester

Authors: P.K. Browning, B. Browning, J Clegg, G. Cunningham, P. Dooling, S. Gee, K. Gibson, D. Kitson, M.G. Rusbridge, K Sebti.
Dept of Physics, UMIST, Manchester, UK

Abstract: Details are presented of magnetic field measurements on Sphex, both in the flux conserver and the entrance region, and of their relationship with parameters of the Marshall gun.

Introduction

The Sphex spheromak, described by Browning et al (87), was designed to minimise field errors in the flux conserver, with the intention of minimising the amount of flux penetrating the wall and hence minimising helicity loss. We present here results showing to what extent this has been successful.

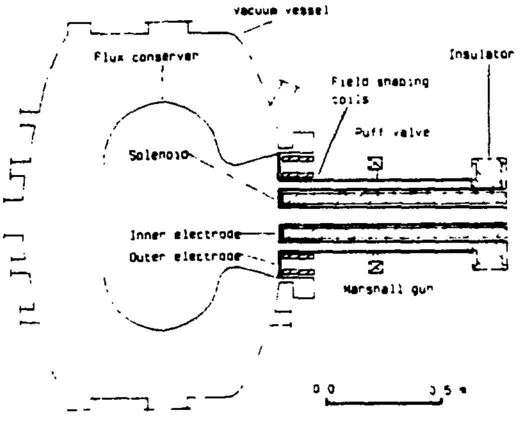

UMIST spheromak SPHEX

Machine characteristics

Fig 1 shows typical shot data. The gun current peaks at up to 70KA, creating a spheromak configuration with poloidal field at the edge of up to 60mT. The duration of the spheromak is apparently determined by the behaviour of the Marshall gun, which imposes a number of critical currents on the machine operation (fig 2). Firstly it is impossible to obtain a well defined spheromak at a gun current less than 35KA or so. Secondly, in order for plasma to be ejected from the gun, the ratio of gun current/solenoid current has to reach a certain critical value, or since $\mu_{gun} = \mu_o I_{gun}/\psi_{gun}$, μ_{gun} has to be greater than $23m^{-1}$. Thirdly, when the gun current falls below 30KA the main spheromak terminates, leaving a small residual field, which finally terminates when μ_{gun} falls below a second critical value of $12m^{-1}$.

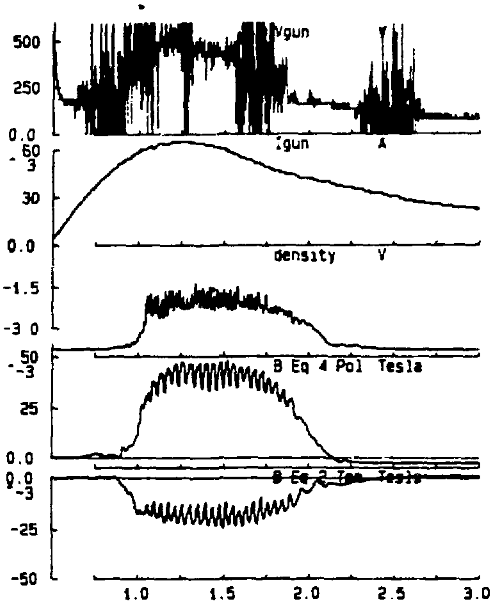

Fig 2, Critical gun currents

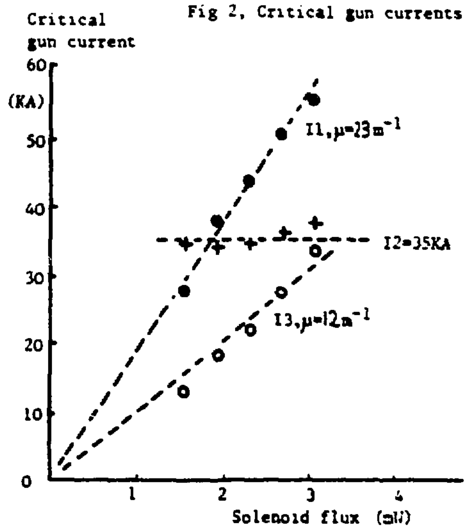

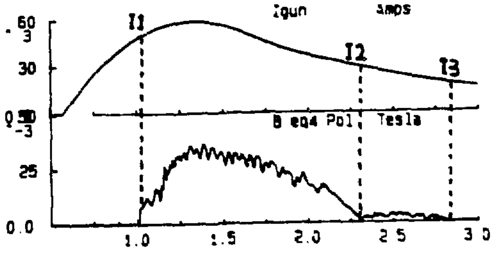

The strength of the poloidal field at the edge is found to be almost completely determined by the solenoid flux (fig 3), if the solenoid current is held constant and the gun current increased then the duration of the spheromak increases but the peak field strength does not. Since the mean μ in the spheromak only increases very weakly with the μ of the gun, one must conclude that the excess current remains within the gun or entrance region.

fig 3. 'Optimum' plot

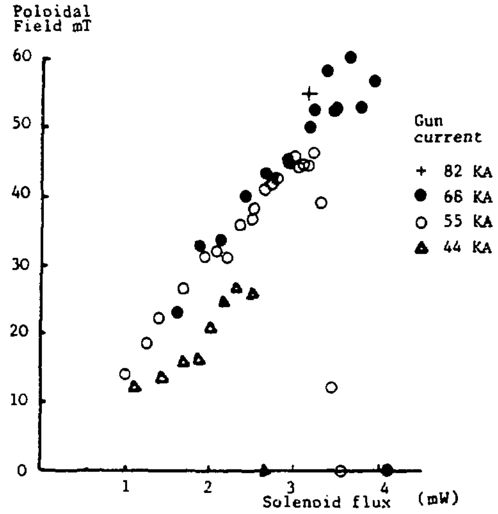

The electron density is measured with a single chord CO_2 laser interferometer, and can be varied from 2.10^{19} to $2.10^{20} m^{-3}$ by regulating the hydrogen supply pressure to the puff valves and using a backing fill. At a given hydrogen supply and μ_{gun}, the density correlates strongly with poloidal field strength (fig 4). There is no sign of an initial pump-out, and in general the time dependence of the density matches that of the edge poloidal field closely.

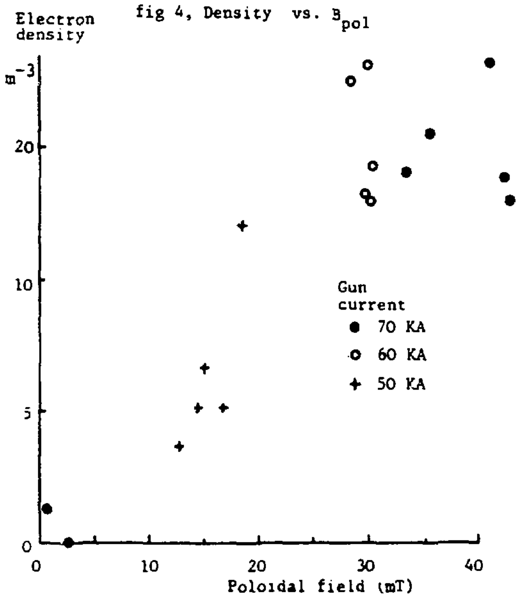

We do not yet have a direct measure of either electron or ion temperature, and the only indication is the presence of a strong C III line at 2298A (excitation potential 18V). The monochromator has a range of 2000A to 6000A, but examination of other species is hampered by the presence of numerous Fe lines.

Wall current

As fig 1 shows, the toroidal field at the edge is not zero, so there must be a significant current flowing to the end wall of the flux conserver. By installing extra probes (fig 5) we have determined that the bulk of this current flows to the walls in the regions where the field is highest, and in fact a very small proportion of the gun current returns to the outer gun electrode. On the other hand, having calculated the proportion of flux which will diffuse into the wall during the shot, we know that the current is not simply flowing along field lines. Further investigation is in progress to try to identify processes causing this cross-field current flow.

fig 5. Current flowing to wall

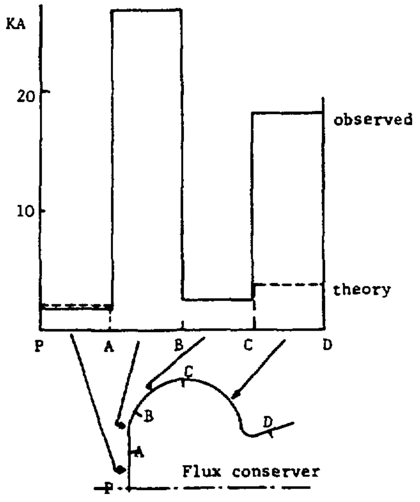

Mean magnetic fields

Using a probe array of 8 toroidal and poloidal coils at 3cm spacing, we have made extensive measurements of the internal field profile, both on the equatorial plane and in the entrance region (fig 6). Apart from the non-zero toroidal edge field, the equatorial fields match the results of relaxation code calculations using a μ which rises from around $9\mathrm{m}^{-1}$ on the magnetic axis to $13\mathrm{m}^{-1}$ at the wall (a uniform μ gives an eigenvalue of μ=$11.1\mathrm{m}^{-1}$). If we calculate the total poloidal flux as

$$\Psi_t = \int_{axis}^{wall} 2\pi r\, B_{pol}\, dr$$

and calculate the *gun* flux from the solenoid dimensions and current, then the flux amplification can be plotted against μ_{gun} (fig 7a) (note that μ_{gun} varies during a shot). These curves can all be extrapolated back to zero at $\mu_{gun} \simeq 11\mathrm{m}^{-1}$, which confirms the view that the gun cannot inject helicity when its μ is less than the flux conserver eigenvalue. Defining a mean μ as $\langle\mu\rangle = \Psi_t / I_t$, we find that $\langle\mu\rangle$ varies weakly with μ_{gun}, and re-plotting the flux amplification against $\langle\mu\rangle$ (fig 7b) shows a resonance at $\langle\mu\rangle \simeq 10\ \mathrm{m}^{-1}$, consistent with the theorum that $\langle\mu\rangle$ cannot be greater than the eigenvalue irrespective of the spatial μ profile (Kitson and Browning 89). Furthermore, the resonance curve seems somewhat broader than simulations predict, but since the shape of the resonance curve is a function of the distance between the electrodes, this would be consistent with current leaving the system at the flux conserver instead of the outer gun electrode (Dixon et al 89).

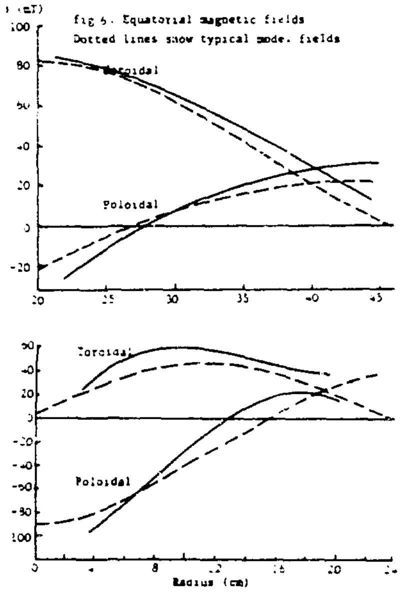
fig 6. Equatorial magnetic fields
Dotted lines show typical mode. fields

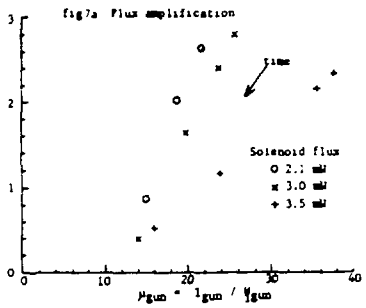
fig7a Flux amplification

fig7b Flux amplification

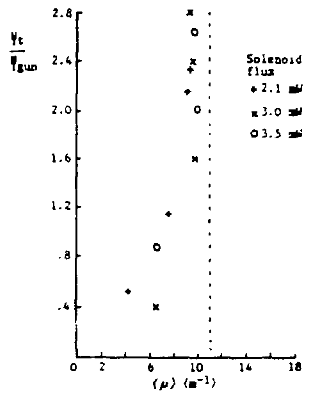

Measurements in the entrance region seek to determine whether there is an X point or a current sheet generated by reconnection , and whether 'short' field lines connecting the electrodes directly exist. In this case the measured field profiles are a rather poor fit to the calculated ones since there is virtually no current or flux returning to the outer electrode. There are no strong discontinuities to indicate current sheets in the region so far investigated. However, plotting the total plasma current and flux as a ratio of the gun current and flux (fig 8), shows that these ratios approach but remain less than unity (fig 9), so that there must be some 'short' flux carrying current.

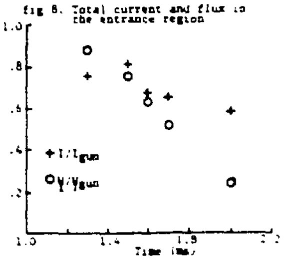
fig 8. Total current and flux to the entrance region

n=1 mode

Measurements from all the diagnostics are dominated by a large mode with frequency ≃ 20kHz, and by looking at several field probes spaced around the equator, it is clear that the mode number is 1. An internal probe array with coils in the poloidal, toroidal and radial directions has been used to examine this mode, with results in fig 9. Interestingly, the phase of the radial component on the outside of the spheromak leads the phase on the inside, suggesting that the mode is driven from the outside. The time dependence (fig 10)shows an amplitude which has a *minimum* during the shot, and a frequency which falls later in the shot. These observations would be consistent with a mode driven by E×B force between the electric field in the gun and poloidal field in the spheromak, but it is not yet known whether there is an associated bulk plasma rotation. Such a mode has also been observed on CTX (Knox et al 86).

fig 9 Radial component of mode

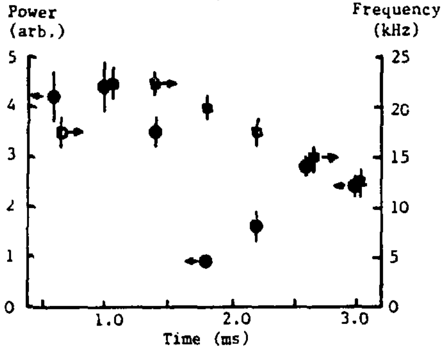

fig 10 Radial component of mode

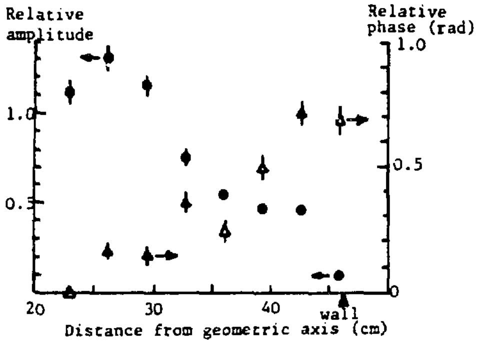

The internal fields have been analysed in terms of a simple non-resistive n=1 mode with both tilt and shift components, and a good fit to the amplitude and phase of the radial and toroidal components can be obtained with a tilt:shift amplitude ratio of 1:4. However the poloidal component cannot be fitted to this model, perhaps because the outer poloidal field lines are connected to the gun. Experiments to try to stabilise this mode are planned, including imposition of a toroidal (tokamak like) field by passing current down an axial conductor (ref Bruhns 87), and there is great interest in whether this mode plays a part in increasing the current flowing to the flux conserver wall, or in the relaxation process itself.

Summary

Sphex is producing magnetic field configurations which are close to an ideal spheromak and show considerable flux amplification. The magnitude of the spheromak field is essentially controlled by the solenoid flux rather than the gun current, provided the latter is high enough to eject plasma into the flux conserver. However there is clearly current flowing to the wall, probably caused by processes other than flux diffusion.

Acknowledgements

The authors are grateful to the UK SERC and UKAEA for providing the financial resources to support this work.

References

Browning et al. Proc Varenna Summer School Vol2 p 559, ed Ortolani and Sindoni

Kitson and Browning 89 submitted to Plasma Phys and Appl. Fusion

Knox et al. 86 Phys Rev Lett, v56, p842

Bruhns et al. 87 Nuc Fus v27 p2178

Pressure Effect on Equilibrium Configuration of CTCC-II Spheromak

M. Nishikawa, Y. Kato, N. Satomi, and K. Watanabe
Course of Electromagnetic Energy Engineering,
Faculty of Engineering, Osaka University,
2-1 Yamada-oka, Suita, Osaka 565, Japan.

1. Introduction

In CTCC-II experiment, the initial plasma is produced by a magnetized gun and ejected into a metallic aluminum flux conserver(FC) with thickness of 15 mm. The spheromak is formed in the FC during a life time of 1.5 ms, in which the plasma is isolated from any external feeder. A choking-field-generating coil is equipped on the entrance of the spheroidal FC. The choking field is suppressing some leakage of spheromak field along the entrance duct, which is made of thin stainless steel plate (0.8 mm) for rapid penetration of the choking magnetic field. This resistive part acts as an effective plasma current limiter, which produces stable currentless region (flux hole). The flux hole increases magnetic shear without inserting a central conducting pole along the symmetric axis and is controlled to decrease with the choking field strength. Thus in CTCC-II spheromak, a stable oblate spheroidal boundary is rigidly fixed by the metal wall of FC and the entrance hole of FC is effectively closed by choking magnetic field, so that it is suitable to investigate precisely a fine structure of configuration.

In spheromak configuration whose aspect ratio is near one, the ratio of the magnetic strength at the inner part to that at the outer part on equi-flux surface (mirror ratio) becomes very large in comparison with that of a large aspect ratio. This extreme configuration with a high mirror ratio may be associated with an anisotropic pressure effect even in collisional state like as our experimental condition. We have investigated the pressure effect on spheromak configuration in more detail.

The obtained equilibrium profile is grossly explained by a theoretical profile on assuming low beta limit until now. However, we observe a systematic discrepancy between a measured poloidal profile and a theoretical one as mentioned above, i.e. the measured value tends to the value smaller than the theoretical one assumed as low beta limit in the region of the outward profile from the magnetic axis. As taking an anisotropic pressure into consideration, this discrepancy may be dissolved to obtain a better fitting.

2. Experimental

The plasma parameters are experimentally obtained as the average electron density n_e=2-4x10^{19} m^{-3} and the electron temperature T_e=20-60 eV. The beta value at magnetic axis is estimated to be about 7-12% from the measurements by Thomson scattering method.

In order to measure the magnetic profiles of spheromak equilibrium configuration, the magnetic probe array (15 ch) with two components on each channel is inserted from the wall of the FC across the geometrical axis in the mid-plane. The each channel of the probe array is set at regular intervals of 30 mm as shown in Fig. 1. The measured profiles is shown in Fig.2

3. Effect of plasma pressure on magnetic configuration

3-1. Equilibrium

An anisotropic static equilibrium for an axisymetric system can be written by the equations as follows.

$$\nabla \cdot \mathbb{P} = \mathbb{J} \times \mathbb{B} \qquad (1),$$

$$\mathbb{P} = \mathbb{I}\, P_\perp + \left[\frac{(P_\parallel - P_\perp)}{B^2} \right] \mathbb{B}\mathbb{B} \qquad (2),$$

$$\mu_0 \mathbb{J} = \nabla \times \mathbb{B} \qquad (3),$$

$$\nabla \cdot \mathbb{B} = 0 \qquad (4),$$

where $P_\parallel$ and $P_\perp$ are functions of the poloidal flux function and the magnitude of the magnetic field. It is convenient to introduce the anisotropic function ζ

$$\zeta \equiv \frac{(P_\parallel - P_\perp)}{(B^2/\mu_0)} = 1 - \sigma \qquad (5).$$

Finally we can obtain the anisotropic Grad-Shafranov equation as

$$\rho \frac{\partial}{\partial \rho}\left(\frac{1}{\rho} \frac{\partial \psi}{\partial \rho}\right) + \frac{\partial^2 \psi}{\partial z^2} = -\left(\frac{\mu_0 \rho^2}{\sigma}\right) \frac{\partial P_\parallel(\psi, B)}{\partial \psi} - \left(\frac{1}{\sigma} \right) (\nabla \sigma \cdot \nabla \psi) - \left(\frac{1}{\sigma^2}\right) \frac{d G(\psi)}{d \psi} \qquad (6),$$

where $G(\psi) \equiv \dfrac{I^2 \sigma^2}{2}$ (7).

Here, taking into consideration of anisotropic mirror effect, we assume the functions of ψ and B as follows.

$$P_\parallel(\psi, B) = H(\psi - \psi_h) \left[p_0 \left(\frac{\psi - \psi_h}{1 - \psi_h}\right)^{c1} + \varepsilon \left(1 - \frac{\psi}{\psi_0}\right) \frac{B_0 B}{\mu_0} \right] (8),$$

$$P_\perp(\psi) = p_0 H(\psi - \psi_h) \left(\frac{\psi - \psi_h}{1 - \psi_h}\right)^{c1} \qquad (9),$$

$$G(\psi) = \frac{c^2}{2} H(\psi - \psi_h) \left[\left\{ \left(\frac{\psi - \psi_h}{\psi_0}\right)^2 + \left(\frac{\delta}{\psi_0}\right)^2 \right\}^{1/2} - \frac{\delta}{\psi_0} \right]^2, \qquad c = \lambda_0^{1/2} \psi_0 / \rho_0 \qquad (10),$$

$$\zeta(\psi, B) = \varepsilon H(\psi - \psi_h) \left(1 - \frac{\psi}{\psi_0}\right) \frac{B_0}{B} \qquad (11),$$

where ε is the index of anisotropic effect.
These equations include in the case of a scalar pressure and the low beta limit.

3-2. Data processing

Each point on the magnetic profile plots represents the average value of 51 data every 2 μs at the time interval from 150 μs to 250 μs for one shot in order to eliminate white noise. The shot number is 32 in the case of applying no choking field. In the case of applying choking field, there are profiles for 23 shots.

Plots in Fig.3 represent the average values in 32 shots and those deviations.

In order to fit a theoretical curve to the measured profile, the optimization of parameters has to be carried out by minimizing the value of the evaluation function defined as follows.

$$f = \sum_{j}^{shot} \sum_{i}^{ch} (B_{i}^{eq.} - \alpha_{j} B_{ij}^{obs.})^{2} \qquad (12),$$

where $B_{i}^{eq.}$, $B_{ij}^{obs.}$ and α_j are theoretical profile in total magnetic energy of 1 kJ, a measured profile for j th shot and a normalized factor for the total magnetic energy, respectively.
The parameters are estimated by using the simplex method.

3-3. Results

(A) Low beta limit

Substituting $\varepsilon=0$ and $P_0=0$ into eq.(8) - eq.(10), the equations are reduced to those in the low beta limit. The solid curve shows the fitting curve with optimized parameters. In this case, the standard deviation is estimated to be about 150 Gauss.

The obtained equilibrium profile is grossly fitted by a theoretical profile on assuming low beta limit. However, we observe a systematic discrepancy between a measured poloidal profile and a theoretical one as mentioned above, i.e. the measured value tends to the value smaller than the theoretical one assumed as low beta limit in the region of the outward profile from the magnetic axis. The toroidal fitting is also not so good.

(B) Scalar pressure ($\varepsilon=0$)

As taking the plasma pressure into consideration, this discrepancy tends to be dissolved to obtain a better fitting as shown in Fig.4, where the beta is postulated to be 10 % from the experimental result. If the parameter optimization including beta is performed, the beta value is estimated to be above 35%, which value is different from experimental result. The magnetic axis is observed to shift outward due to plasma pressure.

(C) Anisotropic pressure

The pressure along the magnetic line becomes larger than that perpendicular to the magnetic line with increase of anisotropic index . This anisotropic effect is postulated to be remarkable near the plasma boundary as shown in Fig.5. When $\varepsilon = 1\times10^{-3}$, the best fitting is obtained in comparison with other two cases mentioned above. The top of toroidal magnetic profile is found to be suppressed to fit on the measured plots as shown in Fig.6.
Degree of anisotropy defined as $2\zeta/\beta_{axis}$ is 5 % at maximum value.

4. Summary

Fine structure of magnetic configuration is discussed from an anisotropic point of view. Even in collisional state of our experimental condition (collision length is order of 10 cm), the anisotropy is estimated to be 5 %. This anisotropic effect will be important in collisionless plasma of spheromak configuration.

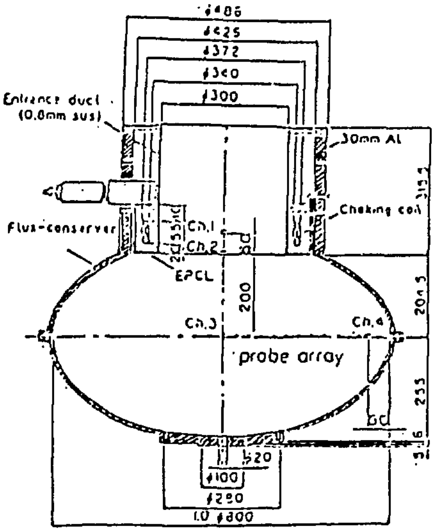

Fig.1 Setting of magnetic probe and choking coil

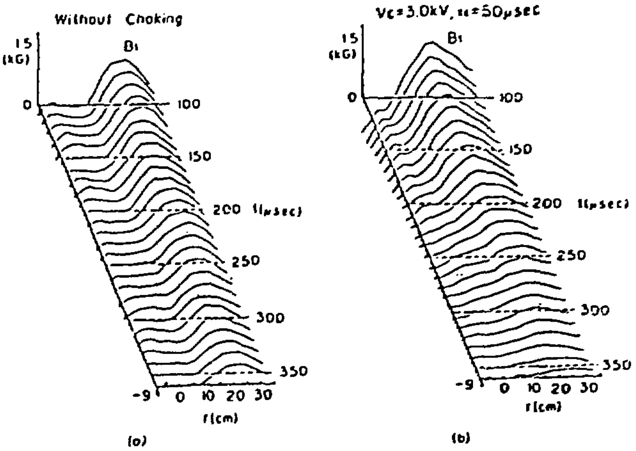

Fig.2 Toroidal field profile(R=-9~30cm)
(a) without choking field
(b) with choking field (Vc =3 kV)

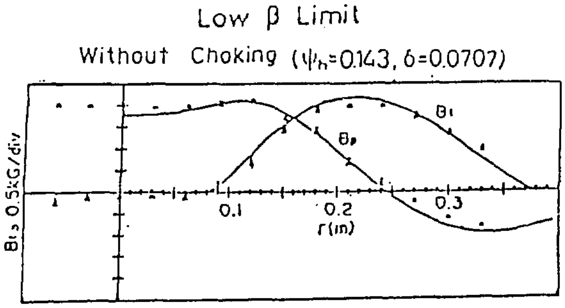

Fig.3 Measured profile without choking field and curve fitting for low beta limit (Ψ_h =0.14, δ =0.07, S.D.=145 Gauss)

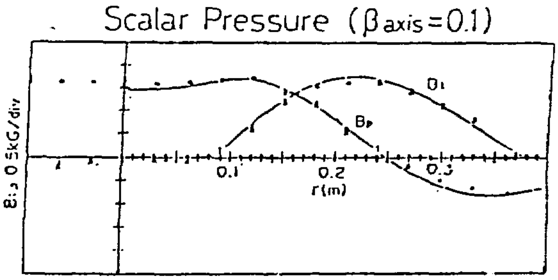

Fig.4 Curve fitting for scalar pressure (β_{axis}= 0.1)
(Ψ_h =0.14, δ =0.07, S.D.= 123 Gauss)

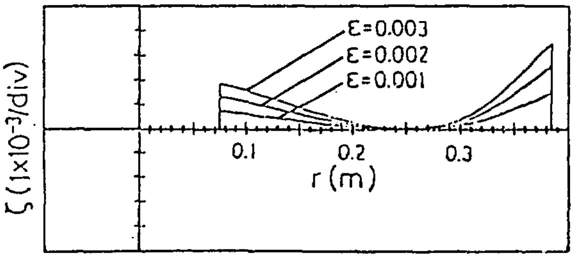

Fig.5 Radial distribution for index of anisotropy
(Ψ_h=014, δ =0.07,β_{axis}=0.1)

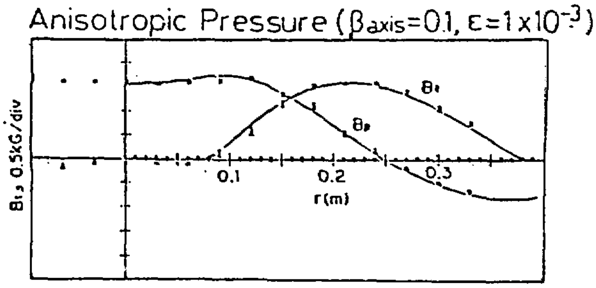

Fig.6 Curve fitting for anisotropic pressure (β_{axis}= 0.1)
(Ψ_h=0.14, δ =0.07, ε =1x10^{-3},
S.D.=100 Gauss)

COMPUTATIONAL SIMULATION OF COMPACT TOROIDAL PLASMA FORMATION

C. R. Sovinec, C. J. Clouse[1], J. H. Degnan, D. Dietz, and K. E. Hackett; Weapons Laboratory, Kirtland Air Force Base, NM 87117-6008

J. Buff, M. H. Frese[2], R. E. Peterkin, and N. F. Roderick, Mission Research Corporation, Albuquerque, NM 87106

I. INTRODUCTION

The following computational efforts are part of the MARAUDER (magnetically accelerated rings to achieve ultra-high directed energy and radiation) research program at the High Energy Plasma Division of the Weapons Laboratory. The program is investigating plasma toroids with magnetic fields similar to those of tokamaks. These fields confine the plasma between a pair of cylindrical conductors. The objective of the research is to first form such toroids and then compress and accelerate them. A 500 kJ capacitor bank will be used for the formation, and the 9 MJ Shiva Star will be used for acceleration. The first set of experiments and current computational work consider only the formation process.

The computer program used for these simulations is MACH2. It is a two-dimensional MHD code and was originally developed by Mission Research Corporation under a Weapons Laboratory contract to support z-pinch research. MACH2 is an Arbitrary Lagrangian-Eulerian code with an adaptive mesh capability. Its diffusion routines use a multigrid technique to accelerate convergence. Recently, a second-order advection scheme has been added.

II. SIMULATION DESCRIPTION

Figure 1 shows the calculational mesh for the simulation. The narrow section at the bottom is considered the "gun region" because it is essentially a magnetized coaxial plasma accelerator. The wide section is the "formation region" where the field will expand and reconnect forming the torus. In the MARAUDER experiment, the gun is 40 cm long. An array of sixty gas valves approximately 25 cm above the breech will puff neutral gas into the gun before the capacitor bank is fired. When the bank is switched, it will place a potential across the gap between the conductors. The gas will ionize and conduct current. The pressure from the resulting toroidal magnetic field will accelerate the mass upward.

This simulation simplifies this by truncating the gun at the valves. A "circuit boundary" that provides toroidal magnetic field based on a self-consistently solved current is placed at the bottom of the gun region. This is also an open boundary, and ionized hydrogen (5×10^{-6} kg/m^3 for this simulation) flows in as the magnetic field from the circuit pushes it. The entire ionization process is therefore simplified. The 108 μF capacitor bank is initially charged to 60 kV, and the portion of the circuit outside the computational region has 1 mΩ resistance and 27.5 nH inductance.

The initial poloidal field is also idealized. Two solenoidal coils, one inside the inner conductor, one outside the outer, will provide the field in the experiment. Steady-state calculations show it to be mostly radial in the upper half of the gun with the null point being near the valves. This is simulated by a purely radial field in the gun with a magnitude of 0.3 T at the inner conductor. This field is imbedded in a plasma with a 5×10^{-6} kg/m^3 density. Only a background density with negligible field is initially in the formation region.

Magnetic diffusion in the stainless steel walls occurs on a long time scale compared to the duration of the plasma torus, so Dirichlet boundary conditions are used to keep the fields at their initial values. Velocities are fixed at zero along the walls to keep the poloidal field lines from breaking during the hydrodynamics.

Resistive diffusion in the plasma is important for the reconnection of the poloidal field after the plasma has been pushed into the formation region. In this simulation a constant diffusivity of 250 m^2/s is fixed for all plasma above 1×10^{-7} kg/m^3. This gives a diffusion time of 0.4 μs for 1 cm. This is roughly the expected magnitude of the anomalous diffusion. Hopefully, comparison with experiments will provide more insight. A better resistivity model is planned. However, in the primitive simulations run without thermal conduction and radiative cooling, with only a temperature ceiling of 50 eV to keep temperatures reasonable, a better model may not yield more accurate results.

III. Results and Conclusions

This simulation is successful at producing a plasma torus. At 4 μs the toroidal field from the circuit has pushed the plasma and poloidal field into the formation region--see figures 2 through 5. The current peaked with 3.3 MA at 2.5 μs, and by 4 μs mass is flowing back out the bottom. This produces a rarefaction wave that travels up the gun. The velocities at the top of the gun at 4 μs are still upward along the poloidal field lines. At 6 μs the rarefaction wave has reached the top of the gun. The poloidal fields are then able to compress the flow, and the compression drives the reconnection. The torus is formed at 7 μs. At this time the mass density and toroidal magnetic induction in the center of the torus are 1.1×10^{-5} kg/m^3 and 0.24 T, respectively.

Comparisons between simulations that are successful at forming toroids and those that are not show an important relationship between the initial poloidal field strength, circuit energy, mass density, and resistivity. Successful simulations always have a large ratio of magnetic field energy to kinetic energy before reconnection. If mass density from the bottom boundary is too low, more circuit energy will end up in kinetic energy and less in toroidal field. This coupled with a weak poloidal field and a resistivity that is too high will not allow the pinch of the flow at the top of the gun. The field just diffuses across the mass and does not reconnect. The pinching seems critical to the reconnection. This is consistent with Axford's discussion of the reconnection process [1].

Future efforts will center on adding more accuracy to the simulation. They include a realistic initial mass distribution from the valves, an ionization model, and a better anomalous resistivity treatment.

---

[1] Present address: LLNL, Livermore, CA 94551

[2] Present address: NumerEx, Albuquerque, NM 87106

REFERENCE

1. Axford, W. I. "Magnetic Field Reconnection." Magnetic Reconnection in Space and Laboratory Plasmas. E. W. Hones, ed. American Geophysical Union, Washington, D. C., 1984.

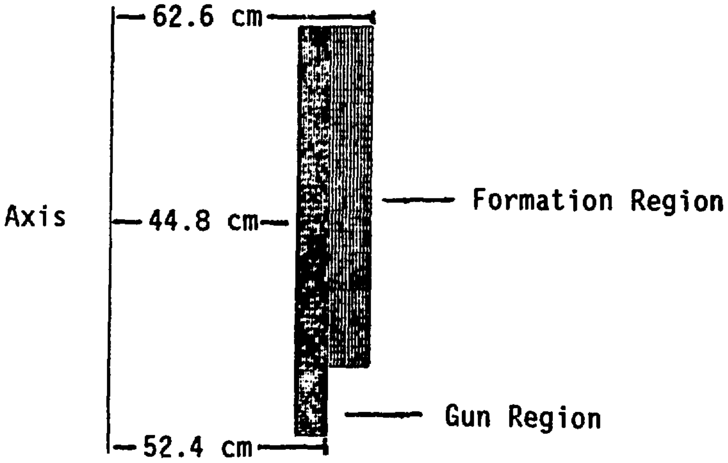

Figure 1. Computational mesh and experiment configuration.

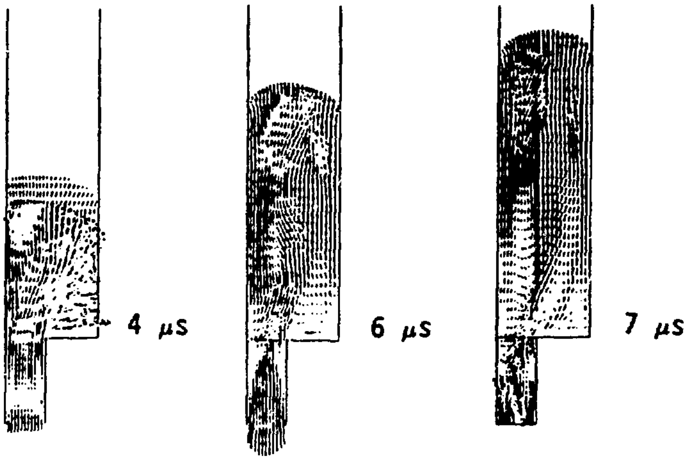

Figure 2. Velocity vectors.

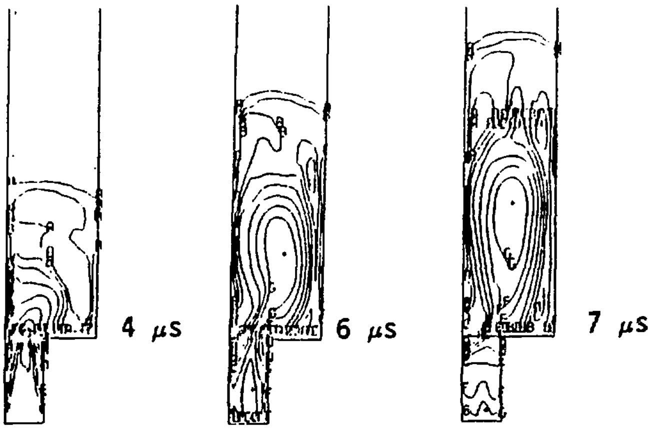

Figure 3. Mass density.

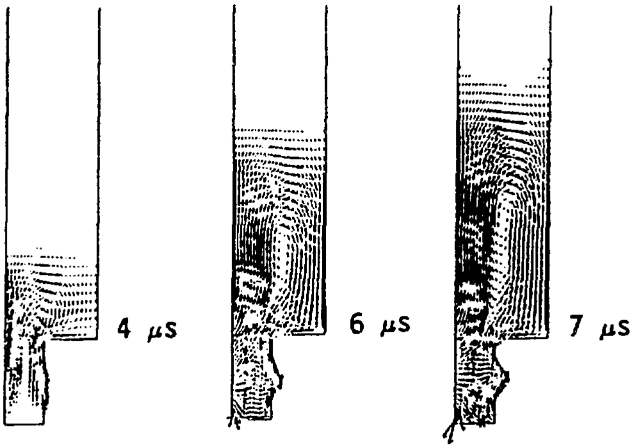

Figure 4. Poloidal magnetic field vectors.

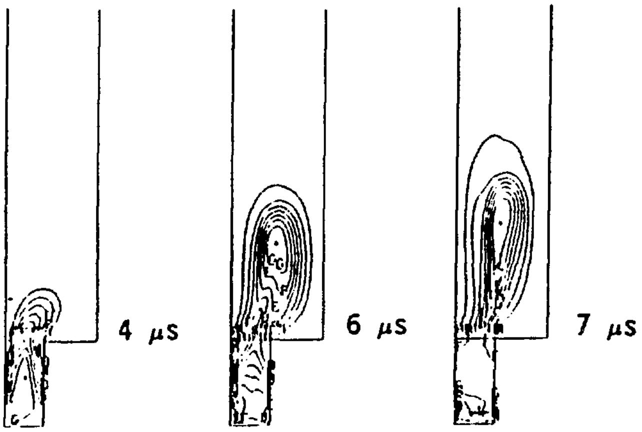

Figure 5. Toroidal magnetic field.

Structure of Maryland Spheromak Plasmas

Roger Hess, Cecil Chinfatt, Claude Cote, Alan DeSilva, Alex Filuk,
George Goldenbaum, Jean-Luc Gauvreau, and Fu-Kwun Hwang

Laboratory for Plasma Research
University of Maryland
College Park, MD 20742

ABSTRACT

Recent efforts on the Maryland Spheromak (MS) have concentrated on detailed measurement of magnetic field structures in order to better understand the formation and evolution of the spheromak configuration. These efforts were prompted by results showing a very rapid decay of the magnetic field under certain conditions. It was not known if this loss was a rapid movement of the plasma to the walls of the vacuum vessel, or by some mechanism causing a rapid decay of a more or less stationary field.

Magnetic probe data are shown in figure 1 for three shots that were nominally identical except for the magnitude of the bias magnetic field. The bias field magnitude determines the size of the spheromak configuration. The greater the bias field, the smaller the radius of the spheromak separatrix. These data were taken with an array of magnetic field probes in the midplane, and located at different radial positions. As figure 1 shows, with the smaller configurations, a very rapid loss of the magnetic field is seen after approximately 2.3 msec. To investigate the magnetic field structure in more detail, an array of magnetic probes was built that could be moved from shot to shot so as to acquire a complete map of the three magnetic field components in a plane containing the symmetry axis of the machine.

Figure 2 shows some data taken with these probes in a case where the rapid loss of field occurs. Figure 2a shows the B_z field as a function of R and Z at approximately the time of its maximum value. It is asymmetric with the peak field to the left of $R = 0$ on the graph. Figure 2b, 150 μsec later, shows that the field is peaked at about the same position, but has decayed in magnitude. Figure 2c, 28 μsec later, shows the peak has shifted to the right in the graph. Comparing (b) and (c), the configuration has shifted with a velocity of about $1 cm/\mu sec$.

Further analysis of the data shows that the instability that forms is a combination of tilt and shift. The initial asymmetry of the magnetic field is possibly due to the non-symmetric configuration of the reversal field coils,

or the non-symmetric cabling to the I_z electrodes.

Several configurations of conductors were installed in the machine to act as passive stabilizers to prevent the tilt/shift instability from occuring. A stainless steel cylindrical liner was installed surrounding the plasma except at the ends. This was used along with a cylindrical "hard core" conductor placed on the symmetry axis. Further tests were performed replacing the hard core with copper plates mounted near the ends of the machine and supporting aluminum cones projecting towards the center of plasma. All of these configurations had little effect on the tilt instability. Figure-8 type coils were then installed at the ends of the machine, where they could be positioned at different Z positions. While these coils did not prevent the instability, it was slowed, with the most effect being seen when the figure-8 coils were nearest to the plasma.

The waveform and timing of the I_z and reversal currents were also varied. The timing of the crowbar circuits for the I_z bank, as well as its timing with respect to the reversal bank, were found to have a strong effect on the life time of the magnetic field structure. The lifetime of the plasma could be substantially increased by crowbaring the I_z near peak current so as to prolong it as long as possible. Figure 3 shows magnetic field plots with longer I_z current, and with the figure-8 coils. The data show the same initial asymmetry as is seen in figure 2, but the rapid shift of the plasma does not occur, and the plasma decays slowly in place.

Efforts have been made to reduce radiation losses by decreasing impurities present in the plasma. Glow discharge cleaning, titanium gettering, and use of a metallic liner were all tried as methods to reduce the generation of impurities from surfaces within the machine. None of these methods had a substantial effect on impurity levels as determined from spectroscopic observations. Different I_z electrode materials were used to try to reduce impurities from that source. Stainless steel, Ta coated Al, and Elkonite (Cu/W allow) were used. The Elkonite electrodes gave the best results.

Future work will concentrate on eliminating the inital plasma asymmetry by eliminating any asymmetries in the machine, and on stopping the tilt/shift instability by different configurations for the passive stabilization coils.

Work supported by DOE

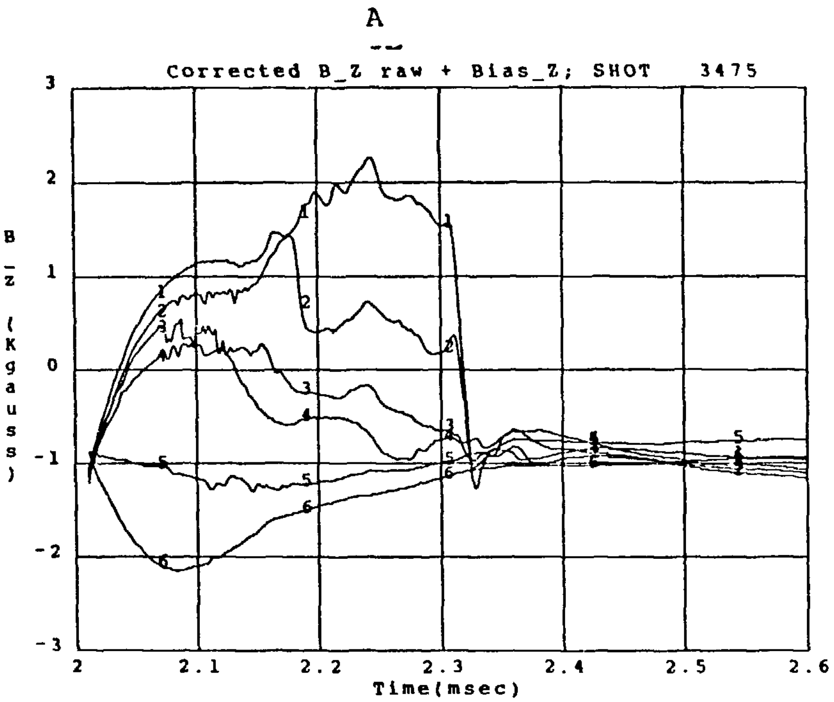

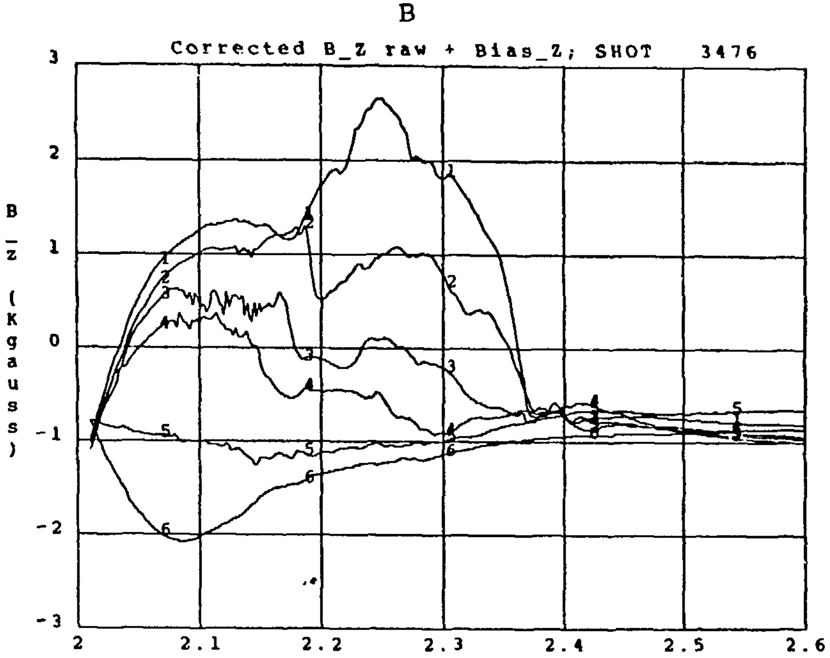

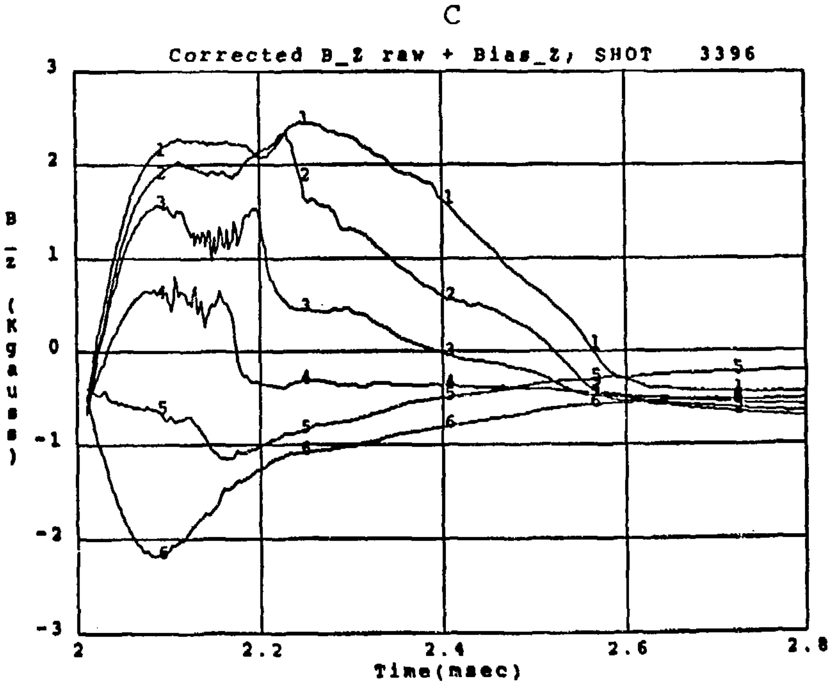

Figure 1. Bz component of field at Z=0 vs. time (discharge starts at 2.07 msec) at different radii. Current in bias coil (amp):
(a) 500 (b) 450 (c) 400.
Probe radial positions (cm):
(1) 5 (2) 12 (3) 20 (4) 28 (5) 35 (6) 43.

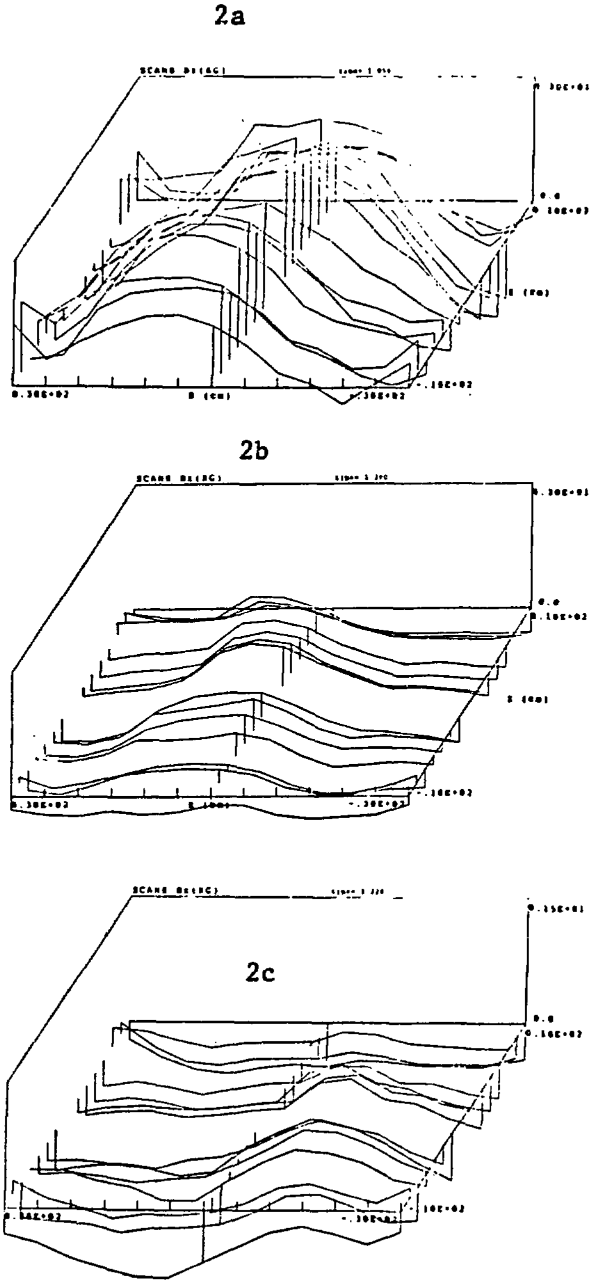

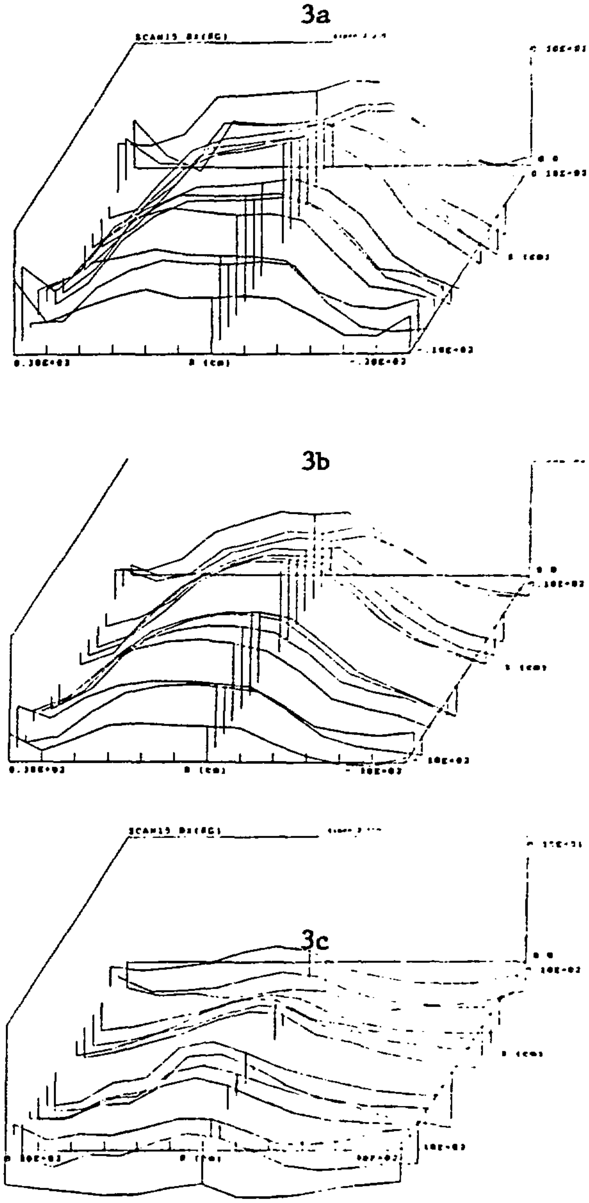

Figure 2: Bz as function of r and z.
Horizontal axis is R coordinate. Vertical axis is Bz (kG).
Depth axis is Z coordinate. Vertical lines are drawn at R=0 to show Bz at that position.
Time after start of discharge (msec): (a) 0.15 (b) 0.30 (c) 0.328.
Figure 3: Same as Fig. 2 with sustained Iz current.
Times: (a) 0.18 (b) 0.28 (c) 0.48.

Observations and Modelling of Electron Density on the Maryland Spheromak*

A. B. Filuk, G. C. Goldenbaum, C. Chin-Fatt,
A. W. DeSilva, R. A. Hess
Laboratory for Plasma Research, University of Maryland, College Park, MD, 20742

Introduction

Knowledge of a laboratory plasma's density is useful in calculating the plasma beta, for progressing to higher temperatures through lower densities, in studying particle transport, and in detecting the presence of large amounts of impurities or plasma compression. The multiple-beam interferometer diagnostic on the Maryland Spheromak [1] provides such information. Data have been collected under a wide range range of MS shot conditions. To better understand the observations, a computer model of particle/energy balance has been used. With the data and model, conclusions about the present MS conditions and projections for more desirable conditions can be made.

Density Diagnostic Results

The density diagnostic on MS is a multiple-beam quadrature laser interferometer. The laser wavelength is 632.8 nm, the plasma path length is about 75 cm (beams make two passes along this length); precautions are taken to minimize and account for background vibration effects. The interferometer is operated in two modes. In one case, 4 transverse beams pass through the $z = 0$ plane of the spheromak, along chords parallel to a major diameter. These 4 beams are scanned across half of the $z = 0$ plane to map out density as a function of chord parameter. With an assumption of axisymmetry, the data may be inverted to obtain a density profile $n(r,t)$. In the second mode, 3 transverse beams are used while a separate beam is directed axially down the length of MS, parallel to the plasma z axis. For visualizing line-averaged density $\overline{n}_e = \frac{1}{L}\int n_e\,dl$, a path length L was determined from the location of the plasma separatrix.

Data have been gathered under the variety of MS machine configurations: gettering, metallic liners, stabilizing aluminum end cones, various fill gases and electrode materials. In general, the plasma density only changed significantly in two cases. First, the density increased with increasing I_z discharge current in low density shots with tantalum-coated aluminum (Al/Ta) electrodes. However, the density observed was much higher than that expected from a fully-ionized gas fill, probably the result of substantial impurity content and compression during formation and relaxation. Second, the use of Elkonite electrodes, requiring operation at higher gas fills, resulted in an equilibrium/decay density was in good agreement with the fully-ionized fill. Table 1 compares results with Al/Ta and Elkonite

---

*Research supported by the US DoE.

electrodes. Figure 1 shows some typical line-averaged density data from 3 transverse beams

Electrodes	Fill (mT D_2)	Density if fully ionized	Pre-compression density observed	Peak density observed
Al/Ta	2, static	1.3	4-5	10
Elkonite	6, puffed	6-7	7	15-17

Table 1: Comparison of densities observed with two types of electrodes. All densities in units of 10^{14} cm^{-3}.

and 1 axial beam for a shot with Elkonite electrodes. The axial beam almost always indicated substantially larger density than the transverse beams during the decay phase of the discharge,possibly due to plasma streaming out along field lines at the ends of the spheromak.

From the decay of density after formation/relaxation, a particle loss time $\tau_p = 95 \pm 10\,\mu$s was found. Shots with helium in place of D_2 showed, after about 50 shots, 20% lower peak densities, but the density during the decay phase was almost halved, indicating a reduction in plasma refueling due to cleaner vessel wall conditions. Estimates of particle refueling rates yielded $5.9 \pm .9 \times 10^{18}$ s^{-1}cm^{-3} for D_2 shots, and $3.7 \pm .6 \times 10^{18}$ s^{-1}cm^{-3} for helium shots.

Figure 2 shows the result of an axisymmetric inversion to obtain the profile $n(r,t)$. The inversion method used is a variation of that due to Cormack [2,3,4]. Since the magnetic probe data showed a shifting of plasma center, the interferometer chord parameters were adjusted accordingly. It should be noted that the magnetic probe data also showed a degree of non-axisymmetry about the shifted center, introducing a significant amount of uncertainty into the inversion process. From the profile's approximate gradient length scale and the particle loss time, the average particle diffusion coefficient may be estimated and compared with theoretical estimates, as shown in Table 2.

MS (estimated) $D_\perp \simeq \frac{L^2}{\tau_p}$	Classical $D_\perp = \frac{\rho_i^2}{2\tau_p}$	Bohm $D_\perp \propto \frac{T_e}{B}$
1×10^6	6×10^5	6×10^4

Table 2: Comparison of estimated particle diffusion coefficients, in cm^{2}s^{-1}.

Computer Model

To better understand the mechanisms underlying the observed densities, a computer code was written to account for the particle flux and associated energy fluxes. This model for the plasma is similar to that used by others [5]. For practicality, and because detailed information about local plasma quantities is unavailable, a 0-dimensional model is used. The model also uses a coronal non-equilibrium treatment of impurities, since the $\simeq 70\,\mu$s timescales of change in MS may not be sufficient for equilibrium [6]. Power balance processes included are ohmic heating, radiation (bremstrahlung, dielectronic and radiative recombination, line, and charge exchange excitation), thermal conduction, electron-ion transfer, heating of influxing neutrals, ionization, lost ions, and charge exchange. It was found necessary to include self-consistent compression [7] in order to model the MS data.

Figure 3 shows code results for a run in reasonable agreement with the density data for a shot with Elkonite electrodes. Other than the presence of various impurity ions detected spectroscopically, there was no temperature history available to fit the model to. With sufficient compression to fit the measured density, the compressed magnetic field was too strong to agree well with the measured field. However, in modelling present MS shots, the code results were relatively insensitive to small changes of parameters; the code indicated a cold ($T_e \simeq 11$ eV), radiation-dominated plasma. A readily obtainable 40% increase in discharge current and hypothetical 40% decrease in density would result in plasma temperatures of about $20eV$, according to the model. In fact, hot plasmas ($T_e \simeq 50$ eV) are predicted only if the density can be reduced to $1-2 \times 10^{14}$ cm^{-3}.

Conclusion

Density observations with the multiple-beam interferometer, and density modelling with the 0-dimensional code, portray the MS plasmas obtained to date as dense, cold, and radiation-dominated. Apparently, the only feasible way to substantially increase the temperatures is to lower the density. Presently, the lower bound of MS density is determined by breakdown of the fill gas, whether static fill or puff. Some form of pre-ionization of this fill is required, and a microwave pre-ionizer has been constructed for MS. The code's usefulness in predicting desirable operating conditions could be improved by having a temperature history from MS; a probe measurement would be sufficient for the present low-temperature plasmas, while laser scattering would likely be needed for hotter plasmas.

References

[1] A. B. Filuk and G. C. Goldenbaum, *Bull. Am. Phys. Soc.* **33** 1923 (1988).

[2] A. M. Cormack, *J. Appl. Phys.* **34** 2722 (1963).

[3] A. M. Cormack, *J. Appl. Phys.* **35** 2908 (1964).

[4] Y. Nagayama, *J. Appl. Phys.* **62** 2702 (1987).

[5] C. W. Barnes, T. R. Jarboe, H. W. Hoida, B. L. Wright, R. A. Hulse, D. E. Post, *Nucl. Fus.* **25** 1657 (1985).

[6] P. G. Carolan and V. A. Piotrowicz, *Plasma Phys.* **25** 1065 (1983).

[7] D. D. Meyerhofer, R. A. Hulse, E. G. Zweibel, *Nucl. Fus.* **26** 235 (1986).

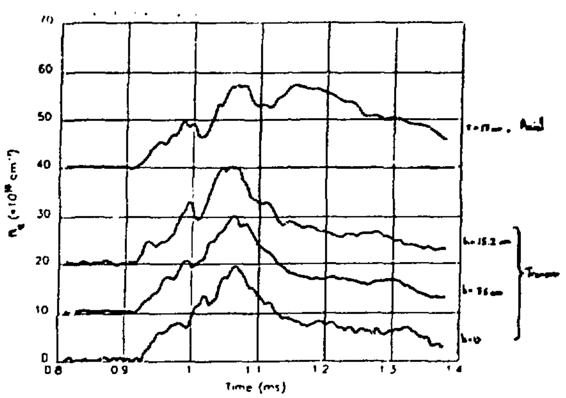

Figure 1: Time histories of 3 transverse beams and 1 axial beam of line-integrated densities. Transverse beams are located 0, 7.6, and 15.2 cm away from the machine axis, while axial beam is at r =17 cm.

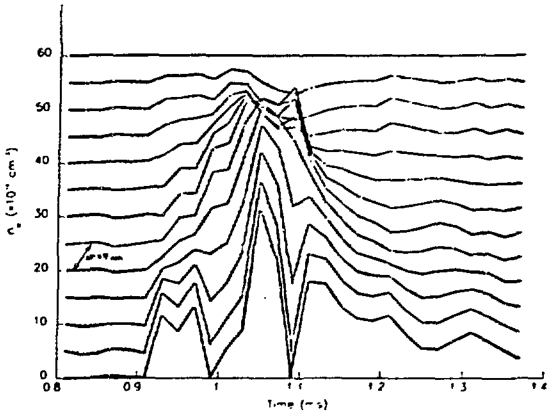

Figure 2: Density profile $n(r,t)$ using the inversion method of Nagayama.

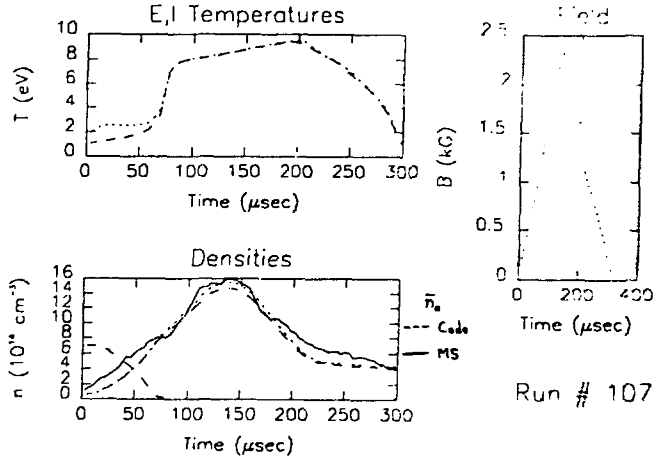

Figure 3: Computer model results for an Elkonite electrode MS shot, showing temperature, density, and field histories. On density plot, solid line is MS interferometer data, while dotted line is code result.

Observation of wavelength profiles during formation in the Maryland Spheromak. *

J.-L. Gauvreau, G. C. Goldenbaum, C. Chin-Fatt, A. W. DeSilva,
R. A. Hess
Laboratory for Plasma Research
University of Maryland, College Park, MD, 20742

Abstract

Observations of the line widths of OII(4591 Å), OIII(3059 Å) and OIV(3063 Å) at 15 cm off the symmetry axis have a Gaussian profile and show maximum ion temperatures of 30±10, 75±20 and 90±20 eV respectively. Higher temperatures are obtained on the axis. However, with a stainless steel liner surrounding the plasma, line profiles appear to be non-Gaussian under some conditions, indicating some motional Doppler effects. Velocities in the order of 1 ± .25 cm/μs are measured in the poloidal direction. Toroidal velocities of .5 ± .25 cm/μs could be present at formation on and off the midplane. Spatial pictures taken with the OMA from the end of the machine in the UV and in the visible show an asymmetric emission of light from the electrodes, possibly indicating a nonuniform breakdown of the plasma. The use of Elkonite instead of stainless steel for the electrodes removed most of the chromium lines, but copper lines are now more intense.

INTRODUCTION

An Optical Multichannel Analyser (OMA) is used to study the light emission profiles from the Maryland Spheromak (MS) in order to estimate the electron and ion temperatures as well as any possible flow speed. When coupled with a spectrometer and the proper optics, we can obtain spatial and wavelength resolution simultaneously. The OMA is sensitive over a broad range of the spectrum, from 2000 Å to 8000 Å. It is basically an array of 500 x 500 detectors that can accumulate light for a period ranging from 1 μs to several hundred μs; for our intensities, 10 to 30 μs is sufficient. It therefore takes several shots to scan a time evolution of the spectrum. We are using a 1 meter spectrometer, and the grating has a blaze angle optimized for 10,000 Å. For a selected time, a 50 Å wide spectrum of visible light can be seen in second order with a resolution of .1 Å. The entrance slit of the spectrometer maps a 10 cm line in the plasma. The head of the OMA is divided in several tracks in the spatial direction, each

---

*Work supported by the US DoE.

track corresponding to one line of sight. The two principal lines of sight are radially, 12.5 cm away from the midplane and paraxially at r=15 cm. See Fig. 1. For a single wavelength setting of the spectrometer, OIII(3059 Å) and OIV(3063 Å) can be seen simultaneously in third order, CIII(2297 Å) in fourth order and OII(4591 Å) in second order. A thorium lamp is used for wavelength calibration.

ION TEMPERATURE

Assuming Doppler broadening, we use the ion line widths to determine the plasma temperature. Maximum ion temperatures of 30±10, 75±20 and 90±20 eV are obtained for OII, OIII and OIV respectively for a 4 mTorr deuterium fill. The temperature observed roughly scales as the inverse of the fill pressure. Fig. 2 shows the temperature behavior in time of the three oxygen ion species for a 6 mTorr helium fill and an I_z rise time of 100 μs (slow mode). Lower ion temperatures are achieved for an I_z current rise time of 40 μs (fast mode). Radial line of sight and paraxial line of sight give similar temperatures.

Despite cooling the OMA in order to increase the signal to noise ratio, we did not observe CV (2271 Å). This puts an upper bound of about 70 eV on the electron temperature. However, results from a zero dimensional plasma simulation code [1], indicate that the impurity radiation barrier probably keeps the electron temperature below 20 eV. Ion temperature of OII(4591 Å) as measured with a 3/4 meter monochromator and a P.M. tube looking on axis gave 90±15 eV at formation time, in disagreement with the OMA measurements. This could be due to motional Doppler effects on axis. At later times the monochromator gives 30±10 eV, in agreement with the OMA.

TOROIDAL AND POLOIDAL MOTIONS

When looking parallel to the axis at r=15 cm, non-Gaussian profiles were observed with a liner surrounding the plasma. If the line profiles are fitted to two Gaussians, velocities of about ±1cm/μs are calculated. A small toroidal velocity of .5± .25 cm/μs might be present at formation time. See Fig. 3. This was measured with a fast I_z current discharge and off the midplane. More measurements will be made.

SPATIAL PICTURES

The OMA was also used as a time framed camera by setting the spectrometer to zeroth order and by removing the entrance slit. Using different filters, we took pictures in the UV and at different visible wavelengths. Pictures were taken on axis with a view of all the electrodes. These pictures show that each electrode is not emitting the same intensity of light,possibly indicating a nonuniform breakdown of the plasma. This nonuniformity persists throughout the life of the plasma with some shot to shot variations.

IMPURITIES

After opening the machine, a dozen cleaning shots are needed before we can get reproducible results. The impurity content of the plasma is then dominated by oxygen.

nitrogen, carbon and copper, the latter coming from the Elkonite electrodes. Residual Gas Analysis shows a high content of nitrogen, water vapor and oxygen, as well as argon in smaller amounts.

CONCLUSION

In summary, ion temperatures of 70 eV and higher are obtained for OIV(3063 Å) in a deuterium as well as helium plasma. This is about three times the estimated electron temperature. Turbulance at formation and motional Doppler effect could be a factor. Evidence for a small toroidal motion exists on and off the midplane. In similar spheromak experiments [2] [3] multiple rings of toroidally flowing plasma have been found during the formation phase. Rotation is also expected in MS [4]. We will investigate further the toroidal motion on and off the midplane. Time framed pictures taken of the electrodes indicate a possible nonuniform breakdown at formation. To further investigate this, individual electrode current measurements will be made using Rogowski coils.

References

[1] A. B. Filuk, G. C. Goldenbaum, C. Chin-Fatt, A. W. DeSilva, R. A. Hess, Proceedings of the eleventh US-Japan compact toroid workshop (1989).

[2] T. Peyser and G. C. Goldenbaum, Phys. Rev. Lett. **61**, 955 (1988).

[3] B. Barrow and G. .C. Goldenbaum (to be published).

[4] P. N. Guzdar, J. Finn, K. W. Whang and A. Bondeson, Phys. Fluids **28**. 3154 (1985).

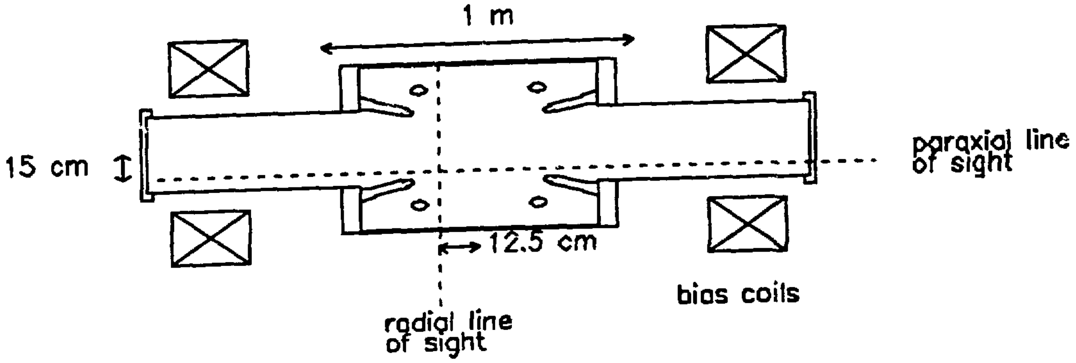

TOP VIEW OF MS CHAMBER

Fig.1 Set up

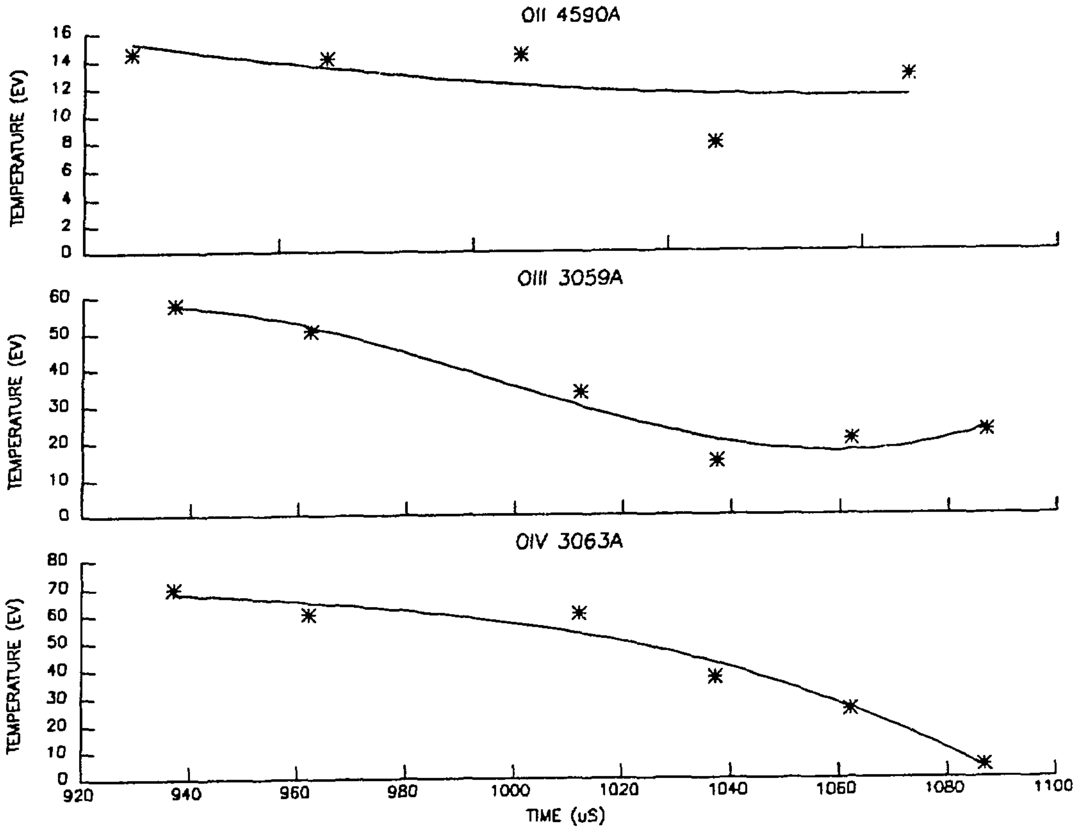
OII 4590A
OIII 3059A
OIV 3063A
TEMPERATURE (EV)
TEMPERATURE (EV)
TEMPERATURE (EV)
0
2
4
6
8
10
12
14
16
0
10
20
30
40
50
60
0
10
20
30
40
50
60
70
80
920
940
960
980
1000
1020
1040
1060
1080
1100
TIME (uS)

Fig. 2

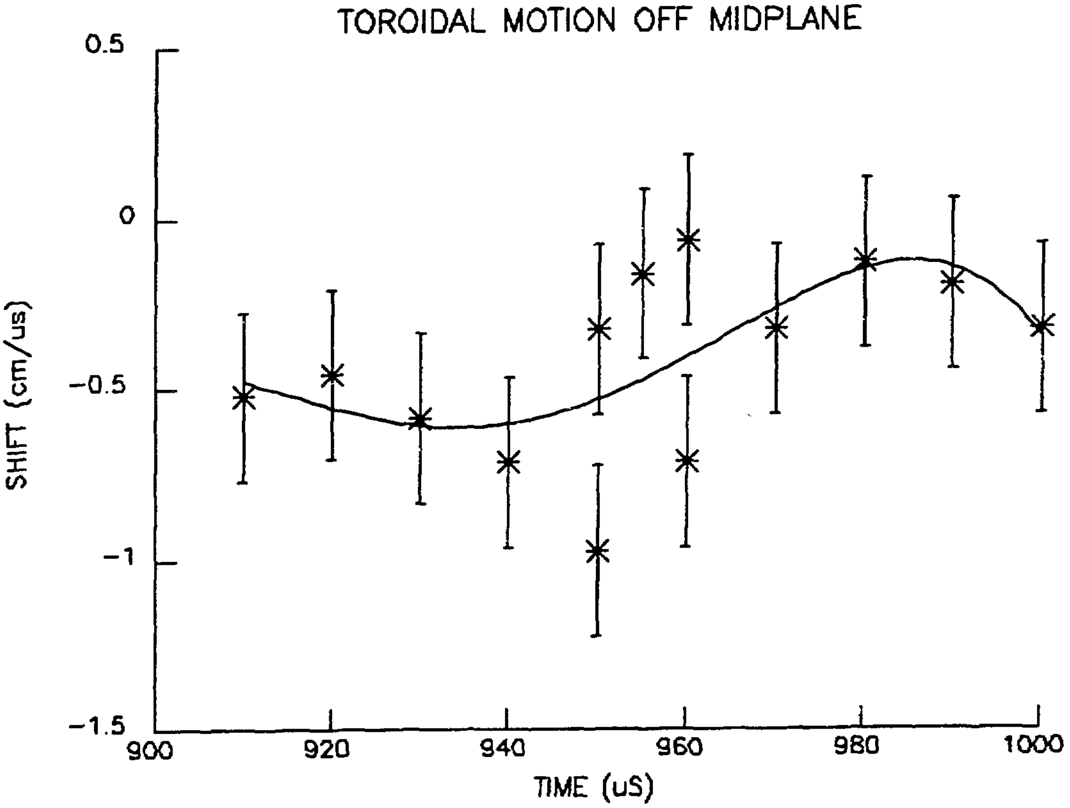
TOROIDAL MOTION OFF MIDPLANE
SHIFT (cm/us)
0.5
0
-0.5
-1
-1.5
900
920
940
960
980
1000
TIME (uS)

Fig. 3

Bolometry, Spectroscopy, and Doppler T_i Measurements in High Current Density CTX Spheromaks[*]

J. C. Fernández, R. M. Mayo, F. J. Wysocki, I. Henins, T. R. Jarboe[†] and G. J. Marklin

Los Alamos National Laboratory, Los Alamos, NM 87545

Presently, the CTX facility is aimed towards increased magnetic field and magnetic-energy decay time (τ_{B^2}) of small spheromaks. Such spheromaks are appropriate for compression with a solid wall driven by high explosives, for the purpose of accelerating a metallic projectile to high velocities[1, 2]. Towards this goal, clean He spheromak plasmas with volume-averaged magnetic fields $\sqrt{\langle B^2\rangle_{vol}} \approx 1$ T in a cylindrical flux conserver (0.28 m radius and length) have been studied extensively. These are typical clean discharges obtained with gun main-bank voltages of 5–5.5 kV, such as those studied with Thomson scattering[2]. This paper will concentrate on the spheromak-decay phase. In all these discharges, the plasma gun is turned off at time 200 μs.

The experimental geometry is illustrated in Fig. 1. In a spheromak at the minimum-energy state (uniform j/B), expected to occur at time 250–400 μs, B_3 (see Fig. 1) accurately represents $\sqrt{\langle B^2\rangle_{vol}}$. In this paper, the spheromak magnetic energy content $W \equiv \int B^2 dvol$ and τ_{B^2} will be

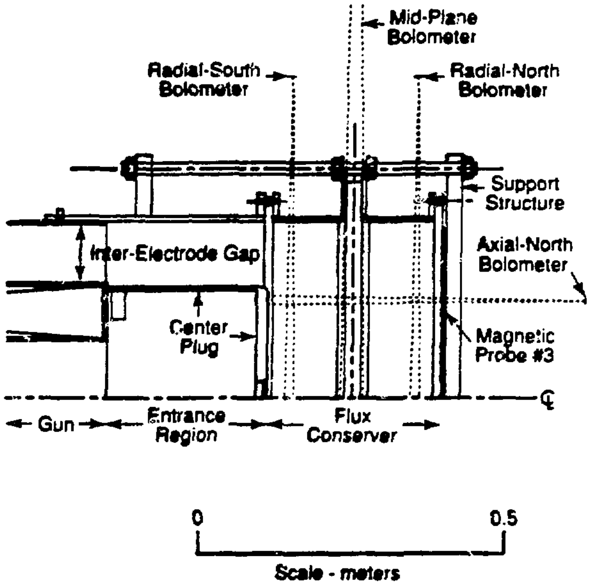

Figure 1: This figure illustrates the experimental geometry, including the copper flux conserver, the plasma gun, the copper entrance region and associated copper center plug, and the support structure. One of four magnetic-probe arrays (located at 90° toroidal intervals), which measure the spheromak poloidal magnetic field at the surface, are illustrated. In particular, magnetic probe # 3 (which measures B_3) is indicated. The four bolometer lines of sight are shown. The remaining plasma diagnostics provide measurements at the spheromak midplane.

---

[*] This work is supported by the US DOE.

[†] Present address: Univ. Washington, Seattle, WA 89195

calculated using only B_3. A more accurate estimate valid throughout the spheromak evolution requires fitting the data from all the probes to the results from an MHD equilibrium code[3]. These results have not yet been obtained.

The impurity radiation has been quantified by simultaneous measurements from four bolometers described previously[4]. All four have new apertures subtending a 1.6° angle. As shown in Fig. 1, three bolometers view along axially-displaced diameters ($z = 0$ and ± 0.103 m), while the fourth views axially ($r = 0.16$ m). As a typical example, discharge 18666 has initially $W = 28$ kJ during decay, and has completely decayed by $t = 875$ μs. During decay, the radial–south bolometer measures 8 J/m^2, corresponding to a radiated-energy density of 280 kJ/m^3. (The electrical noise level on the bolometers is $\approx$ 0.25 J/m^2.) The mid–plane and radial–north bolometers measure 0.5 J/m^2 (17.5 kJ/m^3) and 2.5 J/m^2 (87.5 kJ/m^3), respectively. A simple average of these three chords yields a total of 9$\pm$0.6 kJ (128$\pm$9 kJ/m^3) of radiation. As a consistency check, the axial-north bolometer observes 1.25 J/m^2 (87.5 kJ/m^3), corresponding to 6 kJ. Thus we conclude the spheromak radiates 9$\pm$3 kJ ($\approx$ 1/3 of its magnetic energy) during decay, and thus the main energy loss channel is not radiation. Near the walls, the radiation density is much higher (higher signals from the radial–south and radial-north bolometers), as expected. However, the much higher radiation density at the south side is surprising. This may be rooted in the tendency of these spheromaks to tilt, for a short period, into the entrance region immediately after sustainment, perhaps lifting impurities from the wall in the process.

In these discharges, the n=2 rotating kink-mode[3], appearing 100-200 μs into the decay, degrades particle confinement[2], as previously observed[4] in the 0.67 m radius mesh flux conserver (MFC). MFC plasmas were dominated by the effects of magnetic-field penetration into the wall (field errors)[5]. This is contrary to the behavior in the 0.61 m radius, solid flux conserver[6], designed to minimize field errors. In addition, once the n=2 mode reaches a certain amplitude and rotation frequency, the magnetic field decay changes from exponential to linear in time, with a serious degradation of τ_{B^2}. This is illustrated in Fig. 2. This behavior, similar to that in the MFC, suggests the dominant presence of field errors. The quantitative relation between the n=2 mode and the degradation in τ_{B^2} is presently under study.

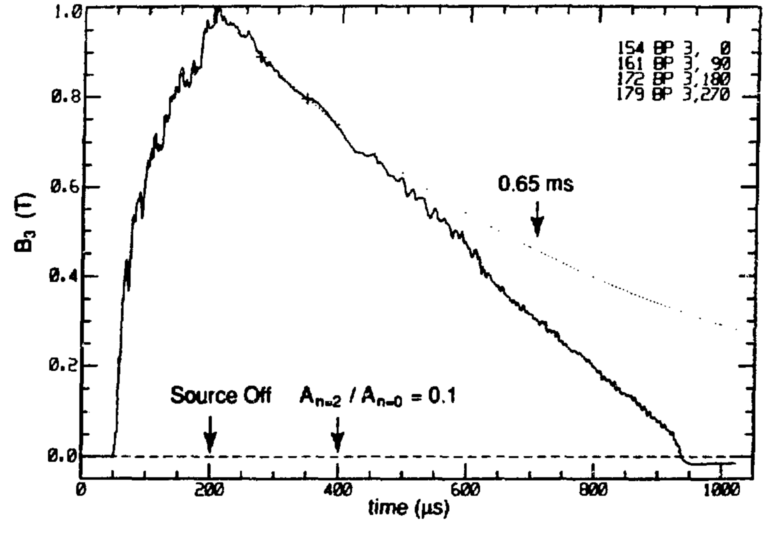

Figure 2: This figure is a plot of the azimuthally–averaged B_3 versus time for typical discharge 18662.

In these discharges, up to three different UV atomic radiation lines are simultaneously moni-

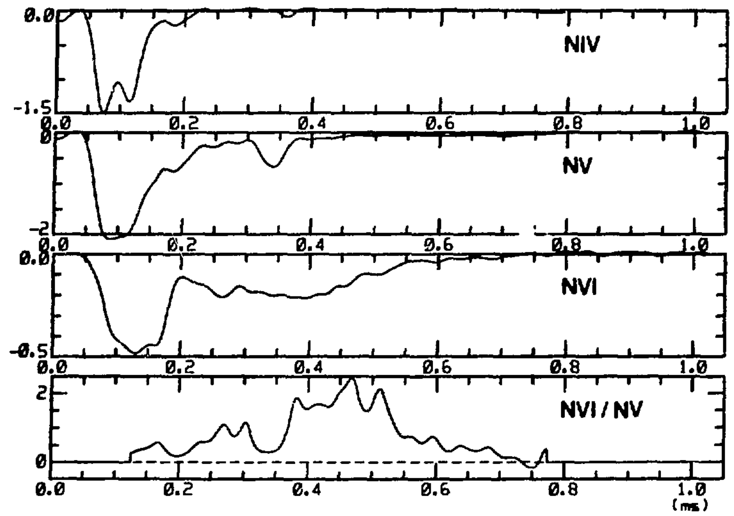

Figure 3: This figure is a plot of radiation intensity (arbitrary units) versus time (ms) from, (top to bottom) NIV (1718.6 Å, $E_e = 23.4$ eV), NV (2980.8 Å, $E_e = 88.4$ eV), NVI (1896.8 Å, $E_e = 426.3$ eV), and the ratio NVI/NV, as seen by single-chord spectrometers pointed at the geometric axis along the midplane. E_e is the excitation energy of the line. The NIV, NV and NVI signals are time-averaged with a 50 μs low-pass filter.

tored. Colder lines like CIII (intense during early spheromak sustainment) disappear soon after the source is turned off, in contrast to hotter lines like CV and NVI, which grow in intensity until the n=2 kink mode becomes too large and the density pump-out begins. As an illustration, discharge 18493 (Main Bank voltage of 5 kV) has a maximum B_3 = 0.85 T, exponentially decaying with τ_{B_3} = 550 μs until 450 μs. Subsequently, B_3 decays linearly with a 1.3 T/ms slope. Fig. 3 shows the time history of NIV, NV, NVI, and the ratio of NVI/NV. One important caveat is that different lines might come from different plasma locations. Otherwise, the data is consistent with nitrogen, initially in the spheromak early during sustainment, almost completely burning through to He-like NVI during a relatively short t = 100–450 μs period. Even late NIV and NV bursts around 350 μs do not persist. The NVI/NV ratio, rising until 450 μs, is consistent with the increasing T_e (up to 400 eV at 310 μs in a similar discharge) observed with Thomson scattering during early decay (before the n=2 kink mode grows significantly)[2]. The decreasing NVI signal and NVI/NV ratio after 450 μs coincides with the density pump-out associated with the n=2 kink mode. Although this might suggest a falling T_e (presently unmeasured at such late times), the uncertainties introduced by the decreased particle confinement time and by profile effects cast serious doubts over such a conclusion.

Doppler-temperatures T_D from various lines have been obtained using the polychromator previously described[5]. The polychromator is now movable on the mid-plane, allowing it to scan chords with tangency radii in the 0-0.22 m range (relative to the geometric axis). At any available tangency radius, the HeII T_D never significantly surpasses 100 eV. This probably reflects overwhelming HeII emission from the colder plasma edge. Multichord T_D of OV (2781.0 Å, E_e = 72 eV) and of CV (2270.9 Å, E_e = 304 eV) have been obtained. The ion temperature and emission profiles appear to be fairly flat (subject to the uncertainties associated with the inaccessibility of chords with larger tangency radii). Fig. 4 shows the quality of a typical fit for CV. The time history of both the OV and CV T_D is similar to that observed on the MFC. T_D is typically in the 750–1000 eV during sustainment, when the current profile is peaked towards the outer flux surfaces (and the n=1 kink mode is active). After the source is turned off and the spheromak current profile flattens, T_D decays towards the 200-500 eV level. The current profile further peaks towards the inner flux surfaces (the large-amplitude n=2 kink mode appears), and T_D increases back up to its previous level during sustainment. This is illustrated in Fig. 5, the T_D history for OV at a tangency radius of 0.22 m (discharge 18656). This anomalous ion heating has been associated with the modes providing strong relaxation current drive at the outer flux surfaces, which intersect the wall and have a very high-resistivity plasma[5]. This interpretation is consistent with the degraded linear decay of the magnetic field, coincident with the anomalous ion heating later during decay[4]. Azimuthal rotation of these impurities (indicated by the relative line shift evolution observed with the polychromator) associated with the rotating kink mode has been detected. A more detailed study of this motion is proceeding.

Acknowledgements: The authors acknowledge the expert technical assistance of Robert Bollman, Dennis Martínez and Richard Scarberry.

References

[1] I. Henins *et al.*, these proceedings.

[2] F. J. Wysocki *et al.*, these proceedings.

[3] S. O. Knox *et al.*, Phys. Rev. Lett. **56**(8):842, 1986.

[4] J. C. Fernández *et al.*, Nucl. Fusion **28**(9):1555, 1988.

[5] J. C. Fernández *et al.*, Nucl. Fusion 1990 (in press).

[6] F. J. Wysocki *et al.*. Phys. Rev. Lett. **61**(21):2457, 1988.

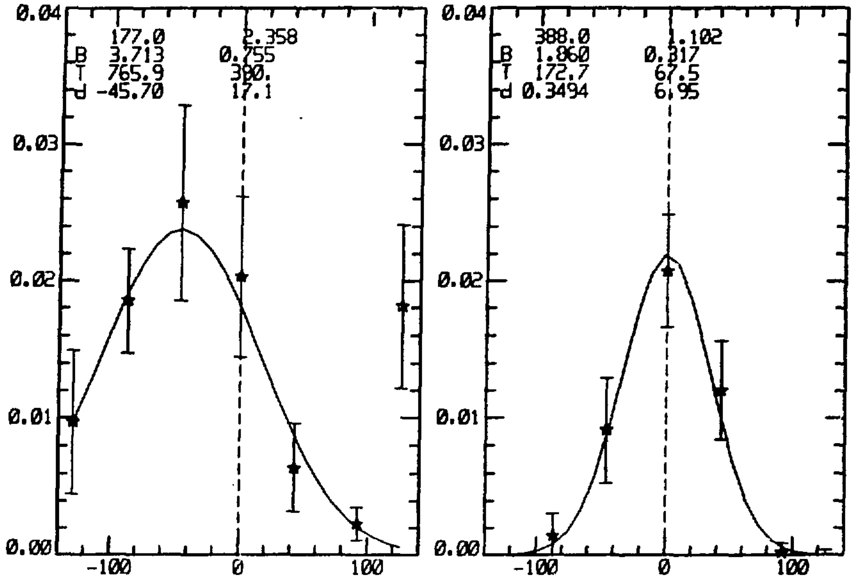

Figure 4: This figure is a plot of radiation intensity (arb. units) versus wavelength (pm) at the seven polychromator channels from the CV line in discharge 18459 at t = 177 (left) and 388 μs (right). The values for brightness (B), temperature (T) and wavelength displacement (d) (and their corresponding uncertainties), as derived from the Gaussian fit, are indicated in each plot.

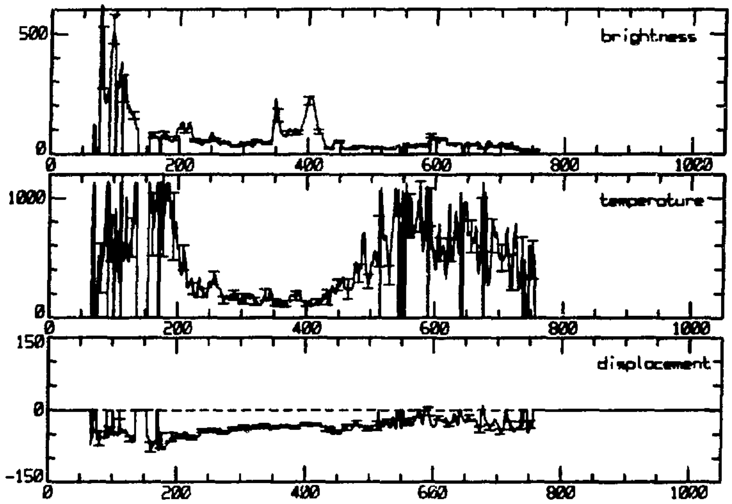

Figure 5: This figure is a plot versus time (μs) of, (from top to bottom) the OV line brightness (arb. units), T_D (eV), and the wavelength displacement (pm) of the line relative to the nominal wavelength dial setting (accurate to about 1/2 Å).

MHD Stable High Beta Spheromak Equilibrium*

G. Marklin
Los Alamos National Laboratory

Recent observations of a pressure driven mode in CTX[1] indicate that its performance is being limited by the low beta stability requirements typical of conventional spheromak designs. Improved designs with higher beta limits therefore have the potential to dramatically increase the temperature and lifetime of CTX and other spheromak experiments. This paper describes the results of an optimization study examining radically different geometries, but all with minimum energy current profiles which can easily be created experimentally and should be automatically stable to all ideal and resistive current driven modes.

The starting point is the general solution for axisymmetric Taylor states in spherical coordinates[2]

$$\psi\,(r,\theta) = \sum_{l=1}^{\infty} C_l\, r \sin\theta\, j_l(\lambda r)\, P'_l\,(\cos\theta)$$

where $\lambda = \mu_0 j_{||}/B$ is constant. This gives a minimum energy magnetic field configuration for any set of coefficients C_l. Conventional spheromaks are typified by the pure $l = 1$ term which has a very low beta limit of ~0.2%. The addition of an $l = 3$ component can create a variety of radically different shapes, some of which have much higher beta limits. Closed flux surfaces exist for $-40.0 \leq C_3/C_1 \leq 0.4$, with the maximum beta limit of 3.0% (volume averaged) at $C_3/C_1 = -40.0$. This configuration is called the bowtie and is shown in Figure 1. The high beta is achieved by having a short connection length between the "poles", reducing q to a low value at the edge and increasing the shear. Since this is one of the general Taylor solutions, it will be stable to current driven modes provided there are no nonaxisymmetric Taylor states with lower energy per unit helicity λ. This has not been checked but should be satisfied because of the highly oblate structure.

The beta limits were computed nonselfconsistently by evaluating the Mercier criterion using the stated zero beta analytic equilibrium for each value of C_l, and finding a pressure profile that would produce marginal stability at every flux surface and integrating it to get the beta limit.

A bowtie flux conserver designed to interface with the CTX plasma gun is shown in Figure 2 with a typical equilibrium solution. The plasma gun attaches at the right. The pressure and q profiles are also shown. In an experiment the plasma would be sustained by helicity injection from some source. This requires a nonuniform λ profile. Since helicity is injected at the edge and "flows" downhill in λ, the λ profile will have to be peaked at the edge and decrease monatomically toward the center. This is modelled by taking

$$\lambda(\psi) = \bar{\lambda}\ [1 + \alpha(2\psi - 1)]$$

with $\alpha < 0$. During sustainment a spheromak will usually run with α sufficiently negative to produce an $n = 1$ instability which provides the necessary dynamo activity to transport the helicity to the center. Figure 3 shows a.) the $\langle\beta\rangle$ limit and b.) the q values at the center and the edge, and the ideal MHD stability eigenfrequencies for c.) the $n = 1$ and d.) the $n = 2$ mode as a function of α for the bowtie configuration. The hash is due to numerical uncertainty caused by lack of resolution. These are again nonselfconsistent because they assume a zero beta equilibrium.

The $n = 1$ mode becomes unstable at $\alpha \sim -0.7$ which would imply sustained operation at $\langle\beta\rangle \sim 10\%$; however, the $n = 2$ mode is weakly unstable at $\alpha \sim -0.3$ which would make $\langle\beta\rangle \sim 5\%$. Since the $n = 2$ mode is only weakly unstable, it can probably be eliminated by fine tuning the geometry. This would make the spheromak operate at the higher 10% beta limit. This is an order of magnitude improvement over the standard tuna can configuration.

* This work supported by DOE contract No. W7405-ENG-36.

[1] F. J. Wysocki et al., *Phys. Rev. Lett.* 61, 2457 (1988).

[2] M. N. Rosenbluth and M. N. Bussac, *Nucl. Fusion* 19, 489 (1979).

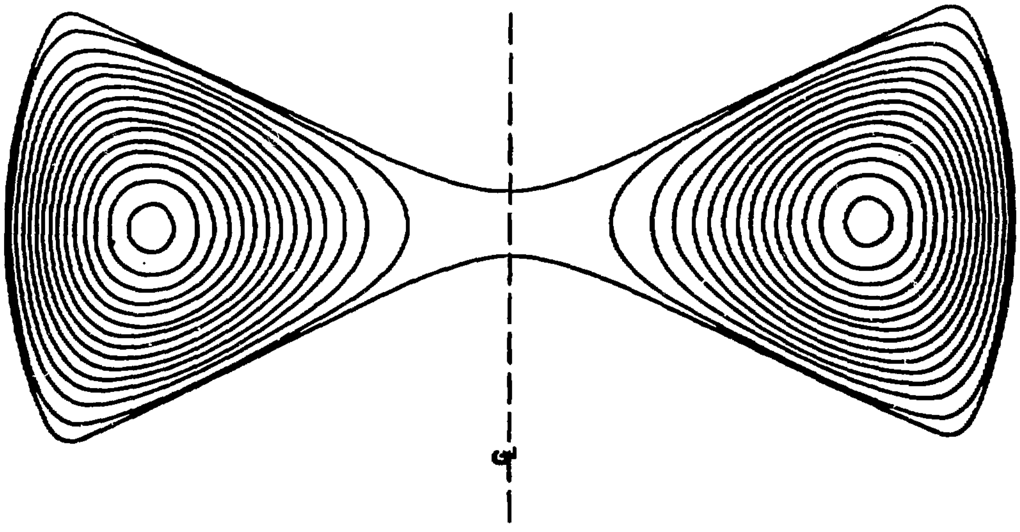

Figure 1 The Bowtie.

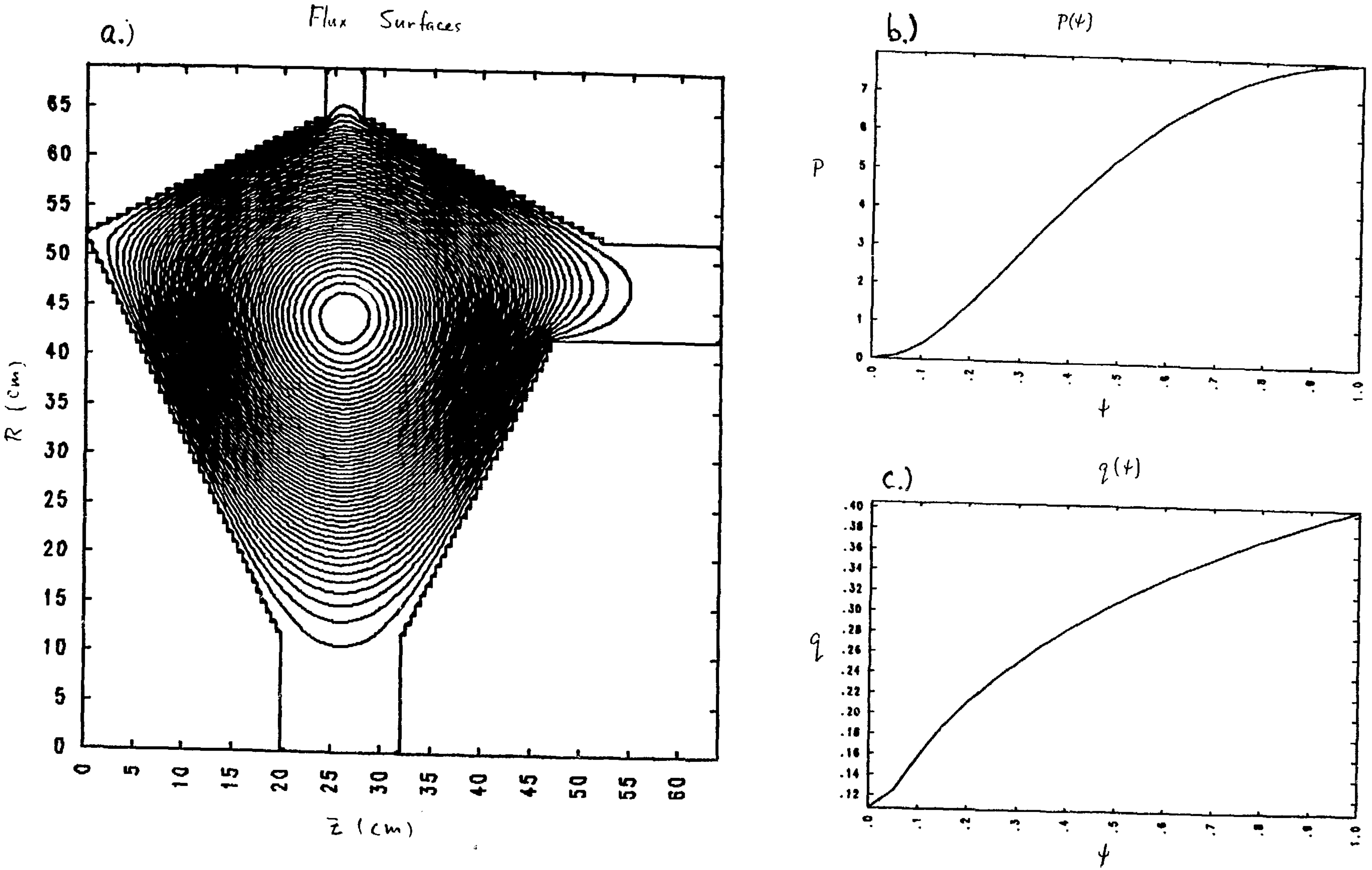

Figure 2 a.) Bowtie flux conserver for CTX.

b.) Prussure v.s. flux function.

c.) q profile v.s. flux function.

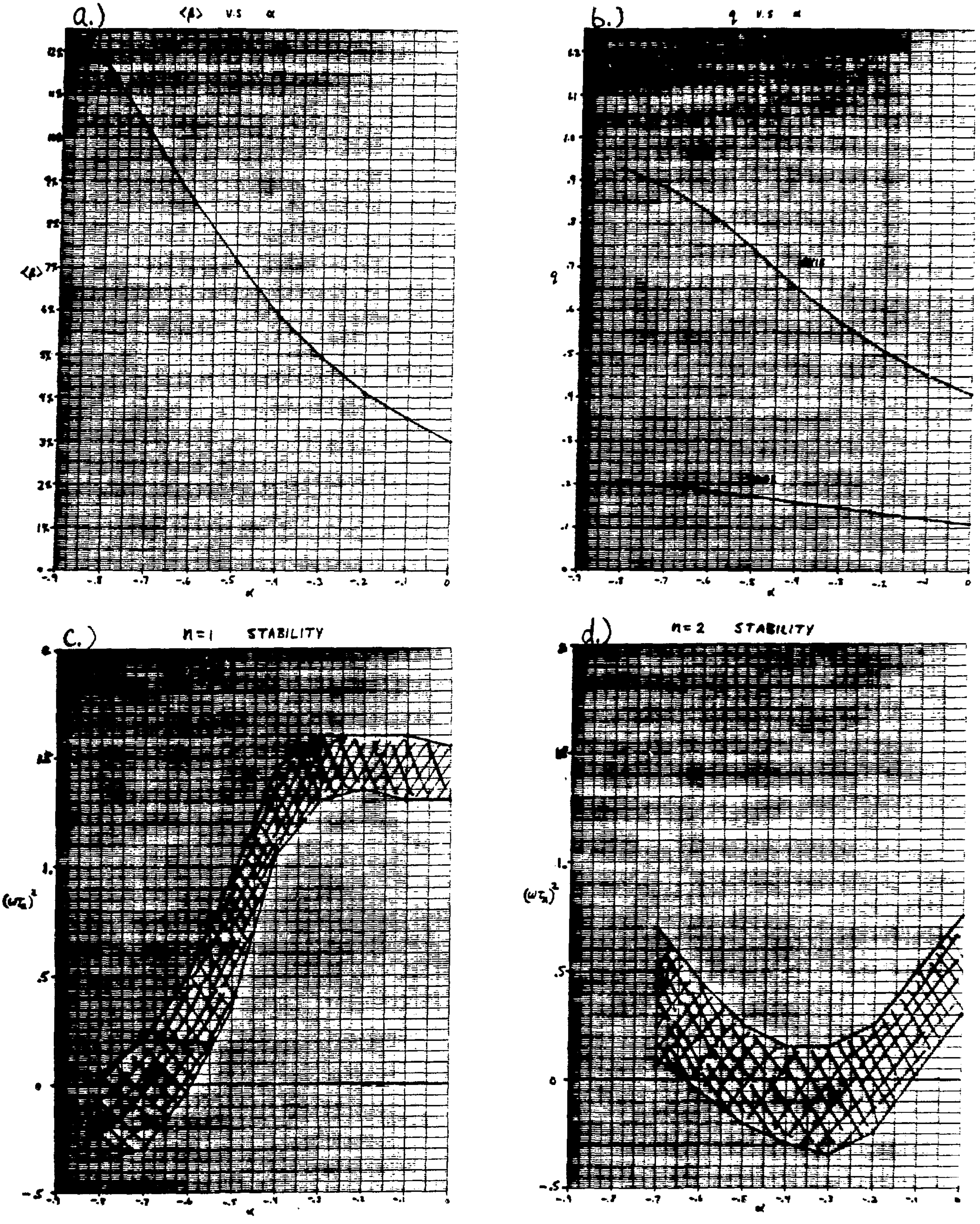

Figure 3 a.) Volume averaged beta v.s. alpha. b.) q at center and edge v.s. alpha.

c.) n=1 stability eigenfrequency. d.) n=2 stability eigenfrequency.

Progress with Small, High-Magnetic-Field Spheromaks in CTX*

F. J. Wysocki, J. C. Fernández, I. Henins,
T. R. Jarboe†, G. J. Marklin, and R. M. Mayo

Los Alamos National Laboratory,
Los Alamos, NM 87545

INTRODUCTION

The current CTX program is directed towards using spheromaks as an energy transfer medium to accelerate metal plates to hypervelocity. In the proposed scheme, the spheromak is first compressed by accelerating a large plate to moderate velocity (3 – 5 km/s) with high explosives (HE). Another smaller plate is designed such that it experiences little force until the spheromak is compressed to a size comparable to the small plate. Then the force on the small plate rises quickly, accelerating this plate to high velocity. Figure 1 shows the present design for a proof-of-principle experiment. Present theoretical calculations indicate velocity gain of the small plate over the large plate as high as four (geometry not the same as Fig. 1), which could produce 20 km/s small plate velocity. In principle, the final velocity is limited only by the sound speed of the spheromak (which is very high), and in practice, is probably limited by ohmic heating in the plate (leading to melting), the amount of energy that can be delivered to the large compression plate, and the energy dissipated by the spheromak during compression. Taking these effects into account, final velocities in the range 40 – 100 km/s might be achievable.

Final velocities approaching 100 km/s will require compressed spheromak energy densities comparable to that of HE ($B \approx 100$ T). The desire to keep the quantity of compression HE down to moderate levels (of order 100 pounds) dictates small initial spheromak size ($\lesssim 0.3 - 0.4$ m). Thus, it is necessary to be able to produce small spheromaks with as high an initial magnetic field strength as possible. A proof-of-princple, velocity gain greater than one, experiment probably requires the initial maximum internal spheromak field to be $\gtrsim 3$ T, and future experiments may require $\gtrsim$10 T. In addition, the spheromak magnetic energy dissipated during compression should be minimized. Although compression times of 80 – 100 μs are short compared to magnetic decay times in large (0.5 – 1 m) spheromaks, the decay time drops as the spheromak is compressed to small size. Thus, it is desirable to have the spheromak as hot as possible, and any "anomalous" resistivity should be minimized. Figure 2 shows the expected velocity gain as a function of both the initial maximum internal magnetic field and the initial magnetic decay time, for the geometry shown in Fig. 1.

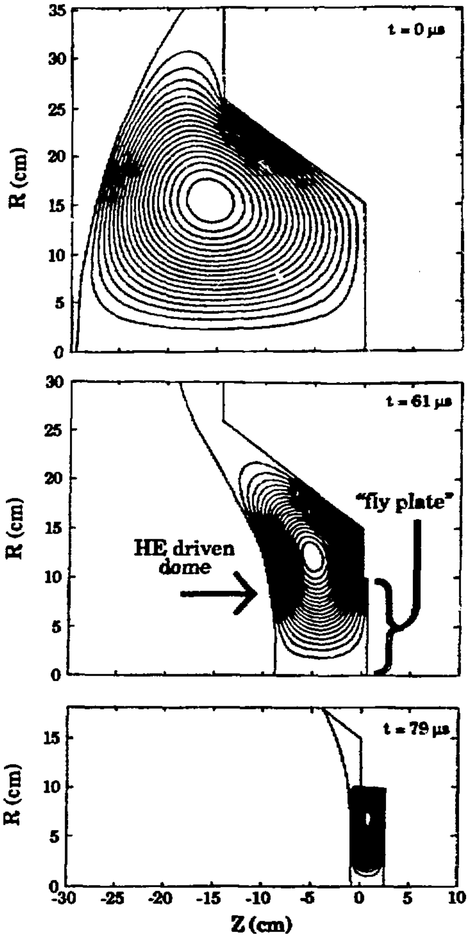

Figure 1: Numerical simulation of spheromak dynamics in the presence of a compressing dome. The "fly plate" is the small plate that is accelerated (starting at ≈ 79 μs) to hypervelocity. Spheromak resistive decay is included in this simulation.

The CTX facility is being used to develop needed techniques to produce small, high-field, low-resistance spheromaks in the laboratory. This will soon include testing a new plasma gun which is inexpensive enough to eventually "blow up" at an HE firing site. The present experiments use the same gun which was used for the 0.67-m mesh flux conserver and the 0.61-m solid-wall flux conserver experiments. Figure 3 shows the new solid-wall low-magnetic-field-error flux conserver that has been installed with both radius and length equal to 0.28-m,

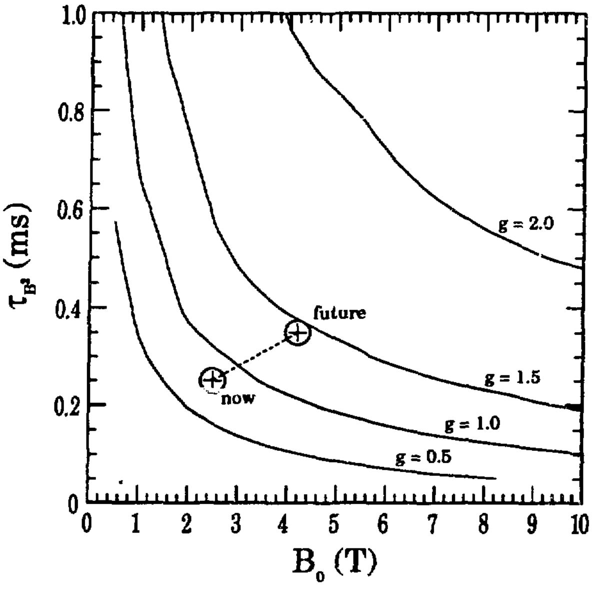

Figure 2: Required initial decay time vs. initial internal spheromak magnetic field for velocity gain of 0.5, 1.0, 1.5, and 2.0. The dashed line connects the point of present spheromak parameters with that we expect in the near future.

which is equal to the outer-electrode radius of the gun. The inter-electrode spacing is no longer a small perturbation on the spheromak. The advantage of this arrangement is the increased energy efficiency of the gun due to better λ matching of the gun and the spheromak. In addition, the external capacitor bank circuit has been changed to give shorter ($\approx$ 180 μs), higher-powered pulses to the plasma gun.

RESULTS

The highest maximum internal field obtained to date is ≈ 3.5 T, but the majority of the data obtained thus far is from spheromaks with $\approx 2.2 - 2.6$ T maximum internal field. The longest spheromak lifetime is ≈ 1 ms for these conditions. Thomson scattering electron temperature profiles show T_e as high as 350 – 400 eV. (Ability to measure still higher temperatures requires a modification to the Thomson scattering spectrometer, which is currently underway.)

In many figures in this report, reference is made to the value B_3 (measured by the four magnetic probes at position #3 seperated by 90° toroidally, see Fig. 3). For reference, the maximum internal field is roughly 2.2 times as great as B_3, and 1 MA of toroidal plasma current produces 1.3 T for B_3.

Several interesting types of spheromak behavior have been observed in this flux conserver. The spheromak tends to n=1 tilt (or kink) globally into the entrance region after sustainment, which has not been observed before in CTX. This is related to the fact that the flux conserver diameter is now exactly the same as the gun and entrance region diameters. Fortunately, this tendency is substantially reduced for the hotter spheromaks obtained, as shown in Fig. 4. Another observation is the degradation of energy and particle confinement times, which is associated with the standard n=2 kink mode present during decay of hot spheromaks, shown in Fig. 5. While this phenomenon was previously observed in the mesh-walled flux conserver, the degradation was attributed to the large magnetic field errors. The n=2 kink mode had no apparent degradation on discharges in the 0.61-m solid-wall flux conserver, which used a low-field-error design. The present flux conserver also has a solid wall and is designed to have few field errors. The new data indicate a source of field errors that was not anticipated. Possibilities include the entrance region, which is perforated with 1" diameter holes, 2" center to center (for historical

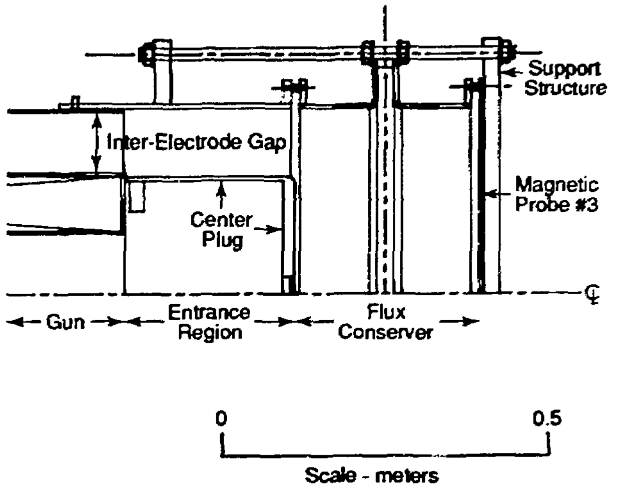

Figure 3: This figure shows the present small flux conserver used in CTX (made of OFHC copper). Also indicated are the end of the plasma gun, the entrance region and associated center plug (both made of OFHC copper), the magnetic probes (seven positions indicated, each with 4 probes seperated by 90° toroidally), and the support structure. The magnetic pressure developed in present spheromaks was causing the flux conserver to crack. The support structure (made of 304SS) was installed to prevent cracking. The position of the probes which give the B_3 data refered to in the text is indicated.

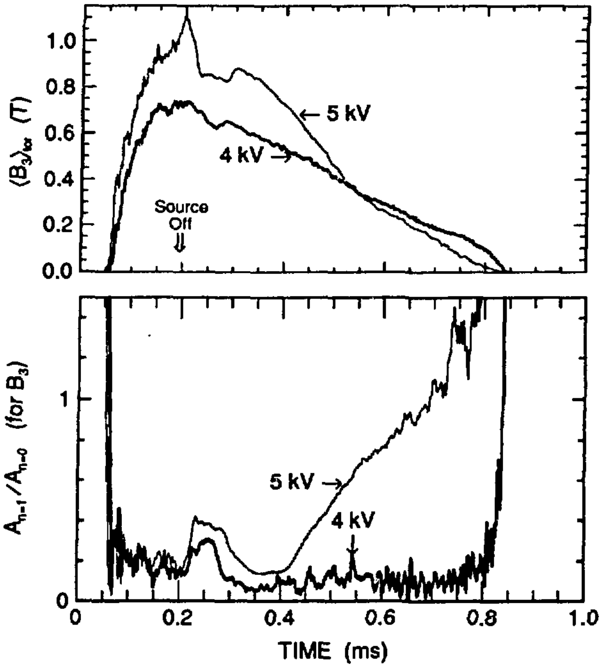

Figure 4: This data indicates the behavior of the n=1 distortion which is frequently observed after sustainment for two sequential discharges. The quantity $A_{n=1}/A_{n=0}$ represents the ratio of the amplitudes for the n=1 distortion to the axisymmetric state, as determined by the B_3 data (see Fig. 3). Notice the growth and decay of the mode between $t = 0.2$ to $t \approx 0.3$ ms in both discharges, however only the 5 kV discharge distorts starting at $t = 0.4$ ms (the voltage refers to the capacitor bank voltage for the gun). Thomson scattering data at $t = 0.41$ ms indicates that the 4 kV discharge had central electron temperature and density of 145 eV and 1.8×10^{14} cm^{-3}, while the 5 kV discharge had only 48 eV and 5.6×10^{14} cm^{-3}. While hot discharges without n=1 distortions have been produced at 5 kV (see Fig. 5 for example), there tends to be strong n=1 distortion for colder discharges regardless of bank voltage.

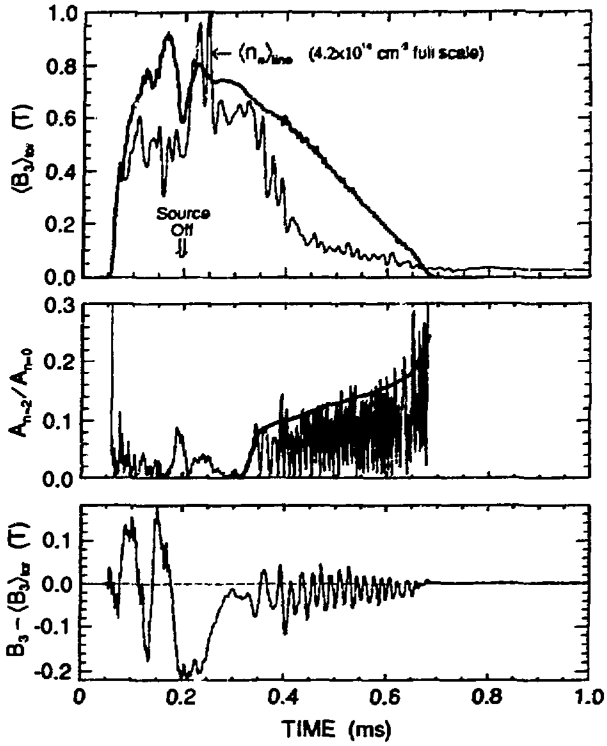

Figure 5: This data indicates the degradation of particle and energy confinement times correlated with n=2 activity normally present during decay of hotter discharges. The quantity $A_{n=2}/A_{n=0}$ represents the ratio of the amplitudes for the n=2 mode to the axisymmetric state, as determined by the B_3 data (see Fig. 3). The fast oscillatory behavior after $t = 0.34$ ms is an artifact of the simplistic technique used to obtain $A_{n=2}$; the real value is the envelope, as indicated by the heavy line. Notice the "pump out" of plasma density starting as soon as the n=2 activity starts, and the increased decay rate of B_3 starting ≈ 0.08 ms later. The detriment is believed to be caused by unexpected magnetic field errors.

reasons), rounded corners with too small a radius of curvature leading to flux penetration, and the fact that the flux conserver is (unfortunately) distorded and out-of-round. Additionally, the comparatively large inter-electrode spacing may make the n=2 kink mode intrinsically more detrimental. An effort to understand this situation is ongoing.

The data in Figs. 6 – 8 summarize some of the best results obtained in the latest configuration. The line average density is obtained from the CO_2 interferometer, and the Thomson scattering data is from the multi-point system, which covers an entire radius of the flux conserver, and is absolutely calibrated for density using Raman scattering in nitrogen.

ACKNOWLEDGMENTS

The authors acknowledge the expert technical assistance of Robert Bollman, Richard Scarberry, and Dennis Martinez.

* Work supported by Los Alamos National Laboratory Internal Scientific Research funds.

† Present Address: University of Washington, Seattle, WA 89195

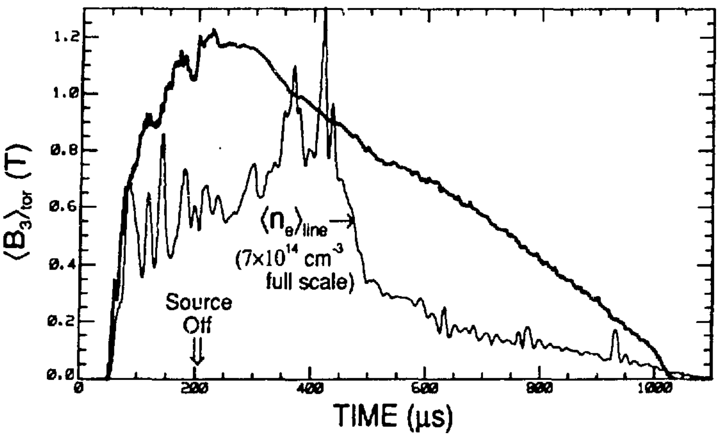

Fig. 6. This figure shows a long lived, high field discharge. The highest field produced at present is 1.6 T wall field, but these discharges are not yet optimized, and therefore do not last as long.

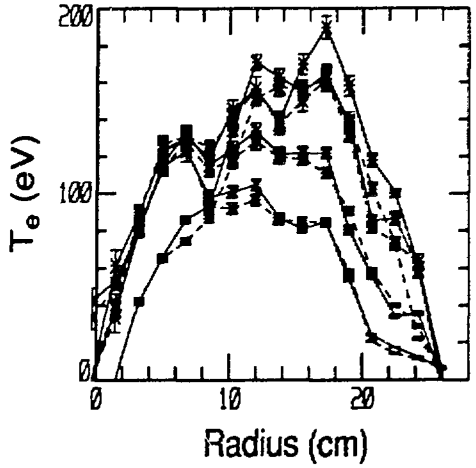

Fig. 7. This figure shows the Thomson scattering data at 260 μs from four discharges with 1.0 T maximum wall field and ≈ 6×10^{14} density at the laser firing time.

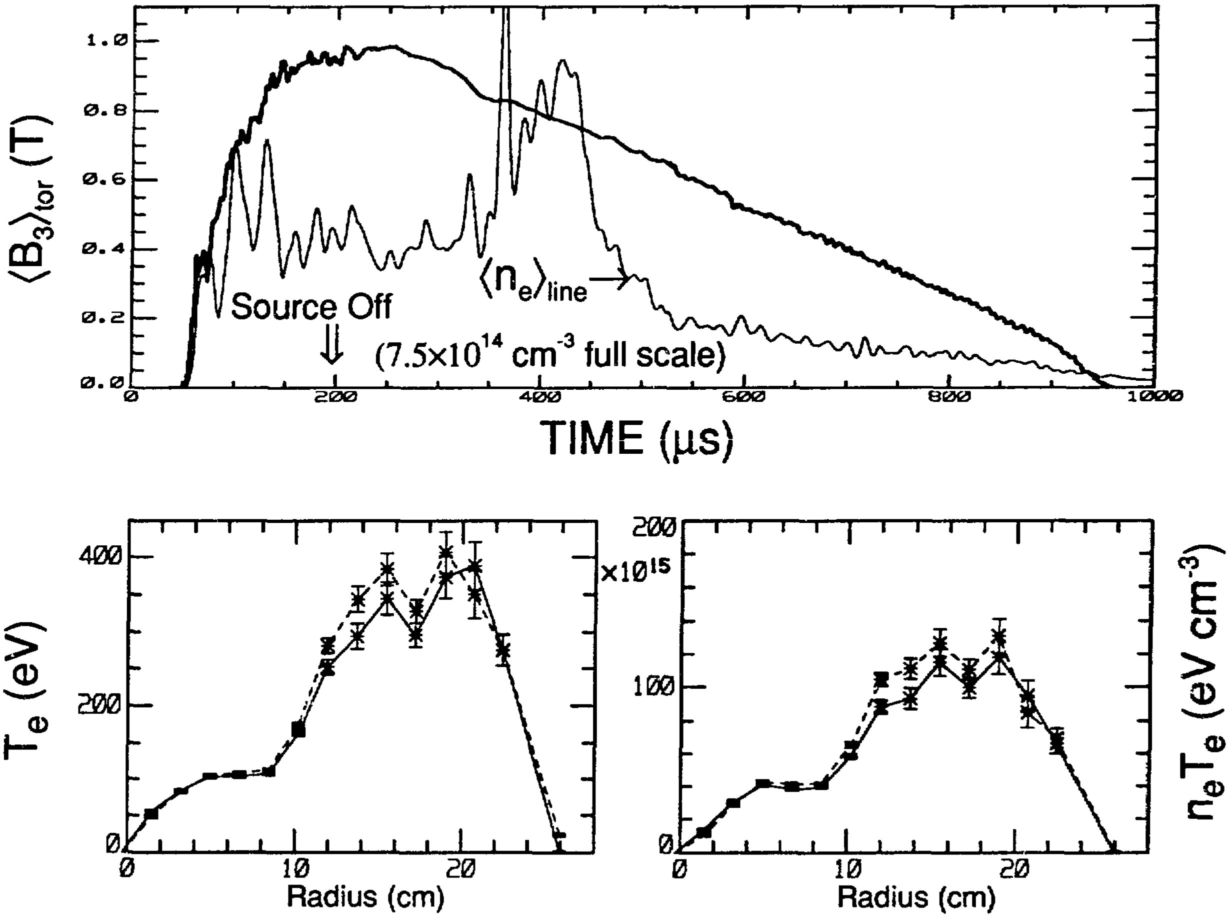

Fig. 8. This figure shows the wall field and density vs time, and the Thomson scattering data at 310 μs for one of several discharges with data above 200 eV.

Recent Progress on the HESS Experiment

R. M. Mayo, D. C. Barnes, B. Freeman, I. Henins, T. R. Jarboe,* and D. Platts

Los Alamos National Laboratory, Los Alamos, NM 87545

I. Introduction

The new objective of the Los Alamos spheromak program is to assess the use of magnetized plasmas as an energy transfer medium to accelerate material objects to hyper-velocities ($\gtrsim$ 20 km/s). In meeting this objective, we are committed to the subordinate goals of (1) creating high field, long-lived spheromak discharges, (2) examining the technical feasibility of employing High Explosives (HE) to compress seed spheromaks, and (3) investigate the technical requirements involved in forming spheromaks by Mechanical Helicity Injection (MHI) using HE. This paper describes the recent efforts of the CTR-5, M-4, and M-6 groups at Los Alamos in assessing the feasibility of generating magnetic helicity by mechanical means in the High Explosive Spheromak Source (HESS) experiment.

II. The HESS Experiment

A technique for the direct conversion of mechanical energy into magnetic helicity has been theoretically considered in a recent paper by Barnes, *et al.*.[1] In this work, the scenario of MHI is described. Briefly, the requirement is to have two electrically conducting shells collide, at least one of which is magnetized prior to the implosion. As the interface of the two conductors advances across $\vec{B}$, $\vec{B}$ is compressed into a thin gap and an electric field is induced along $\vec{B}$. This $\vec{E}$ parallel to $\vec{B}$ produces a net helicity gain, $\dot{K} = 2\int_V \vec{E}\cdot\vec{B}\,dV$, into the compressing volume.

An implementation of MHI is demonstrated in Fig. 1. Here, in cylindrical geometry, the inner conductor expands radially contracting the volume bounded by it and the magnetized outer conductor. The initial axial flux twists as helicity is generated. As the geometry evolves, the relaxed MHD state will change in time from a linear tokamak, to a linear RFP, to an $m = 1$ double helix,[2] and finally to an axisymmetric spheromak.[3]

This convenient geometry is exploited in the HESS experiment shown in Fig. 2. Here an initial B_z bias field is applied by a solenoid and flux plate arrangement to $\sim$ 70 kG. A coaxial metal cylinder has its $\frac{3}{8}$-in thick wall driven radially outward by an axially-propagating pressure front from an exploding cylindrical core. Helicity is generated when the axial flux twists as it is forced into the helical Copper grooves which surround the HE driven armature and have the initial B_z soaked in. The expanding armature then

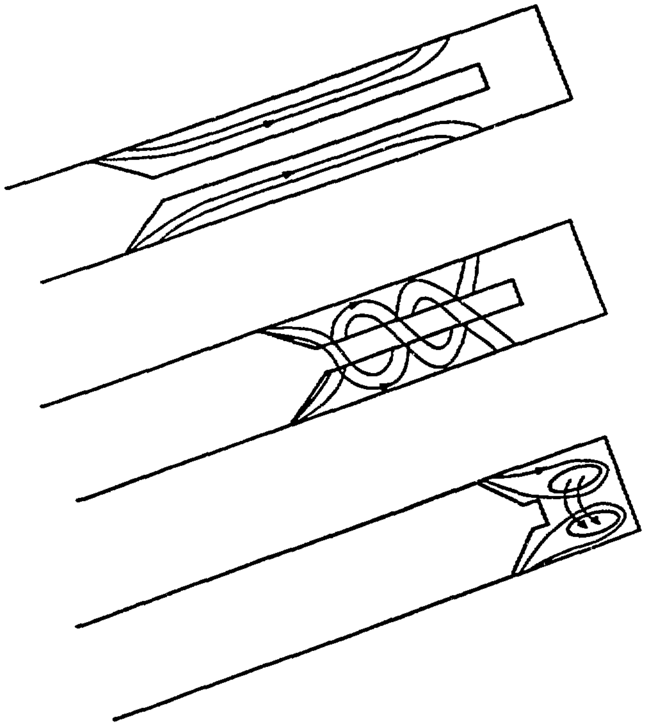

Figure 1: Mechanical Helicity Injection sequence.

compresses the formed equilibria. In this way, very high energy density spheromaks can be formed. As an example, an 81 kG axial fields can yield a spheromak mean field of 300 kG.

Initial experimental investigations will concentrate on studying the time evolution of the magnetic field structure. An array of 54 magnetic probes, flux loops, and Rogowskii coils have been designed to make a coarse map of the fields as the plasma progresses through its many stages of evolution.

III. Recent Progress on HESS

Progress to date on the HESS experiment includes simulation of the HE driven armature motion, fabrication and electrical testing of the solenoid coil and flux plates, fabrication of the Copper helix, and the construction of two armature "case motion" detonation experiments.

Figure 3 shows the results of a simulation of the Aluminum armature motion after detonation. The experiment is a point detonation at the lower far left and the frames shown are for 0, 32, 44, and 62μs following detonation. The structure at top center is

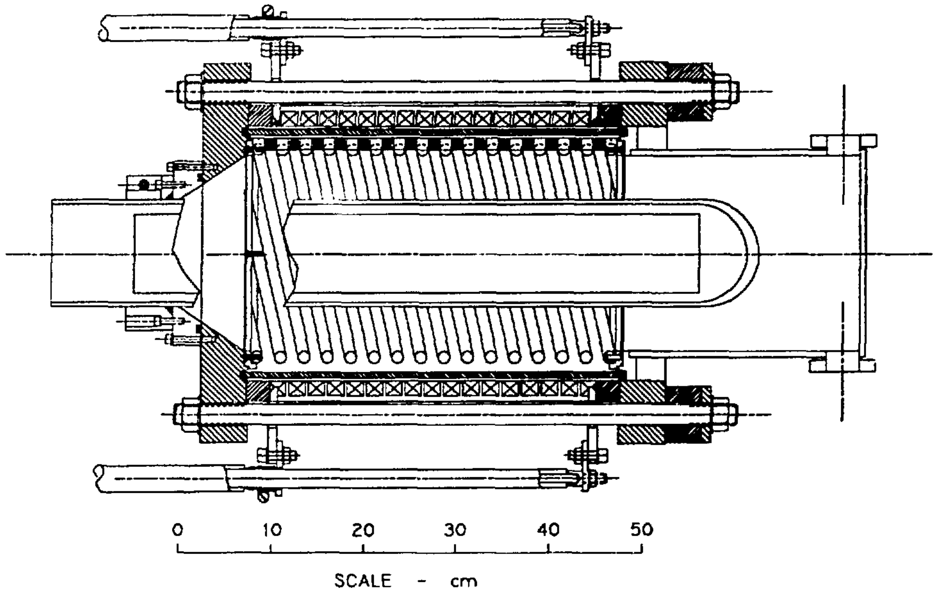

Figure 2: The HESS assembly.

a mock-up of the Copper helix. The Aluminum armature appears to progress smoothly without any punctures or jets. This is extremely important for the plasma experiments, since any introduction of metal or HE by-products would severely impede production of long-lived spheromaks.

To experimentally verify intact armature motion, two "case motion" (armature only) HE experiments are planned. In the first of these, the test volume will be filled with Helium so that air will not be shocked, creating a bright discharge which would mask the fast photos. Since the HE is separated from the test volume by only the thin Aluminum liner, a second experiment will be performed in which the test volume is evacuated to $\lesssim$ 10 mTorr. A fast ion gauge pressure probe will be used to examine the vacuum integrity.

The Copper helix and Aluminum solenoid coil with Aluminum flux plates have been fabricated. The solenoid has been pulse (600μs $\frac{1}{4}$ wave) electrically tested at 6 kV ($\sim$ 50% of rated voltage) with no apparent defects. However, at 9 kV signs of arcing were noticed and redesign of this coil is presently underway.

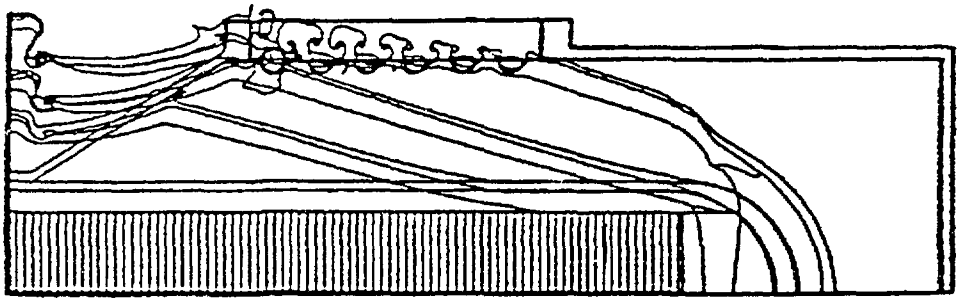

Figure 3: The dynamics of the HESS armature.

References

[1] D. C. Barnes, Phys. Fluids **31**, 2214 (1988).

[2] J. B. Taylor, Phys. Rev. Lett. **33**, 1139 (1974).

[3] poster presented at this meeting by D. C. Barnes, *et al.*

*Present Address: University of Washington, Seattle, WA 89195

DESIGN OF A SPHEROMAK COMPRESSOR DRIVEN BY HIGH EXPLOSIVES.*

I. Henins, J.C. Fernández, T.R. Jarboe,** S.P. Marsh, G.J. Marklin,
R.M. Mayo, F.J. Wysocki.

Los Alamos National Laboratory, Los Alamos, NM 87545

INTRODUCTION

High energy density spheromaks can be used to accelerate a thin section of the flux conserver wall to high velocities. The energy density of a spheromak, formed by conventional helicity injection into a flux conserver, can be increased by reducing the flux conserver volume after the spheromak is formed. A method of accomplishing this is by imploding one wall of the flux conserver with high explosives. The velocity of a wall driven by high explosives is about 3-5 km/sec, which is not exceptionally fast. Magnetic equilibrium calculations show that for some imploding flux conserver geometries, the energy density of the spheromak can be suddenly increased on an Alfvén time scale by the tendency of the spheromak to maintain a state of minimum energy per unit helicity, which is equivalent to minimizing $\lambda = \mu_o j/B$. In this process, as the initial flux conserver dimensions are reduced under the explosive drive, the characteristic λ of the configuration increases. Then, if there is an attached flux conserver region whose dimensions are such that its λ becomes lower than for the imploding region, the spheromak will quickly transfer to this region, even if its volume is smaller, thus increasing the energy per unit volume. We call this the "natural switching" feature of spheromaks. The simplest such geometry is a cylindrical flux conserver with one end being driven by high explosives. An attached, smaller-diameter on-axis cylinder has a thin end wall which is accelerated when the spheromak switches into the smaller cylinder [1].

We have embarked on a program to demonstrate that a spheromak can be used as an energy transfer medium, and that a velocity gain over high-explosive driven plate velocities can be achieved. To do this, a plasma gun helicity source that will inject a spheromak with suitable initial energy density and lifetime [2] is needed. Also, an implodable flux conserver that remains intact and clean during the implosion must be developed. The flux conserver problem is probably the more challenging one, because very little experimental work has been done in the past on explosively driven metal plates into a high vacuum, with sizes and travel distances appropriate for our application.

FLUX CONSERVER COMPRESSION WITH HIGH EXPLOSIVES

There are two necessary practical requirements for an explosive compression of a flux conserver. The first is that the imploding wall does not rupture. The second is that gasses or other debri are not ejected which could penetrate and poison the spheromak plasma, and thus reduce the spheromak lifetime below what is necessary to carry out the spheromak compression and the subsequent acceleration of the flyer plate. Our first inclination was to go with the cylindrical flux conserver geometry. However, two early small-scale experiments of an explosively driven end plate in a cylinder showed that the sliding seal against the cylinder walls allowed explosive by-products to penetrate into the cylinder volume. In addition, scaling to larger sizes would have been difficult, because it is complicated and expensive to initiate a plane wave detonation over a large area. Therefore, we decided to design and test a deforming geometry, with no sliding seals, in which an initial shallow dome is inverted during the implosion. For economic reasons, we decided to use a simple circular slab of explosive, detonated at a single point in the center. The curvature of the dome and other dimensions were optimized through numerical hydrodynamic simulation of the explosion and the subsequent motion of the metal wall.

We decided on the following full-scale dimensions for the first test: 61-cm spherical radius, 69-cm circular radius, and 0.3-cm thickness for the aluminum (1100-H14 alloy) dome; 58.4-cm diameter and 7.6-cm thickness for the high explosive, placed 1.0-cm from the apex of the dome. Total needed on-axis displacement of the dome is about 30 cm. The expected final on-axis velocity of the aluminum surface was 4.5 km/sec. The diagnostics consisted of a sequence of 25 fast-framing-camera stereo color photographs taken at 3.0-μsec intervals. Fiducial markings were made on the dome and on a transparent plastic plate 30 cm from the pole of the dome to allow measurement of the dome profile from the stereo photographs. The space between the dome and the plastic plate was to be filled with helium to eliminate glow from air being shocked by the imploding dome. Unfortunately, the helium purge was not complete, and the photographs were obscured by the bright glow after about 40 microseconds from the time of detonation of the HE, during which time the dome displacement was only about 12 cm. Until then, we could see the aluminum surface deforming, as expected, but small surface irregularities were formed as the explosive force struck the dome. It is suspected that by that time, some of these small bumps may have already perforated, and we do not know what happened at later times.

Based on the results of the first test, we changed the dome thickness to 0.95-cm of 5052-H32 aluminum alloy. Other dimensions remained the same. Also, we sealed and evacuated the space in front of the dome to about 20 mTorr, and the space between the dome and the explosive to about 50 mTorr. This time, no bright light emission was observed in the vacuum region. The bumps on the dome surface were still present. but they were larger in diameter and farther apart, suggesting a scaling with dome thickness. The detailed nature of the bumps is still not understood. Measurements of the dome profiles at various times were made from the stereo photographs. These agreed well with the computer simulation, as shown in Fig. 1. There may have been some perforations of the metal surface near the edge of the dome at 87 microseconds, but these are in locations and at late enough time, such that they should not affect the performance of the speromak compression. The predicted velocity at the center was 3.1 km/sec, and the measured velocity was 3.0 km/sec. The velocity reaches a nearly constant value about 60 microseconds after the detonation is initiated. It would be desirable to have a higher implosion velocity, but otherwise, these results appear to be satisfactory.

We still have to assess the vacuum quality in front of the imploding metal surface. To do this on future tests, we will produce a better vacuum, and install fast ion gauges to make pressure measurements during the implosion.

DESIGN OF PLASMA GUN

We have designed and fabricated a plasma gun to be used for injecting the initial spheromak plasma into the collapsible flux conserver. The diameter of the gun was dictated by the requirement that the injection had to take place along the periphery of the flux conserver. Figure 2 shows a cross sectional diagram of the gun. The inner and outer electrode diameters are 53.3 and 68.6 cm, respectively. The gun electrodes are stainless steel. A 21-cm long copper entrance region leads to the flux conserver. The gun will be powered by a 12-mF, 20-KV (max.) capacitor bank available at the firing site. The dome to be imploded is attached to the end, and forms one wall of the flux conserver. The opposite wall is shaped so that the entrance gap will at all times during the implosion be narrower than the smallest characteristic dimension of the flux conserver. This will prevent the spheromak from escaping back into the gun. Eventually, the entrance gap will be closed completely, thus trapping the spheromak. When the magnetic pressure becomes large enough, the thin "flyer plate", which will be scored at the edges, will break away and the spheromak will transfer into the cylindrical space behind it. While this (domed-end) geometry of the flux conserver may not be as efficient as a cylindrical one to utilize the "natural switching" effect, we expect to be able to demonstrate a velocity gain of the flyer plate over the velocity of the imploding flux conserver wall.

---

* Work supported by Los Alamos Laboratory Internal Scientific Research Funds.

** Present Address: University of Washington, Seattle, WA 89195

REFERENCES

[1] G. Marklin, in Proc. 8th U.S. Compact Toroid Symposium (University of Maryland, College Park, Md., 1987) p. 66.

[2] F.J. Wysocki, et al., "Progress with Small High-Magentic-Field Spheromaks in CTX", This conference.

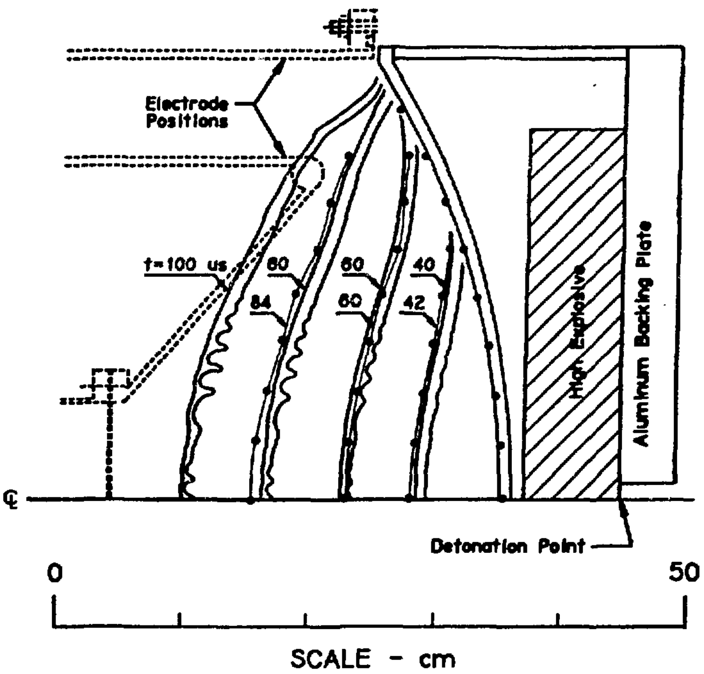

FIG. 1. Profiles of the high-explosive driven 0.95-cm thick aluminum dome at various times after detonation at t = 0. The solid lines are plots of the numerically simulated positions of the aluminum layer, and the dots show the measured positions of the surface, at the times indicated. The dashed lines outline the entrance region and the opposite wall of the flux conserver, if they were present as in Fig. 2.

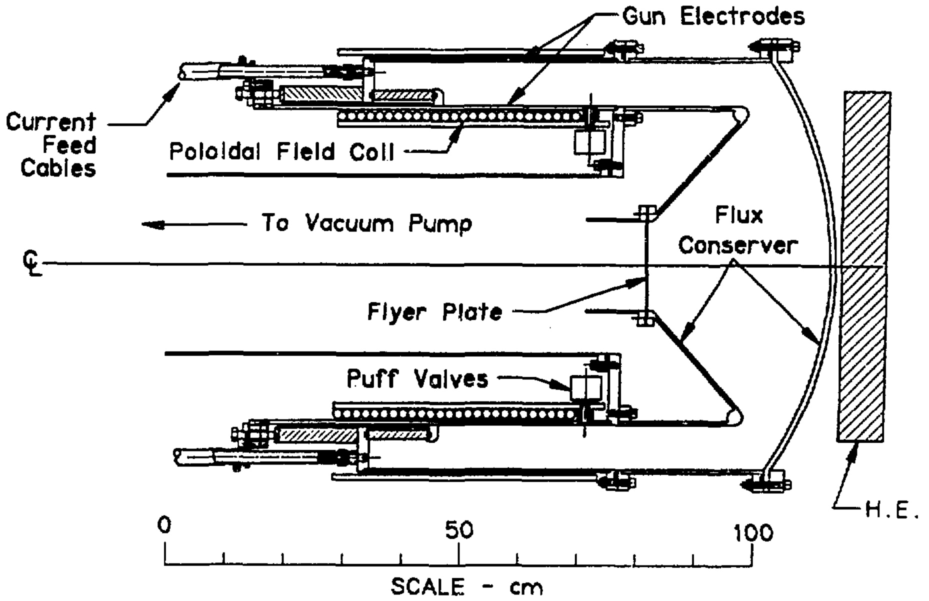

FIG. 2. Cross sectional diagram of the plasma gun, flux conserver, and high explosive assembly.

Acceleration of Spheromak Toruses, Experimental Results and Fusion Applications*

C. W. Hartman, J. L. Eddleman, J. H. Hammer, B. G. Logan, A. W. Molvik
Lawrence Livermore National Laboratory

November, 1989

In this paper we describe the Compact Torus Accelerator (CTA) concept, summarize the status of CTA development in the RACE (Plasma Ring Accelerator Experiment) program, and discuss fusion applications.

Fig. 1 shows schematically the CTA. The Spheromak-type CT is formed using a magnetized, coaxial plasma gun located at the breach of the accelerator. Shown are pre-established B-field lines which are entrained and swept into the formation region by plasma and B_θ field ejected when a gun discharge takes place between the outer two coaxial electrodes. The B_r, B_z field lines reconnect, as shown in the formation region to form the CT, dipole-like B_r, B_z fields and entrapped B_θ field and plasma. This highly stable, nearly self-contained, toroidal plasma confinement configuration can then be quastatically compressed (compression, Fig. 1) by B_θ field introduced by discharging a driver capacitor bank connected across the inner two coaxial electrodes at the breach. During slow compression (~10-100 μs) magnetic energy is stored inductively in behind the ring and then released rapidly (1-10 μs) when the ring enters the acceleration region of Fig. 1 where the ring acts as a moving armature, as in a coaxial rail gun. During compression the outward radial equilibrium force of the ring is balanced by the inward accelerator B_θ force while acceleration takes place with the equilibrium force supported by the straight, coaxial electrodes.

Following acceleration, the CT is injected into a focusing cone section where the ring momentum carries it to small radius and the ring magnetic fields (constrained by the conducting cone electrodes) are compressed along with the confined plasma. The compression is predicted to be self-similar (ring length $\propto$ ring radial width $\propto$ ring radius) so that the timescale

---

*This work was performed under the auspices of the U.S. Department of Energy by Lawrence Livermore National Laboratory under contract W-7405-ENG-48.

$\tau \equiv L_{ring}/V_{ring}$ is reduced to the order of 10 nsec and the ring power $U_{kinetic}/\tau$ correspondingly increased.

We believe it is possible to scale the CTA to high energy (100 MJ or so) with accelerator lengths of 20-30 m for fusion applications. An important aspect of the CTA for scaling to high energies is the utilization of low-voltage, low-cost driver capacitor banks. A 100 MJ accelerator driver bank (the main electrical cost) was costed using off-the-shelf capacitors at about 30 M$.

Development of the CTA has been carried out with the RACE experiment shown in Fig. 2. This proof-of-principle experiment (at 0.26 MJ maximum driver energy) has successfully demonstrated CT ring formation and acceleration in a straight coaxial electrode system (1). Acceleration to ring kinetic energy of 10-20 KJ, $V = 1.4 \times 10^8$ cm/sec was obtained with interferometer measurements showing the plasma to be localized in the ring fields, and with trajectory and accelerator inductance analysis giving good agreement with the observed ring trajectory. Accelerated CT rings have been focused and, without focusing, have been stagnated on an impact plate for soft x-ray production. Recently, we have demonstrated energy scaling to 40 KJ ring kinetic energy achieved at the maximum accelerator bank energy of 200 KJ. Energy scaling is shown in Fig. 3. Fig. 4 shows typical signals of B_z at the outer wall, and $\bar{n}_e$ measured with an interferometer. Table 1 summarizes goals, predictions, and results for the RACE program, showing that all of the techniques shown in Fig. 1 and discussed in the first three previously have been experimentally demonstrated, except for the compression stage after the gun.

We have recently installed an electrode system with a precompression cone and tests are scheduled to be started December, 1989. Successful demonstration of precompression, acceleration, and focusing can lead to multi keV plasma temperatures spheromaks as illustrated in Table 2.

Next, we consider possible high energy density fusion applications as shown in Fig. 5. The first, application A, would utilize a CTA to produce a

5 MJ energy, keV temperature CT for compression by a gas-gun accelerated tungsten projectile. Compression of the CT to ignition with refueled DT burn could produce a high gain (120), high energy yield (25 GJ) magnetically insulated, inertially confined fusion (MICF) system. A principal aspect of this application is the projected low driver cost.

Application B would inject a high kinetic energy (100 MJ) CT into a cannon ball confinement sphere. Transition to high $\beta >> 1$ would take place by shock heating of the CT converting kinetic energy to ion temperature. A refueled MICF burn would give gain for 7 GJ yield.

In application C, the CTA would be the main energy source for indirect drive ICF.

---

[1] Experimental Demonstration of Acceleration and Focusing of Magnetically Confined Plasma Rings," J. H. Hammer, C. W. Hartman, J. L. Eddleman, Lawrence Livermore National Laboratory, Livermore, CA, 94550, Phy. Rev. Lett., Vol. 61, No. 25, p. 2843-2846, (12/19/88).

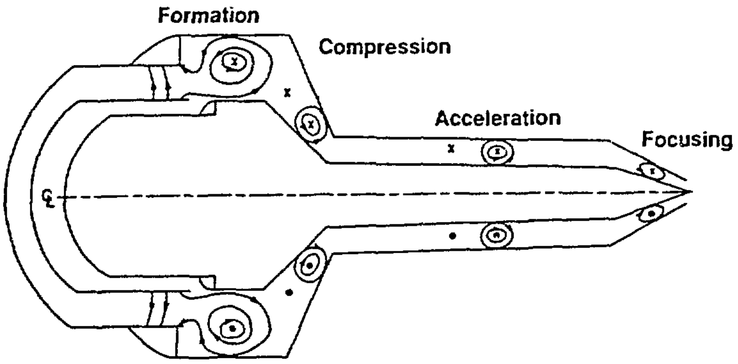

Figure 1. Schematic illustration of the Compact Torus Accelerator.

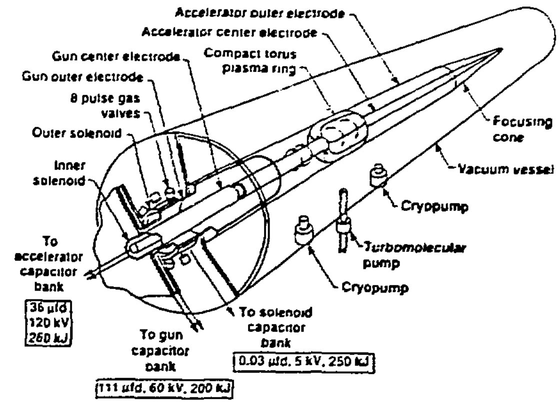

Figure 2. *The RACE experiment configured without a precompression cone* but with a 2 m long focusing cone. The straight acceleration electrode section is 4 m long, 50 cm OD, 20 cm ID. The results discussed here were obtained using the gun outer solenoid only.

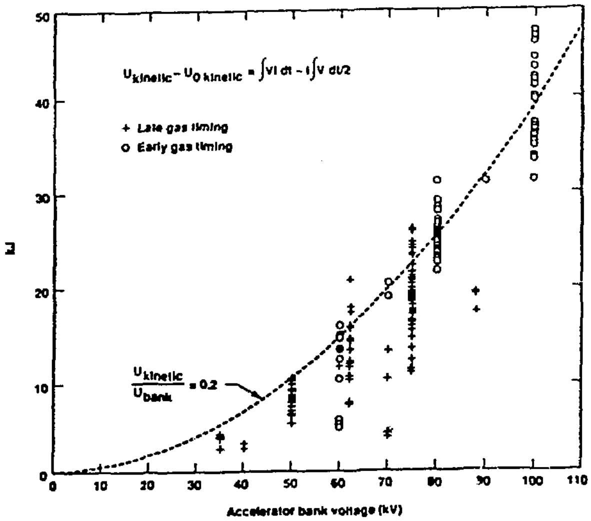

Figure 3. Ring kinetic energy inferred from the accelerator inductance is plotted vs. accelerator bank voltage for late and early gun timing. The results are consistent with the constant efficiency (20%) curve shown.

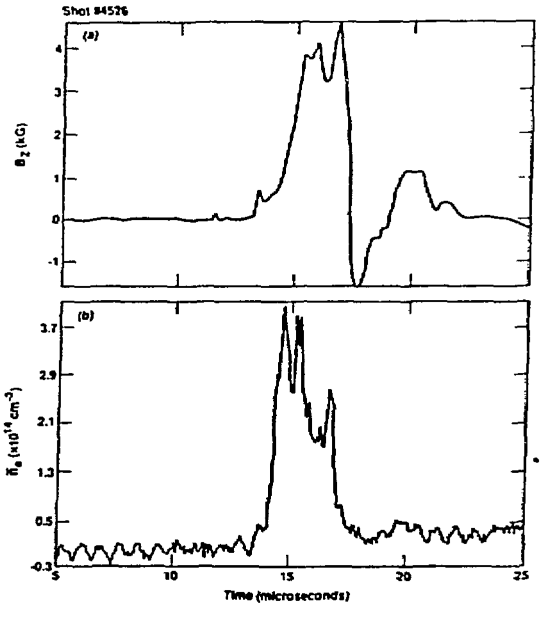

$\bar{n}_e$ is ≈10 times greater than previous last ring operation — consistent with ~10 times mass

Figure 4. The ring B_Z field measured at the outer electrode, Z = 124 cm from the accelerator breach, and $\bar{n}_e$ measured with a HeNe interferometer at the same Z position.

Table 1. RACE Program Summary

Goals	Predictions		Results to Date
Demonstrate ring formation	Magnetic energy	2–10 kJ	2–10 kJ
	Mass	5–500 microgram	5–500 microgram
	Length	70 cm	50–100 cm
Demonstrate acceleration in linear coaxial system	Velocity	1–2 x 10^8 cm/sec	1–3 x 10^8cm/sec
	Energy	*Up to 100 kJ*	40 kJ*
	Efficiency	0.4	0.2–0.4
	$U_{kinetic}/U_{magnetic}$	5	10
Demonstrate ring focusing	R_{focus}/R_0 -	1/5	~1/3
Demonstrate x-ray generation	Radiated energy	1.8–4.1 kJ (for U_k = 10 kJ)	2.7 kJ
	Spectrum	$h\nu_{peak}$ = 35–40eV	$h\nu$ > 10ev

Table 2 Projected RACE Performance with Precompression
M_{ring} = 10 μgm (H^+ + .05 O^+), U_0 ≈ 180 KJ

Parameter	Initial	Compressed	Accelerated	Focussed
R (cm)	11.5	5.5	5.5	0.8
$U_{magnetic}$ (KJ)	1	2	2	15
T_e (eV)	200	800	800	40 X 10^3
T_i (eV)	80	300	300	18 X 10^3
n_i (cm^{-3})	~ 10^{14}	~ 10^{15}		1.7 X 10^{18}
B (KG)	5	20	20	1400
$U_{kinetic}$ (KJ)	~ 0	~ 0	70 (V ≈ 2 X 10^8 cm/sec)	~ 0

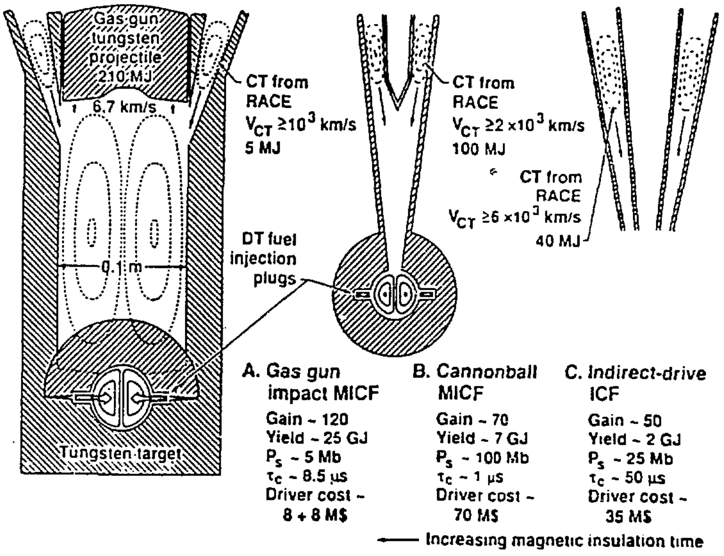

Figure 5. Three possible fusion applications of the CTA.

X-ray Production Experiments on the RACE Compact Torus Accelerator

J.H. Hammer, J. L. Eddleman, C.W. Hartman,
H.S. McLean, A.W. Molvik and M. Gee

Lawrence Livermore National Laboratory
Livermore, California

I. INTRODUCTION

The purpose of the Compact Torus Accelerator[1] (CTA) program at LLNL is to prove the principle of a unique accelerator concept based on magnetically confined compact torus (CT) plasma rings and to study applications. Successful achievement of these goals could lead to a high power-density driver for many applications including an intense x-ray source for nuclear weapons effects simulation and an inertial fusion driver. Fusion applications and a description of the CTA concept are included in a companion paper at this conference[2]. This paper will describe the initial experiments on soft x-ray production conducted on the plasma Ring ACcelerator Experiment (RACE) and compare the results to modeling studies.

The experiments on CT stagnation and soft x-ray production were conducted with unfocused rings as a first test of CT dynamics and the physics of x-ray production. The x-ray fluences observed are consistent with expectations based on calculations employing a radiation-hydrodynamics code. We conclude with a discussion of future x-ray production studies that can be conducted on RACE and a possible multi-megajoule upgrade.

II. AN X-RAY SOURCE BASED ON THE CTA

For use as an intense pulsed source of ≈10 keV x-rays, an accelerated ($v > 10^8$ cm/s) and tightly focused (dimensions ≈ few cm) CT impacts a plate and undergoes rapid ion shock heating[3]. For a CT composed of the appropriate gas (e.g., xenon), and focused to high plasma density (≈10^{18} cm^3), the electrons confined in the CT heat by electron-ion equilibration and excite K and L-shell line radiation. Conversion efficiencies of CT kinetic energy to x-rays as high as 50% are predicted using a radiation-hydrodynamics code[3]. There are many other applications in the field of high energy density/ high power density physics if the accelerator can be successfully developed. Since the device has the potential of large power amplification factors (output power/input power = 100-1000), the driving bank can be relatively low power. The CT accelerator may then provide an economical path to the multi-megajoule regime.

III. EXPERIMENTAL RESULTS

The RACE experiment is more fully described in Refs. 1,2. The CT is formed with a magnetized plasma gun then accelerated by JxB forces in a 5m long, straight coaxial rail gun configuration. Typical plasma velocities produced on RACE are in the range 10^7 - 3 x 10^8 cm/s with directed kinetic energies from 4 - 40 kJ and a peak accelerator bank energy of 260kJ. The initial tests of shock heating and radiation production have been conducted with unfocused CT's, so a stagnation plate has been inserted at the end of the straight acceleration stage. These experiments provide a test of the CT dynamics, electron-ion energy exchange and radiation, although at much lower power densities than required for multi-keV photon production. The latter will require CT focusing to dimensions of a few cm.

The geometry of the stagnation region is shown in fig. 1. The stagnation plate is 519 cm downstream from the gun muzzle/accelerator breech. The final 2m of outer electrode (50cm diameter) and the stagnation plate are composed of 53% transparent copper screen with .75 inch mesh spacing to allow diagnostic access. Two x-ray diodes (XRD's) on loan from the Air Force Weapons Laboratory, Albuquerque NM were deployed to view the plasma near the plate. The diodes have a polished aluminum photocathode biased to -3kV. One of the diodes was unfiltered while the other was covered by a Kimfoil filter that excluded photons of energy less than 200 eV. Three VUV detectors, also employing polished aluminum photocathodes and biased -250V, were arrayed axially upstream from the stagnation plate as shown in fig. 1. Soft x-ray energies were measured with a VUV spectrometer that is gated on for a 10μs duration. Other CT properties were determined by magnetic probes, a HeNe laser interferometer, a visible light monochrometer, and an optical multichannel analyzer.

For most of these experiments, the gun and accelerator were operated in a mode such that comparatively heavy, slow but well localized CT's were produced ($M \approx 10^{-3}$g, $v \approx 10^7$ cm/s). Ring mass and speed are controlled largely through the timing and amount of gas inlet by the pulsed gas valves as well as the degree of conditioning of electrode surfaces. For heavy rings, much of the plasma in the CT is apparently derived from electrode surface contaminants -- mainly carbon and oxygen. The modeling of x-ray production indicates that carbon and oxygen are (fortuitously) about the right Z for efficient coupling in this CT parameter regime.

Many shots showed large signals (<10V) on the bare XRD and VUV detectors, coincident with the arrival of the CT as determined by magnetic probes. During stagnation, the CT shrinks from its usual 50-100 cm length to a 10-30 cm length, based on comparing signals from VUV detectors 10 and 30 cm from the plate and also from the axially-arrayed magnetic probes. The CT does not typically bounce away from the plate but remains pinned against it by the accelerating field.

The filtered XRD gave no detectable signal, consistent with its sensitivity and the spectroscopic observations indicating that most of the energy is at a few 10's of eV. Fig 2 shows the XRD signal for shot #3520 along with theoretical estimates of U_{RAD}, the radiated energy, and t_{RAD}, the half-width of the radiated power. A 2mg carbon CT with a velocity of 10 cm/μs was assumed for the calculations. The calculated spectrum for a 1D radiation/hydrodynamics code simulation of this case is shown in fig. 3 along with the observed spectrum of a heavy ring shot. There are factor-of-two uncertainties in the experimentally measured U_{RAD} due to uncertainties in the total radiating volume of CT plasma and possible non-uniformities. The value for U_{RAD} does not include contributions from the "foot" on the pulse or the protracted tail, which are presumed due to the balance of ohmic heating with radiation and therefore unrelated to the shock heating contribution. VUV detectors upstream of the stagnation plate typically show ≈ 2V signals before a heavy CT strikes the plate, as expected from an ohmically heated CT.

Fast rings with $v > 10^8$ cm/s and $M \approx 10^{-5}$g produced no detectable signals on the XRD's as predicted by the modeling for unfocussed CT's. Some moderately fast rings at higher bank energy did produce significant soft x-ray fluxes, however, as shown in fig. 4. For shot #4526 shown in fig. 4 with $v = 6\times10^7$ cm/s and $M \approx 250$ μg, an analytic theory underestimates the output radiation by more than an order-of-magnitude while the 1D simulation is in closer agreement. The coronal equilibrium assumption used in the analytic theory is probably invalid due to the lower density of the moderate speed rings. The simulations show a similar output spectrum for both moderate speed and slow CT's with the exception of fairly weak K-shell excitation in the moderate speed case at photon energies of ≈ 300eV (outside the range of the VUV spectrometer). The simulations predict transient (≈ 2 μs) electron temperatures of 100 eV for the moderate speed CT as opposed to 15 eV for the slow CT. The lower level XRD signal following the peak is often nearly exponential in character. For shot #4526 the decay time is 43μs, consistent with a resistive decay at $7 < Te < 14$ eV.

IV. SCALING OF X-RAY GENERATION TO HIGHER ENERGIES

The next tests of x-ray generation on RACE will be conducted with focused CT's. 2-D MHD simulations and the 0-D Ring Acceleration Code give predictions of focusing to ≈ 1-2 cm dimension for CT's moving at speeds of ≈ 10^8 cm/s in the new precompression geometry. If these parameters can be achieved, RACE could produce as much as 10kJ of 1-3 keV photons in a ≈ 20 ns burst at full bank energy. Argon or other material of similar Z would be used to give efficient coupling to radiation.

The 0-D and 2-D models have also been used to scope out CTA's scaled to multimegajoule drivers. The models indicate that the accelerator size grows slowly with energy (≈ 20M length at 100 MJ bank energy) and that the driving bank voltages remain reasonable (≈ 500 kV for the 100 MJ driver vs. 120 kV on RACE). Table 1 shows the radiation-hydrodynamics code predictions for different accelerator bank energies given the assumption of focusing to ≈ 2 cm and 50% efficiency of conversion of bank energy to directed CT energy.

Table I. Predicted X-ray Yield vs. Accelerator Bank Energy

Accelerator Energy	Total X-Ray Yield	X-Ray Output between 7-10 keV	X-Ray Output between 10-100 keV
1 MJ	160 KJ	5.9 KJ	2.5 KJ
10 MJ	1.8 MJ	80 KJ	130 KJ
100 MJ	22 MJ	1.7 MJ	8.0 MJ

References

1. J.H. Hammer, C.W. Hartman, J.L. Eddleman and H.S. McLean, Phys. Rev. Lett. 61, 2843 (1988).

2. C.W. Hartman, J.L. Eddleman, J.H. Hammer, B.G. Logan, and A.W. Molvik, "Acceleration of Spheromak Toruses: Experimental Results and Fusion Applications," in Proceedings of the 11th US-Japan Workshop on Compact Toroids, Nov. 7-9, 1989.

3. J.H. Hammer, C.W. Hartman and J.F. Holzrichter, "The Compact Torus Accelerator, A New X-ray Source for High-Fidelity Nuclear Weapons Effects Simulation," Lawrence Livermore National Laboratory Report LLL-PROP-00212, July 5, 1988.

Performed for USDoE by LLNL under contract W-7405-48.

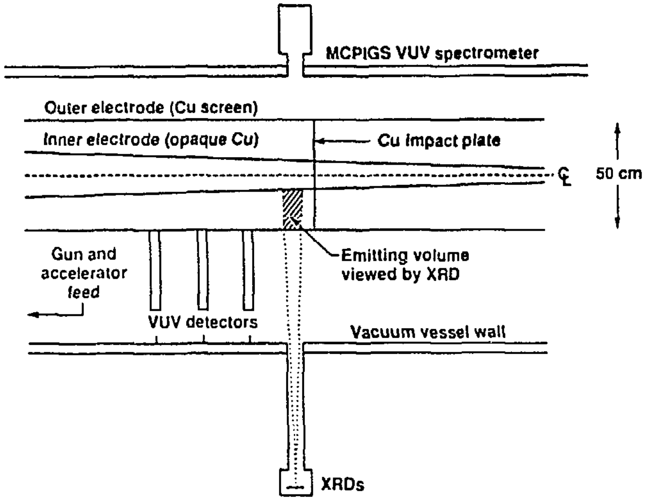

Fig. 1. The compact torus stagnation region on RACE

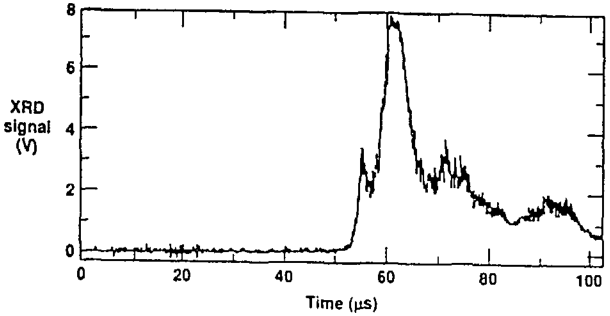

Analytic x-ray output theory	LASNEX	Observation shot # 3520
$\ell_{shocked} = 25$ cm	$\ell_{shocked} \cong 21$ cm	—
$U_{p_{shocked}} = 5$ kJ	—	—
$U_{RAD} = 1.8$ kJ	$U_{RAD} = 4.1$ kJ	$U_{RAD} = 2.7$ kJ ($\ell = 25$ cm assumed)
$\tau_{RAD} = \frac{\ell_{\ell}}{v} = 5\ \mu s$	$\tau_{RAD} = 3\ \mu s$	$\tau_{RAD} \cong 7\ \mu s$
$h\nu = T_e = 40$ eV	$h\nu_{peak} = 35$ eV	$h\nu > 10$ eV

Fig. 2. Bare XRD signal on shot #3520 and comparisons with modeling

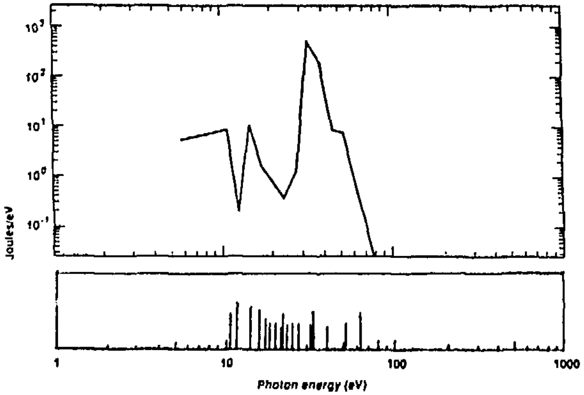

Fig. 3. LASNEX predicted spectrum and observed spectrum for a heavy ring shot.

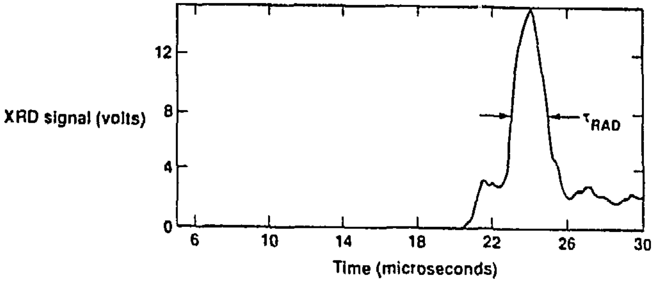

$U_K = 45$ kJ, $v = 60$ cm/μs, $M \sim 250\ \mu g$

Analytic theory (C)	LASNEX (1/3C, 2/3H)	Shot 4526
$U_{RAD} = 0.05$ kJ	$U_{RAD} = 0.4$ kJ	$U_{RAD} \sim 1.4$ kJ
$\tau_{RAD} = 1.7\ \mu s$	$\tau_{RAD} = 1.4\ \mu s$	$\tau_{RAD} \sim 1.8\ \mu s$

Fig. 4. Bare XRD signal on shot #4526 and comparisons with modeling

Current Drive by Spheromak Injection into a Tokamak

M. R. Brown* and P. M. Bellan, Caltech

ABSTRACT: We report the first observation of current drive by spheromak injection into a tokamak due to the process of helicity injection. Current drive is observed in Caltech's ENCORE tokamak (30% increase, $\Delta I > 1$ kA) *only* when both the tokamak and injected spheromak have the same sign of helicity (where helicity is defined as positive if current flows parallel to magnetic field lines and negative if anti-parallel). The initial increase (decrease) in current is accompanied by a sharp decrease (increase) in loop voltage and the increase in tokamak helicity is consistent with the helicity content of the injected spheromak. In addition, the injection of the spheromak raises the tokamak central density by a factor of six. The radial density profile peaks sharply upon injection, then becomes hollow, indicative of a pressure gradient induced interchange instability which terminates the high current/high density discharge after 30 μs. The introduction of cold spheromak plasma causes sudden cooling of the tokamak discharge from 12 eV to 4 eV which results in a gradual decline in tokamak plasma current by a factor of three. In a second experiment, we inject spheromaks into the magnetized toroidal vacuum vessel (with no tokamak plasma). An $m = 1$ magnetic structure forms in the vessel after the spheromak undergoes a double tilt; once in the cylindrical entrance between gun and tokamak, then again in the tokamak vessel. A horizontal shift of the spheromak equilibrium is observed in the direction opposite that of the static toroidal field. In the absence of net toroidal flux, the structure develops a helical pitch as predicted by theory. Experiments with a number of refractory metal coatings have shown that tungsten and chrome coatings provide some improvement in spheromak parameters. We have also designed and will soon construct a larger, higher current spheromak gun with a new accelerator section for injection experiments on the Phaedrus-T tokamak.

HELICITY INJECTION: We report several recent results and improvements with the Caltech Spheromak Injection Experiment wherein small (r = .04 m) spheromaks are injected into the ENCORE tokamak (R = .38 m, r = .12 m, $B_{tor} = 700$ G, $I_p = 2$ kA). We have observed for the first time current drive in a tokamak by the injection of a high helicity content spheromak (see fig. 1a-d). An initial 30% increase in plasma current is observed (from 2.0 to 2.6 kA) *only when both spheromak and tokamak have the same sign of helicity* [where helicity is defined as positive (right-handed) if current flows parallel to magnetic field lines and negative (left-handed) if anti-parallel]. Increases of over 1 kA have been recorded by injecting higher energy spheromaks ($I_g > 100$ kA) but these shots abruptly terminate the tokamak discharge. A decrease in current is observed if spheromak and tokamak have opposite helicity. The increase (decrease) in plasma current is accompanied by a sharp decrease (increase) in loop voltage (see fig. 2). The addition of cooler spheromak plasma lowers the tokamak plasma temperature from 12 eV to 4 eV and gradually reduces the plasma current by a factor of three (fig 1e).

DENSITY INCREASE: The tokamak central density is increased by a factor of six due to spheromak injection (fig 1f). Measurement of the radial density profile (with a Langmuir probe array) shows that the density profile peaks sharply upon injection then becomes hollow indicating an interchange instability (fig 3). The profile peaks about 50 μs after the gun is fired and the interchange occurs in less than 10 μs. The interchange together with the sudden cooling of the tokamak plasma terminates the high current/high density phase of the discharge.

MOTION IN TOROIDAL VESSEL: In another set of experiments, we inject the spheromak into the magnetized tokamak vessel configured with arrays of magnetic probes (without tokamak plasma). These measurements show that the spheromak is (i) initially generated with its axis aligned with that of the gun (axisymmetric), then (ii) tilts while in the cylindrical entrance region between gun and tokamak and moves into the tokamak vessel (with its axis *anti-aligned* with the dc toroidal field), then finally (iii) tilts again forming an $m = 1$ (non-axisymmetric) equilibrium in the tokamak vessel. Measurements with poloidal arrays at two toroidal locations on either side of the entrance port show that the spheromak shifts horizontally in the direction opposite that of the dc toroidal field. Figure 4 shows data (for no net applied toroidal flux) from a pair of cross-shaped probes. Note that a helical twist of the m=1 structure develops at 23 μs. We have also noted that the sense of the twist depends on the sign of the spheromak helicity.

REFRACTORY ELECTRODE COATINGS: We have coated the steel center electrode of our coaxial plasma gun with a number of refractory metal coatings in order to improve gun performance and spheromak parameters. We electroplated the electrode with copper, nickel, chromium and rhodium (0.001" to 0.002" thickness) and plasma coated with tungsten (0.006" thickness). Global plasma parameters were monitored for each electrode as well as the visible emission spectrum (230 nm to 890 nm) from the plasma in the gun breech. The goal was to reduce the level of high Z impurities sputtered into the plasma thereby increasing the spheromak magnetic lifetime. Increased lifetime is particularly important to the previously mentioned helicity injection experiment; the helicity decay time ($\tau_K \cong \tau_B/2$) must be longer than the traversal time of spheromak to tokamak or little helicity is deposited. In general, the macroscopic parameters of the spheromak were roughly the same for each electrode ($n_e \cong 10^{21} m^{-3}, T_e < 10eV, \tau_B \cong 20\mu s$) and nearly all of the emission lines resolved were observed for each electrode. However, a few important differences were noted. First, the previously reported helicity injection result was observed only with the tungsten and chrome electrodes. Second, a few lines were suppressed in the tungsten and chrome electrodes (the normally bright CII line at 426.7 nm was strongly suppressed in the tungsten and chrome electrodes). Third, sputtering of electrode material onto the 1 mm quartz capillary used to observe the emission was not as severe with the tungsten and chrome electrodes.

NEW SPHEROMAK ACCELERATOR: We have designed and will soon begin construction of a new spheromak gun with an accelerator section similar to that of the Livermore RACE facility. The acceleration stage will provide additional kinetic energy so that the spheromak can be injected into the higher magnetic field Phaedrus-T tokamak at Wisconson. The new gun will have inner electrode diameter of 7.5 cm and outer electrode diameter of 15 cm. Both gun and accelerator will be powered by 15 kV capacitor banks. Special attention has been paid to system cleanliness and high vacuum. The inner and outer electrodes will be fitted with liners that can be heated by the passage of large cw current while under vacuum.

*US DOE Fusion Energy Postdoctoral Research Fellow

FIGURES:

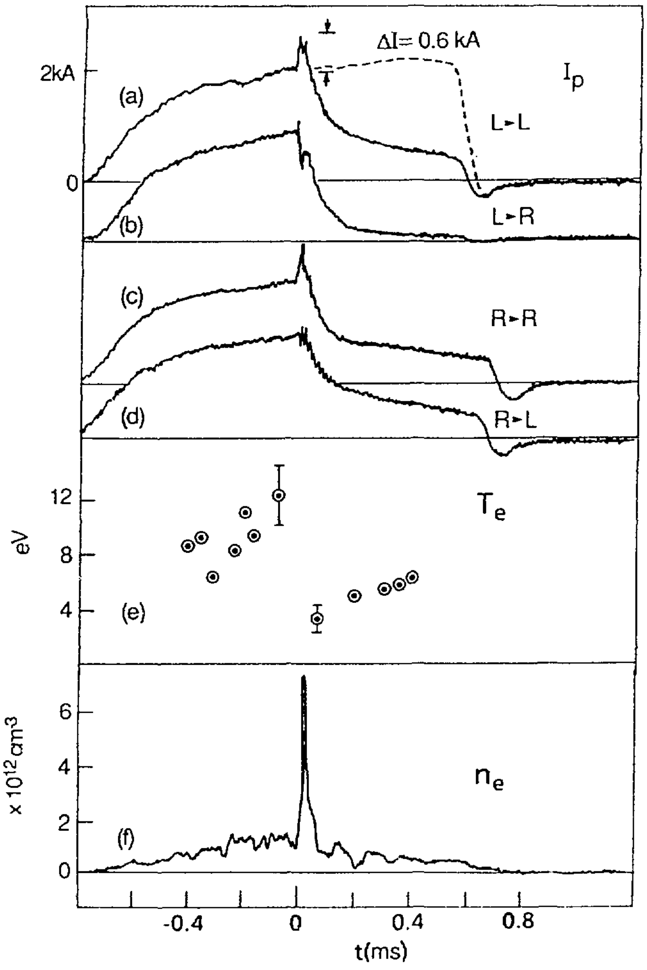

Fig. 1: Spheromak injection

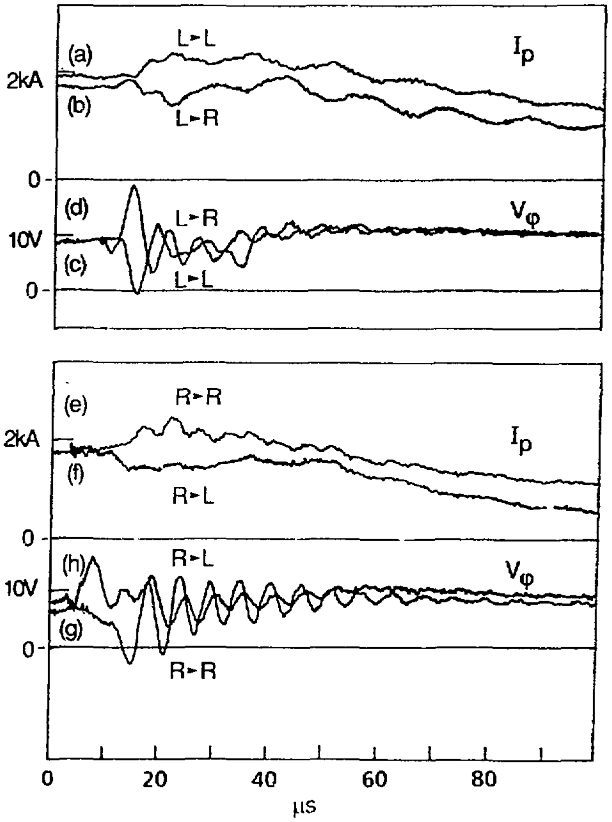

Fig. 2: Plasma current and loop voltage

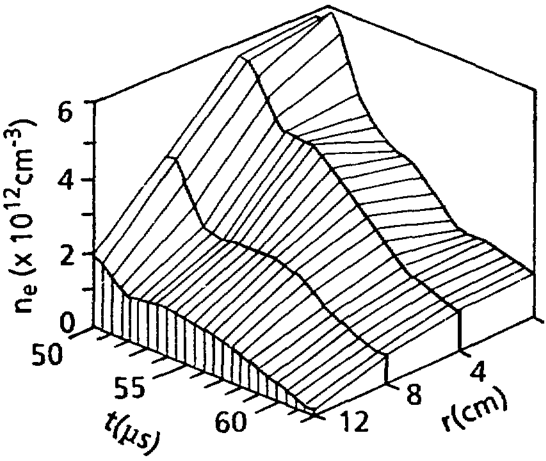

Fig. 3: Interchange instability: peaked profile a
50 μs becomes hollow and flattens by 60 μs.

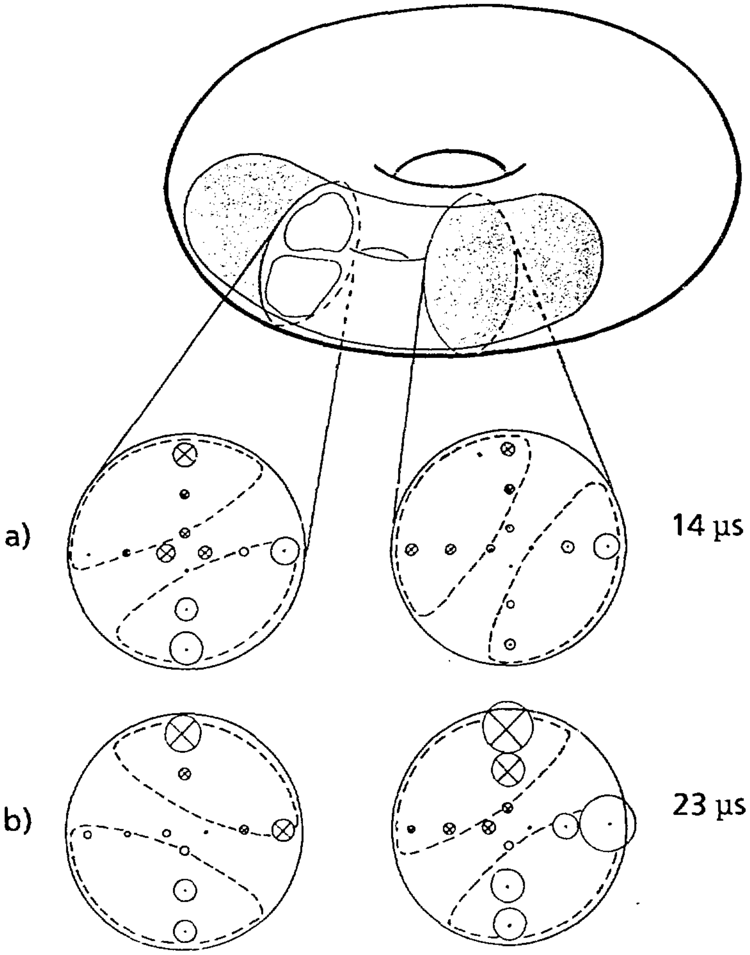

Fig. 4: Magnetic probe data from cro
shaped array, no tokamak plasma, no a
plied toroidal field, non-axisymmetric sp
mak equilibrium: (a) an m=1 equilibriu
is ultimately formed (left-handed) and (
develops a 60° helical twist (largest circ
represent 300 G).

APPENDIX A

AGENDA

US-JAPAN WORKSHOP ON FRCs WITH STEADY STATE HIGH-TEMPERATURE FUSION PLASMAS

11th US-JAPAN WORKSHOP ON COMPACT TOROIDS

J. Robert Oppenheimer Study Center
Los Alamos National Laboratory
November 7-9, 1989

TUESDAY NOVEMBER 7:

Morning Session M. Ohnishi and J. B. Taylor, presiding

Reactor studies:

08:55 - 09:00 D. C. Barnes, Los Alamos National Laboratory
Welcoming Remarks (Steady-State FRC Workshop)

09:00 - 09:30 H. Momota, National Institute for Fusion Science, Nagoya
Direct Energy Conversion for 15 MeV Fusion Protons

09:30 - 10:00 Y. Tomita, National Institute for Fusion Science, Nagoya
Dynamics of FRC Equilibria to D-^{3}He Ignition State

10:00 - 10:30 W. Kernbichler, Graz University of Technology
Reactor Potential of Steady-State FRCs

10:30 - 10:45 Break

10:45 - 11:00 Reactor discussions

Large orbit stability:

11:00 - 11:30 A. Ishida, Niigata University
Gyroviscosity Effect on Tilt Mode in an FRC

11:30 - 12:00 H. Berk, University Texas, Austin
MIGMA EXYDER: A Large Larmor Radius Device

12:00 - 12:30 D. C. Barnes, Los Alamos National Laboratory
Effects of Beam Ion on the FRC Tilt Model

Poster

13:30 - 14:30 Poster Session

Afternoon Session A. Ishida and R. Nebel, presiding

14:30 - 14:45 Large-orbit stability discussions

Transport:

14:45 - 15:15 M. Ohnishi, Kyoto University
Effects of Turbulent Transport on FRC Equilibrium with External Momentum Input

15:15 - 15:45 H. Momota, National Institute for Fusion Science, Nagoya
Ambipolar Plasma Diffusion in Steady-State FRCs

15:45 - 16:15 L. C. Steinhauer, Spectra Technology, Inc.
1.4-D Quasistatic Profile Model of Transport in an FRC

16:15 - 16:45 A. G. Sgro, Los Alamos National Laboratory
The Lower-Hybrid-Drift Instability and the Evolution of Plasma Gradients

16:45 - 17:00 Transport discussions

WEDNESDAY NOVEMBER 8:

Morning Session I D. C. Barnes and H. Momota, presiding

09:00 - 10:00 *Theory Workshop Summary*

10:00 - 10:15 Photograph

10:15 - 10:30 Break

Morning Session II M. Katsurai and B. W. Wright, presiding

10:30 - 10:35 D. J. Rej, Los Alamos National Laboratory
Welcoming Remarks (CT Workshop)

10:35 - 10:40 W. F. Dove, USDOE
Opening Remarks (CT Workshop)

10:40 - 11:20 J. T. Slough, Spectra Technology, Inc.
FRC Formation with Large Bias Fields

11:20 - 12:00 Y. Nogi, Nihon University
Stabilization of Rotational Instability in FRC by an Axial Current

12:00 - 12:30 R. D. Brooks, University of Washington
The Coaxial Slow Source: Parallel Operation and the Radiation Barrier

Afternoon Session

R. D. Milroy and M. Nishikawa, presiding

13:30 - 14:00 R. Hess, University of Maryland
Structure of Maryland Spheromak Plasmas

14:00 - 14:40 M. Katsurai, University of Tokyo
Experimental and Theoretical Studies on the Magnetic Configuration of Bumpy-Z-Pinch/Flux-Core-Spheromak

14:40 - 15:10 C. Hartman, Lawrence Livermore National Laboratory
Acceleration of Spheromak Compact Toruses, Experimental Results and Fusion Applications

15:10 - 15:30 Break

15:30 - 16:00 M. Brown, Caltech
Current Drive by Spheromak Injection into a Tokamak

16:00 - 16:30 J. C. Fernandez, Los Alamos National Laboratory
The Spheromak Program at Los Alamos

16:30 - 17:00 T. Jarboe, University of Washington
Advances in Spheromak Understanding and Parameters

17:00 - 17:30 E. C. Morse, University California, Berkeley
Berkeley Compact Torus Experiment: Experimental Results and Progress

Banquet

19:30 Banquet at *Rancho de Chimayo*

THURSDAY NOVEMBER 9:

Morning Session — C. W. Barnes and Y. Nogi, presiding

09:00 - 09:40	M. Tuszewski, Los Alamos National Laboratory *Observation of Tilt Asymmetries in FRCs*
09:40 - 10:20	S. Goto, Osaka University *Large Volume FRC Plasma Production and High-Energy Particle Injection Experiments in the FIX Machine*
10:20 - 10:50	Break
10:50 - 11:20	G. Cunningham, University of Manchester *Progress on SPHEX, the Spheromak at UMIST*
11:20 - 12:00	M. Nishikawa, Osaka University *Pressure Effect on Equilibrium Configuration of CTCC-II Spheromak*

Poster

13:00 - 15:00	Poster Session

Summary Session — J. Fernandez and S. Goto, presiding

15:00 - 15:30	CT Workshop Summary

Laboratory tours

15:45 - 16:45	The *FRX-C* FRC experiment	Garrett Barnes
	The *CTX* spheromak experiment	Fred Wysocki
17:15 - 17:45	The *CPRF/ZTH* facility	David Weldon
18:00 - 18:30	The *ZEBRA* high-density Z-pinch experiment	Franz Jahoda

Posters I: FRC Theory

A1. A. Kuthi, University California, Los Angeles
Scaling Laws of Toroidally Coupled FRCs

A2. J. L. Staudenmeier, D. C. Barnes, and H. R. Lewis, Penn State and LANL
Linear Kinetic Stability of an FRC with Two Ion Components

A3. R. Gerwin, Los Alamos National Laboratory
Resistivity at the Field Null of the FRC Plasma

A4. T. Tajima and W. Horton, University Texas at Austin
FRC Collisionless Resistivity

A5. P. -R. Chiang and M. -Y. Hsiao, The Pennsylvania State University
Particle Confinement Time Scaling with Collisional Velocity-Space Particle Loss in FRCs

Posters II: FRC Experiments

B1. S. Sugimoto, Y. Nishizawa, and S. Goto, Osaka University
Tomographic Observation of Two-Dimensional Profile of FIX Plasma

B2. A. L. Hoffman, Spectra Technology, Inc.
Design and Status of the Large s Experiment

B3. D. J. Rej *et al.,* Los Alamos National Laboratory
Initial Results from FRC Compression Experiments on FRX-C/LSM

B4. D. P. Taggart *et al.,* Los Alamos National Laboratory
End-on Soft X-Ray Imaging of FRCs on the FRX-C/LSM Experiment

B5. R. E. Chrien and M. H. Baron, Los Alamos National Laboratory
Neutron Measurements in the FRX-C Magnetic Compression Experiment

B6. M. H. Baron and R. E. Chrien, Los Alamos National Laboratory
Doppler Broadening Measurements in FRX-C/LSM

B7. J. B. Greenly, A. Dunning, and G. D. Rondeau, Cornell University
A 0.1 TW Gas-Breakdown Plasma-Anode Ion Diode

B8. H. H. Fleischmann, Cornell University
Tilt Stabilization of FRCs Using High-Energy Ion Rings: Review of Projections, Present Status, and Development.

Posters III: Spheromaks

C1. C. W. Barnes *et al.*, Princeton Plasma Physics Lab and LANL
The Impedance and Energy Efficiency of a Coaxial Magnetized Plasma Source Used for Spheromak Formation and Sustainment

C2. A. Filuk *et al.*, University of Maryland
Observations and Modeling of Particle Balance on MS

C3. J. -L. Gauvreau, University of Maryland
Observation of Wavelength Profiles During Formation in MS

C4. J. H. Hammer, Lawrence Livermore National Laboratory
Soft X-Ray Production Experiments on the RACE Compact Torus Accelerator

C5. G. J. Marklin, Los Alamos National Laboratory
MHD-Stable High-Beta Spheromak Equilibria

C6. S. Hamaguchi, University Texas at Austin
Anomalous Heat Transport Caused by Ion Temperature Gradient-Driven Turbulence

C7. J. C. Fernandez *et al.*, Los Alamos National Laboratory
Bolometry, Spectroscopy, and Doppler T_i Measurements in High-Current-Density CTX Spheromaks

C8. F. J. Wysocki *et al.*, Los Alamos National Laboratory
Progress with Small, High-Magnetic-Field Spheromaks in CTX

C9. I. Henins *et al.*, Los Alamos National Laboratory
Design of a Spheromak Compressor Driven by High Explosives

C10. R. M. Mayo *et al.*, Los Alamos National Laboratory
Recent Progress on the HESS Experiment

C11. C. R. Sovinec *et al.*, AFWL & MRC
Computational Simulation of Compact Toroidal Plasma Formation

APPENDIX B: Workshop Participants

Naoyuki Amemiya
Dept. of Electrical Engineering
University of Tokyo
Hongo 7-3-1, Bunkyo-ku
Tokyo, 113 Japan

Cris Barnes
Box 451
Princeton Plasma Physics Lab
Princeton, NJ 08543

Daniel C. Barnes
Los Alamos National Lab.
CTR-6, MS F642
Los Alamos, NM 87545

Miles Baron
LANL/Auburn University
CTR-3, MS K638
Los Alamos, NM 87545

Herbert L. Berk
Institute for Fusion Studies
Univ. Texas Austin
RLM 11.222
Austin, TX 78712

Robert Brooks
University of Washington
AERB, FL-10
Seattle, WA 98195

Michael R. Brown
Caltech
Applied Physics Dept / 128-95
Pasadena, CA 91125

Robert E. Chrien
Los Alamos National Lab.
CTR-3, MS K638
Los Alamos, NM 87545

Edward A. Crawford
Spectra Technology, Inc.
2755 Northup Way
Bellevue, WA 98004-1495

Geof Cunningham
Dept. of Physics
University of Manchester
P.O. Box 88
Manchester M60 1QD, U.K.

William F. Dove
ER-543, Office of Fusion
Energy
U. S. Department of Energy
Washington, D.C. 20545

Harry Dreicer
Los Alamos National Lab.
MS F640
Los Alamos, NM 87545

Juan C. Fernández
Los Alamos National Lab.
CTR-5, MS F302
Los Alamos, NM 87545

Alex Filuk
Lab. for Plasma Research
University of Maryland
College Park, MD 20742

Jean-Luc Gauvreau
Lab. for Plasma Research
University of Maryland
College Park, MD 20742

Richard Gerwin
Los Alamos National Lab.
CTR-6, MS F642
Los Alamos, NM 87545

Seiichi Goto
Plasma Physics Lab.
Faculty of Engineering
Osaka University
Yamada-oka, Suita
Osaka 565, Japan

John B. Greenly
Lab. of Plasma Studies
Upson Hall, Cornell Univ.
Ithaca, NY 14853

Satoshi Hamaguchi
Institute for Fusion Studies
University Texas Austin
Austin, TX 78712

James Hammer
Lawrence Livermore Nat. Lab.
L-630, P. O. Box 808
Livermore, CA 94550

Charles Hartman
Lawrence Livermore Nat. Lab.
L-637, P.O. Box 808
Livermore, CA 94550

Ivars Henins
Los Alamos National Lab.
CTR-5, MS F302
Los Alamos, NM 87545

Roger Hess
Lab. for Plasma Research
University of Maryland
College Park, MD 20742

Alan L. Hoffman
Spectra Technology, Inc.
2755 Northup Way
Bellevue, WA 98004-1495

Ming-Yuan Hsiao
231 Sackett Building
Pennsylvania State University
University Park, PA 16802

Akio Ishida
8050 Ikarashi-Ninocho
Niigata University
Niigata, 950-21, Japan

Thomas R. Jarboe
AERB, FL-10
University of Washington
Seattle, WA 98195

Makoto Katsurai
Dept. Electrical Engineering
University of Tokyo
Hongo, Bunkyo-ku
Tokyo 113, Japan

Winfried Kernbichler
Institute for Theoretical
Physics
Graz University of Technology
Petersgasse 16
A-8010 Graz, Austria

Rulon Linford
Los Alamos National Lab.
CTR-DO, MS F640
Los Alamos, NM 87545

George Marklin
Los Alamos National Lab.
CTR-6, MS F642
Los Alamos, NM 87545

Robert Mayo
Los Alamos National Lab.
CTR-5, MS F302
Los Alamos, NM 87545

Richard Milroy
Spectra Technology, Inc.
2755 Northup Way
Bellevue, WA 98004-1495

A. W. Molvik
Lawrence Livermore Nat. Lab.
P.O. Box 5511, L-637
Livermore, CA 94550

Hiromu Momota
Nat. Inst. for Fusion Science
Furo-cho
Nagaya 464-01, Japan

Edward Morse
Nuclear Engineering Dept.
4115 Etcheverry
Univ. California Berkeley
Berkeley, CA 94720

Richard A. Nebel
Los Alamos National Lab.
CTR-6, MS F642
Los Alamos, NM 87545

Masahiro Nishikawa
Faculty of Engineering
Osaka University
2-1, Yamada-oka, Suita
Osaka 565, Japan

Yasuyuki Nogi
Nihon University
108 Kanda Surugadai,
Chiyoda-ku
Tokyo 101, Japan

Masami Ohnishi
Institute of Atomic Energy
Kyoto University
Uji, Kyoto 611, Japan

David Platts
Los Alamos National Lab.
CTR-5, MS F302
Los Alamos, NM 87545

Warren E. Quinn
Los Alamos National Lab.
CTR-DO, MS F640
Los Alamos, NM 87545

Donald J. Rej
Los Alamos National Lab.
CTR-3, MS K638
Los Alamos, NM 87545

Edward Ruden
Weapons Lab/AWX
Kirtland AFB, NM 87117-6008

Edl Schamiloglu
UNM Electrical Eng. Dept.
323C EECE Building
Albuquerque, NM 87131

Anthony G. Sgro
Los Alamos National Lab.
CTR-6, MS F642
Los Alamos, NM 87545

Arthur Sherwood
Los Alamos National Lab.
CTR-DO, MS F640
Los Alamos, NM 87545

Richard Siemon
Los Alamos National Lab.
CTR-3, MS K638
Los Alamos, NM 87545

John Slough
Spectra Technology, Inc.
2755 Northup Way
Bellevue, WA 98004-1495

Carl Sovinec
Weapons Lab/AWX
Kirtland AFB, NM 87117-6008

Russell Stachowski
UC Berkeley
Nuclear Engineering Dept.
Berkeley, CA 94720

Joseph Staudenmeier
231 Sackett Bldg.
Dept. of Nuclear Engineering
Penn State University
University Park, PA 16801

Loren C. Steinhauer
Spectra Technology, Inc.
2755 Northup Way
Bellevue, WA 98004-1495

Satoshi Sugimoto
Plasma Physics Lab.
Faculty of Engineering
Osaka University
2-1 Yamada-oka, Suita-city
Osaka 565, Japan

Daniel P. Taggart
Los Alamos National Lab.
CTR-3, MS K638
Los Alamos, NM 87545

Toshi Tajima
Institute for Fusion Studies
University Texas Austin
Austin, TX 78712

J. B. Taylor
Institute for Fusion Studies
University Texas Austin
Austin, TX 78712

Yukihiro Tomita
Nat. Inst. for Fusion Science
Furo-cho
Nagaya 464-01, Japan

Michel Tuszewski
Los Alamos National Lab.
CTR-3, MS K638
Los Alamos, NM 87545

Bradford L. Wright
Los Alamos National Lab.
CTR-3, MS K638
Los Alamos, NM 87545

Fred Wysocki
Los Alamos National Lab.
CTR-5, MS F302
Los Alamos, NM 87545

AUTHOR INDEX

*U.S. GOVERNMENT PRINTING OFFICE: 1990-0-773-034/20023